# Modeling and Controller Design of a Wind Energy Conversion System Including a Matrix Converter

by

**S. Masoud Barakati**

A thesis

presented to the University of Waterloo

in fulfillment of the

thesis requirement for the degree of

Doctor of Philosophy

in

Electrical and Computer Engineering

Waterloo, Ontario, Canada, 2008

# AUTHOR'S DECLARATION

I hereby declare that I am the sole author of this thesis. This is a true copy of the thesis, including any required final revisions, as accepted by my examiners.

I understand that my thesis may be made electronically available to the public.

# Abstract

In this thesis, a grid-connected wind-energy converter system including a matrix converter is proposed. The matrix converter, as a power electronic converter, is used to interface the induction generator with the grid and control the wind turbine shaft speed. At a given wind velocity, the mechanical power available from a wind turbine is a function of its shaft speed. Through the matrix converter, the terminal voltage and frequency of the induction generator is controlled, based on a constant *V/f* strategy, to adjust the turbine shaft speed and accordingly, control the active power injected into the grid to track maximum power for all wind velocities. The power factor at the interface with the grid is also controlled by the matrix converter to either ensure purely active power injection into the grid for optimal utilization of the installed wind turbine capacity or assist in regulation of voltage at the point of connection. Furthermore, the reactive power requirements of the induction generator are satisfied by the matrix converter to avoid use of self-excitation capacitors.

The thesis addresses two dynamic models: a comprehensive dynamic model for a matrix converter and an overall dynamical model for the proposed wind turbine system.

The developed matrix converter dynamic model is valid for both steady-state and transient analyses, and includes all required functions, i.e., control of the output voltage, output frequency, and input displacement power factor. The model is in the *qdo* reference frame for the matrix converter input and output voltage and current fundamental components. The validity of this model is confirmed by comparing the results obtained from the developed model and a simplified fundamental-frequency equivalent circuit-based model.

In developing the overall dynamic model of the proposed wind turbine system, individual models of the mechanical aerodynamic conversion, drive train, matrix converter, and squirrel-cage induction generator are developed and combined to enable steady-state and transient simulations of the overall system. In addition, the constraint constant *V/f* strategy is included in the final dynamic model. The model is intended to be useful for controller design purposes.

The dynamic behavior of the model is investigated by simulating the response of the overall model to step changes in selected input variables. Moreover, a linearized model of the system is developed at a typical operating point, and stability, controllability, and observability of the system are investigated.

Two control design methods are adopted for the design of the closed-loop controller: a state-feedback controller and an output feedback controller. The state-feedback controller is designed based on the Linear Quadratic method. An observer block is used to estimate the states in the state-feedback controller. Two other controllers based on transfer-function techniques and output feedback are developed for the wind turbine system.

Finally, a maximum power point tracking method, referred to as mechanical speed-sensorless power signal feedback, is developed for the wind turbine system under study to control the matrix converter control variables in order to capture the maximum wind energy without measuring the wind velocity or the turbine shaft speed.

# Acknowledgements

I would like to express my deepest gratitude to my supervisors, Professor Mehrdad Kazerani and Professor J. Dwight Aplevich for their generous support and supervision, and for the valuable knowledge that they shared with me. I learned valuable lessons from their personality and their visions.

I am also grateful to my Doctoral Committee Members, Professor Daniel E. Davison, Professor Claudio A. Canizares, and Professor Amir Khajepour and also the external examiner, Professor M. Reza Iravani.

With great thanks, I want to acknowledge the partial financial support of the Iranian Ministry of Science, Research, and Technology and the Natural Sciences and Engineering Research Council (NSERC) of Canada.

My thanks are also extended to the ECE Department of the University of Waterloo for a nice atmosphere, kind treatment and support.

Special thanks to my friends, Dr. X. Chen, Naghmeh Mansouri and Fariborz Rahimi for their helpful discussion and valuable comments, and also thanks to Mrs Jane Russwurm for proofreading.

My grate thanks to my parents, brothers and sister for their unconditional love and their support during the long years of my studies.

Finally, and most importantly, I would like to express my deep appreciation to my beloved wife, Mehri, for all her encouragement, understanding, support, patience, and true love throughout the ups and downs.

As always, I thank and praise God by my side.

# Dedication

This thesis is dedicated to my mother, my wife, Mehri, and my lovely angel, Samin.

# Table of Contents

# List of Figures

xiii

# List of Tables

# List of Symbols

<u>**A**</u>

$a$ : Constant parameter for adjusting the MC input displacement power factor

$A_i$ : Amplitude of the wind speed fluctuation

$A_i$ : Amplitude of the i$^{th}$ harmonic

$\alpha_{out}$ : Output source phase angle,

$\alpha_i$ : Input source voltage phase angle

$\alpha_o$ : Output voltage angle of the MC

$A_r$ : Area covered by the rotor

<u>**B**</u>

$B$ : Damper with damping coefficient

$\beta$ : Rotor blade pitch angle [rad.]

<u>**C**</u>

$C$ : Input filter capacitor per phase per phase

$C_{final}(s)$ : Final controller matrix

$C_I$ : Capacitance matrix.

$C_p$ : Performance coefficient (or power coefficient)

<u>**D**</u>

$D$ : Transformation matrix

$D^{-1}$ : Inverse transformation matrix of the MC

$D_I(\omega_o)$: Direct transformation matrix of MC

$d_{ij}$ $(i=a,b,c, j=A,B,C)$ : Duty cycle between phase $i$ and phase $j$

$d_j$ : Minimum distance of the $j^{th}$ eigenvalue from the desired region in the s-plan

$\delta\theta = \theta_T - \theta_g / n_{gear}$ : Angle difference

$\delta\omega = \omega_T - \omega_g / n_{gear}$ : Angular speed difference

$DPF_{in}$ : Input displacement power factor

xvii

$DPF_{out}$ : Output displacement power factor

**F**

$\varphi_i$ : MC input displacement angle

$\varphi_o$ : Output (or load) angle of MC current

$f_r$ : Rotor angular speed (in Hz)

$f_o$ : MC output frequency

$f_i$ : MC input frequency

**G**

$G_{aug}(s)$ : Augmented system transformer function matrix

**H**

$h$ : Height at which the wind speed signal

**I**

$I$ : Identity matrix

$\bar{i}_{abc}$ : Input vectors of MC current at input frequency frame

$i_{ABC}$ : Current vector of the output source

$\bar{i}_{abcC}$ : Capacitor current vector

$\bar{i}_{abci}^{D}$ : Fictitious input source current vector

$\bar{i}_{abci}$ : Vector of current of the input source

$\bar{i}_{\alpha\beta\gamma}^{D}$ : Current vector transferred to the MC output frequency frame

$i_i$ *(i=a,b,c)* : Three-phase MC input currents

$i_j$ *(j=A,B,C)* : Three-phase MC output currents

$\bar{i}_{qdoC}^{D}$ Fictions capacitor current vector transferred to *qdo* in the MC output frequency reference frame

$I_r$ : Rotor current

**J**

$J$ : Total shaft moment inertia

$J_G$ : generator rotor inertia

$J_T$ : wind turbine rotor inertia

**K**

$K$ : Feedback gain constant matrix

$K_o^{-1}$ : Inverse matrix of $K_o$

$\zeta^* = cos(\theta^*)$: Acceptable values for damping ratio

$K_I$ : Integrator gain controller

$K_o$ : *abc* to *qdo* transformation matrix

$K_p$ : Proportional gain controller

$K_s$ : stiffness coefficient

$K_{VF}$ : Constant parameter

$K_W$ : Proportionality constant

$L$ : Turbulence length

$\lambda$ : Tip-speed-ratio (TSR)

$\lambda_{opt}$ : Optimal tip-speed-ratio

$L_i$ : Input source plus filter inductance per phase
$L_I$ : Combined inductance matrix of the input source filter

$L_{lr}$ : Rotor inductance (referred to stator circuit)

$L_{ls}$ : stator inductance

$L_M$ : magnetizing inductance

$L_o$ : Output source inductance
**M**

$m_v$: Modulation index of voltage source inverter

## N

*N* : the number of blades

$n_e$ : Number of closed-loop eigenvalues

$n_{gear}$ : Gear box ratio

$n_p$ : Population number

## O

$\omega_T$ : angular speed of the turbine shaft [rad/s]

$\omega_{r_{opt}}$ : Angular shaft speed corresponding to maximum power point

$\omega_{g_{opt}}$ : Optimal mechanical shaft speed

$\omega_{s_{opt}}$ : Optimal generator synchronous speed

$\omega_{P_{max}}$ : Angular shaft speed corresponding to the maximum power

$\omega_i$ : MC input angular speed

$\omega_o$ : MC output angular speed

$\omega_b$ : Base electrical angular speeds

$\omega_e$ : Stator angular electrical frequency

$\omega_{e\_rated}$ : MC rated output frequency

$\omega_g$ : Generator shaft speed [rad/s]

$\omega_{Grid}$ : Generator synchronous frequency

$\omega_{re}$ : rotor electrical angular speed

$\omega_s$ : synchronous speed

## P

*P* : number of poles

$P_{gen-opt}$: Optimal generator powers

$P_{max}$ : Maximum power

$P_{opt}$ : Optimal power

$P_{out}$ : MC active power at the output source terminals

$\psi_i$ : A random phase angle

$\psi_{dr}$ : d-axis rotor flux linkages

$\psi_{ds}$ : d-axis stator flux linkages

$\psi_{qr}$ : q-axis rotor flux linkages

$\psi_{qs}$ : q-axis stator flux linkages

$P_T$ : Mechanical power extracted from turbine rotor

## Q

$Q$ : State weighting matrix of LQ method

$q = V_{om}/V_{im}$: MC output-to-input voltage gain.

$Q_{fic}$ : State weighting matrix of LQ method in observer design

$Q_{out}$ : MC reactive power at the output source terminals

$q_{rated}$ : MC rated voltage gain

## R

$R$ : Turbine rotor radius

$R$ : Output weighting matrix of LQ method

$R_{fic}$ : Output weighting matrix of LQ method in observer design

$R_i$ : Input source resistance per phase
$R_I$ : Combined resistance matrix of the input source filter

$r_{max}$ : Maximum radii

$r_{min}$ : Minimum radii

$R_o$ : Output source resistance per phase
$\rho$: Air density [kg/m$^3$]

$r_r$ : rotor resistance

$r_s$ : stator resistance

**S**

$s$ : slip

$S(\omega)$ spectral density function

$S_{ij}$ $(i=a,b,c, j=A,B,C)$ : Switch between phase $i$ and phase $j$

$\sigma^*$: Acceptable values for real part

$\sigma$ : standard deviation

**T**

$T_e$ : electromechanical torque

$\tau$ : Filter time constant

$T_c$ : Counter torque that is developed in the induction generator

$T_C$ : Induction generator counter-torque

$T_e$ : Generator electromechanical torque

$\theta_{VSI}$: Angle between the reference vector and the closest clockwise state vector

$\theta_{CSI}$: Input space vector angle current

$T_g$ : Induction generator torque

$T_L$: Load torque

$T_{opt}$:  Optimal turbine torque

$T_T$ : Mechanical torque extracted from turbine rotor

$\theta_g$ :Generator shaft angle [rad]

$\theta_T$ : Wind Turbine shaft angle [rad]

**V**

$\overline{v}_{abci}^{D}$ : Fictitious input source voltage vector

$\overline{v}_{abc\_in}$ : Vector of voltage of the input source

$\overline{v}_{ABC\_out}$ : Voltage vector of the output source

$v_{dr}$: $d$-axis rotor voltages

$v_{ds}$: $d$-axis stator voltages

$V_{Gm}$ : Peak value of the grid phase voltage

$V_{Grid\text{-}rated}$ : Grid rated voltage

$v_i, i_i$ $(i=a,b,c)$ : Three-phase MC input voltages

$v_{i\_in,}$ $(i=a,b,c)$ : Three-phase input voltage sources

$V_{im}$ : peak values input voltage magnitudes

$v_j, (j=A,B,C)$ : Three-phase MC output voltage

$v_{j\_out}$ $(j=A,B,C)$ : Three-phase output voltage sources

$V_{m\_in}$ : Input source voltage peak value

$V_{m\_Out}$ : Output source voltage peak value

$\overline{v}_{abc}$ : Input vectors of MC voltages at input frequency frame

$\overline{v}_{ABC}$ : Output voltage vector of MC

$\overline{v}_{\alpha\beta\gamma}^{D}$ : Voltage vector transferred to the MC output frequency frame

$v_{dG}^{D}$ : Grid voltage in the $d$- frame referred to output side

$v_{qG}^{D}$ : Grid voltage in the $q$- frame referred to output side

$V_{oL\_ref}$: Vector line voltage reference

$V_{om}$ : Peak values of output voltage magnitudes

$\overline{v}_{qdoO}^{D}$ Output voltage vector of the MC, $\overline{v}_{ABC}$ , transferred to the $qdo$ reference frame

$v_{qr}$: $q$- axis rotor voltages

$v_{qs}$: $q$-axis stator voltages

$V_W$ : Velocity of the wind [m/s]

$V_{WM}$ : Mean value of wind speed

## $\underline{\textbf{\textit{W}}}$

$W_c$ : Controllability Gramian

$W_o$ : Observability Gramian

## $\underline{\textbf{X}}$

$\hat{x}$ : Estimated state variable vector

$X_{lr}=\omega_e L_{lr}$ : Rotor leakage reactance

$X_{ls}=\omega_e L_{ls}$ : Stator leakage reactance

$X_m=\omega_e L_{ml}$ : Magnetization reactance

# Acronyms

BDFIG: Brushless Doubly-Fed induction generator

DFIG: Doubly-Fed Induction Generator

DPF: Displacement Power Factor

GA: Genetic Algorithm

HAWT: Horizontal-axis wind turbines

IG: Induction Generator

LQ: Linear-Quadratic

MC: Matrix Converter

MIMO: Multi Input Multi Output

MPPT: Maximum Power Point Tracking

O&M: Operation and Maintenance

P&O: Perturbation and Observation

PE: Power Electronic

PEC: Power Electronic Converter

PI: Proportional Integrator

PM: Permanent Magnet

PSF: Power Signal Feedback

PWM: Pulse-Width Modulation

SC: Squirrel-Cage

SCIG: Squirrel-Cage Induction Generator

SISO: Single Input Single Output

SLC: Sequential Loop Closure

SVM: Space Vector Modulation

SVPWM: Space Vector Pulse-Width Modulation

SVD: Singular Value Decomposition

THD: Total Harmonic Distortion

V/f: Voltage/frequency

VAWT: Vertical-axis wind turbine

VSC: Voltage-Source Converters

WECS: Wind Energy Conversion Systems

WR: Wound-Rotor

WRIG: Wound-Rotor Induction Generator

WSM: Wind Speed Measuring

# Chapter 1

# Introduction

## 1.1 Research Motivation

Wind is one of the most abundant renewable sources of energy in nature. The economical and environmental advantages offered by wind energy are the most important reasons why electrical systems based on wind energy are receiving widespread global attention.

### 1.1.1 Growth of Installed Wind Turbine Power

Due to the increasing demand on electrical energy, a considerable amount of effort is being made to generate electricity from new sources of energy. Wind energy is now achieving exponential growth and has great potential. For example, Fig. 1-1 illustrates the installed wind turbine power in Canada and worldwide [1][2]. According to the figure, installed capacity of wind energy system has multiplied fourfold worldwide and more than tenfold in Canada between 2000 until 2006.

   As another example, Ontario had a wind generation capacity of 15MW in 2003. By the end of 2008, that number will jump to over 1,300 MW and put Ontario in first place for wind generation in Canada [3]. Meanwhile, Ontario government has a target to generate 10 per cent of its total energy demand from new renewable sources including wind by 2010.

**Installed Power (MW)** — World

| | '93 | '97 | '98 | 99 | '00 | '01 | '02 | '03 | '04 | '05 | '06 |
|---|---|---|---|---|---|---|---|---|---|---|---|
| World | 3000 | 7475 | 9663 | 13696 | 18039 | 24320 | 31164 | 39290 | 47686 | 59004 | 73904 |

**Installed Power (MW)** — Canada

| | '00 | '01 | '02 | '03 | '04 | '05 | '06 | '07 |
|---|---|---|---|---|---|---|---|---|
| Canada | 137 | 198 | 236 | 322 | 444 | 684 | 1460 | 1588 |
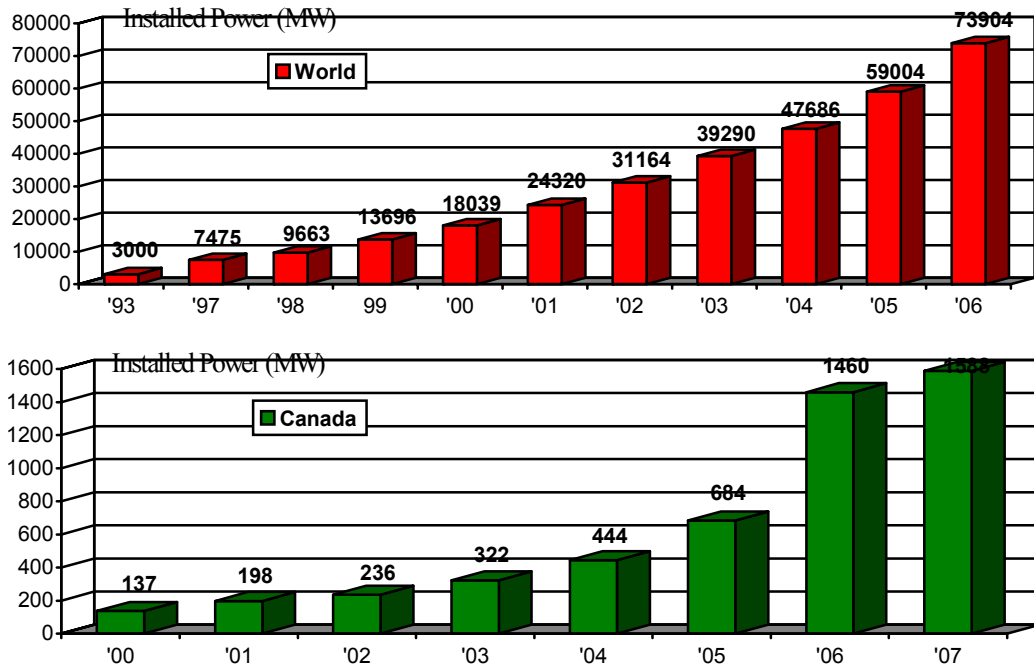
Fig. 1-1: Installed wind turbine power worldwide and in Canada [1][2]

### 1.1.2 Environmental Advantages of Wind Energy

Nowadays, we are faced with environmental disasters that threaten our well-being and existence. Rising pollution levels and dramatic changes in climate demand a reduction in environmentally-damaging emissions. One of the major sources of air pollution is fossil fuel combustion in power plants for producing electricity. Preferred solutions to prevent emissions are using renewable and cleaner energy sources. In fact, for every 1 kWh of electricity generated by wind, the emission of $CO_2$ is reduced by 1kg, and operation of a wind turbine weighing 50 tons prevents burning of 500 tons of coal annually [4].

## 1.2 Historical Background and Literature Survey

Although wind energy was used for the generation of electricity in the 19<sup>th</sup> century, the low price of fossil fuels, such as oil and coal, made this option economically unattractive. With the oil crisis of 1973, research on the modern Wind Energy Conversion Systems (WECS) was revived. First, research was concentrated on making modern wind turbines with larger capacity, which led to the development of enormous machines as research prototypes. At that time, the making of huge turbines

2

was hindered by technical problems and high cost of manufacturing [5]. Therefore, attention was turned to making low-price turbines. These systems comprised of a small turbine, an asynchronous generator, a gearbox, and a simple control method. The turbines had ratings of at least several tens of kilowatts, with normally three fixed blades. In this kind of system, the shaft of the turbine rotates at a constant speed. The asynchronous generator is a proper choice for this system. These low-cost and small-sized components made the price reasonable even for individuals to purchase [6].

As a result of successful research on wind energy conversion systems, a new generation of wind energy systems was developed on a larger scale. During the last two decades, as the industry has gained experience, the production of wind turbines has grown in size and power rating. It means that the rotor diameter, generator rating, and tower height have all increased. During the early 1980s, wind turbines with rotor spans of about 10 to 15 meters, and generators rated at 10 to 65 kW, were installed. By the mid-to late 1980s, turbines began appearing with rotor diameters of about 15 to 25 meters and generators rated up to 200 kW. Today, wind energy developers are installing turbines rated at 200 kW to 2 MW with rotor spans of about 47 to 80 meters. According to American Wind Energy Association (AWEA), today's large wind turbines produce as much as 120 times more electricity than early turbine designs, with Operation and Maintenance (O&M) costs only modestly higher, thus dramatically cutting O&M costs per kWh. Large turbines do not turn as fast, and produce less noise in comparison to small wind turbines [7].

Another modification has been the introduction of new types of generator in wind system. Since 1993, a few manufacturers have replaced the traditional asynchronous generator in their wind turbine designs with a synchronous generator, while other manufacturers have used doubly-fed asynchronous generators.

In addition to the above advances in wind turbine systems, new electrical converters and control methods were developed and tested. Electrical developments include using advanced power electronics in the wind generator system design, and introducing the new concept, namely variable speed. Due to the rapid advancement of power electronics, offering both higher power handling capability and lower price/kW [8], the application of power electronics in wind turbines is expected to increase further. Also, some control methods were developed for big turbines with the variable-pitch blades in order to control the speed of the turbine shaft. The pitch control concept has been applied during the last fourteen years.

A lot of effort has been dedicated to comparison of different structures for wind energy systems, as well as their mechanical, electrical and economical aspects. A good example is the comparison of variable-speed against constant-speed wind turbine systems. In terms of energy capture, all studies come to the same result that variable speed turbines will produce more energy than constant speed turbines [9]. Specifically, using variable-speed approach increases the energy output up to 20% in a typical wind turbine system [10]. The use of pitch angle control has been shown to result in increasing captured power and stability against wind gusts.

For operating the wind turbine in variable speed mode, different schemes have been proposed. For example, some schemes are based on estimating the wind speed in order to optimize wind turbine operation [11]. Other controllers find the maximum power for a given wind operation by employing an elaborate searching method [12]-[14]. In order to perform speed control of the turbine shaft, in attempt to achieve maximum power, different control methods such as field-oriented control and constant Voltage/frequency (*V/f*) have been used [15]-[18].

## 1.3 Wind Energy Conversion System (WECS)

Wind energy can be harnessed by a wind energy conversion system, composed of wind turbine blades, an electric generator, a power electronic converter and the corresponding control system. Fig. 1-2 shows the block diagram of basic components of WECS. There are different WECS configurations based on using synchronous or asynchronous machines, and stall-regulated or pitch-regulated systems. However, the functional objective of these systems is the same: converting the wind kinetic energy into electric power and injecting this electric power into a utility grid.
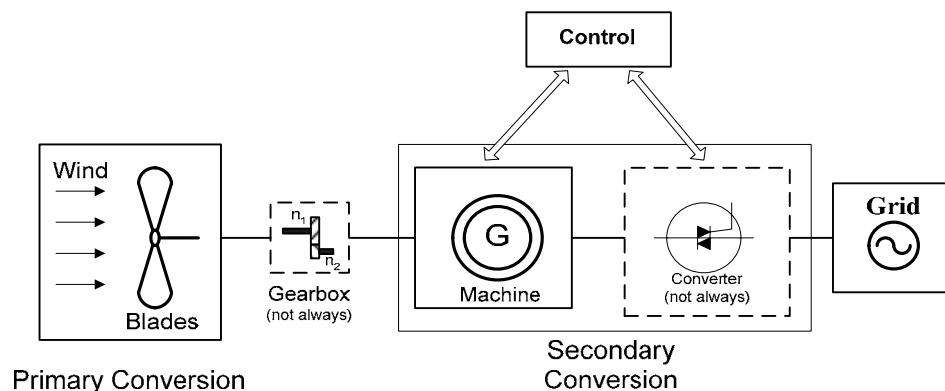


Fig. 1-2: Block diagram of a WECS

As mentioned in the previous section, in the last 25 years, four or five generations of wind turbine systems have been developed [19]. These different generations are distinguished based on the use of different types of wind turbine rotors, generators, control methods and power electronic converters. In the following sections, a brief explanation of these components is presented.

## 1.3.1 Classification of Wind Turbine Rotors

Wind turbines are usually classified into two categories, according to the orientation of the axis of rotation with respect to the direction of wind, as shown in Fig. 1-3 [20][21]:

- Vertical-axis turbines

- Horizontal-axis turbines
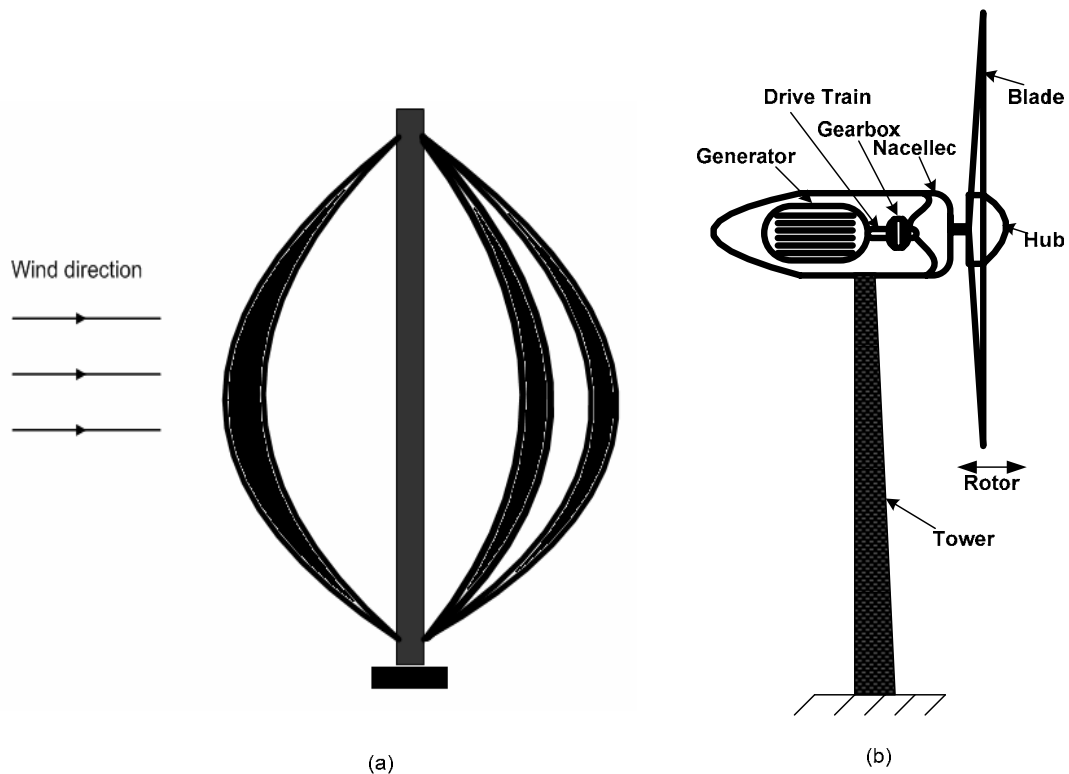
Fig. 1-3: (a) a typical vertical-axis turbine (the Darrius rotor) (b) a horizontal-axis wind turbine

5

## 1.3.1.1 Vertical-axis wind turbine (VAWT)

The first windmills were built based on vertical-axis structure. This type has only been incorporated in small-scale installations. Typical VAWTs include the Darrius rotor, as shown in Fig. 1-3 (a). Advantages of the VAWT [22][23] are:

- Easy maintenance for ground mounted generator and gearbox,

- Receive wind from any direction (No yaw control required), and

- Simple blade design and low cost of fabrication.

Disadvantages of vertical-axis wind turbine are:

- Not self starting, thus, require generator to run in motor mode at start,

- Lower efficiency (the blades lose energy as they turn out of the wind),

- Difficulty in controlling blade over-speed, and

- Oscillatory component in the aerodynamic torque is high.

## 1.3.1.2 Horizontal-axis wind turbines (HAWT)

The most common design of modern turbines is based on the horizontal-axis structure. Horizontal-axis wind turbines are mounted on towers as shown in Fig. 1-3 (b). The tower's role is to raise the wind turbine above the ground to intercept stronger winds in order to harness more energy.

Advantages of the HAWT:

- Higher efficiency,

- Ability to turn the blades, and

- Lower cost-to-power ratio.

Disadvantages of horizontal-axis:

- Generator and gearbox should be mounted on a tower, thus restricting servicing, and

- More complex design required due to the need for yaw or tail drive.

The HAWT can be classified as upwind and downwind turbines based on the direction of receiving the wind, as shown in Fig. 1-4 [24][25]. In the upwind structure the rotor faces the wind directly,

while in downwind structure, the rotor is placed on the lee side of the tower. The upwind structure does not have the tower shadow problem because the wind stream hits the rotor first. However, the upwind needs a yaw control mechanism to keep the rotor always facing the wind. On the contrary, downwind may be built without a yaw mechanism. However, the drawback is the fluctuations due to tower shadow.
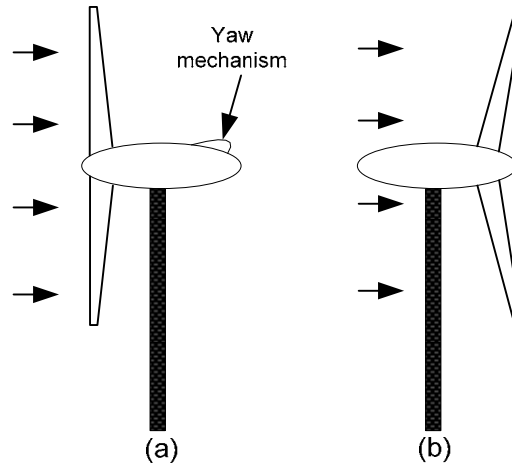


Fig. 1-4: (a) Upwind structure (b) Downwind structure[23]

## 1.3.2 Common Generator Types in Wind Turbines

The function of an electrical generator is providing a means for energy conversion between the mechanical torque from the wind rotor turbine, as the prime mover, and the local load or the electric grid. Different types of generators are being used with wind turbines. Small wind turbines are equipped with DC generators of up to a few kilowatts in capacity. Modern wind turbine systems use three phase AC generators [23]. The common types of AC generator that are possible candidates in modern wind turbine systems are as follows:

- Squirrel-Cage (SC) rotor Induction Generator (IG),

- Wound-Rotor (WR) Induction Generator,

- Doubly-Fed Induction Generator (DFIG),

- Synchronous Generator (With external field excitation), and

- Permanent Magnet (PM) Synchronous Generator.

7

Chapter 1. Introduction

For assessing the type of generator in WECS, criteria such as operational characteristics, weight of active materials, price, maintenance aspects and the appropriate type of power electronic converter, are used.

Historically, induction generator (IG) has been extensively used in commercial wind turbine units. Asynchronous operation of induction generators is considered an advantage for application in wind turbine systems, because it provides some degree of flexibility when the wind speed is fluctuating.

There are two main types of induction machines: squirrel cage (SC), and wound rotor. Another category of induction generator is the doubly fed induction generator (DFIG). The DFIG may be based on the squirrel-cage or wound-rotor induction generator.

The induction generator based on Squirrel-Cage rotor (SCIG) is a very popular machine because of its low price, mechanical simplicity, robust structure, and resistance against disturbance and vibration.

The wound-rotor is suitable for speed control purposes. By changing the rotor resistance, the output of the generator can be controlled and also speed control of the generator is possible. Although wound rotor induction generator has the advantage described above, it is more expensive than a squirrel-cage rotor.

The Doubly-Fed Induction Generator (DFIG) is a kind of induction machine in which both the stator windings and the rotor windings are connected to the source. The rotating winding is connected to the stationary supply circuits via power electronic converter. The advantage of connecting the converter to the rotor is that variable-speed operation of the turbine is possible with a much smaller, and therefore much cheaper converter. The power rating of the converter is often about 1/3 the generator rating [26].

Another type of generator that has been proposed for wind turbines in several research articles is synchronous generator [27]-[29]. This type of generator has the capability of direct connection (direct-drive) to wind turbines, with no gearbox. This advantage is favorable with respect to lifetime and maintenance. Synchronous machines can use either electrically excited or permanent magnet (PM) rotor.

The PM and electrically-excited synchronous generators differ from the induction generator in that the magnetization is provided by a Permanent Magnet pole system or a dc supply on the rotor, featuring providing self-excitation property. Self-excitation allows operation at high power factors and high efficiencies for the PM synchronous.

It is worth mentioning that induction generators are the most common type of generator use in modern wind turbine systems [8].

## 1.3.3 Mechanical Gearbox

The mechanical connection between an electrical generator and the turbine rotor may be direct or through a gearbox. In fact, the gearbox allows the matching of the generator speed to that of the turbine. The use of gearbox is dependent on the kind of electrical generator used in WECS. However, disadvantages using a gearbox are reductions in the efficiency and, in some cases, reliability of the system.

## 1.3.4 Control Method

With the evolution of WECS during the last decade, many different control methods have been developed. The control methods developed for WECS are usually divided into the following two major categories:

- Constant-speed methods, and

- Variable-speed methods.

### 1.3.4.1 Variable-Speed Turbine versus Constant-Speed Turbine

In constant-speed turbines, there is no control on the turbine shaft speed. Constant speed control is an easy and low-cost method, but variable speed brings the following advantages:

- Maximum power tracking for harnessing the highest possible energy from the wind,

- Lower mechanical stress,

- Less variations in electrical power, and

- Reduced acoustical noise at lower wind speeds.

In the following, these advantages will be briefly explained.

Using shaft speed control, higher energy will be obtained. Reference [30] compares the power extracted for a real variable-speed wind turbine system, with a 34-m-diameter rotor, against a constant-speed wind turbine at different wind speeds. The results are illustrated in Fig. 1-5. The figure shows that a variable-speed system outputs more energy than the constant-speed system. For

example, with a fixed-speed system, for an average annual wind speed of 7m/s, the energy produced is 54.6MWh, while the variable-speed system can produce up to 75.8MWh, under the same conditions.
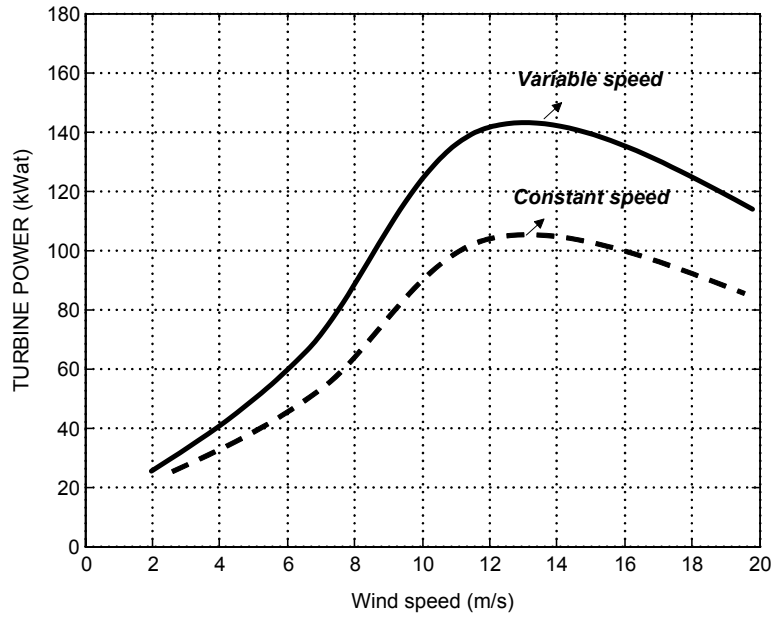


Fig. 1-5: Comparison of power produced by a variable-speed wind turbine and a constant-speed wind turbine at different wind speeds

During turbine operation, there are some fluctuations related to mechanical or electrical components. The fluctuations related to the mechanical parts include current fluctuations caused by the blades passing the tower and various current amplitudes caused by variable wind speeds. The fluctuations related to the electrical parts, such as voltage harmonics, is caused by the electrical converter. The electrical harmonics can be conquered by choosing the proper electrical filter. However, because of the large time constant of the fluctuations in mechanical components, they cannot be canceled by electrical components. One solution that can largely reduce the disturbance related to mechanical parts is using a variable-speed wind turbine. References [31] and [9] compare the power output disturbance of a typical wind turbine with the constant-speed and variable-speed methods, as shown in Fig. 1-6. The figure illustrates the ability of the variable-speed system to reduce or increase the shaft speed in case of torque variation. It is important to note that the disturbance of the rotor is related also to the mechanical inertia of the rotor.

Although variable-speed operation is adopted in modern wind turbines, this method has some disadvantages, such as additional cost for extra components and complex control methods [12][32].



(a)                                         (b)
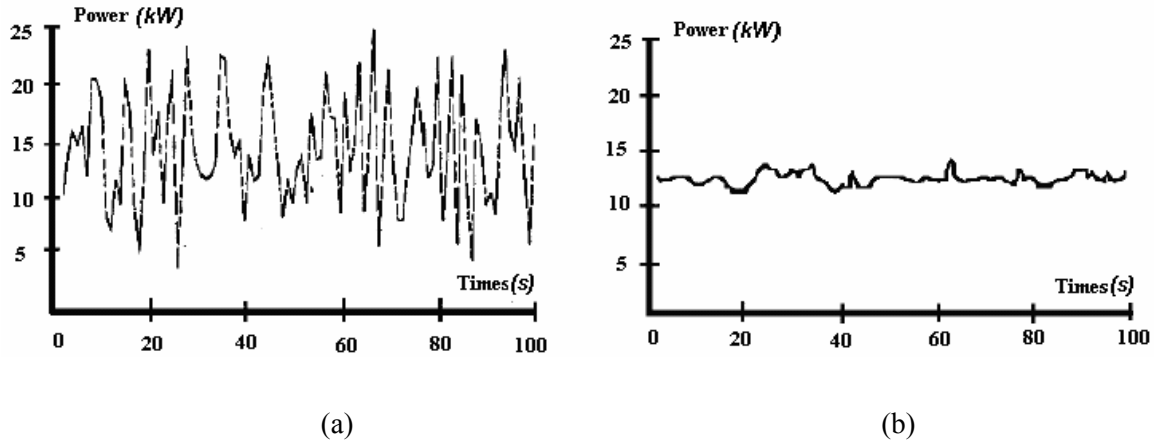
Fig. 1-6: Power output disturbance of a typical wind turbine with (a) constant-speed method and (b) variable-speed methods [31] and [9]

## 1.3.5 Power Electronic Converter

The power electronic (PE) converter has an important role in modern WECS with variable-speed control method. The constant-speed systems hardly include a PE converter, except for compensation of reactive power. The important challenges for the PE converter and its control strategy in a variable-speed WECS are [33]:

- Attain maximum power transfer from the wind, as the wind speed varies, by controlling the turbine rotor speed, and

- Change the resulting variable-frequency and variable-magnitude AC output from the electrical generator into a constant-frequency and constant-magnitude supply which can be fed into an electrical grid.

As a result of rapid developments in power electronics, semiconductor devices are gaining higher current and voltage ratings, less power losses, higher reliability, as well as lower prices per kVA. Therefore, PE converters are becoming more attractive in improving the performance of wind turbine generation systems. It is worth mentioning that the power passing through the PE converter (that determines the capacity the PE converter) is dependent on the configuration of WECS. In some

applications, the whole power captured by a generator passes through the PE converter, while in other categories only a fraction of this power passes through the PE converter.

The most common converter configuration in variable-speed wind turbine system is the rectifier-inverter pair. A matrix converter, as a direct AC/AC converter, has potential for replacing the rectifier-inverter pair structure.

### 1.3.5.1 Back-to-back rectifier-inverter pair

The back-to-back rectifier-inverter pair is a bidirectional power converter consisting of two conventional pulse-width modulated (PWM) voltage-source converters (VSC), as shown in Fig. 1-7. One of the converters operates in the rectifying mode, while the other converter operates in the inverting mode. These two converters are connected together via a dc-link consisting of a capacitor. The dc-link voltage will be maintained at a level higher than the amplitude of the grid line-to-line voltage, to achieve full control of the current injected into the grid. Consider a wind turbine system including the back-to-back PWM VSC, where the rectifier and inverter are connected to the generator and the electrical grid, respectively. The power flow is controlled by the grid-side converter in order to keep the dc-link voltage constant, while the generator-side converter is responsible for excitation of the generator (in the case of squirrel-cage induction generator) and control of the generator in order to allow for maximum wind power to be directed towards the dc bus [82]. The control details of the back-to-back PWM VSC structure in the wind turbine applications has been described in several papers [33]-[36].
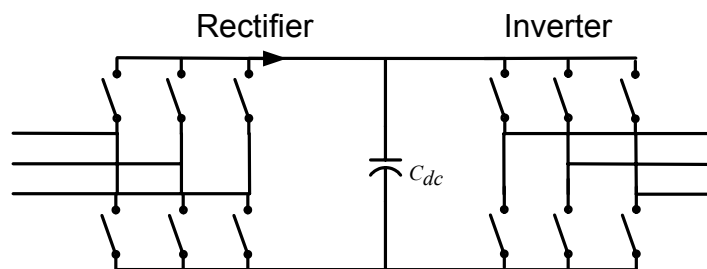


Fig. 1-7: The back-to-back rectifier-inverter converter

Among three-phase AC/AC converters, the rectifier-inverter pair structure is the most commonly used, and thus, the most well-known and well-established. Due to the fact that many semiconductor device manufacturers produce compact modules for this type of converter, the component cost has

gone down. The dc-link energy-storage element provides decoupling between the rectifier and inverter. However, in several papers, the presence of the dc-link capacitor has been considered as a disadvantage. The dc-link capacitor is heavy and bulky, increases the cost, and reduces the overall lifetime of the system [37]-[40].

## 1.3.5.2 Matrix Converter

Matrix converter (MC) is a one-stage AC/AC converter that is composed of an array of nine bidirectional semiconductor switches, connecting each phase of the input to each phase of the output. This structure is shown in Fig. 1-8.

The basic idea behind matrix converter is that a desired output frequency, output voltage and input displacement angle can be obtained by properly operating the switches that connect the output terminals of the converter to its input terminals.

The development of MC configuration with high-frequency control was first introduced in the work of Venturini and Alesina in 1980 [41][42]. They presented a static frequency changer with nine bidirectional switches arranged as a 3×3 array and named it a matrix converter. They also explained the low-frequency modulation method and direct transfer function approach through a precise mathematical analysis. In this method, known as direct method, the output voltages are obtained from multiplication of the modulation transfer matrix by input voltages [43]. Since then, the research on the MC has concentrated on implementation of bidirectional switches, as well as modulation techniques.
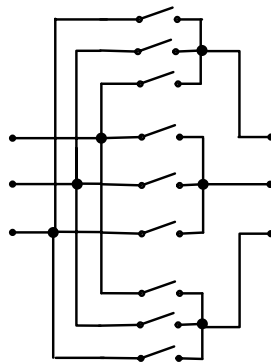


Fig. 1-8: Matrix converter structure

One of practical problems in the implementation of MC is the use of four-quadrant bidirectional switches. Using this type of switch is necessary for successful operation of MC. The earlier works

applied thyristors with external forced commutation circuits to implement the bidirectional controlled switch [44][45], but this solution was bulky and its performance was poor. Monolithic four-quadrant switches are not available to date. However, the introduction of power transistors provided the possibility of implementing four-quadrant switches by anti-parallel connection of two two-quadrant switches. Another problem in implementing MC is the switch commutation problem that produces over-current, due to short circuiting of the ac sources, or over-voltage spikes, due to open circuiting the inductive loads, that can destroy the power semiconductor. Safe commutation has been achieved by the development of several multi-step commutation strategies and the "semi-soft current commutation" technique [46]-[49].

A different modulation method that has been introduced in the literature is the indirect transfer matrix based on a "fictitious dc link". This method was introduced by Rodriguez in 1983 [50]. In this method, based on the conventional PWM technique, at each switching period, each output line connects two input lines that have maximum line-to-line voltage [51]. In 1986, Ziogas [52][53] expanded this method by mathematical analysis. At the same time, another useful modulation method that was introduced instead of PWM was space vector modulation [54][55]. In the next few years, the principles of this method were developed for MC by researchers [56][57].

In 2001, a novel MC topology with a simple switching method, without commutation problems, was developed by Wei and Lipo [58][59]. The improved matrix converter is based on the concept of "fictitious dc link" used in controlling the conventional matrix converter. However, there is no energy storage element between the line-side and load-side converters.

Nowadays, the operational and technological research on MC is continuing [60]. The following items show the state of the art research on MC:

- New topology of MC [59][61],

- Safe and practical commutation strategies [62][63],

- Abnormal operational conditions [64][65],

- Protection issues and ride-through capability [66][67],

- New bidirectional switches and packaging [68][69],

- Input filter design [70][71], and

- New control methods [72][73].

### 1.3.5.3 Comparison of MC with the rectifier-inverter pair

As in the case of rectifier-inverter pair under PWM switching strategy, MC provides low-distortion sinusoidal input and output waveforms, bi-directional power flow, and controllable input power factor [74]. The main advantage of the MC is in its compact design which makes it suitable for applications where size and weight matter, such as in aerospace applications [66][75].

The following drawbacks have been attributed to matrix converters: The magnitude of the MC output voltage can only reach 0.866 times that of the input voltage, input filter design for MC is complex, and because of absence of a dc-link capacitor in the MC structure the decoupling between input and output and ride-through capability do not exist, limiting the use of MC [66][67][76].

In [77] and [78], the efficiencies of an MC and a rectifier-inverter pair with the same ratings are compared. Based on the results, one can conclude that at low switching frequencies, the MC has higher efficiency than the rectifier-inverter pair under PWM. However, adopting different modulation schemes can reduce the switching losses in the rectifier-inverter pair [79]. In an MC, loss reduction is possible by reducing the number of switchings [80] and using a modified SVM approach.

### 1.3.6 Different Configurations for Connecting Wind Turbines to the Grid

The connection of the wind turbine to the grid depends on the type of electrical generator and power electronic converter used. Based on the application of PE converters in the WECS, the wind turbine configurations can be divided into three topologies: directly connected to the grid without any PE converter, connected via full-scale the PE converter, and connected via partially-rated PE converter. In the following, the generator and power electronic converter configurations most commonly used in wind turbine systems are discussed.

As a simple, robust and relatively low-cost system, a squirrel-cage induction generator (SCIG), as an asynchronous machine, is connected directly to the grid, as depicted in Fig. 1-9. For an induction generator, using a gearbox is necessary in order to interface the generator speed and turbine speed. The capacitor bank (for reactive power compensation) and soft-starter (for smooth grid connection) are also required. The speed and power are limited aerodynamically by stall or pitch control. The variation of slip is in the range of 1-2%, but there are some wind turbines based on SCIG in industry with increased rotor resistance and, therefore, increased slip (2-3%). This scheme is used to allow a little bit of speeding up during wind gusts in order to reduce the mechanical stresses. However, this

configuration based on almost fixed speed is not proper for a wind turbine in a higher power range and also for locations with widely varying wind velocity [8][81].
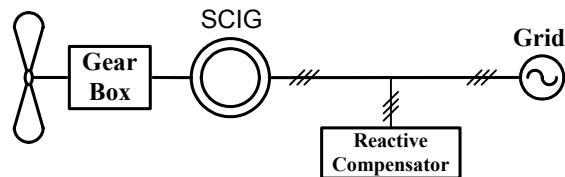


Fig. 1-9: Wind turbine system with SCIG

Three wind turbine systems based on induction generators, with the capability of variable-speed operation are shown in Fig. 1-10 [8][19]. The wind turbine system in Fig. 1-10 (a) uses a wound-rotor induction generator (WRIG). The idea of this model is that the rotor resistance can be varied electronically using a variable external rotor resistance and a PE converter. By controlling the rotor resistance, the slip of the machine will be changed over a 10% range (speed range 2-4%) [8]. In normal operation, the rotor resistance is low, associated with low slip, but during wind gusts the rotor resistance is increased to allow speeding up.

Fig. 1-10 (b) shows a configuration employing a Doubly-Fed Induction Generator (DFIG) and a power electronic converter that connects the rotor winding to the grid directly. With this configuration, it is possible to extend the speed range further without affecting the efficiency. The reason for speed control without loss of efficiency is that slip power can be fed back to the grid by the converter instead of being wasted in the rotor resistance. Note that the power rating of the power converter is $sP_{nom}$ , where '$s$' is the maximum possible slip and $P_{nom}$ is the nominal power of the machine. The rotor slip ($s$) can be positive or negative because the rotor power can be positive or negative, due to the bidirectional nature of power electronic converter. For example, if the power rating of the converter is 10% of the power rating of the generator, the speed control range is from 90% to 110% of the synchronous speed. It means at 110% speed, s=-0.1 and power is fed from the rotor to the grid, whereas at 90% speed, the slip is s=+0.1, and 10% of the power is fed from the grid to the rotor through the converter. With these attributes, i.e., a larger control range and smaller losses, the configuration in Fig. 1-10 (b) is more attractive than the configuration in Fig. 1-10 (a).
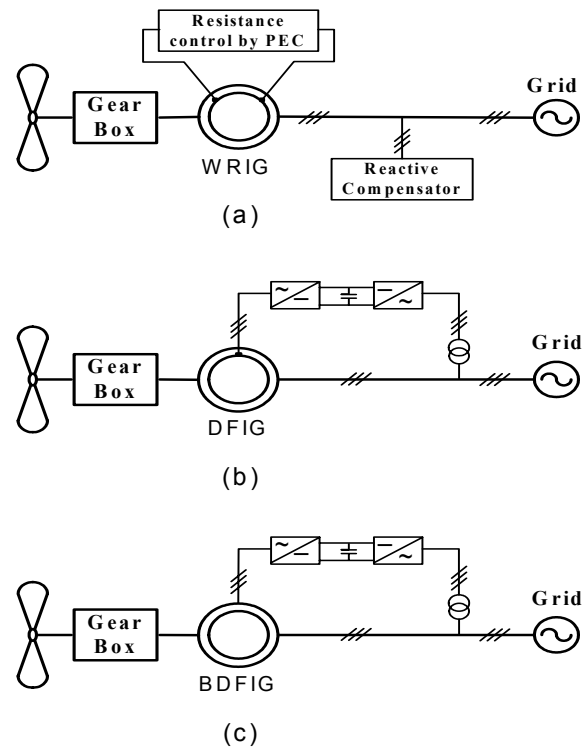
Fig. 1-10: Wind turbine systems based on induction generator with capability of variable-speed operation: (a) Wound-Rotor, (b) Doubly-Fed, and (c) Brushless Doubly-Fed induction generators

In the configurations shown in Fig. 1-10 (a) and Fig. 1-10 (b), with wound-rotor induction generator, the access to the rotor is possible through the slip rings and brushes. Slip rings and brushes cause mechanical problems and electrical losses. In order to solve the problems of using slip rings and brushes one alternative is using the Brushless Doubly-Fed induction generator (BDFIG), shown in Fig. 1-10 (c). In this scheme, the stator windings (main winding) are directly connected to the grid, while the three-phase auxiliary winding is connected to the electrical grid through a PE converter. By using the appropriate control in the auxiliary winding, it is possible to control the induction machine at almost any speed. Also, in this configuration, a fraction of the generator power is processed in the converter.

In the third category, the electrical machine is connected to the electrical grid via a fully-rated converter. It means that the whole power interchanged between the wind turbine and the electrical grid must be passed through a PE converter. This implies extra losses in the power conversion. However this configuration will improve the technical performance. In this configuration, as an electrical machine, it is possible to use induction machine or synchronous machine, as shown in Fig.

1-11 [8][19][82]. Note that the system of Fig. 1-11 (a) uses a gearbox together with a SC induction generator. The systems of Fig. 1-11 (b) and (c) use synchronous generators without a gear box.

The configuration in Fig. 1-11 (b) the synchronous generator needs a small power electronic converter for field excitation, and slip rings. An advantage of using the synchronous generator is the possibility of eliminating the gearbox in the wind turbine (direct-drive wind turbine). Direct drive generators essentially have a large diameter because of the high torque. In gearless drives, induction machines cannot be used because of the extreme excitation losses in these large machines due to the large air gap. However, synchronous machines can be used in direct-drive wind turbines, with either electrically excited or permanent-magnet rotor structures (Fig. 1-11 (c)). Direct-drive systems with permanent magnet excitation are more expensive, because of the high price of magnets, but have lower losses. Nowadays, the price of permanent magnets is decreasing dramatically. Another disadvantage of using permanent magnet synchronous machine is the uncontrollability of its excitation.

All configurations shown in Fig. 1-11 have the same control characteristics since the power converter between the generator and the grid enables fast control of active and reactive power. Also, the generator is isolated from the grid by a dc-link capacitor. But, using fully-rated power electronic converter is the disadvantage of these configurations.

Different wind turbine manufacturers produce different configurations. Comparing different systems from different points of view shows a trade-off between cost and performance.

## 1.3.7 Starting and disconnecting from electrical grid

When wind velocities reach approximately 7 miles per hour wind turbine's blades typically start rotating, but, at 9 to 10 mph, they will start generating electricity. To avoid damage, most turbines automatically shut themselves down when wind speeds exceed 55 to 65 mph. When the wind turbines are connected to or disconnected from the grid, voltage fluctuation and transient currents can occur. The high current can be limited using a soft-start circuit [22].
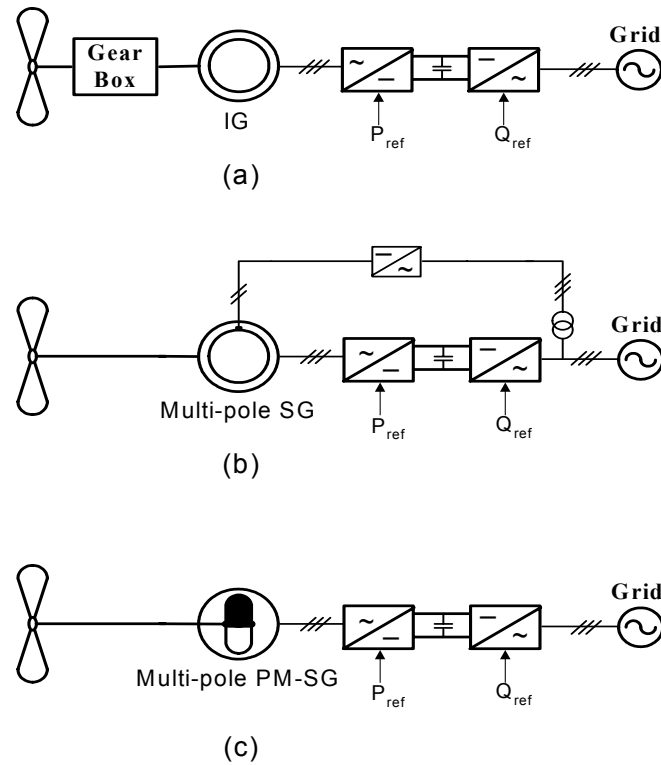
Fig. 1-11: Wind turbine systems with fully-rated power converter between generator terminals and the grid: (a) induction generator with gearbox, (b) synchronous and, (c) PM synchronous generator

## 1.4 Literature Survey on Using Matrix Converters in Wind Turbine Systems

Some researchers have adopted MC as a PE converter in variable-speed wind turbine systems. In reference [83], an MC is used to interface the grid and the induction generator. A closed-loop speed observer is adopted to estimate the generator variables, i.e., shaft speed, generator active power, and stator flux. The main drawback of this method is using an observer that dramatically decreases the gain and phase margin of the system. Also, the closed-loop system needs a reference for the stator flux. Furthermore, the system does not include maximum power point tracking.

A variable-speed wind turbine system with a DFIG, using an MC in the rotor circuit has been presented in [84]. In this system, the MC is used to control the DFIG based on a sliding mode control technique to extract the maximum energy from the wind. The induction generator can operate under

19

or above the synchronous speed with a smooth operation. However, the system needs a stator flux estimator to obtain the current reference. Adding a flux observer adds complexity to the system.

In [85]-[89], the advantages of an MC and a brushless doubly-fed machine (BDFM) are combined in a variable-speed wind turbine system. In these papers, an MC is used to control the generator and capture the maximum energy from the wind. A field-oriented vector control method is used in [85] to control a BDFM in order to capture maximum wind energy and improve the generated electric power quality. The output frequency of the BDFM is kept constant and the output power regulated by controlling the exciting voltage of control winding when the shaft speed of machine varies. This topology needs a turbine shaft speed sensor as well as power and flux estimators. In [86]-[89], the control of BDFM is based on field-oriented vector control and a decoupling control of the active and reactive powers of the generator. The control method suffers from a number of drawbacks due to measuring a lot of variables such as: wind velocity, generator shaft speed, stator and rotor currents, and rotor voltage.

## 1.5 Thesis Objectives

Based on the state-of-the-art in wind energy conversion research discussed above, this work aims to investigate the application of MC in wind energy conversion systems for two reasons: first, MC is an emerging technology with the potential of replacing rectifier-inverter pair, and second, no thorough study of this application has been made.

The main objectives of this thesis are as follows**:**

1- Developing a low-to-medium-power (below 1MW), variable-speed wind turbine system based on a matrix converter and an induction generator,

2- Adopting the MC control functions to control active and reactive powers injected into the grid,

3- Developing a comprehensive dynamic model for the MC to satisfy all functions of the MC, including the control of the displacement power factor,

4- Developing a comprehensive dynamic mathematical model for the wind turbine system including MC to be used for controller design purposes,

5- Control of the induction machine based on constant *V/f* strategy to avoid saturation of the induction generator,

6- Designing a state-feedback and an output-feedback controller for the system to improve the system performance, and

7- Developing a maximum power point tracking method to vary MC control variables in order to capture maximum wind energy, without measuring the wind velocity or the mechanical speed of turbine shaft.

## 1.6 The Proposed Wind Energy Conversion System

Based on the objectives stated in the previous section, a wind energy conversion system based on a squirrel cage induction generator (SCIG) and an MC is proposed. Fig. 1-12 shows the block diagram of the proposed wind energy conversion system.
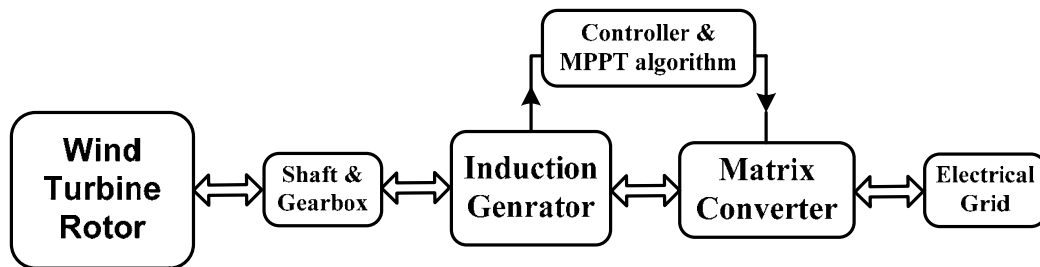


Fig. 1-12: Block diagram of the proposed wind energy conversion system

The SCIG is a low-cost and robust machine and the industry has a lot of experience in dealing with it. In addition, the induction generator has high reliability and the right mechanical properties for wind turbines, such as slip and a certain degree of overload capability. These are the main reasons for choosing this type of generator in the proposal system.

The wind turbine is followed by a gearbox which steps up the shaft speed. Note that working at a low shaft speed translates into a low induction generator terminal frequency which can result in core saturation unless a low terminal voltage is imposed. At low terminal voltages, the operating current will be high, making the scheme impractical.

As a power electronic converter, a matrix converter is used. MC interfaces the SCIG with the grid and implements shaft speed control. In the proposed system, the MC input is connected to the grid and the generator terminals are connected to the MC output. The MC provides direct AC/AC conversion and is considered an emerging alternative to the conventional two-stage AC/DC/AC

converter. MC is highly controllable and allows independent control of the output voltage magnitude, frequency, and phase angle, as well as input power factor. Compared with the dc-link AC/AC converter system, an advantage of MC is the elimination of the dc-link, including bulky capacitors. Therefore, it can be recognized as a full-silicon structure in a compact design. Furthermore, the structure is inherently capable of four-quadrant operation.

The space vector pulse width modulation (SVPWM) technique can be applied to control the switching in an MC, and some solutions such as a four-step switching method and the improved MC topology can be adopted to solve the commutation problem.

The closed-loop controller adjusts the MC controller variables in order to improve the system steady-state and transient performance. The controller including the MPPT method controls the shaft speed to maximize the power captured from the wind.

## 1.7 Thesis Outline

Chapter 2 is dedicated to development and validation of a comprehensive dynamic model for MC in the *qdo* reference frame.

Chapter 3 presents an overall nonlinear dynamic mode for the proposed system in the *qdo* reference frame. The final model is expanded to include the constant *V/f* strategy. Based on the overall model, a linearized model is developed to investigate local stability and system performance.

Chapter 4 discusses the design of a closed-loop feedback controller based on the linear model. A state-feedback controller with observer is designed for the system and evaluated. Then, to improve the system performance, two other controllers based on transfer function techniques are designed.

Chapter 5 starts with introducing three different MPPT methods, i.e., Perturbation and Observation (P&O), Wind Speed Measuring (WSM), and Power Signal Feedback (PSF). Then, the mechanical speed-sensorless PSF method is developed for the wind turbine system under study.

Chapter 6 summarizes the thesis main points and contributions, and proposes future directions for research.

Finally, the thesis ends with appendixes as listed in the table of contents.

# Chapter 2

# Matrix Converter Structure and Dynamic Model

## 2.1 Introduction

Power electronic converters (PECs) play two important roles in modern variable-speed wind energy conversion systems: interfacing the wind turbine to the electrical utility grid and controlling the wind turbine. A static frequency changer can satisfy the requirements of a variable-speed wind turbine. The two main structures that are suitable for this application are: dc-link AC/DC/AC converter and matrix converter (MC). The most common power electronic configuration for SCIG-based variable-speed WECS is an AC/DC/AC converter with a large dc-link capacitor.

The MC provides direct AC/AC conversion and is considered an emerging alternative to the conventional two-stage AC/DC/AC converter topology [60][66]. An MC offers a high degree of controllability that allows independent control of the output voltage magnitude, frequency, and phase angle, as well as the input power factor. When compared with the dc-link AC/DC/AC converter system, a principal feature of the MC is elimination of the dc-link and the bulky capacitors.

In the proposed system, the MC controls the terminal voltage and frequency of the induction generator in such way that the wind turbine is operated at its maximum power point. In addition, the MC implements unity power factor at the interface with the grid. This system targets small-to-medium-power wind turbines.

In this chapter, first the MC topology and its switching method is introduced. Then a comprehensive dynamic model for the MC will be developed which is valid for both steady-state and transient analyses. The comprehensive model satisfies all normal functions of MC, i.e., control of the output voltage magnitude, output frequency, and input displacement power factor. The developed model is in *qdo* reference frame and is based on the MC input and output voltage and current fundamental components. The validity of this model will be confirmed by comparing the results obtained from the model with those obtained from a simplified fundamental-frequency equivalent circuit-based model and the simulation results from PSIM simulation package.

## 2.2 Static Frequency Changer (AC/AC Converter)

A static frequency changer is a converter which can convert ac power at a given frequency to ac power at a different frequency. In this conversion, voltage magnitude and phase angle can be controlled as well. Fig. 2-1 shows the block diagram of a three-phase to three-phase static frequency changer. The side-1 of the static frequency changer is connected to a three-phase ac power supply with balanced sinusoidal voltages at the frequency $f_1$, voltage magnitude $V_1$ and phase angle $\varphi_1$, while a three-phase load is connected on side-2. The frequency changer converters the three-phase balanced sinusoidal voltage on side-1 to a three-phase balanced sinusoidal system on side-2 at new electrical characteristics, frequency $f_2$, voltage magnitude $V_2$ and voltage phase angle $\varphi_2$ [90].
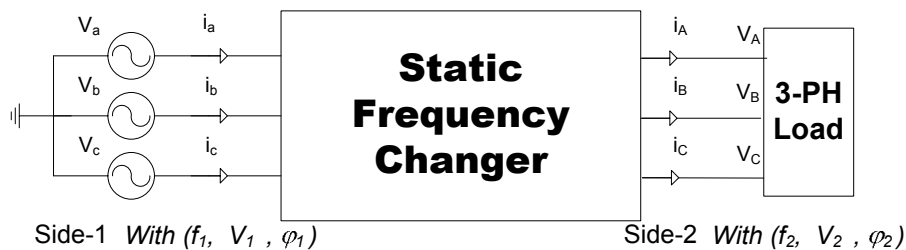


Fig. 2-1: Block diagram of a three-phase to three-phase static frequency changer

From the viewpoint of structure, static frequency changers are divided into two categories: two-stage or rectifier-inverter pair (indirect topology), and single-stage (direct topology). The term direct

means that the energy does not appear in the form of dc in the conversion process. Therefore, electrical energy can be transferred between the input and output of the converter without a dc-link. A single-stage static frequency changer can be realized by thyristors. In that case, it is called a naturally-commutated cycloconverter, featuring restricted frequency conversion. It is also possible to realize a single-stage static frequency changer by controllable switches. In this case, it is called a forced-commutated cycloconverter or a Matrix Converter (MC).

## 2.3 Matrix Converter Structure

The structure of a MC is shown in Fig. 2-2 and the parameters of the circuit are defined in Table 2.1 The MC connects the three-phase ac voltages on input side to the three-phase voltages on output side by a 3×3 matrix (or array) of bi-directional switches. In total, MC needs 9 bi-directional switches, one switch between each input phase and each output phase. A second-order L-C filter is used at the input terminals to filter out the high frequency harmonics of the input currents [90]-[92].

The MC, as an AC/AC converter, satisfies the requirement of providing a sinusoidal voltage on the load side and a sinusoidal current on the source side. Meanwhile, it is possible to adjust the input displacement angle and control the output voltage magnitude and phase angle by properly operating the switches. Since there is no dc-link as compared with a two-stage conventional AC/DC/AC converter, MC can be recognized as a full-silicon structure in a compact design. Also, the structure is inherently capable of a four-quadrant operation, with the output voltage and input current sinusoidally shaped with low distortion.

The disadvantages of a MC are in the high number of devices in the power circuit (18 switches and 18 diodes) and complexity of topology. Appendix A explains the practical switch configurations and compares the bidirectional switch structures for the MC.
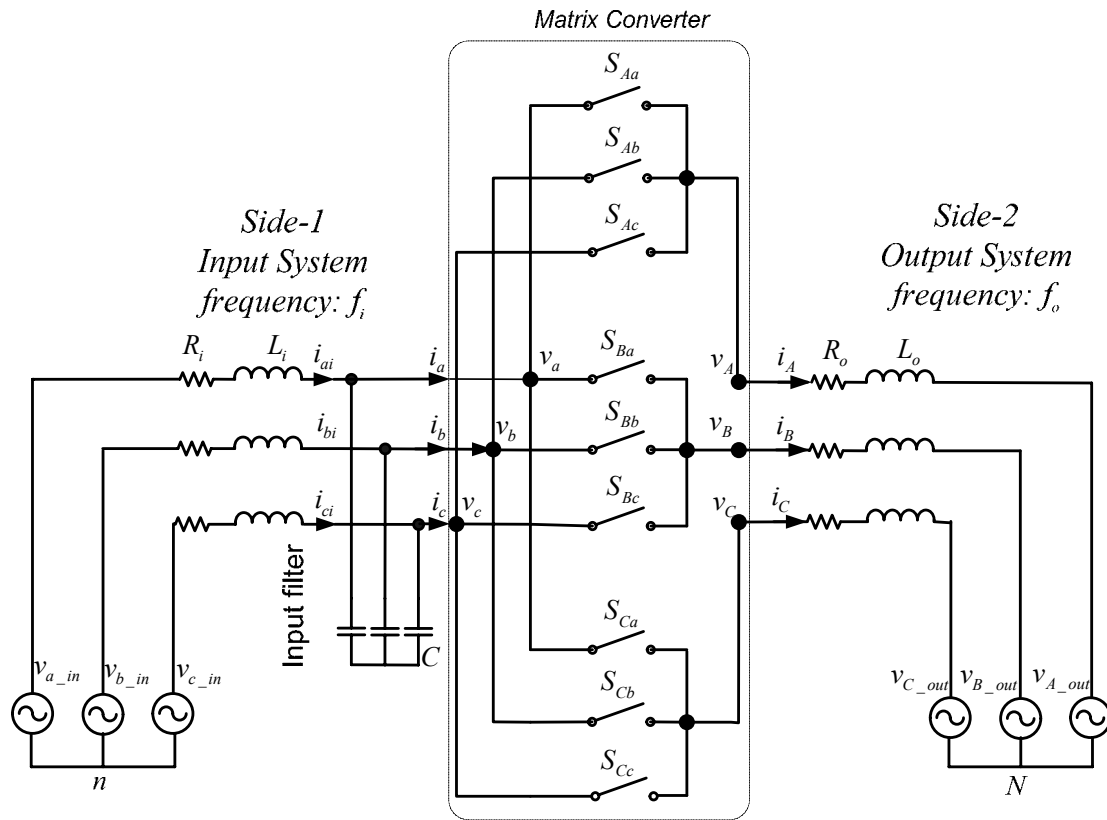
Fig. 2-2: A matrix converter circuit

Table 2.1: Parameters of the MC circuit.

| Parameters | Descriptions |
|---|---|
| $v_i, i_i$   (i=a,b,c) | Three-phase MC input voltages and currents |
| $v_j, i_j$   (j=A,B,C) | Three-phase MC output voltage and currents |
| $v_{i\_in,}$   (i=a,b,c) | Three-phase input voltage sources |
| $v_{j\_out}$ (j=A,B,C) | Three-phase output voltage sources |
| $R_i$ | Input source resistance per phase |
| $L_i$ | Input source plus filter inductance per phase |
| $C$ | Input filter capacitor per phase per phase |
| $R_o$ | Output source resistance per phase |
| $L_o$ | Output source inductance |
| $S_{ij}$ (i=a,b,c, j=A,B,C ) | Switch between phase $i$ and phase $j$ |

26

## 2.4 Modulation Strategy for the Matrix Converter

In the MC the switching method should be chosen in such a way that the output voltages have sinusoidal waveforms at the desired frequency, magnitude and phase angle. Also, the input currents should be sinusoidal at the desired displacement power factor. In order to achieve this target, a proper choice of the switching pattern should be applied to the switches of the MC in a switching period. A proper switching pattern is obtained by choosing a suitable modulation method. The modulation problem in general starts with choosing a switching function for the switches of the MC as follows [60][93]:

$$S_{ij}(t) = \begin{cases} 1 & , \quad S_{ij} \qquad closed \\ 0 & , \quad S_{ij} \qquad open \end{cases}, \qquad i = A, B, C, \quad j = a, b, c. \tag{2.1}$$

The following constraint applies to the switching functions:

$$S_{ia} + S_{ib} + S_{ic} = 1, \qquad i = A, B, C. \tag{2.2}$$

This constraint comes from the fact that MC is supplied from a voltage source and generally feeds an inductive load. Connecting more than one input phase to one output phase causes a short circuit between two input sources (Fig. 2-3(a)). Also, disconnecting all input phases from an output phase results in an open circuit in the load (Fig. 2-3 (b)) [55].
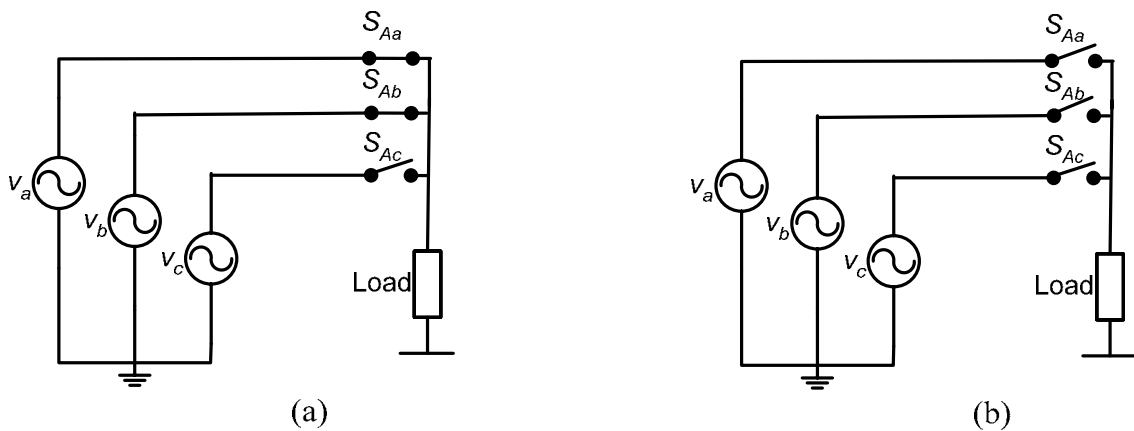


Fig. 2-3: Undesirable situations in MC: (a) short circuit of input sources (b) open circuit of inductive load

27

By considering two states for each switching function based on (2.1), there are 512 states for a total of 9 switches in the MC. By applying the constraint (2.2) to the switching algorithms of the MC of Fig. 2-2, only 27 allowable combinations can exist. These switching state combinations are shown in Appendix B.

Finding a proper modulation strategy for MC starts with considering a set of input and output voltages and currents, based on MC circuit of Fig. 2-2, as follows:

$$\overline{v}_{abc} = \begin{bmatrix} v_{an} \\ v_{bn} \\ v_{cn} \end{bmatrix}, \ \overline{v}_{ABC} = \begin{bmatrix} v_{AN} \\ v_{BN} \\ v_{CN} \end{bmatrix}, \ \overline{i}_{abc} = \begin{bmatrix} i_a \\ i_b \\ i_c \end{bmatrix}, \ \overline{i}_{ABC} = \begin{bmatrix} i_A \\ i_B \\ i_C \end{bmatrix},$$

(2.3)

where $\overline{v}_{abc}$ and $\overline{v}_{ABC}$ are the MC input and output phase-to-neutral voltage vectors, and $\overline{i}_{abc}$ and $\overline{i}_{ABC}$ are the MC input and output current vectors.

Based on the definition of switching function given by (2.1), the MC instantaneous switching function matrix is as follows [90]-[95]:

$$S = \begin{bmatrix} S_{Aa} & S_{Ab} & S_{Ac} \\ S_{Ba} & S_{Bb} & S_{Bc} \\ S_{Ca} & S_{Cb} & S_{Cc} \end{bmatrix}.$$

(2.4)

The input-side and output-side voltages and currents are related by the following equations:

$$\overline{v}_{ABC} = S \cdot \overline{v}_{abc}, \ \text{and} \ \overline{i}_{abc} = S^T . \overline{i}_{ABC},$$

(2.5)

where $S^T$ is the transpose of $S$. The elements of $S$ should be chosen properly to obtain the desired fundamental components of output voltages and input currents. This means that in a certain period of time, the switches of the MC have to be turned on and off according to a specific switching pattern.

Assuming that the switching frequency is much higher than the input and output frequencies, the switching functions can be replaced by their low-frequency components, as far as the fundamental components of input-side and output-side voltages and currents are concerned. Based on this, the switching functions in $S$ can be replaced by the 'duty cycles' of switches. The duty cycle is defined as:

$$d_{ij}(t) = \frac{t_{ij}}{T_{Seq}}, \qquad i = A, B, C \qquad j = a, b, c, \tag{2.6}$$

where $t_{ij}$ is the ON period of the switch $ij$ in a switching sequence time. For example, as illustrated in Fig. 2-4, during a certain sequence period $T_{seq}$, the output phase *"A"* is connected to input phase *"a"* during time period $t_{Aa}$ and is connected to phase *'b'* and *'c'* during time periods $t_{Ab}$ and $t_{Ac}$ , respectively [60].
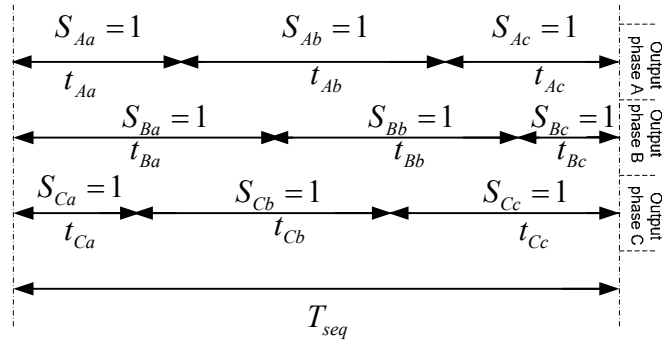


Fig. 2-4: The switching pattern in a sequence period

The following two restrictions apply to the duty cycle based on the (2.2):

$$\begin{cases} 0 \le d_{ji} \le 1 \\ d_{ja} + d_{jb} + d_{jc} = 1 \end{cases}, \quad j \in (A, B, C), \quad i \in (a, b, c). \tag{2.7}$$

By considering the duty cycles of the switches, the matrix S can be replaced by matrix D, given by (2.8), where elements are the low-frequency components (or local averages) of $S$ matrix elements.

$$D = \begin{bmatrix} d_{Aa} & d_{Ab} & d_{Ac} \\ d_{Ba} & d_{Bb} & d_{Bc} \\ d_{Ca} & d_{Cb} & d_{Cc} \end{bmatrix}. \tag{2.8}$$

The matrix $D$ is called modulation matrix or low-frequency transformation matrix.

The solution to the modulation problem is that of finding the elements of matrix $D$ in such a way that the desired output voltage and input current vectors are obtained, and the restrictions given by (2.7) are satisfied. Therefore the equation (2.5) can be rewritten as [91][93][94]

$$\bar{v}_{ABC} = D \cdot \bar{v}_{abc}, \text{ and } \bar{i}_{abc} = D^T . \bar{i}_{ABC},$$ (2.9)

where $\bar{v}_{abc}$ and $\bar{i}_{ABC}$ are a set of sinusoidal input voltages and output currents, and $\bar{v}_{ABC}$ and $\bar{i}_{abc}$ are the desired fundamental-frequency output voltages and input currents at the MC terminals.

Based on the concept of high-frequency switching and low-frequency transfer function, the following steps should be taken in finding a control method for the MC:

- choosing a modulation algorithm based on the structure of the transformation matrix,
- finding a proper duty cycle formula, $d_{ij}$, for switching to realize the transformation matrix and satisfy the duty cycle restrictions, given by equation (2.7), and
- determining the states of the nine switches in the MC in each sequence period based on the duty cycle.

Appendix C is dedicated to describing two major modulation algorithms, i.e., direct and indirect approaches. The indirect method, which is based on the concept of fictitious rectifier-inverter pair and dc-link, is an appropriate method for implementing Pulse Width Modulation (PWM) and Space Vector PWM (SVPWM) techniques. The details of the (SVPWM) technique are given in Appendix C. In addition, a comparison between PWM and SVPWM modulation techniques is presented in Appendix D.

## 2.5 Commutation Problems in Matrix Converter

As mentioned in previous section, in order to avoid short circuiting the input lines, no two bidirectional switches should be switched on to the same output phase at any instant. Also, for preventing an open circuit in inductive load on the output side of the MC, bidirectional switches linked to the same output phase should not all be turned off at any instant. Since practical semiconductor switches have propagation delays and finite switching times, switches cannot be switched on and off instantaneously. These two issues are commutation problems in the MC that are more difficult to overcome than in conventional voltage source converters. The following two solutions have been pointed out in the literatures for the commutation problems in MC:

- Safe commutation in switching sequence
- Indirect MC topology

Appendix E is dedicated to describing these solutions.

## 2.6 Simulation Results of the Matrix Converter Based on SVPWM

In this section, the simulation results of a MC circuit, Fig. 2-2, using the SVPWM technique are presented. Fig. 2-5 illustrates the MC circuit set up in PSIM environment. This circuit is implemented in MC module of Fig. 2-6. This figure shows the whole system required for simulation of the MC based on the SVPWM technique. The DLL block executes the SVPWM method and contains four control variables (or desired values) that can be used to control the MC output voltage magnitude, frequency and phase angle, as well as the input displacement angle.

As an example to assess the performance of MC of Fig. 2-6, the input source characteristics, control variables and load characteristics are set as follows:

- Input Source: $V_{in\text{-}peak}$=140V (Phase-to-Neutral), $f_{in}$=60Hz,

- MC control variables: Voltage gain = 0.571, output frequency =75Hz, output voltage angle=0, input displacement power factor=1, and

- Load: Three-phase RL load (Y-connected), $R_{load}$=20Ω, $L_{load}$=50mH (all per phase).

Fig. 2-7 shows the results of simulation. As shown in the figure, the fundamental components of the output line-to-line voltages, output currents and input currents are sinusoidal. The simulation results confirm that the desired values for the output frequency, voltage magnitude and phase angle, as well as the input displacement angle are achievable. Fig. 2-7 (a) shows the output frequency is 75 Hz. Also, Fig. 2-7 (d) illustrates that the input phase current and voltage are in-phase, due to the fact that the input displacement angle is set to zero.
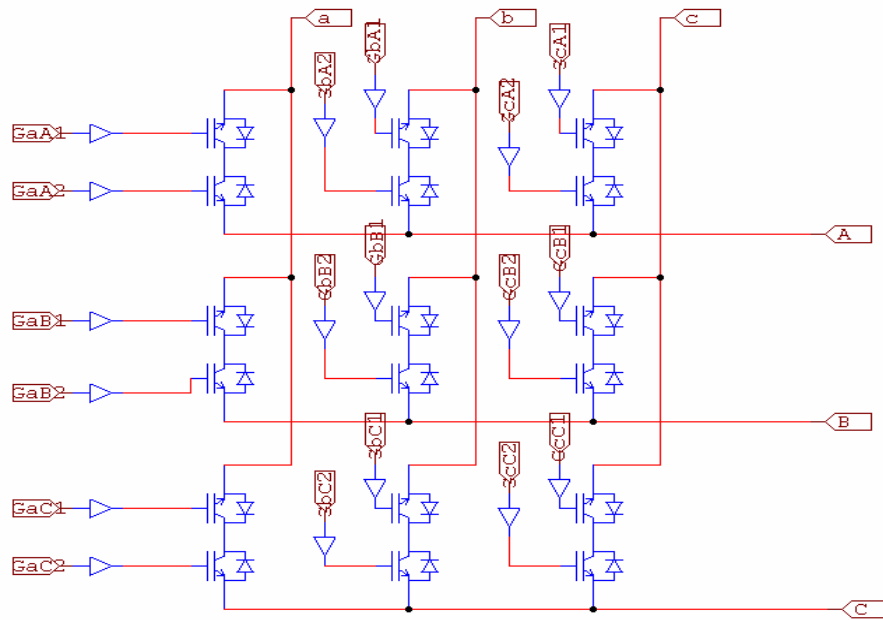
Fig. 2-5: Implementing MC circuit in PSIM environment
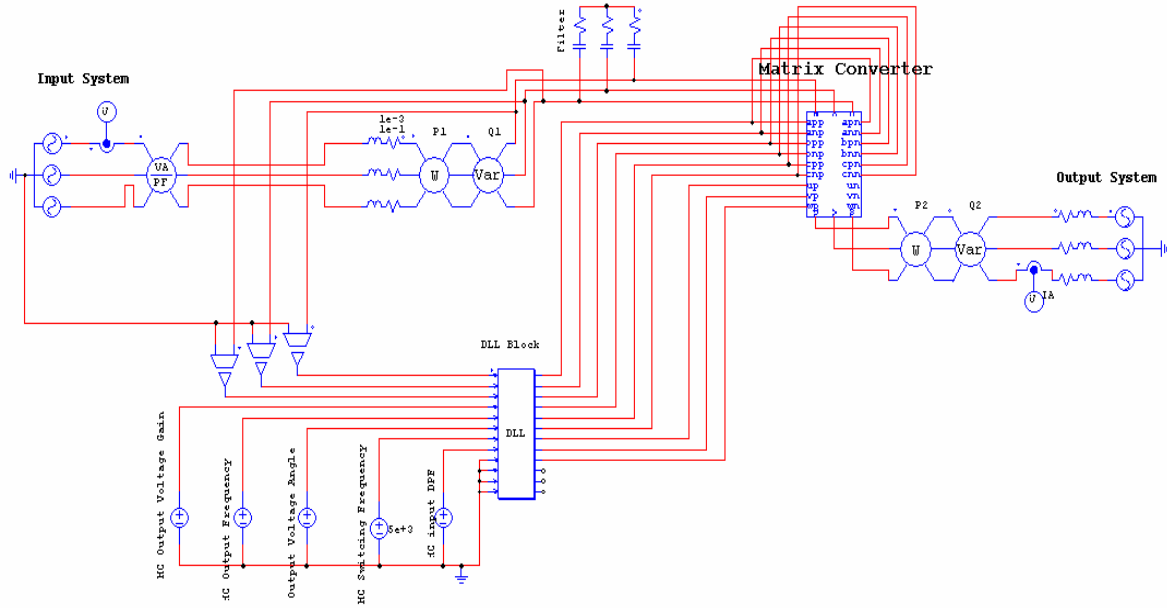


Fig. 2-6: Implementing the whole MC system in PSIM environment for simulation based on the SVPWM technique, DLL block executes the SVPWM method
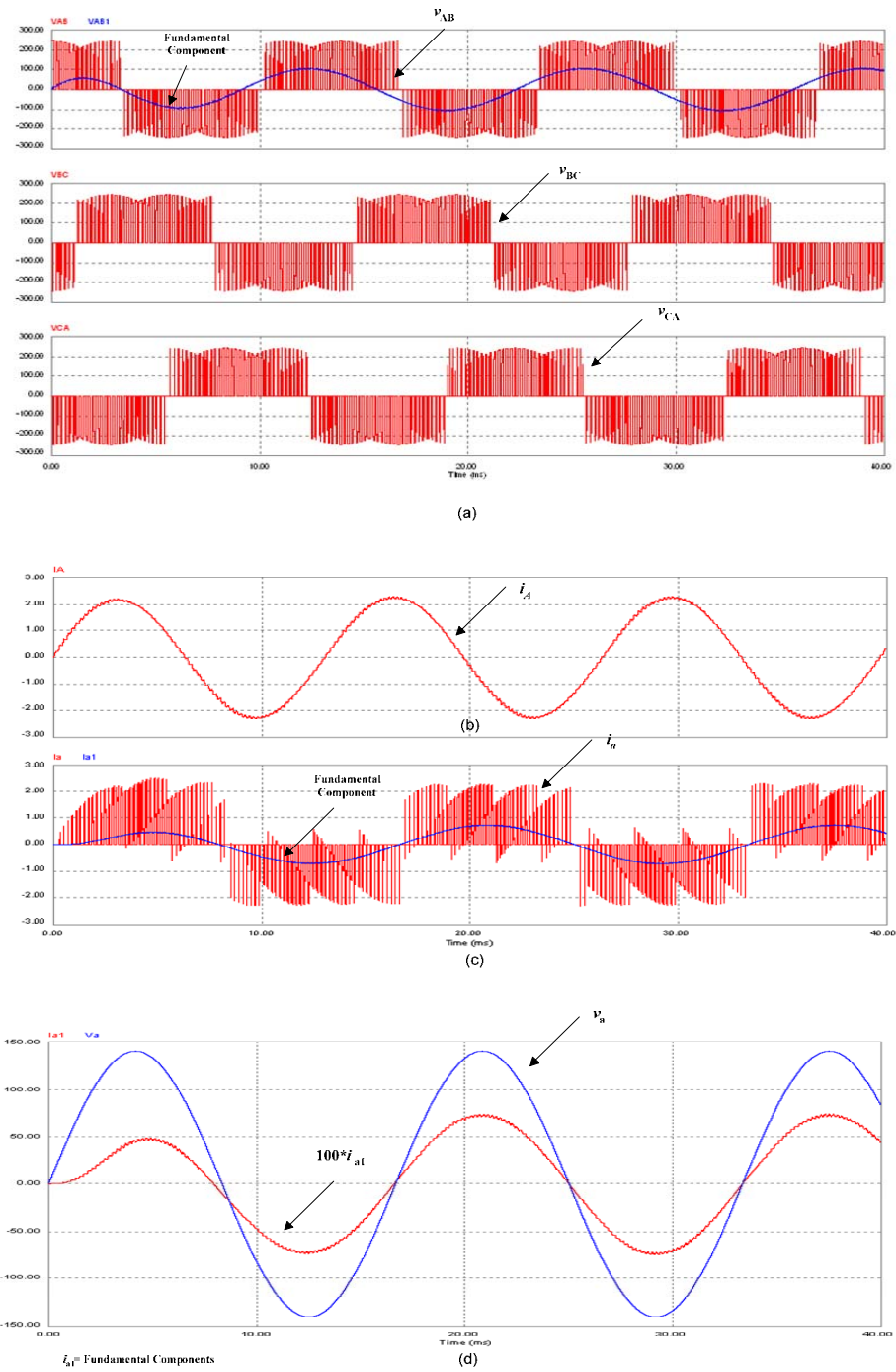
Fig. 2-7: Simulation results of the MC: (a) output line-to-line voltages, (b) phase-A output current, $i_A$, (c) phase-a input current, $i_a$, and (d) phase-a input phase voltage, $v_a$ , and input current fundamental component, $i_{a1}$.

33

## 2.7 An Overall Dynamic Model for a the Matrix Converter System

In this section, a comprehensive dynamic model for a matrix converter (MC) is developed which is valid for both steady-state and transient analyses. The comprehensive model includes all normal functions of the MC, i.e., control of the output voltage magnitude, output frequency, and input displacement power factor. The model is in the *qdo* reference frame for the MC input and output voltage and current fundamental components. The validity of this model is confirmed by comparing the results obtained with those of a simplified fundamental-frequency equivalent circuit-based model and the simulation results from PSIM package.

### 2.7.1 Low- Frequency Transformation Matrix

As mentioned in section 2.4, as far as the fundamental components of the MC input and output voltages and currents are concerned, the switching function matrix *S* can be replaced by the transformation matrix *D*. The transformation matrix D should satisfy the following three requirements:

  (a)  restrictions on duty cycle, described by equation (2.2),

  (b)  sinusoidal output voltages with controllable frequency, magnitude and phase angle,

  (c)  sinusoidal input currents,

  (d)  desired input displacement power factor.

The following low-frequency transformation matrices are two basic solutions that individually satisfy the requirements (a), (b) and (c) [55][60][91][93][94].

$$D_1 = \frac{1}{3}\begin{bmatrix} 1+2q\cos(\theta_{s1}) & 1+2q\cos(\theta_{s1}-2\pi/3) & 1+2q\cos(\theta_{s1}+2\pi/3) \\ 1+2q\cos(\theta_{s1}+2\pi/3) & 1+2q\cos(\theta_{s1}) & 1+2q\cos(\theta_{s1}-2\pi/3) \\ 1+2q\cos(\theta_{s1}-2\pi/3) & 1+2q\cos(\theta_{s1}+2\pi/3) & 1+2q\cos(\theta_{s1}) \end{bmatrix} \qquad (2.10)$$

$$D_2 = \frac{1}{3}\begin{bmatrix} 1+2q\cos(\theta_{s2}) & 1+2q\cos(\theta_{s2}-2\pi/3) & 1+2q\cos(\theta_{s2}+2\pi/3) \\ 1+2q\cos(\theta_{s2}-2\pi/3) & 1+2q\cos(\theta_{s2}+2\pi/3) & 1+2q\cos(\theta_{s2}) \\ 1+2q\cos(\theta_{s2}+2\pi/3) & 1+2q\cos(\theta_{s2}) & 1+2q\cos(\theta_{s2}-2\pi/3) \end{bmatrix} \qquad (2.11)$$

where $\theta_{s1} = \omega_i t - (\omega_o t + \alpha_o)$ , $\theta_{s2} = \omega_i t + (\omega_o t + \alpha_o)$, $\omega_i = 2\pi f_i$, $f_i$ : MC input frequency, $\omega_o = 2\pi f_o$, $f_o$ : output frequency of the MC, $\alpha_o$ : output voltage angle of the MC (input voltage angle as a

reference), and $q=V_{om}/V_{im}$: MC output-to-input voltage gain. Note that $0 \le q \le 0.87$ and $V_{om}$ and $V_{im}$ are peak values of output and input voltage magnitudes.

It is worth mentioning that matrices $D_1$ and $D_2$ satisfy the duty cycle restriction, giving by equation (2.2), and are invertible, a property useful for future calculations.

Note that neither $D_1$ nor $D_2$ alone can control the input displacement power factor. In fact, matrix $D_1$ gives the same phase displacement at the input as at the output, whereas matrix $D_2$ yields a phase displacement at the input equal in magnitude and opposite in sign to that at the output [94][95]. However, the combination of the two transformation matrices given by (2.12) provides controllability of input displacement power factor.

$$D = aD_1 + (1-a)D_2 \,.$$
(2.12)

In (2.12), $a$ is a constant parameter varying between 0 and 1 ($0 \le a \le 1$).

In order to get a unity displacement power factor at the MC input terminals, the parameter $a$ should be set at 0.5. Note that this dose not result in a unity displacement power factor at input source terminals.

### 2.7.2 Output voltage and input current of Matrix Converter

To find the output terminal voltage and input terminal current, consider the low-frequency transformation function (2.12) and a set of sinusoidal input voltages, as follows:

$$\overline{v}_{abc} = V_{im} \begin{bmatrix} \cos(\omega_i t) \\ \cos(\omega_i t - 2\pi/3) \\ \cos(\omega_i t + 2\pi/3) \end{bmatrix},$$
(2.13)

where $\varphi_o$ is the output (or load) angle. Using equation (2.9), the MC output voltages can be written as follows:

$$\overline{v}_{ABC} = D\overline{v}_{abc} = (aD_1 + (a-1)D_2)\overline{v}_{abc} = qV_{im} \begin{bmatrix} \cos(\omega_o t + \alpha_o) \\ \cos(\omega_o t + \alpha_o - 2\pi/3) \\ \cos(\omega_o t + \alpha_o + 2\pi/3) \end{bmatrix}.$$
(2.14)

The output currents will be therefore be:

$$\bar{i}_{ABC} = I_{om} \begin{bmatrix} \cos(\omega_o t + \alpha_o + \varphi_o) \\ \cos(\omega_o t + \alpha_o + \varphi_o - 2\pi/3) \\ \cos(\omega_o t + \alpha_o + \varphi_o + 2\pi/3) \end{bmatrix}. \tag{2.15}$$

Using equation (2.9), the input currents will be as follows:

$$\bar{i}_{abc} = D^T \bar{i}_{ABC} = qI_{om} \left\{ a \begin{bmatrix} \cos(\omega_i t + \varphi_o) \\ \cos(\omega_i t + \varphi_o - 2\pi/3) \\ \cos(\omega_i t + \varphi_o + 2\pi/3) \end{bmatrix} + (1-a) \begin{bmatrix} \cos(\omega_i t - \varphi_o) \\ \cos(\omega_i t - \varphi_o - 2\pi/3) \\ \cos(\omega_i t - \varphi_o + 2\pi/3) \end{bmatrix} \right\}. \tag{2.16}$$

Assume the desired input currents to be :

$$\bar{i}_{abc} = I_{im} \begin{bmatrix} \cos(\omega_i t + \varphi_i) \\ \cos(\omega_i t + \varphi_i - 2\pi/3) \\ \cos(\omega_i t + \varphi_i + 2\pi/3) \end{bmatrix}, \tag{2.17}$$

where $\varphi_i$ is input displacement angle. Then, one can write:

$$qI_{om}\{a\cos(\omega_i t + \varphi_o) + (1-a)\cos(\omega_i t - \varphi_o)\} = I_{im}\cos(\omega_i t + \varphi_i),$$

and after expanding,

$$qI_{om}\{\cos(\omega_i t)\cos(\varphi_o) + (1-2a)\sin(\omega_i t)\sin(\varphi_o)\}$$
$$= I_{im}\{\cos(\omega_i t)\cos(\varphi_i) - \sin(\omega_i t)\sin(\varphi_i)\}. \tag{2.18}$$

Equations (2.18) can be manipulated to obtain the following:

$$qI_{om}\cos(\varphi_o) = I_{im}\cos\varphi_i, \tag{2.19}$$

$$qI_{om}(1-2a)\sin(\varphi_o) = -I_{im}\sin\varphi_i. \tag{2.20}$$

From equations (2.19) and (2.20), one can deduce:

$$a = \frac{1}{2}(1 + \frac{\tan\varphi_i}{\tan\varphi_o}). \tag{2.21}$$

In addition, the input displacement power factor can be obtained in terms of displacement power factor as follows:

$$DPF_{in} = \cos\{\tan^{-1}[(21-1)\tan(\cos^{-1}(DPF_{out}))]\},$$

(2.22)

where $DPF_{in} = \cos(\varphi_i)$ and $DPF_{out} = \cos(\alpha_o)$ are the input and output displacement power factors. Equation (2.22) shows the variation of input displacement power factor as a function of parameter $a$ and output displacement power factor.

### 2.7.3 Matrix Converter Equivalent Circuit Model

Based on to the transformation matrix given by (2.12), MC can be represented by dependent current and voltage sources at the input and output terminals, respectively. In fact, the voltage and current dependent sources model the MC transformation matrix. This fundamental-frequency equivalent circuit is shown in Fig. 2-8, corresponding to the MC circuit in Fig. 2-2 [94]. In comparison with other MC equivalent-circuit models proposed in literature [92], the model of Fig. 2-8 is new in the sense that it uses the transformation matrix given by (2-12). This model will be used as a reference model to verify the state-space model developed in section 2.8.
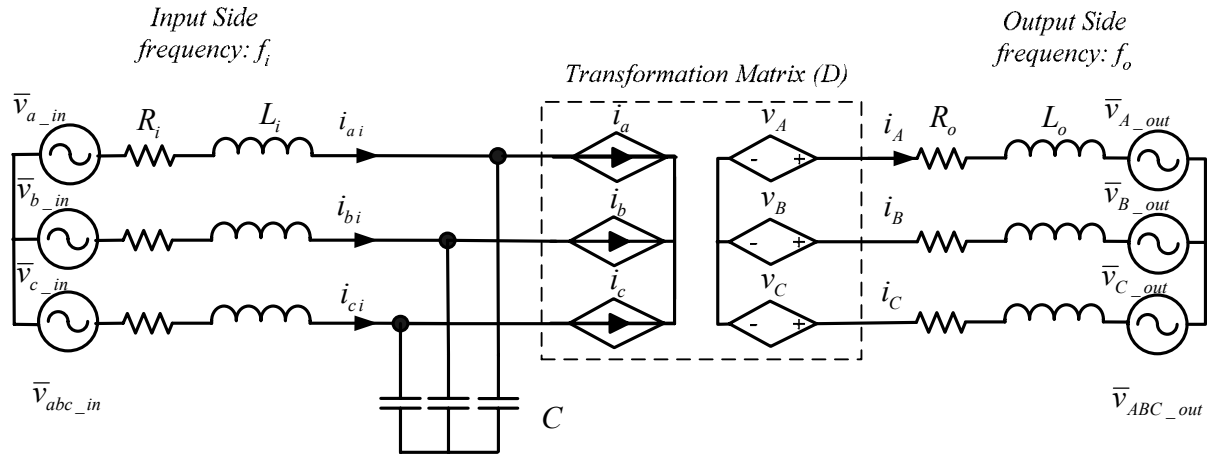


Fig. 2-8 : One-line, fundamental-frequency equivalent circuit of the MC system

### 2.7.4 Evaluation of Matrix Converter Equivalent Circuit Model

In this subsection, first the MC equivalent circuit model of Fig. 2-8 is evaluated. For this purpose, a typical MC system (Fig. 2-2) that is connected to two electrical systems with different frequencies and impedances is simulated. For simplicity, the side-2 system is considered to be a passive load. The

MC is assumed to be composed of ideal switches and is controlled by the SVPWM switching method, referred to as MC-SVM from now on. Then the simulation results are compared with those obtained from simulation of the MC equivalent circuit (Fig. 2-8). Both circuits are simulated in the PSIM environment. The schematic diagrams of the fundamental-frequency equivalent circuit and MC-SVM system in PSIM are illustrated in Fig. 2-9 and Fig. 2-6, respectively. For both systems, the source at the input-side is represented by three-phase sinusoidal voltages. To be consistent with MC-SVM system in Fig. 2-6, the equivalent circuit model (Fig. 2-8) contains a simple three-phase passive load, with resistance $R_{Load}$ and inductance $L_{Load}$, on the output side. The parameters of the MC system are shown in Table 2.2. In the following, selected simulation results of the MC equivalent system are presented.
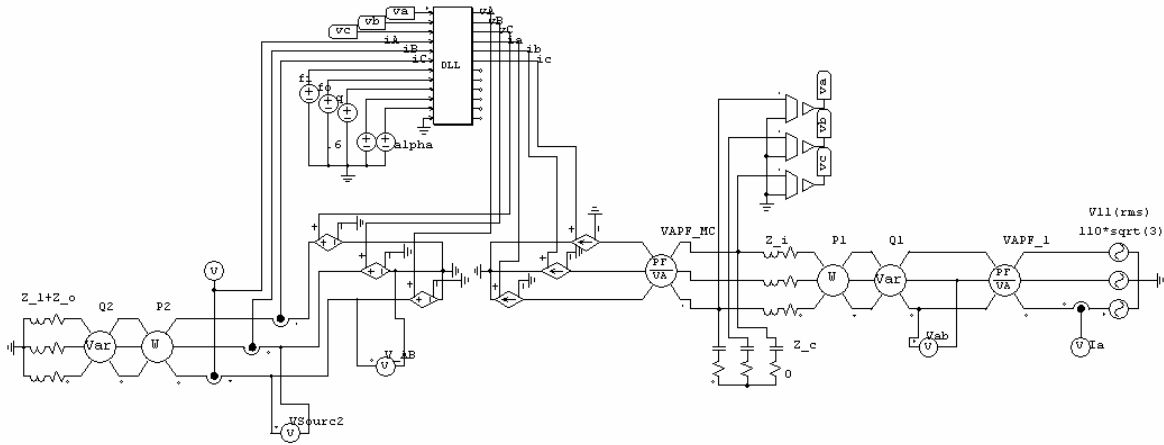


Fig. 2-9: Schematic diagram of the equivalent circuit in PSIM environment; the DLL block simulates the transformation matrix D

Table 2.2: Parameters of the simulated MC system

| Input System | Output System | Matrix Converter |
|---|---|---|
| $V_{ph\_in}$= 110 [V], $R_i$= 0.1[Ω] | $R_{o=}$= 0.1[Ω], $L_i$ = 0.1 [mH] | Voltage gain $q$=0.5 |
| $L_i$ = 0.1 [mH], $C$=20[μF] | $R_{Load=}$= 0.1[Ω], $L_{load}$ = 0.1 [mH] | Output voltage angle $\alpha_o$=0 |
| $f_i$=60[Hz] | $f_o$=50[Hz] | Switching frequency=5 [kHz] |

Fig. 2-10 shows the line-to-line output voltage waveforms of MC from the two models. For the MC-SVM system, the output voltage is pulsed; however, its fundamental component has the same

38

frequency and approximately the same magnitude as the output voltage of the equivalent-circuit model.

The waveforms input source currents for the two systems are illustrated in Fig. 2-11. The input source current of the MC-SVM is a pulsed waveform; however, as shown in Fig. 2-11, the corresponding source current is a sinusoidal with the same magnitude as the MC input source current of the equivalent circuit MC model.

The active and reactive powers at the input and output terminals, as well as the input displacement power factors are compared in Table 2.3. Based on the data presented in Table 2.3, there are minor differences between the active powers of the two models. This is because of the minor difference betweens the magnitude of input current and output voltage waveforms in the two models. However, there is a rather large difference between the output reactive powers of the two models. The main reason for this is the inclusion of harmonic components in the output voltage of MC-SVM model in calculation of output reactive power, whereas in the equivalent-circuit MC model, only the fundamental component of the output voltage has been considered. Filtering the output voltage signal of MC-SVM model before reactive power calculation should bring the results much closer.
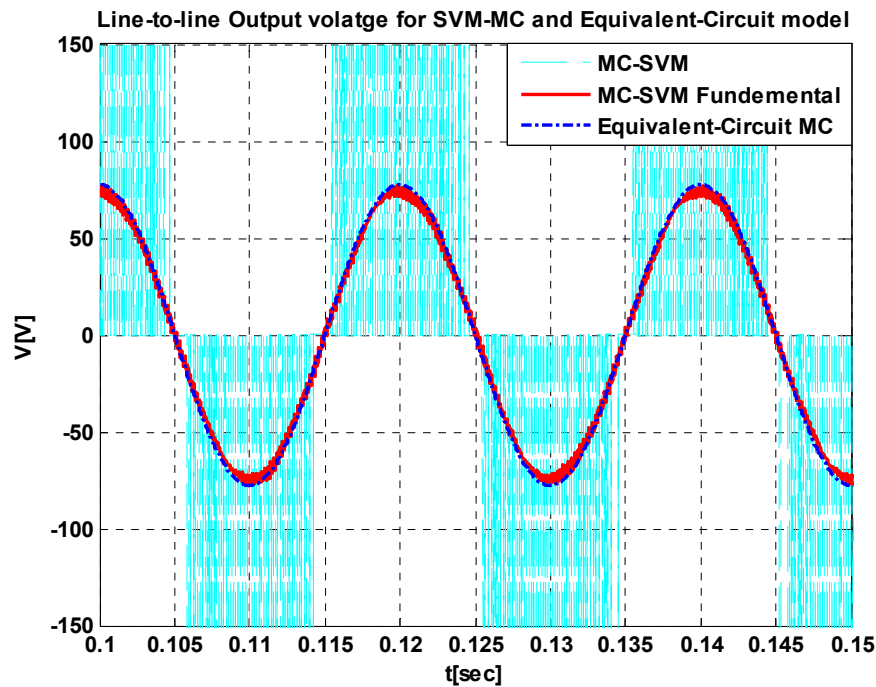


Fig. 2-10: Line-to-Line output voltages of the MC-SVM and equivalent-circuit models.
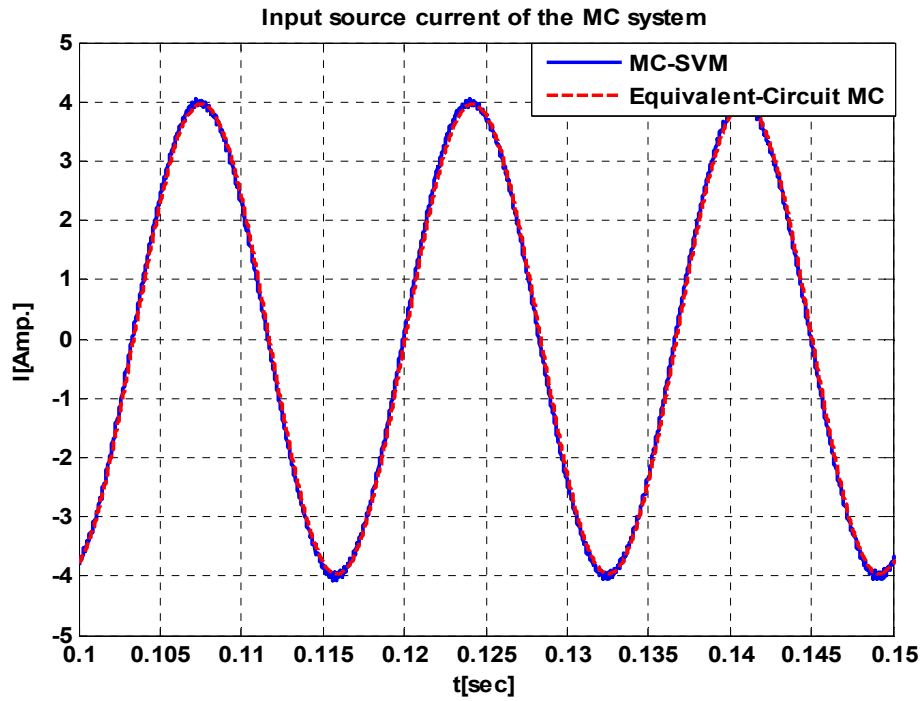
Fig. 2-11: Phase-a input source currents of the MC-SVM and equivalent-circuit models

Table 2.3: A comparison of active and reactive powers and displacement power factors of MC-SVM and equivalent-circuit models

|  | $P_{in}$(W) | $P_{out}$(W) | $Q_{in}$(Var) | $Q_{out}$(Var) | $DPF_{in}$ |
|---|---|---|---|---|---|
| MC-SVM | 883.86 | 881.73 | 244.9 | 138.5 | 0.963 Lagging |
| Equivalent-Circuit MC | 895.34 | 889.16 | 247.78 | 116.38 | 0.964 Lagging |
| Error% | 1.3 | 0.84 | 1.1 | 15.97 | 0.1 |

## 2.8 Matrix Converter State-Space Dynamic Model

### 2.8.1 Matrix Converter Equations Referred to One-Side

The ideal MC, itself, contains no energy-storage elements, and thus, has no dynamics. However, the impedances of connecting lines and input filters should be included in a complete dynamic model. As shown in Fig. 2-1, the two circuits connected to the input and output terminals of the MC are operated at two different frequencies. To establish an overall model for the system under study, the variables (voltages and currents) should be transferred to a common frequency frame. In this work, all quantities are referred to the output frequency frame.

In order to transfer the quantities from *abc* coordinates at input frame frequency to a new frame $\alpha\beta\gamma$, at the output frequency, one can write [91][92][95]:

$$\overline{f}_{\alpha\beta\gamma}^{D} = D\overline{f}_{abc} \quad \text{or} \quad \overline{f}_{abc} = D^{-1}\overline{f}_{\alpha\beta\gamma}^{D}, \tag{2.23}$$

where $\overline{f}_{\alpha\beta\gamma}^{D} = [f_{\alpha}^{D} \quad f_{\beta}^{D} \quad f_{\gamma}^{D}]^{\mathrm{T}}$, $\overline{f}_{abc} = [f_{a} \quad f_{b} \quad f_{c}]^{\mathrm{T}}$, and $D$ and $D^{-1}$ are the transformation matrix and inverse transformation matrix of the MC. As a result, the input voltages and currents of the MC circuit can be transferred to output frequency frame as follows:

$$\overline{v}_{\alpha\beta\gamma}^{D} = D\overline{v}_{abc}, \tag{2.24}$$

$$\overline{i}_{\alpha\beta\gamma}^{D} = D\overline{i}_{abc}, \tag{2.25}$$

where $\overline{v}_{abc} = [v_a \quad v_b \quad v_c]^T$ and $\overline{i}_{abc} = [i_a \quad i_b \quad i_c]^T$ are the input vectors of voltages and current at input frequency frame of the MC, respectively. The vector $\overline{v}_{\alpha\beta\gamma}^{D}$ and $\overline{i}_{\alpha\beta\gamma}^{D}$ are the voltages and currents transferred to the output frequency frame.

In equation (2.24), suppose $\overline{v}_{\alpha\beta\gamma}$ to be the MC input terminal voltages, i.e., $\overline{v}_{\alpha\beta\gamma} = \overline{v}_{abc}$, according to (2.14):

$$\overline{v}_{ABC} = \overline{v}_{\alpha\beta\gamma}^{D} = D\overline{v}_{abc} \tag{2.26}$$

where the $\overline{v}_{ABC} = [v_A \quad v_B \quad v_C]^T$ is the output voltage vector of the MC.

Equation (2.26) states that the input terminal voltages transferred to the output frequency frame correspond to output terminal voltages. However, it is worthwhile to note that the current vector $\bar{i}_{\alpha\beta\gamma}^{D}$, given by equation (2.25), has no equivalent variable on the output circuit of Fig. 2-1; in other words, it is a fictitious variable.

## 2.8.2 Voltage Equations at Input Side of Matrix Converter Circuit

To obtain a state-space-*qdo* model for the system, the first step is to develop the equations in the input frequency frame and then transfer them to the output frequency frame. The voltage equation (KVL) of the input circuit, in the input frequency frame, can be written as follows:

$$\bar{v}_{abc} = \bar{v}_{abc\_in} - R_I \bar{i}_{abci} - L_I \frac{d}{dt} \bar{i}_{abci},$$
(2.27)

where $\bar{v}_{abc\_in} = [v_{a\_in} \quad v_{b\_in} \quad v_{c\_in}]^T$ and $\bar{i}_{abci} = [i_{ai} \quad i_{bi} \quad i_{ci}]^T$ are the vectors of voltage and

current of the input source, respectively, and $R_I = \begin{bmatrix} R_i & 0 & 0 \\ 0 & R_i & 0 \\ 0 & 0 & R_i \end{bmatrix}$ and $L_I = \begin{bmatrix} L_i & 0 & 0 \\ 0 & L_i & 0 \\ 0 & 0 & L_i \end{bmatrix}$ are the

combined resistance and inductance matrices of the input source and input filter, respectively. Pre-multiplying the two sides of the equation (2.27) by transformation matrix $D$ we have:

$$D\bar{v}_{abc} = D[\bar{v}_{abc\_in} - R_I \bar{i}_{abci} - L_I \frac{d}{dt} \bar{i}_{abci}].$$
(2.28)

From (2.24)-(2.26), (2.28) can be rewritten as follows:

$$\bar{v}_{ABC} = \bar{v}_{abc\_in}^{D} - R_I \bar{i}_{abci}^{D} - D(L_I \frac{d}{dt} \bar{i}_{abci}),$$
(2.29)

where $\bar{v}_{abci}^{D}$ and $\bar{i}_{abci}^{D}$ are fictitious input source voltage and current vectors, respectively, transferred by transformation matrix $D$ from the input frequency frame to the output frequency frame, respectively.

## 2.8.3 Voltage Equations at the Output Side of Matrix Converter Circuit

The following equation shows the KVL at the output side of MC circuit of Fig. 2-2.

$$\bar{v}_{ABC} = \bar{v}_{ABC\_out} + R_O \bar{i}_{ABC} + L_O \frac{d}{dt}(\bar{i}_{ABC}),\tag{2.30}$$

where $\bar{v}_{ABC\_out} = [v_{A\_out} \quad v_{B\_out} \quad v_{C\_out}]^T$ and $i_{ABC} = [i_A \quad i_B \quad i_C]^T$ are the voltage and current

vectors of the output source, respectively, and $R_O = \begin{bmatrix} R_o & 0 & 0 \\ 0 & R_o & 0 \\ 0 & 0 & R_o \end{bmatrix}$ and $L_O = \begin{bmatrix} L_o & 0 & 0 \\ 0 & L_o & 0 \\ 0 & 0 & L_o \end{bmatrix}$ are

the resistance and inductance matrices of the output source, respectively. Note that the subscript "o" indicates variables in the output side of the MC.

The right hand sides of the voltage equations (2.29) and (2.30) are equal, so we can write:

$$\bar{v}_{ABC\_out} + R_o \bar{i}_{ABC} + L_o \frac{d}{dt}(\bar{i}_{ABC}) = \bar{v}_{abc\_in}^D - R_I \bar{i}_{abci}^D - D(L_I \frac{d}{dt}\bar{i}_{abci}).\tag{2.31}$$

## 2.8.4 Current Equations

The capacitor current vectors in terms of capacitor voltages can be written in the input frequency frame, as follows:

$$\bar{i}_{abcC} = C_I \frac{d}{dt}(\bar{v}_{abc}),\tag{2.32}$$

where $\bar{i}_{abcC} = [i_{aC} \quad i_{bC} \quad i_{cC}]^T$ is the capacitor current vector, and $C_I = \begin{bmatrix} C & 0 & 0 \\ 0 & C & 0 \\ 0 & 0 & C \end{bmatrix}$ is the

capacitance matrix.

To transfer the capacitor current to the output frequency frame, a fictitious capacitor current can be defined as follows:

$$\bar{i}_{abcC}^D = D\bar{i}_{abcC}.\tag{2.33}$$

From equations (2.26) and (2.33), equation (2.32) can be rewritten as:

$$D^{-1}\bar{i}_{abcC}^D = C_I \frac{d}{dt}(D^{-1}\bar{v}_{ABC}),\tag{2.34}$$

$$\therefore \bar{i}_{abcC}^{D} = DC_{I} \frac{d}{dt}(D^{-1}\bar{v}_{ABC}).$$

Equations (2.27), (2.30) and (2.34) are a set of nine nonlinear equations for the MC dynamic model in three-phase *abc* frame.

## 2.8.5 Matrix converter Equations in qdo Reference Frame

In order to convert time-varying *abc* quantities to quantities with time-invariant steady-state values, the equations of the MC should be transferred to a *qdo* reference frame rotating at the angular frequency $\omega_o$ of the system on the output side. The *abc* quantities are transferred to *qdo* reference frame by an *abc*-to-*qdo* transformation matrix, $K_o$, as follows:

$$\bar{f}_{abc} = K_o \bar{f}_{qdo}, \quad \text{or} \quad \bar{f}_{qdo} = K_o^{-1}\bar{f}_{abc}, \tag{2.35}$$

where $\quad K_o = \dfrac{2}{3}\begin{bmatrix} \cos\theta_o & \cos(\theta_o - \dfrac{2\pi}{3}) & \cos(\theta_o + \dfrac{2\pi}{3}) \\ \sin\theta_o & \sin(\theta_o - \dfrac{2\pi}{3}) & \sin(\theta_o + \dfrac{2\pi}{3}) \\ \dfrac{1}{2} & \dfrac{1}{2} & \dfrac{1}{2} \end{bmatrix}$, $\theta_o(t) = \omega_o t$, and $K_o^{-1}$ is the inverse

matrix of $K_o$ [96].

The *abc* and $\alpha\beta\gamma$ variables in the voltage and current equations of the MC system should be substituted by the corresponding *qdo* variables. Starting with the voltage equation (2.31) and using (2.35), one can deduce:

$$K_o^{-1}\bar{v}_{qdo\_out} + R_o K_o^{-1}\bar{i}_{qdo} + L_o \frac{d}{dt}(K_o^{-1}\bar{i}_{qdoO}) = K_o^{-1}\bar{v}_{qdo\_in}^{D} - R_i K_o^{-1}\bar{i}_{qdoi}^{D} - DL_i \frac{d}{dt}((K_o D)^{-1}(\bar{i}_{qdoi}^{D})),$$

$$\bar{v}_{qdo\_out} + R_o \bar{i}_{qdoO} + L_o \frac{d}{dt}(\bar{i}_{qdoO}) + K_o L_o \frac{d}{dt}(K_o^{-1})\bar{i}_{qdoO}$$
$$= \bar{v}_{qdo\_in}^{D} - R_i \bar{i}_{qdoi}^{D} - (K_o D)L_i \frac{d}{dt}((K_o D)^{-1}(\bar{i}_{qdoi}^{D})). \tag{2.36}$$

Using the $K_o$ definition, one can write:

$$\frac{d}{dt}(K^{-1}{}_o) = \omega_o \begin{bmatrix} -\sin\theta_o & \cos(\theta_o) & 0 \\ -\sin(\theta_o - \frac{2\pi}{3}) & \cos(\theta_o - \frac{2\pi}{3}) & 0 \\ -\sin(\theta_o + \frac{2\pi}{3}) & \cos(\theta_o + \frac{2\pi}{3}) & 0 \end{bmatrix}$$

(2.37)

$$\therefore K_o L_i \frac{d}{dt}(K^{-1}{}_o) = L \begin{bmatrix} 0 & \omega_o & 0 \\ -\omega_o & 0 & 0 \\ 0 & 0 & 0 \end{bmatrix}.$$

The term $K_o D$ in (2.36) can be simplified as follows:

$$K_o D = K_o (aD_1 + (1-a)D_2) =$$

$$\frac{2}{3}aq \begin{bmatrix} \cos(\omega_i t - \alpha_o) & \cos((\omega_i t - \alpha_o) - \frac{2\pi}{3}) & \cos((\omega_i t - \alpha_o) + \frac{2\pi}{3}) \\ \sin(\omega_i t - \alpha_o) & \sin((\omega_i t - \alpha_o) - \frac{2\pi}{3}) & \sin((\omega_i t - \alpha_o) + \frac{2\pi}{3}) \\ \frac{1}{2q} & \frac{1}{2q} & \frac{1}{2q} \end{bmatrix} +$$

$$\frac{2}{3}(1-a)q \begin{bmatrix} \cos(\omega_i t + \alpha_o) & \cos((\omega_i t + \alpha_o) - \frac{2\pi}{3}) & \cos((\omega_i t + \alpha_o) + \frac{2\pi}{3}) \\ -\sin(\omega_i t + \alpha_o) & -\sin((\omega_i t + \alpha_o) - \frac{2\pi}{3}) & -\sin((\omega_i t + \alpha_o) + \frac{2\pi}{3}) \\ \frac{1}{2q} & \frac{1}{2q} & \frac{1}{2q} \end{bmatrix}.$$

(2.38)

For a nonsingular and thus invertible matrix of $K_0 D$, it is necessary to consider the following restriction for parameter $a$:

$$a \neq \frac{1}{2}.$$

(2.39)

Also, the last term on the right side of equation (2.36) can be simplified as follows:

$$(K_0 D)L_I \frac{d}{dt}[(K_0 D)^{-1}] = \begin{bmatrix} 0 & \dfrac{\omega_i}{2a-1}L_i & 0 \\ -\omega_i(2a-1)L_i & 0 & 0 \\ 0 & 0 & 0 \end{bmatrix}.$$  (2.40)

Based on the equations (2.38) and (2.40), equation (2.36) is rewritten as follows:

$$\begin{aligned}
\overline{v}_{qdo\_out} + R_o \overline{i}_{qdoO} + L_o \frac{d}{dt}(\overline{i}_{qdoO}) + L_o \begin{bmatrix} 0 & \omega_o & 0 \\ -\omega_o & 0 & 0 \\ 0 & 0 & 0 \end{bmatrix} \overline{i}_{dqoO} \\
= \overline{v}_{qdo\_in}^D - R_i \overline{i}_{qdoi}^D - L_i \frac{d}{dt}(\overline{i}_{qdoG}^D) - L_i \begin{bmatrix} 0 & \dfrac{\omega_i}{2a-1} & 0 \\ -\omega_i(2a-1) & 0 & 0 \\ 0 & 0 & 0 \end{bmatrix} \overline{i}_{qdoi}^D
\end{aligned}$$  (2.41)

Equation (2.41) shows the state equations for the voltages of the MC output side in *qdo* reference frame.

With the same procedure, the MC current equations (2.32) in *abc* reference frame can be transferred to *qdo* output frequency reference frame directly, using equations (2.26), (2.33), and (2.35) as follows:

$$(K_o D)^{-1} \overline{i}_{qdoC}^D = C_I \frac{d}{dt}((K_o D)^{-1} \overline{v}_{qdoO}),$$  (2.42)

where $\overline{i}_{qdoC}^D$ is the capacitor current vector transferred to *qdo* in the output frequency reference frame of the MC, and $\overline{v}_{qdoO}^D$ is the output voltage vector of the MC, $\overline{v}_{ABC}$, transferred to the *qdo* reference frame. Note that $\overline{i}_{qdoC}^D$ is a fictions current vector.

Equation (2.42) can be rearranged as:

$$\bar{i}_{qdoC}^{D} = (K_oD)C_I\{((K_oD)^{-1})\frac{d}{dt}\bar{v}_{qdo} + \frac{d}{dt}((K_oD)^{-1})\bar{v}_{qdoO}\}$$

$$= C_I\frac{d}{dt}\bar{v}_{qdoO} + (K_oD)C_I\frac{d}{dt}(K_oD)^{-1}\bar{v}_{qdoO}. \tag{2.43}$$

Using (2.40), equation (2.43) can be simplified as follows:

$$\bar{i}_{qdoC}^{D} = C_I\frac{d}{dt}(\bar{v}_{qdoO}) + C\begin{bmatrix} 0 & \dfrac{\omega_i}{2a-1} & 0 \\ -\omega_i(2a-1) & 0 & 0 \\ 0 & 0 & 0 \end{bmatrix}\bar{v}_{qdoO}. \tag{2.44}$$

Equation (2.44) shows the capacitor state equations of the MC output side in *qdo* reference frame.

## 2.8.6 State-Space-qdo Model of the Matrix Converter System

The overall state-space model in *qdo* reference frame of the MC system contains equation (2.41) and (2.44), referred to as state-space-*qdo* model from now on. Note that the system under study is a balanced three-phase system; therefore, the zero-sequence voltage and currents are zero.

Equation (2.41) can be rewritten for q-axis and d-axis as follows:

$$\begin{cases} v_{q\_out} + R_oi_{qO} + L_o\dfrac{d}{dt}(i_{qO}) + L_o\omega_oi_{dO} = v_{q\_in}^{D} - R_ii_{qi}^{D} - L_i\dfrac{d}{dt}(i_{qi}^{D}) - L_i\dfrac{\omega_i}{2a-1}i_{di}^{D}, \\ v_{d\_out} + R_oi_{dO} + L_o\dfrac{d}{dt}(i_{dO}) - L_o\omega_oi_{qO} = v_{d\_in}^{D} - R_ii_{di}^{D} - L_i\dfrac{d}{dt}(i_{di}^{D}) + L_i(2a-1)\omega_ii_{qi}^{D}. \end{cases} \tag{2.45}$$

Reordering equation (2.45) gives:

$$\begin{cases} \dfrac{d}{dt}(i_{qO}) = -\omega_oi_{dO} - \dfrac{R_o}{L_o}i_{qO} - \dfrac{R_i}{L_o}i_{qi}^{D} - \dfrac{L_i}{L_o}\dfrac{d}{dt}(i_{qi}^{D}) - \dfrac{L_i}{L_o}\dfrac{\omega_i}{2a-1}i_{di}^{D} + \dfrac{1}{L_o}(v_{q\_in}^{D} - v_{q\_out}), \\ \dfrac{d}{dt}(i_{dO}) = \omega_oi_{qO} - \dfrac{R_o}{L_o}i_{dO} - \dfrac{R_i}{L_o}i_{di}^{D} - \dfrac{L_i}{L_o}\dfrac{d}{dt}(i_{di}^{D}) + \dfrac{L_i}{L_o}(2a-1)\omega_ii_{qi}^{D} + \dfrac{1}{L_o}(v_{d\_in}^{D} - v_{d\_out}). \end{cases} \tag{2.46}$$

To change (2.46) to a set of state equations, the equation (2.41) should be employed. The right hand side of the equation (2.41) is the output voltages of the MC transferred to the *qdo* reference frame, as follows:

$$\overline{v}_{qdoO} = \overline{v}_{qdo\_in}^{D} - R_i \overline{i}_{qdoi}^{D} - L_i \frac{d}{dt}(\overline{i}_{qdoi}^{D}) - L_i \begin{bmatrix} 0 & \dfrac{\omega_i}{2a-1} & 0 \\ -\omega_i(2a-1) & 0 & 0 \\ 0 & 0 & 0 \end{bmatrix} \overline{i}_{qdoi}^{D}. \tag{2.47}$$

For a balanced three-phase system, equation (2.47) can be rewritten for q-axis and d-axis as follows:

$$\begin{cases} v_{q\_in}^{D} = v_{qO} + R_i i_{qi}^{D} + L_i \dfrac{d}{dt}(i_{qi}^{D}) + L_i \dfrac{\omega_i}{2a-1} i_{di}^{D}, \\[3mm] v_{d\_in}^{D} = \overline{v}_{dO} + R_i i_{di}^{D} + L_i \dfrac{d}{dt}(i_{di}^{D}) - L_i(2a-1)\omega_i i_{qi}^{D}. \end{cases} \tag{2.48}$$

Substituting (2.48) in (2.46), one gets:

$$\begin{cases} \dfrac{d}{dt}(i_{qO}) = -\dfrac{R_o}{L_o} i_{qO} - \omega_o i_{dO} + \dfrac{1}{L_o}(v_{qO} - v_{q\_out}), \\[3mm] \dfrac{d}{dt}(i_{dO}) = \omega_o i_{qO} - \dfrac{R_o}{L_o} i_{dO} + \dfrac{1}{L_o}(v_{dO} - v_{d\_out}). \end{cases} \tag{2.49}$$

Other state equations can be written by reordering equation (2.45) for $\dfrac{d}{dt}(\overline{i}_{qi}^{D})$ and $\dfrac{d}{dt}(\overline{i}_{di}^{D})$, as follows:

$$\begin{cases} L_i \dfrac{d}{dt}(i_{qi}^{D}) = -R_o i_{qO} - L_o \dfrac{d}{dt}(i_{qO}) - L_o \omega_o i_{dO} - R_i i_{qi}^{D} - L_i \dfrac{\omega_i}{2a-1} i_{di}^{D} + v_{q\_in}^{D} - v_{q\_out}, \\[3mm] L_i \dfrac{d}{dt}(i_{di}^{D}) = -R_o i_{dO} - L_o \dfrac{d}{dt}(i_{dO}) + L_o \omega_o i_{qO} - R_i i_{di}^{D} + L_i \omega_i(2a-1)i_{qi}^{D} + v_{d\_in}^{D} - v_{d\_out}. \end{cases} \tag{2.50}$$

Substituting (2.49) in (2.50) yields:

$$\begin{cases} \dfrac{d}{dt}(i_{qi}^{D}) = -\dfrac{R_i}{L_i} i_{qi}^{D} - \dfrac{\omega_i}{2a-1} i_{di}^{D} - \dfrac{1}{L_i} v_{qO} + \dfrac{1}{L_i} v_{q\_in}^{D}, \\[3mm] \dfrac{d}{dt}(i_{di}^{D}) = \omega_i(2a-1)i_{qi}^{D} - \dfrac{R_i}{L_i} i_{di}^{D} - \dfrac{1}{L_i} v_{dO} + \dfrac{1}{L_i} v_{d\_in}^{D}. \end{cases} \tag{2.51}$$

In the following, the last couple of state equations, related to the output terminal voltage of the MC, are derived. In Fig. 2-2, KCL equations at the terminal of the capacitor bank can be written as follows:

Chapter 2. Matrix Converter …

$$\overline{i}_{abcC} = \overline{i}_{abci} - \overline{i}_{abc} . \tag{2.52}$$

Substituting equation (2.16) in (2.52) and transferring the result to output frequency *qdo* reference farme, we have:

$$\overline{i}_{abcC} = \overline{i}_{abci} - D^T \overline{i}_{ABC} ,$$

$$(K_0 D)^{-1} \overline{i}^{D}_{qdoC} = (K_0 D)^{-1} \overline{i}^{D}_{qdoi} - D^T (K_0)^{-1} \overline{i}_{qdoO} ,$$

$$\therefore \overline{i}^{D}_{qdoC} = \overline{i}^{D}_{qdoi} - (K_0 D) D^T (K_0)^{-1} \overline{i}_{qdoO} . \tag{2.53}$$

The term $(K_0 D) D^T (K_0)^{-1}$ is simplified in Appendix F as

$$(K_0 D) D^T (K_0)^{-1} = q^2 \cos(\alpha_o) \begin{bmatrix} \cos(\alpha_o) & \sin(\alpha_o) & 0 \\ (2a-1)^2 \sin(\alpha_o) & (2a-1)^2 \cos(\alpha_o) & 0 \\ 0 & 0 & \dfrac{1}{q^2 \cos(\alpha_o)} \end{bmatrix} . \tag{2.54}$$

From equation (2.54), equation (2.53) can be simplified as follows:

$$\overline{i}^{D}_{qdoC} = \overline{i}^{D}_{qdoi} - q^2 \cos(\alpha_o) \begin{bmatrix} \cos(\alpha_o) & \sin(\alpha_o) & 0 \\ (2a-1)^2 \sin(\alpha_o) & (2a-1)^2 \cos(\alpha_o) & 0 \\ 0 & 0 & \dfrac{1}{q^2 \cos(\alpha_o)} \end{bmatrix} \overline{i}_{qdoO} . \tag{2.55}$$

Finally, substituting equation (2.55) in (2.44), one gets:

$$C_I \frac{d}{dt}(\bar{v}_{qdoO}) = -q^2 \cos(\alpha_o) \begin{bmatrix} \cos(\alpha_o) & \sin(\alpha_o) & 0 \\ (2a-1)^2 \sin(\alpha_o) & (2a-1)^2 \cos(\alpha_o) & 0 \\ 0 & 0 & \dfrac{1}{q^2 \cos(\alpha_o)} \end{bmatrix} \bar{i}_{qdoO}$$

$$+ \bar{i}_{qdoi}^D - C \begin{bmatrix} 0 & \dfrac{\omega_i}{2a-1} & 0 \\ -\omega_i(2a-1) & 0 & 0 \\ 0 & 0 & 0 \end{bmatrix} \bar{v}_{qdoO}. \tag{2.56}$$

For a balanced three-phase system, equation (2.56) can be rewritten for q-axis and d-axis as follows:

$$\begin{cases} C\dfrac{d}{dt}v_{qo} = -q^2 \cos^2(\alpha_o)i_{qO} - q^2 \cos(\alpha_o)\sin(\alpha_o)i_{dO} + i_{qi}^D - C\dfrac{\omega_i}{2a-1}v_{dO}, \\ C\dfrac{d}{dt}v_{do} = -q^2(2a-1)^2 \cos(\alpha_o)\sin(\alpha_o)i_{qO} - q^2(2a-1)^2 \cos^2(\alpha_o)i_{dO} + i_{di}^D + C\omega_i(2a-1)v_{qO}. \end{cases} \tag{2.57}$$

Finally, an overall state-space-*qdo* dynamic model of the balanced three-phase MC system, shown in Fig. 2-2, is given by equations (2.49), (2.51), and (2.57). The overall model is of the form:

$$\frac{d}{dt}\bar{x} = A\bar{x} + B\bar{u} . \tag{2.58}$$

where $\bar{x} = \begin{bmatrix} i_{qo} \\ i_{do} \\ i_{qi}^D \\ i_{di}^D \\ v_{qo} \\ v_{do} \end{bmatrix}$, $\quad \bar{u} = \begin{bmatrix} v_{q\_out} \\ v_{d\_out} \\ v_{q\_in}^D \\ v_{d\_in}^D \end{bmatrix}$,

$$A = \begin{bmatrix}
-\dfrac{R_o}{L_o} & -\omega_o & 0 & 0 & \dfrac{1}{L_o} & 0 \\[2ex]
\omega_o & -\dfrac{R_o}{L_o} & 0 & 0 & 0 & \dfrac{1}{L_o} \\[2ex]
0 & 0 & -\dfrac{R_i}{L_i} & -\dfrac{\omega_i}{2a-1} & -\dfrac{1}{L_i} & 0 \\[2ex]
0 & 0 & \omega_i(2a-1) & -\dfrac{R_i}{L_i} & 0 & -\dfrac{1}{L_i} \\[2ex]
-\dfrac{q^2\cos^2(\alpha_o)}{C} & -\dfrac{q^2\cos(\alpha_o)\sin(\alpha_o)}{C} & \dfrac{1}{C} & 0 & 0 & -\dfrac{\omega_i}{2a-1} \\[2ex]
-\dfrac{q^2(2a-1)^2\cos(\alpha_o)\sin(\alpha_o)}{C} & -\dfrac{(2a-1)^2\cos^2(\alpha_o)q^2}{C} & 0 & \dfrac{1}{C} & \omega_i(2a-1) & 0
\end{bmatrix}, \text{ and}$$

$$B = \begin{bmatrix}
-\dfrac{1}{L_o} & 0 & 0 & 0 \\[2ex]
0 & -\dfrac{1}{L_o} & 0 & 0 \\[2ex]
0 & 0 & \dfrac{1}{L_i} & 0 \\[2ex]
0 & 0 & 0 & \dfrac{1}{L_i} \\[2ex]
0 & 0 & 0 & 0 \\[1ex]
0 & 0 & 0 & 0
\end{bmatrix}.$$

Note that the input vector, $\bar{u}$, contains the input and output source voltages in the *qdo* frame. The output source voltages in the *qdo* frame can be obtained from the balanced sinusoidal three-phase voltages in the *abc* frame that is defined as follows:

$$\bar{v}_{abc\_out} = V_{m\_out} \begin{bmatrix}
\cos(\omega_o t + \alpha_{out}) \\
\cos(\omega_o t + \alpha_{out} - 2\pi/3) \\
\cos(\omega_o t + \alpha_{out} + 2\pi/3)
\end{bmatrix} \tag{2.59}$$

where $V_{m\_Out}$ and $\alpha_{out}$ are the output source voltage peak value and phase angle, respectively. From $K_0$ definition, equation (2.35), the output source voltages in the *qdo* frame is:

$$\bar{v}_{qdo\_out} = K_0 \bar{v}_{abc\_out} = V_{m\_out} \begin{bmatrix} \cos(\alpha_{out}) \\ -\sin(\alpha_{out}) \\ 0 \end{bmatrix}. \tag{2.60}$$

Moreover, if the input source voltages are defined with the balanced sinusoidal three-phase voltages in the *abc* frame, as

$$\bar{v}_{abc\_in} = V_{m\_in} \begin{bmatrix} \cos(\omega_i t + \alpha_i) \\ \cos(\omega_i t + \alpha_i - 2\pi/3) \\ \cos(\omega_i t + \alpha_i + 2\pi/3) \end{bmatrix}, \tag{2.61}$$

where $V_{m\_in}$ and $\alpha_i$ are the input source voltage peak value and phase angle, then, using equation (2.38), the input source voltages in *qdo* frame transferred to output side of the MC are obtained as follows:

$$\bar{v}_{qdo\_in}^{D} = (K_0 D) \bar{v}_{abc\_in} = q V_{m\_in} \begin{bmatrix} \cos(\alpha_o) \\ -\sin(\alpha_o) \\ 0 \end{bmatrix}. \tag{2.62}$$

In (2.62) the input source voltage is considered as the reference, i.e., $\alpha_i = 0$.

## 2.8.7 Power Formula in the State-Space-qdo Model

The active and reactive powers of the input and output sources in the MC system of Fig. 2-1 are output variables in the state-space *qdo* model. In the following, the active and reactive power formulas based on the state variables of the model in *qdo*-frame are presented.

### 2.8.7.1 Output Power Formula

The active and reactive power formulas at the output source terminals can be expressed as follows:

$$P_{Out} = \frac{3}{2}(v_{q\_out} i_{qo} + v_{d\_out} i_{do}), \tag{2.63}$$

$$Q_{Out} = \frac{3}{2}(v_{d\_out} i_{qo} - v_{q\_out} i_{do}). \tag{2.64}$$

Substituting equation (2.60) in (2.63) and (2.64), one gets:

$$P_{Out} = \frac{3}{2} V_{m\_out} (\cos(\alpha_{out}) i_{qo} - \sin(\alpha_{out}) i_{do}), \qquad (2.65)$$

$$Q_{Out} = -\frac{3}{2} V_{m\_out} (\sin(\alpha_{out}) i_{qo} + \cos(\alpha_{out}) i_{do}). \qquad (2.66)$$

### 2.8.7.2 Input Power Formula

The input source active power formula in the *qdo* frame can be defined as follows:

$$P_{in} = \frac{3}{2} \bar{v}_{qdo\_in}^{T} \bar{i}_{qdoi}. \qquad (2.67)$$

To derive the input source active power formula in the *qdo* frame in terms of state variables, it is first necessary to write the input source current in the *qdo* frame, $\bar{i}_{qdoi}$, in terms of the state variables of the model given in (2.58). Using transformation matrix (2.38), the input source current vector can be transformed from *abc* frame to *qdo* frame or vice versa as follows:

$$\bar{i}_{qdoi}^{D} = (K_o(\omega_o)D)\bar{i}_{abci},$$

$$\therefore \bar{i}_{abci} = (K_o(\omega_o)D)^{-1} \bar{i}_{qdoi}^{D}. \qquad (2.68)$$

To transfer the input source current vector to *qdo* frame, based on equation (2.68), one can write:

$$\bar{i}_{qdoi} = K_o(\omega_i)(K_o(\omega_o)D)^{-1} \bar{i}_{qdoi}^{D}. \qquad (2.69)$$

The term $K_o(\omega_i)(K_o(\omega_o)D)^{-1}$ can be simplified as follows:

$$K_o(\omega_i)(K_o(\omega_o)D)^{-1} = \frac{1}{q} \begin{bmatrix} \cos(\alpha_o) & -\sin(\alpha_o) & 0 \\ \dfrac{\sin(\alpha_o)}{2a-1} & \dfrac{\cos(\alpha_o)}{2a-1} & 0 \\ 0 & 0 & \dfrac{1}{q} \end{bmatrix}. \qquad (2.70)$$

The input source voltage in *qdo* frame can be written as:

$$\bar{v}_{qdo\_in} = K_o(\omega_i)\bar{v}_{abc\_in} = V_{im}\begin{bmatrix} \cos(\alpha_i) \\ \sin(\alpha_i) \\ 0 \end{bmatrix}.$$
(2.71)

Substituting (2.69), (2.70) and (2.71) in equation (2.67), the input source active power formula for a balanced three phase system is:

$$
\begin{aligned}
P_{in} &= \frac{3}{2q}\{v_{q\_in}(\cos(\alpha_o)i_{qi}^D - \sin(\alpha_o)i_{di}^D) + \frac{v_{d\_in}}{2a-1}(\sin(\alpha_o)i_{qi}^D + \cos(\alpha_o)i_{di}^D)\} \\
&= \frac{3V_{im}}{2q}\{\cos(\alpha_i)(\cos(\alpha_o)i_{qi}^D - \sin(\alpha_o)i_{di}^D) + \frac{\sin(\alpha_i)}{2a-1}(\sin(\alpha_o)i_{qi}^D + \cos(\alpha_o)i_{di}^D)\}.
\end{aligned}
$$
(2.72)

Taking the input source voltage as the reference, i.e., $\alpha_i = 0$, power formula (2.72) can be simplified as follows:

$$P_{in} = \frac{3}{2q}V_{im}[\cos(\alpha_o)i_{qi}^D - \sin(\alpha_o)i_{di}^D].$$
(2.73)

By inspection, the reactive power formula in *qdo* frame, $Q = \frac{3}{2}(v_d i_q - v_q i_d)$, can be obtained from the power formula, $P = \frac{3}{2}(v_q i_q + v_d i_d)$, if the $v_q$ and $v_d$ are replaced by $v_d$ and $-v_q$, respectively. Therefore, the reactive power formula for input source based on equation (2.72) can be written as follows:

$$
\begin{aligned}
Q_{in} &= \frac{3}{2q}\{v_{d\_in}(\cos(\alpha_o)i_{qi}^D - \sin(\alpha_o)i_{di}^D) - \frac{v_{q\_in}}{2a-1}(\sin(\alpha_o)i_{qi}^D + \cos(\alpha_o)i_{di}^D)\} \\
&= \frac{3V_{im}}{2q}\{\sin(\alpha_i)(\cos(\alpha_o)i_{qi}^D - \sin(\alpha_o)i_{di}^D) - \frac{\cos(\alpha_i)}{2a-1}(\sin(\alpha_o)i_{qi}^D + \cos(\alpha_o)i_{di}^D)\}.
\end{aligned}
$$
(2.74)

With the assumption $\alpha_i = 0$, the reactive power formula (2.74) can be written as:

$$Q_{in} = -\frac{3}{2q}\frac{V_{im}}{2a-1}(\sin(\alpha_o)i_{qi}^D + \cos(\alpha_o)i_{di}^D).$$
(2.75)

Fig. 2-12 illustrates final MC state-space *qdo* mode that is used in the following simulations. In this model, the MC control variables ($\omega_o$, $q$, $a$, and $\alpha_o$) and the input and output source powers are chosen

as the input and output variables, respectively. Note that other constant input variables are not shown in the figure. Also the model is valid for a balanced system without zero-sequence.

Note that, in comparison with the other state-space MC model proposed in [92], the model of Fig. 2-12 is comprehensive in the sense that it includes input displacement power factor as a control variable.

MC state-space-*qdo* model
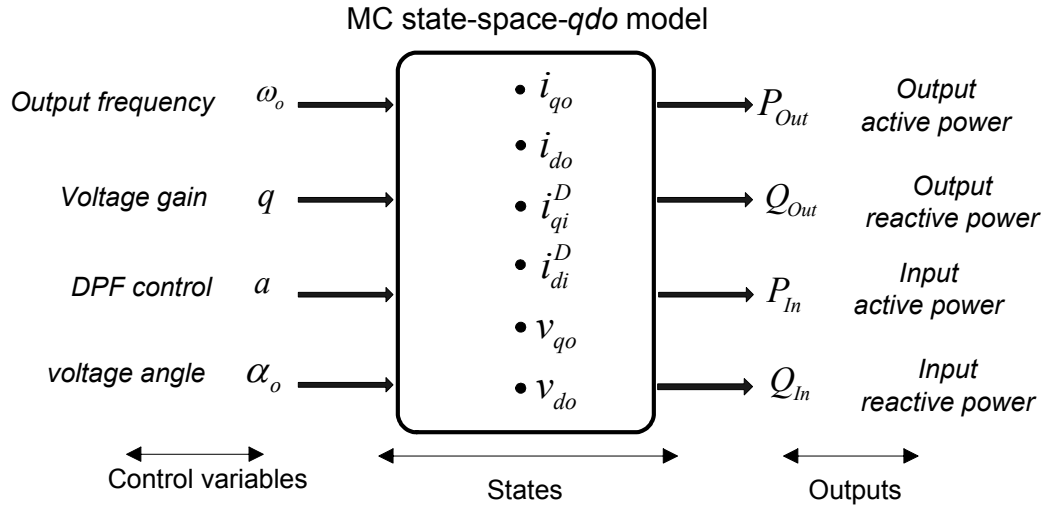


Fig. 2-12: Final MC state-space *qdo* mode

## 2.9 Evaluation of the Matrix Converter Dynamic Model

The objective is to evaluate the performance of the state-space-*qdo* dynamic model of the MC system introduced in the previous section. To validate the MC state-space *qdo* model, first the model is simulated using Matlab/Simulink; then, the simulation results are compared with those of the equivalent-circuit MC model (Fig. 2-8). The MC system parameters are the same as in the previous example (Table 2.2), except for the source and load on the input and output sides. Table 2.4 shows the parameters of the input and output source sides for the system under study.

Table 2.4: Parameters of the input and output sources of the MC system

| Source | Line-to-Line voltage | Frequency |
|---|---|---|
| Input-side | 720(V) | 60 Hz |
| Output-side | 400(V) | 50 Hz |

In the following simulations, the parameter *a* related to input displacement angle is fixed at 0.6 and output voltage angle of the MC is set to zero ($\alpha_o=0$). Meanwhile, the input source voltage is taken as the reference.

The state-space-*qdo* model consist of six state variables in the *qdo* reference frame, given by equation (2.58). First, the steady-state simulation results related to the state variables in the *qdo* reference frame are presented in Table 2.5.

Table 2.5: Steady-state values of the state variables in *qdo* reference frame for the model

| *State variables of the State-Space-qdo model* | $i_{qo}[A]$ | $i_{do}[A]$ | $i_{qi}^{D}[A]$ | $i_{di}^{D}[A]$ | $v_{qo}[V]$ | $v_{do}[V]$ |
|---|---|---|---|---|---|---|
| Value | -239.65 | 78.54 | -1.24 | -59.95 | 300.16 | -0.33 |

In order to verify the model with the equivalent-circuit model of Fig. 2-8, the state variables in the *qdo* reference frame should be transferred to *abc* reference frame. This transformation can be done using inverse transformation matrices of equations (2.35) and (2.38).

Fig. 2-13 and Fig. 2-14 compare phase-*a* voltage at the MC output terminals and currents at input source terminals, respectively, for the MC space-state *qdo* and equivalent circuit MC models. In addition, Fig. 2-15 shows active and reactive power at the output source terminals for the two models. The results confirm the equivalence of the two models.

Table 2.6 shows the steady-state active and reactive powers of the two systems, as well as the input displacement power factors at the operating point (shown in Table 2.5). The numerical results for the two systems are practically identical. Note that the negative sign for the power shows that the direction of power is from input-side source to the output-side source.
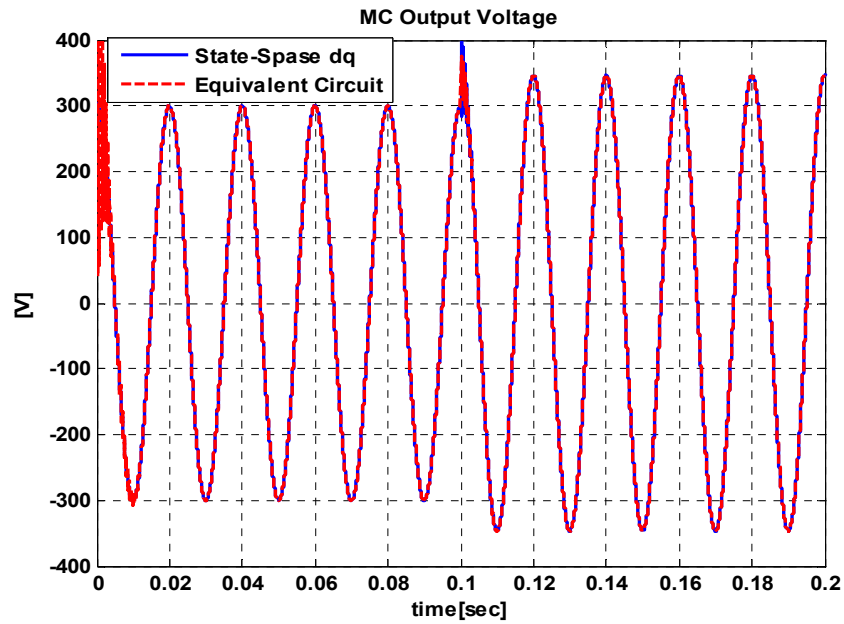
Fig. 2-13: A comparison of the MC output voltage in the state-space *qdo* model and equivalent circuit model with a 20% step change in voltage gain at t=0.1s
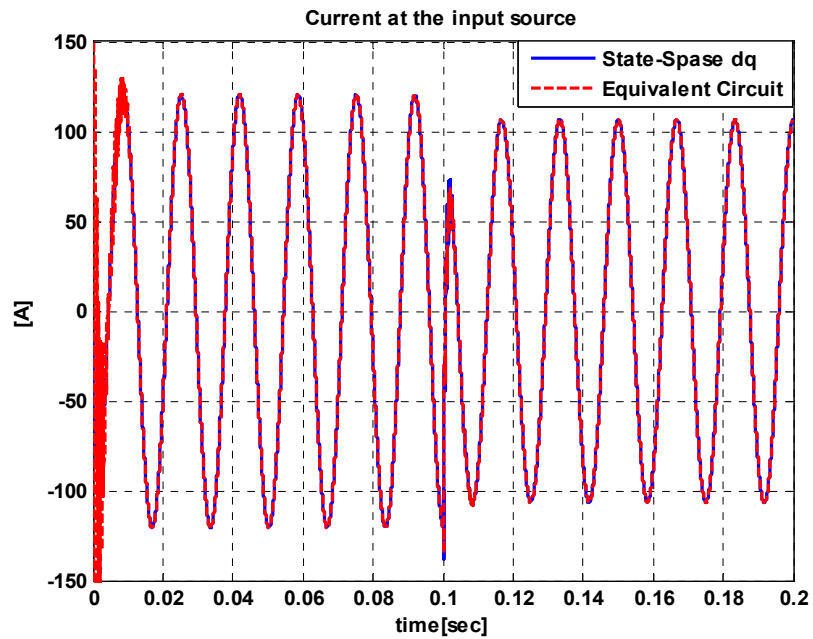


Fig. 2-14: A comparison of the input source current in the state-space *qdo* model and equivalent circuit model with a 20% step change in voltage gain at t=0.1s
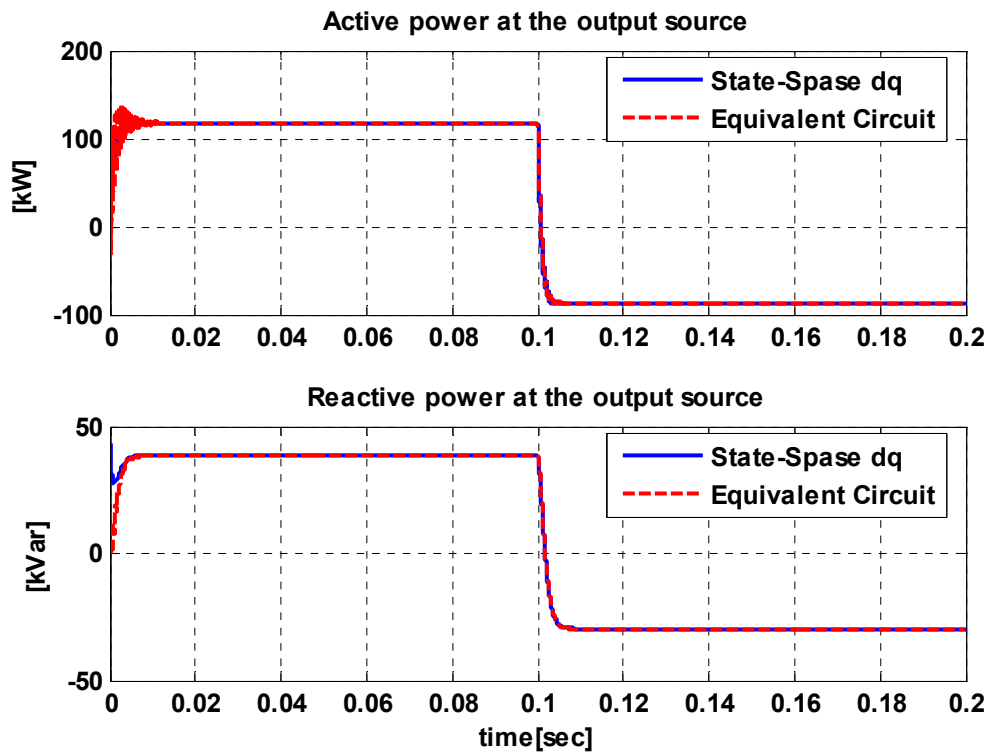
Fig. 2-15: A comparison of the output source P and Q in the state-space *qdo* model and equivalent circuit model with a 20% step change in voltage gain at t=0.1s

Table 2.6 Active and reactive power for the two models

| Model | $P_{in}$(kW) | $P_{out}$(kW) | $Q_{in}$(kVar) | $Q_{out}$(kVar) | $DPF_{in}$ |
|---|---|---|---|---|---|
| State-Space-*qdo* | -105.69 | 117.41 | -10.92 | 38.491 | 0.9947 *Lagging* |
| Equivalent- Circuit | -105.67 | 117.4 | -10.912 | 38.501 | 0.9947 *Lagging* |

## 2.10 Summary

In this chapter, the matrix converter (MC), together with its control methods and overall dynamic model, are discussed. The MC has no limitation on the output frequency. Also, it is possible to adjust the input displacement angle and control the output voltage magnitude and phase angle by properly operating the switches. Since there is no dc-link as compared with a two-stage converter, the MC can be recognized as a full-silicon structure in a compact design. Furthermore, the structure is inherently capable of a four-quadrant operation.

For controlling the switching in a MC, the space vector pulse width modulation (SVPWM) technique can be applied in the same way that it is applied to a DC/AC converter. The SVPWM offers advantages with respect to the conventional PWM methods, such as lower number of switchings in each cycle and better output waveforms, but it is more complex.

The main objective of this chapter is dedicated to developing an overall dynamic model for the MC system. The developed model contains six nonlinear equations in the same frequency frame. The final model contains six state variables and four control variables. Input and output active and reactive power formulas are developed based on the model state variables. To evaluate the MC state-space *qdo* dynamic model, first the model is simulated with Matlab/Simulink; then, the results are compared with the simulation results of a model based on the MC equivalent circuit, obtained from the PSIM simulation package. The results of the two models are fairly close. The state-space model presented is comprehensive in the sense that it includes output voltage magnitude, frequency and phase angle, as well as input displacement power factor as control variables. The proposed model can be used effectively in modeling electrical systems including MC for transient study, stability analysis, and systematic controller design.

# Chapter 3

# Overall Dynamic Model of the Wind Turbine System and Small Signal Analysis

## 3.1 Introduction

In this chapter, first a nonlinear dynamic model of a grid-connected wind-energy conversion system including a MC is developed in *qdo* reference frame. Detailed models of the mechanical aerodynamic conversion, drive train, and squirrel-cage induction generator are developed and combined with that of MC presented in Chapter 2 to enable steady-state and transient analysis of the overall system. Then a linear model is developed by linearization of the nonlinear dynamic equations around an operating point. The linearized model is employed to investigate the local stability of the system at the steady-state operating point. In addition, some of the system properties, such as controllability and observability, are investigated. The validity of the linear model is confirmed by comparing the results obtained with those of the nonlinear model. The linear model is used in Chapter 4 to design a controller in order to improve the steady state and transient performances.

Section 3.2 is dedicated to the dynamic models of the components of the proposed wind turbine system. This includes aerodynamic, mechanical, induction machine, and wind speed models. The overall dynamic model and its verification in the steady-state and the transient are presented in

Sections 3.3 and 3.4, respectively. The dynamic model of the system is completed in Section 3.5, with inclusion of constant *V/f* control strategy for the induction machine. The linear model of the wind turbine system is developed in Section 3.6. In Section 3.8, the linear model is verified by comparison with the nonlinear model. Section 3.9 deals with local stability evaluation, while Section 3.10 analyses controllability and observability. Section 3.11 develops a balanced realization model. Finally, a reduced-order model is obtained in Section 3.12.

## 3.2 Dynamic Model of the Wind Turbine System

Fig. 3-1 illustrates the schematic diagram of the proposed wind turbine system. The system consists of the wind turbine rotors, a gearbox, squirrel-cage induction generator, and a matrix converter (MC).
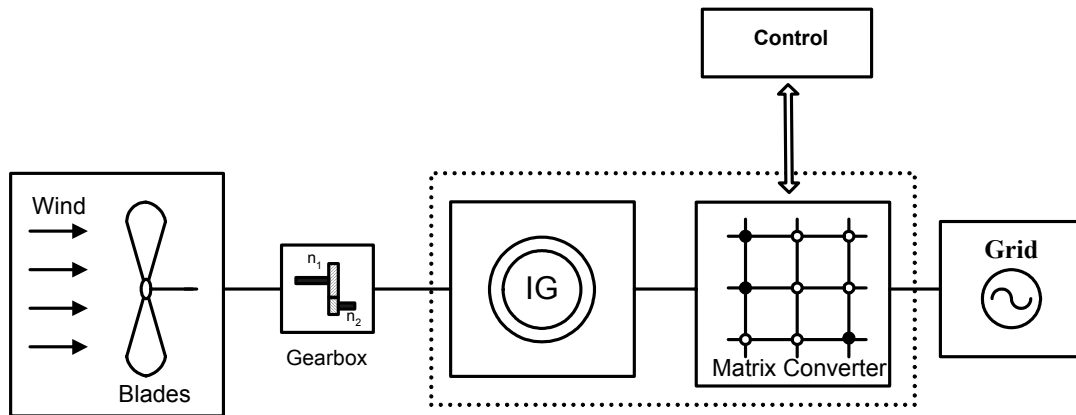


Fig. 3-1: Schematic diagram of the proposed wind turbine system

MC interfaces the induction generator with the grid and implements a shaft speed control methods to achieve maximum power-point tracking at varying wind velocities. It also performs power factor control at the grid interface and satisfies the Var demand at the induction generator terminals.

Different components of the wind turbine system model and the interactions among them are illustrated in Fig. 3-2[95]. The figure shows model blocks for wind speed, the aerodynamic wind turbine, mechanical components, electrical generator, matrix converter, and utility grid. The system may also contain some mechanical parts for blades angle control.

In the following sections, detailed discussions of the building blocks of the overall model are presented. Note that, the dynamic model of the MC was developed in Chapter 2, will be used in this section.
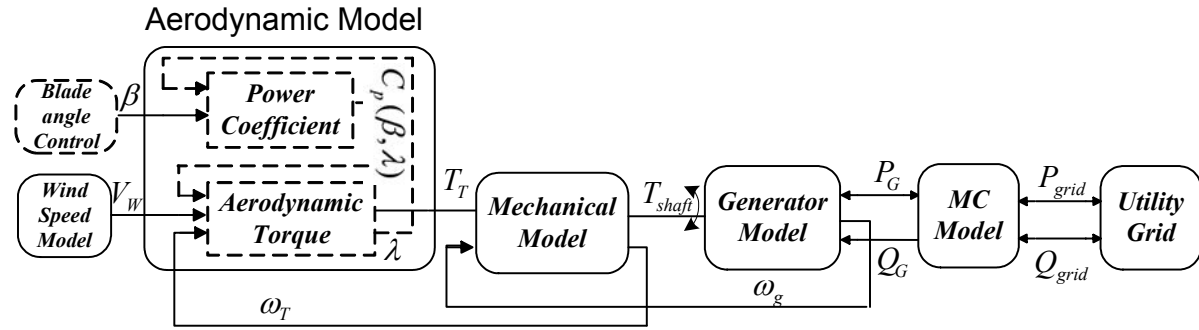
Fig. 3-2 Block diagram of the overall wind turbine system model

## 3.2.1 Aerodynamic Model

As illustrated in Fig. 3-2, the output of the aerodynamic model block is the mechanical torque on the wind-turbine shaft, that is a function of the wind-turbine characteristics, wind speed, shaft speed, and the blade angle. In the following, a formula for the turbine output power and torques will be introduced.

### 3.2.1.1 Wind Turbine Output Torque

As the wind blows, it turns the wind turbine's blades, which turns the generator rotor to produce electricity. The output power of wind turbine is related to two parameters: wind speed and rotor size. This power is proportional to the cubic wind speed, when all other parameters are assumed constant. Thus, the output power of wind turbines will increase significantly as wind speed increases. In addition, larger rotors allow turbines to intercept more wind, increasing their output power. The reason is that the rotors sweep a circular surface whose area is a function of the square of the blade length. Thus, a small increase in blade length leads to a large increase in the swept area and energy capture. But, for economical and technical reasons, the size of the blades in wind turbines has limitations.

The mechanical power and mechanical torque on the wind turbine rotor shaft are given by (3.1) and (3.2), respectively [95][106]-[108].

$$P_T = \frac{1}{2}\rho \, A_r C_p(\beta, \lambda) V_W^3 , \qquad (3.1)$$

$$T_T = \frac{1}{2\omega_T} \rho A_r C_p(\beta, \lambda) V_W^3 , \tag{3.2}$$

where:

$P_T$ = mechanical power extracted from turbine rotor,

$T_T$ = mechanical torque extracted from turbine rotor,

$A_r$ = area covered by the rotor= $\pi R^2$ where R is turbine rotor radius [m],

$V_W$= velocity of the wind [m/s],

$C_p$= performance coefficient (or power coefficient),

$\rho$ = air density [kg/m³],

$\lambda$= tip-speed-ratio (TSR),

$\beta$ = rotor blade pitch angle [rad.],

$\omega_T$ = angular speed of the turbine shaft [rad/s].

The blade tip-speed-ratio is defined as follows:

$$\lambda = \frac{\text{blade tip speed}}{\text{wind speed}} = \frac{\omega_T \times R}{V_W} . \tag{3.3}$$

The power coefficient $C_p$ is related to the tip-speed-ratio $\lambda$, and rotor blade pitch angle, $\beta$. Fig. 3-3 shows a typical $C_p$ versus tip-speed-ratio curve. $C_p$ changes with different values of the pitch angle, but the best efficiency is obtained for $\beta$=0 [21]. In the study reported in this thesis, it is assumed that the rotor pitch angle is fixed and equal to zero.

The power coefficient curve has been described by different fitted equations in the literature [12][21][109]. In this study, the $C_p$ curve is approximated analytically according to [106][107]:

$$C_p(\lambda, \beta) = (0.44 - 0.0167\beta)\sin[\frac{\pi(-3+\lambda)}{15-0.3\beta}] - 0.00184(-3+\lambda)\beta . \tag{3.4}$$

The theoretical upper limit for $C_p$ is 0.59 according to Betz's Law, but its practical range of variation is 0.2-0.4 [21][110].

Equations (3.1)-(3.4) give a model for the transfer of wind kinetic energy to mechanical energy on the shaft of wind turbine. The block diagram of this model is shown in Fig. 3-4.
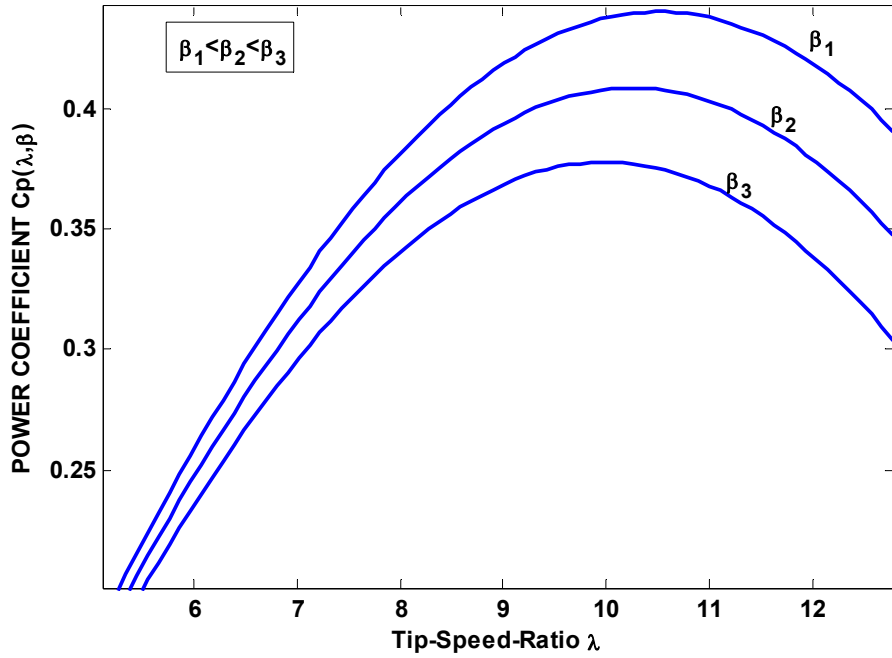
Fig. 3-3: A typical $C_p$ versus $\lambda$ curve
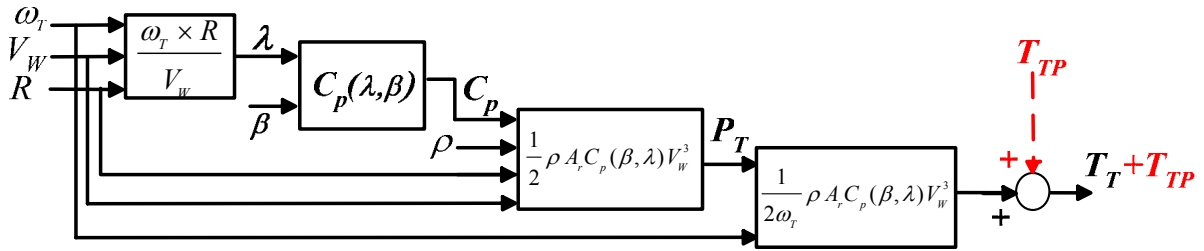


Fig. 3-4: Block diagram of the aerodynamic wind turbine model

### 3.2.1.2 Tower-Shadow Effect

The tower-shadow effect is caused by the periodical passing by of the wind turbine blades past the wind tower [111][112]. This gives a drop in the mechanical torque which is transferred to the generator shaft and subsequently felt as a drop in the output voltage. Usually the tower-shadow effect has a frequency proportional to the number of blades, for example, three per revolution for a three blade turbines. To account for the tower-shadow effect, a periodic torque pulse with frequency $f_{TP}$ is added to the output torque of the aerodynamic model. The frequency of the periodic torque is [81]:

$$f_{TP} = N \times f_r ,$$  (3.5)

where $N$ is the number of blades and $f_r$ the rotor angular speed (in Hz).

64

The magnitude of the torque depends on the type of wind turbine. As mentioned, based on the direction of wind received by the wind turbine, there are two structures: upwind and downwind. The tower-shadow effect is more significant in the downwind turbine. For this case, as a rule of thumb, the magnitude of this torque pulse equals 0.1 p.u., based on the rated torque of the wind turbine. The magnitude of the torque pulse for the upwind rotor is smaller in comparison with that for the downwind rotor [22][23]. The tower-shadow torque should be considered as a disturbance at the output of block diagram Fig. 3-4.

## 3.2.2 Mechanical Model

In this section, a complete mechanical model for the wind turbine shaft dynamics is presented. Since the time constants of some mechanical parts are large in comparison with those of the electrical components, and detailed information on all mechanical parameters is not available [113], the mechanical model has been developed based on reasonable time constant values and the data available. The model of a wind turbine drive train is fundamentally a three-mass model corresponding to a large mass for the wind turbine rotor, a mass for the gearbox and a mass for the generator. The moments of inertia of the shafts and gearbox can be neglected because they are small compared with the moments of inertia of the wind turbine and the generator [114][115]. Therefore, the mechanical model is essentially a two-mass model of rotor dynamics, consisting of a large mass and a small mass, corresponding to the wind turbine rotor inertia $J_T$ and generator rotor inertia $J_G$, respectively [11][108][114]-[116], as shown in Fig. 3-5. The low-speed shaft is modeled as an inertia, a spring with stiffness coefficient $K_s$, and a damper with damping coefficient $B$. An ideal gear box with the gear ratio $1:n_{gear}$ is included between the low-speed and high-speed shafts. Also, the parameters of the mechanical model are defined in Table 3.1.
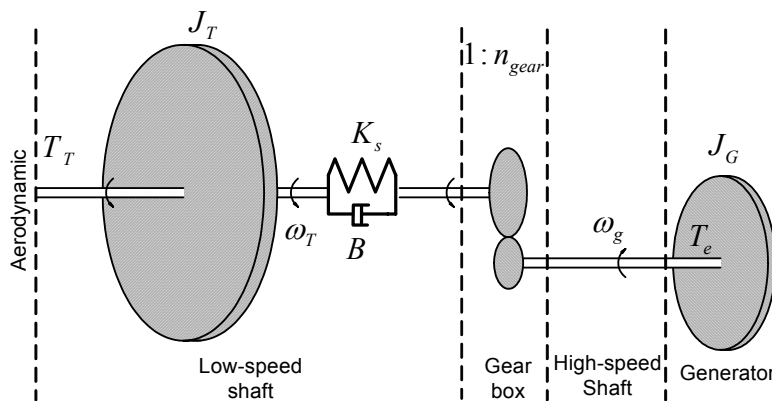


Fig. 3-5: A complete mechanical model of the wind Turbine shaft

Table 3.1: Mechanical model parameters

| Parameter | Description | Parameter | Description |
|---|---|---|---|
| $J_T$ | Wind turbine inertia [kg.m$^2$] | $\omega_T$ | Wind Turbine shaft speed [rad/s] |
| $J_G$ | Generator inertia [kg.m$^2$] | $\omega_g$ | Generator shaft speed [rad/s] |
| $K_s$ | Stiffness coefficient [N.m/rad] | $\theta_T$ | Wind Turbine shaft angle [rad] |
| $B$ | Damper coefficient[N.m/rad./s] | $\theta_g$ | Generator shaft angle [rad] |
| $T_T$ | Wind turbine torque [N.m] | $1{:}n_{gear}$ | Gear ratio |
| $T_e$ | Generator electromechanical torque [N.m] | | |

The drive train converts the aerodynamic torque $T_T$ on the low-speed shaft to the torque on the high-speed shaft $T_e$. The dynamics of the drive train are described by the following three differential equations:

$$\frac{d}{dt}\omega_T = \frac{1}{J_T}[T_T - (K_s\delta\theta + B\delta\omega)], \tag{3.6}$$

$$\frac{d}{dt}(\delta\theta) = \delta\omega, \tag{3.7}$$

$$\frac{d}{dt}\omega_g = \frac{1}{J_G}[\frac{1}{n_{gear}}(K_s\delta\theta + B\delta\omega) - T_e]. \tag{3.8}$$

where $\delta\theta = \theta_T - \theta_g / n_{gear}$, $\delta\omega = \omega_T - \omega_g / n_{gear}$, $T_T$ is the turbine mechanical torque from (3.2) and $Te$ is the generator electromechanical torque which will be introduced in the next section.

It is worth mentioning that as a simple dynamic model, one can consider a single mass model, i.e., one lumped mass accounting for all the rotating parts of the wind turbine. In fact, the stiffness and damping of shaft are used for the sake of completeness and can be removed in case they are not important in a specific application. This removal simplifies the dynamic model and reduces system order, but the completeness of dynamic model will be compromised. In the wind turbine system under study, in order to model the mechanical system, a two-mass model will be adopted. However, at the end of this chapter in section 3.12, some reduced-order methods will be presented to reduce the order of the overall dynamic model of the system.

### 3.2.3 Induction Machine Model

Fig. 3-6 shows an idealized three-phase induction machine consisting of a stator and a rotor [117][118]. Each phase in stator and rotor windings has a concentrated coil structure. The balanced three-phase ac voltages in the stator induce current in the short-circuited rotor windings by induction or transformer action. It can be shown that the stator current establishes a spatially sinusoidal flux density wave in the air gap which rotates at synchronous speed given by:

$$\omega_s = \frac{2}{P}\omega_e,$$  (3.9)

where $\omega_s$ is the synchronous speed in rad/sec, $\omega_e$ stator angular electrical frequency in rad/sec, and $P$ the number of poles. If the mechanical shaft speed of the machine is define as $\omega_r$ (in rad/sec), at any speed $\omega_s$, the speed difference $\omega_s$-$\omega_r$ creates slip ($s$). The slip is defined as follows:

$$s = \frac{\omega_s - \omega_r}{\omega_s}.$$  (3.10)

In the induction generator, at steady-state operating point, $\omega_r$ ($=\omega_g$) is slightly higher than $\omega_s$ (i.e., $s<0$), while in induction motor, $\omega_r$ is slightly lower than $\omega_s$ (i.e., $s>0$).
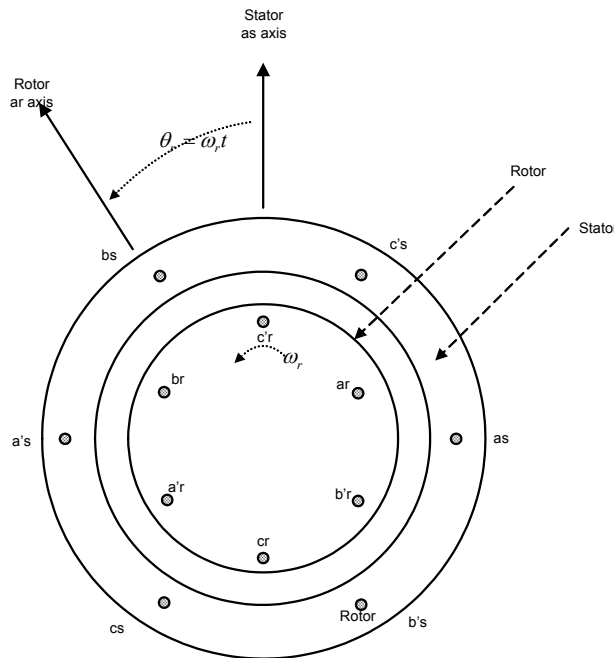


Fig. 3-6: Equivalent circuit for the induction machine [117]

A transformer-like per-phase equivalent circuit for induction machine, in steady-state, is shown in Fig. 3-7.
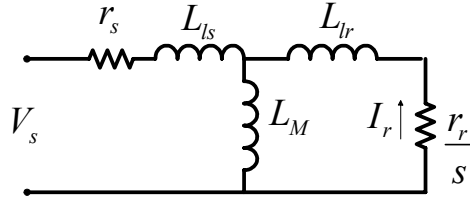
Fig. 3-7: A per-phase equivalent circuit for induction machine

In this equivalent circuit, $r_s$ is the stator resistance, $L_{ls}$ the stator inductance, $L_M$ the magnetizing inductance, $L_{lr}$ the rotor inductance (referred to stator circuit) and $r_r$ the rotor resistance (referred to stator circuit). In the generator mode, the resistance $r_r/s$ has a negative value. This negative resistance implies the existence of a source and therefore, the direction of power in the generator mode is from the rotor circuit to the stator circuit.

In steady-state, the electromechanical torque on the shaft is a function of the rotor current, rotor resistance and slip, as expressed by (3.11) [117][118].

$$T_e = \frac{3}{\omega_s} I_r^2 \frac{r_r}{s} . \tag{3.11}$$

If the terminal voltage and frequency are constant, $T_e$ can be calculated as a function of slip ($s$) from equation (3.11). Fig. 3-8 shows the torque-speed curve, where the value of slip is extended beyond the region $0 \le s \le 2$. In Fig. 3-8 two distinct zones can be identified: generating mode ($s<0$) and motoring mode ($0 \le s \le 1$). The sign of the torque in the motoring and generating regions has been specified based on the convention that: $T_{motor} > 0$ and $T_{generator} < 0$. The magnitude of the counter torque that is developed in the induction generator as a result of the load connected at the machine's stator terminals is then $T_c = - T_e$. The theoretical range of operation in the generator mode is limited between the synchronous angular speed $\omega_s$ and the $\omega_r$ corresponding to the pushover torque.

It is worth noting that, as shown in the equivalent circuit of Fig. 3-7, the induction machines have inductive nature, and therefore, the induction generator (similar to induction motor) absorbs reactive power from its terminals. The reactive power essentially sustains the rotating magnetic field in the air gap between the cage rotor and the stator winding. This reactive power should be supplied by the grid, in grid-connected mode, or by the capacitor-bank that is connected at the stator terminals, in stand-alone mode [118]. Moreover, it is possible to add a power electronic converter, acting as a dynamic Var compensation device, at the stator terminals, for additional and smoother Var control [119].

The output voltage of the generator, in stand-alone operation, can be estimated from the intersection point of the magnetization curve of the machine and the impedance line of the capacitor. This intersection point defines the operating point. Also the output frequency, in a grid connection, is dictated by the grid, while in stand-alone operation, it is a function of the load, rotor speed and excitation capacitance [120].
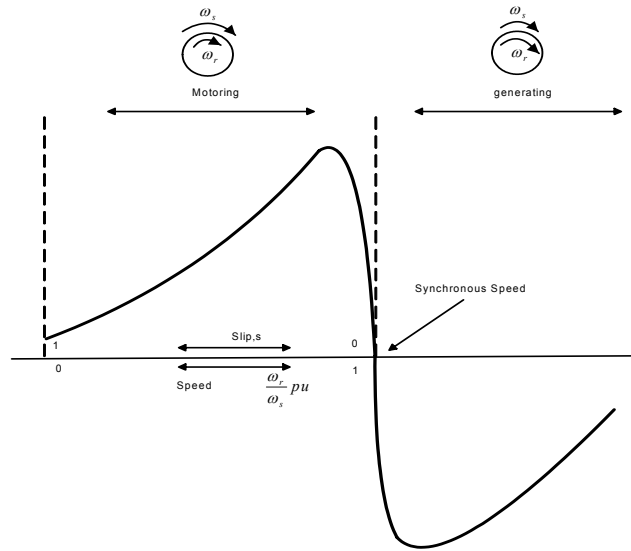


Fig. 3-8: Torque-speed curve of induction machine [117][118]

### 3.2.3.1 Dynamic Model of the Induction Machine

A commonly-used induction machine model is based on the flux linkages [118]. The dynamic equivalent circuit of the induction machine in *qdo* frame is illustrated in Fig. 3-9 [118][121].
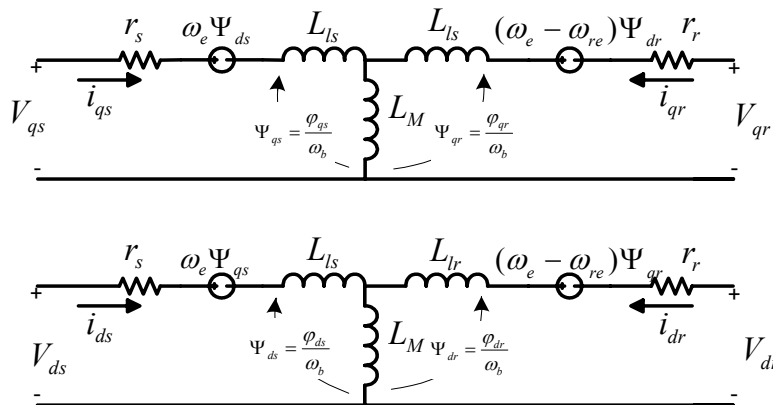


Fig. 3-9: *qdo*-equivalent circuit of an induction machine [118][121]

69

Note that in the *qdo*-equivalent circuit all the rotor parameters are transferred to the stator side. The machine is described by four differential equations based on flux linkage in the *qdo* frame and one differential equation based on rotor electrical angular speed, as follows:

$$\frac{d\psi_{qs}}{dt} = C_1\psi_{qs} - \omega_e\psi_{ds} + C_2\psi_{qr} + \omega_b v_{qs},$$  (3.12)

$$\frac{d\psi_{ds}}{dt} = \omega_e\psi_{qs} + C_1\psi_{ds} + C_2\psi_{dr} + \omega_b v_{ds},$$  (3.13)

$$\frac{d\psi_{qr}}{dt} = C_3\psi_{qs} + C_4\psi_{qr} - (\omega_e - \omega_{re})\psi_{dr},$$  (3.14)

$$\frac{d\psi_{dr}}{dt} = C_3\psi_{ds} + (\omega_e - \omega_{re})\psi_{qr} + C_4\psi_{dr},$$  (3.15)

$$\frac{d\omega_{re}}{dt} = \left(\frac{p}{2J}\right)(T_e - T_L),$$  (3.16)

where

$$C_1 = \omega_b\frac{r_s}{x_{ls}}(\frac{x_{ml}^*}{x_{ls}} - 1), C_2 = \omega_b\frac{r_s}{x_{ls}}\frac{x_{ml}^*}{x_{lr}}, C_3 = \omega_b\frac{r_r}{x_{lr}}\frac{x_{ml}^*}{x_{ls}},$$

$$C_4 = \omega_b\frac{r_r}{x_{lr}}(\frac{x_{ml}^*}{x_{lr}} - 1),\ x_{ml}^* = (x_m^{-1} + x_{ls}^{-1} + x_{lr}^{-1})^{-1},$$

$\psi_{ds}, \psi_{qs}, \psi_{dr}$ and $\psi_{qr}$ : d-axis and q-axis stator and rotor flux linkages,

$r_r$ and $r_s$ : rotor and stator resistances,

$X_{ls}=\omega_e L_{ls}$ and $X_{lr}=\omega_e L_{lr}$ : stator and rotor leakage reactances, $X_m=\omega_e L_{ml}$ : magnetization reactance,

$\omega_e, \omega_b$ : stator and base electrical angular speeds, $\omega_{re}$ : rotor electrical angular speed,

$v_{qs}, v_{ds}$: *q* and *d*-axis stator voltages, $v_{qr}, v_{dr}$: *q* and *d*-axis rotor voltages,

$T_e$ and $T_L$: electromechanical and load torque.

The stator and rotor currents, in the *qdo*-equivalent circuit of Fig. 3-9, can be found as follows:

$$i_{qs} = \frac{1}{x_{ls}}(\psi_{qs} - \psi_{mq}),$$  (3.17)

$$i_{ds} = \frac{1}{x_{ls}}(\psi_{ds} - \psi_{md}),$$ 
(3.18)

$$i_{qr} = \frac{1}{x_{lr}}(\psi_{qr} - \psi_{mq}),$$ 
(3.19)

$$i_{dr} = \frac{1}{x_{lr}}(\psi_{dr} - \psi_{md}),$$ 
(3.20)

where

$$\psi_{mq} = x_{ml}^*[\frac{\psi_{qs}}{x_{ls}} + \frac{\psi_{qr}}{x_{lr}}] \text{ and } \psi_{md} = x_{ml}^*[\frac{\psi_{ds}}{x_{ls}} + \frac{\psi_{dr}}{x_{lr}}].$$

In addition, the electromechanical torque of the machine can be written as follows:

$$T_e = \frac{3}{2}\left(\frac{p}{2}\right)\frac{1}{\omega_b}(\psi_{ds}i_{qs} - \psi_{qs}i_{ds}) = C_5(\psi_{dr}\psi_{qs} - \psi_{qr}\psi_{ds}),$$ 
(3.21)

where $C_5 = \frac{3}{2}\frac{P}{2}\frac{1}{\omega_b}\frac{x_{ml}^*}{x_{ls}x_{lr}}.$

### 3.2.3.2 Constant V/f Speed Control Method

To avoid saturation of induction machine when the stator frequency changes, the stator terminal voltage is also adjusted using a constant a constant *V/f* strategy. This method is well known for the induction machine speed control [122]. A power electronic converter should be employed at the terminals of the induction generator to implement the constant *V/f* strategy. In the study reported in this thesis, this strategy is implemented for adjusting the speed of the turbine shaft to achieve maximum power point tracking.

### 3.2.4 Gearbox Model

As mentioned in Chapter 1, the duty of a mechanical gearbox is transforming the mechanical power from the slow turning rotor shaft to a fast-turning shaft, which drives the generator. The gearbox is mostly used in the wind turbines with induction generators. The need for this transmission arises from the problem that an induction generator cannot be built for very low speeds with good efficiency.

In order to model the gearbox, it is only needed to consider that the generator torque can simply be transferred to the low speed shaft by a multiplication. For example, for gearbox of Fig. 3-5, one can write [123]:

$$\frac{T_T}{T_e} = \frac{\omega_g}{\omega_T} = n_{gear} \,.$$

(3.22)

Note that for a no ideal gearbox, the efficiency of the gearbox should be considered in the model.

## 3.2.5 Grid model

The grid model consists of an infinite bus. The infinite-bus model can be used when the grid power capacity is sufficiently large such that the action of any one user or generator will not affect the operation of the power grid. In an infinite bus, the system frequency and voltage are constant, independent of active and reactive power flows.

## 3.2.6 Wind Speed Model

Although the wind model is not part of the wind turbine model, the output power calculation in the wind turbine rotor requires the knowledge of instantaneous wind speed.

Wind is very difficult to model because of its highly-variable behavior both in location and time. Wind speed has persistent variations over a long-term scale. However, surface conditions such as buildings, trees, and areas of water affect the short-term behaviour of the wind and introduce fluctuations in the flow, i.e., wind speed turbulence.

A brief review of the literature reveals different wind speed models. For example, a wind model based on superposition of components is proposed in [124]. In this method, the wind speed is modeled by four components: mean wind speed, ramp wind component, gust wind component and noise wind component. However, determining all four components is a difficult task.

In this study, wind speed is modeled with a random process. The model is based on Van Der Hoven and Von Karman's models [95][125]. The instantaneous value of wind speed, $v_W\,(t)$, can be described as the wind speed average value plus fluctuations in the wind speed, as follows:

$$v_W(t) = V_{WM} + \sum_{i=1}^{N} A_i \cos(\omega_i t + \Psi_i) ,$$

(3.23)

where $V_{WM}$ is the mean value of wind speed, typically determined as a 10-minute average value, $A_i$ is the amplitude of the wind speed fluctuation at discrete frequency of $\omega_i$ ($i=[1, N]$), $N$ is the number of samples, and $\psi_i$ is a random phase angle with a uniform distribution in the interval $[-\pi, \pi]$.

The amplitudes $A_i$ are based on a spectral density function $S(\omega)$ that is empirically fit to wind turbulence. The function $S(\omega)$ can be determined using Van Der Hoven's spectral model [125]. The independence of the model from the mean wind speed is a drawback of the model. Therefore, it cannot model the low frequency components, and it is not proper for a complete description of the wind speed over a short time scale, i.e., seconds, minuets, or hours [125]. Von-Karman's distribution given by (3.24) [125], a commonly-used turbulence spectral density function, is a solution to this problem.

$$S(\omega) = \frac{0.475\sigma^2 \dfrac{L}{V_{WM}}}{[1+(\dfrac{\omega L}{V_{WM}})^2]^{\frac{5}{6}}} . \tag{3.24}$$

In (3.24), $\sigma$ is the standard deviation of the wind speed, and $L$ is the turbulence length scale [m]. The parameter $L$ equals:

$$\begin{cases} 20h & if \quad h \le 30m \\ 600 & if \quad h > 30m \end{cases}, \tag{3.25}$$

where $h$ is the height at which the wind speed signal is of interest [m], which normally equals the height of the wind turbine shaft.

The amplitude of the $i^{th}$ harmonic, $A_i$ , based on the spectral density function of (3.24), can be defined as:

$$A_i(\omega_i) = \frac{2}{\pi}\sqrt{\frac{1}{2}[S(\omega_i) + S(\omega_{i+1})](\omega_{i+1} - \omega_i)} . \tag{3.26}$$

Fig. 3-10 shows a spectral density function based on equation (3.24). The parameters chosen for the simulation were: $V_{WM}=10$[m/s], $L=180$[m], $\sigma=2$, $N=55$. The instantaneous wind speed fluctuation, based on Von-Karman's spectral density over time is shown in Fig. 3-11.
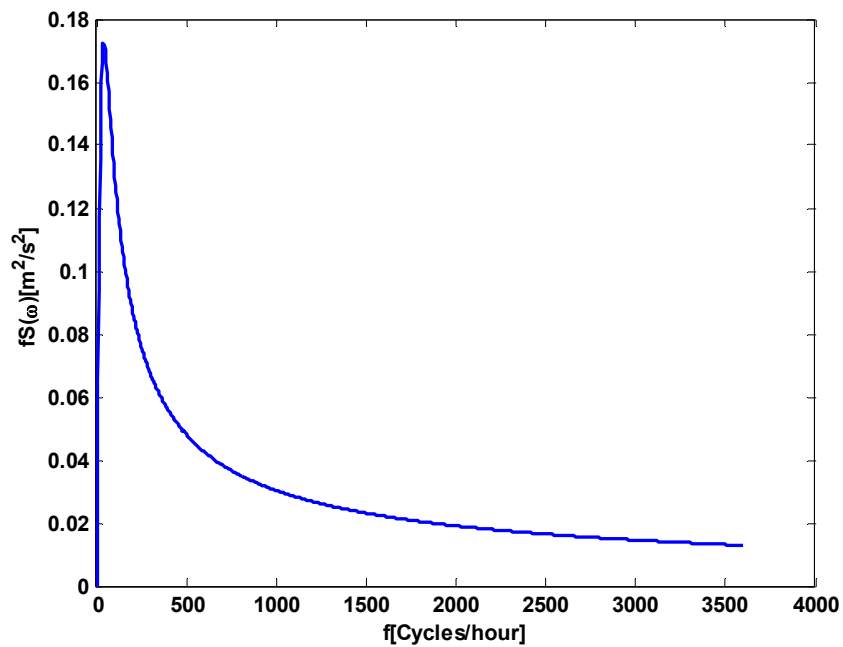
Fig. 3-10: Turbulence spectral density function according to Von-Karman's method
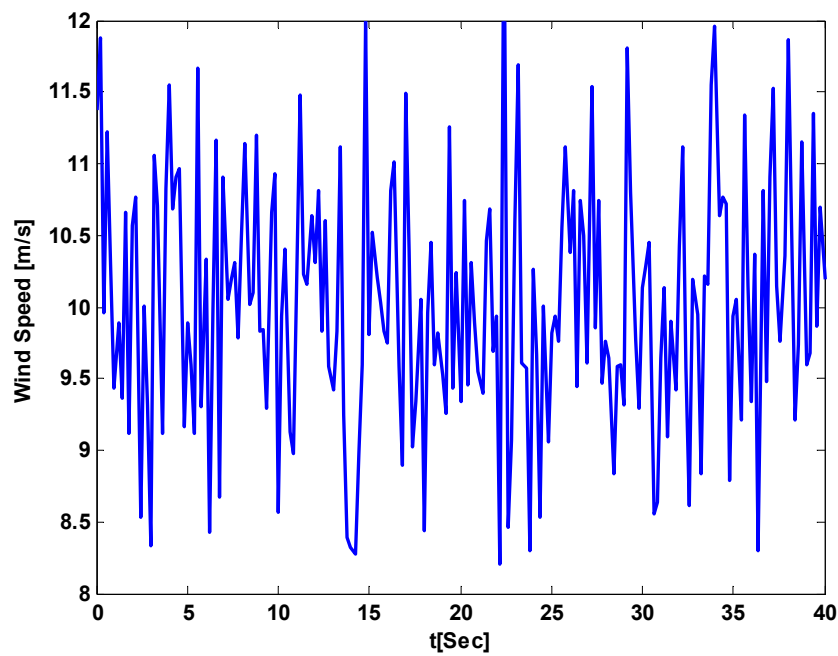


Fig. 3-11: Instantaneous wind speed as a function of time

### 3.2.6.1 High-Frequency Damping Effect

For wind power calculations, the instantaneous wind speed model should be augmented with complex wind effects on the wind turbine blades, including high-frequency damping effects and tower-shadow effects. In this section, the high-frequency damping effect is discussed.

The phenomenon of damping the high-frequency wind speed variations over the blades surface, namely high-frequency damping effect, should be included in the aerodynamic model of the wind turbine [108]. To approximate this effect, a low-pass filter with the following transfer function is employed.

$$H(s) = \frac{1}{1 + \tau s}.$$
(3.27)

The filter time constant $\tau$ depends on the turbine radius, average wind speed at hub height, and the intensity of wind turbulence. Fig. 3-12 shows the instantaneous wind speed and corresponding low-pass filtered signal.
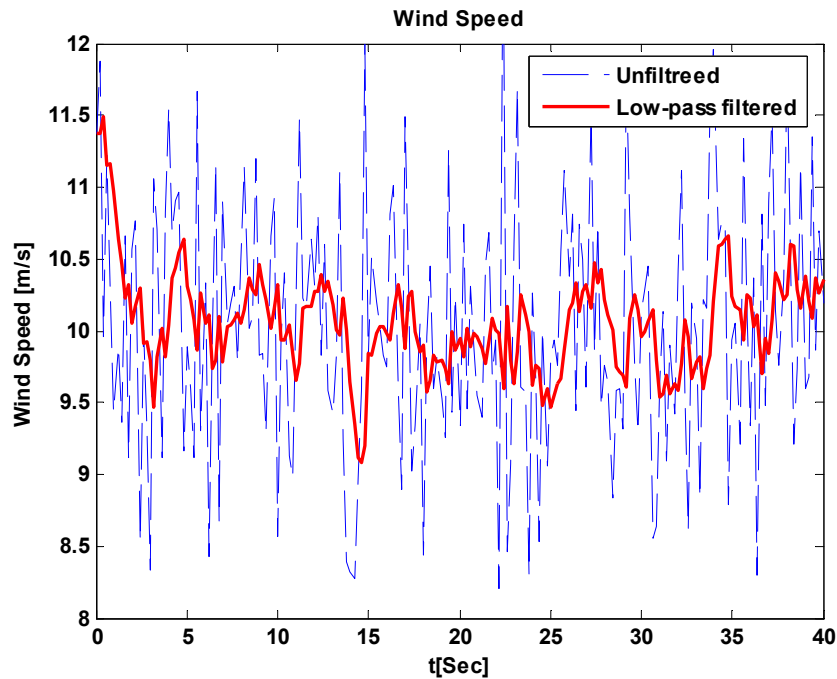


Fig. 3-12: Wind speed fluctuation: unfiltered and low pass filtered.

It is worth mentioning that the low-pass filtered wind speed data can be saved in a memory and used later for simulation, instead of using the instantaneous wind speed data and the low-pass filter dynamic equation.

## 3.3 Overall Dynamic Model of the Wind Turbine System

In the previous section and the pervious chapter, the components of the wind turbine system, shown in Fig. 3-2, were modeled by thirteen nonlinear equations (excluding the wind model): three, given by equations (3.6)-(3.8), for the wind turbine and shafts; six, given by equation (3.55), for the MC in balanced three-phase operation; and four, given by (3.17)-(3.20), for the induction machine. Using these equations, a complete dynamic model of the wind turbine will be developed in this section.

In the proposed system, Fig. 3-1, the input and output sub-circuits of the MC are connected to the electrical grid and the stator terminals of the induction generator, respectively. Therefore, based on the quantities defined in Section 3.2 and Chapter 3, the following equations can be written for the voltages, currents and frequency of the MC, as well as the induction generator terminal voltages:

Generator terminal voltages: $v_{qs} = v_{q\_out}$, $v_{ds} = v_{d\_out}$, $\qquad\qquad$ (3.28)

Generator terminal currents: $i_{qs} = i_{qo}$, $i_{ds} = i_{do}$, $\qquad\qquad$ (3.29)

Generator synchronous frequency and MC input frequency: $\omega_o = \omega_e$, $\omega_i = \omega_{Grid}$, $\qquad$ (3.30)

MC input sub-circuit terminal voltages: $v_{qG} = v_{q\_in}$, $v_{dG} = v_{d\_in}$. $\qquad\qquad$ (3.31)

In generator equations (3.12) and (3.13), the generator terminal voltages, $v_{qs}$ and $v_{ds}$, should be stated in terms of state variables and inputs variables. Note that, for the overall system, the grid voltage, $v_{qG}$ and $v_{dG}$, are the input variables.

From equation (2.49) the generator voltage can be written as follows:

$$v_{qs} = v_{q\_out} = -L_o \frac{d}{dt} i_{qs} - R_o i_{qs} - L_0 \omega_e i_{ds} + v_{qo}, \qquad\qquad (3.32)$$

$$v_{ds} = v_{d\_out} = -L_o \frac{d}{dt} i_{ds} + L_o \omega_e i_{qs} - R_o i_{ds} + v_{do}. \qquad\qquad (3.33)$$

Substituting the generator currents, equations (3.17) and (3.18), and their derivations in equations (3.32) and (3.33), and using equations (3.14) and (3.15), the generator terminal voltages can be expressed as a function of the system state variables, as follows:

$$v_{qs} = \frac{d}{dt}(\psi_{qs})\frac{-L_o}{x_{ls}}[1 - \frac{x_{ml}^*}{x_{ls}}] + \psi_{qs}(C_3\frac{L_o}{x_{ls}}\frac{x_{ml}^*}{x_{ls}} - \frac{R_o}{x_{ls}}[1 - \frac{x_{ml}^*}{x_{ls}}]) - \psi_{ds}\frac{L_0\omega_e}{x_{ls}}[1 - \frac{x_{ml}^*}{x_{ls}}]$$

$$+ \psi_{qr}\frac{x_{ml}^*}{x_{ls}}(C_4\frac{L_o}{x_{ls}} + \frac{R_o}{x_{ls}}) + \psi_{dr}\frac{L_0}{x_{ls}}\frac{x_{ml}^*}{x_{ls}}\omega_{re} + v_{qo},$$

(3.34)

$$v_{ds} = \frac{d}{dt}(\psi_{ds})\frac{-L_o}{x_{ls}}[1 - \frac{x_{ml}^*}{x_{ls}}] + \psi_{qs}(\frac{L_o\omega_e}{x_{ls}}[1 - \frac{x_{ml}^*}{x_{ls}}]) + \psi_{ds}(\frac{L_o}{x_{ls}}\frac{x_{ml}^*}{x_{ls}}C_3 - \frac{R_o}{x_{ls}}[1 - \frac{x_{ml}^*}{x_{ls}}])$$

$$- \psi_{qr}\frac{L_o x_{ml}^*}{x_{ls}x_{ls}}\omega_{re} + \psi_{dr}\frac{x_{ml}^*}{x_{ls}x_{ls}}(L_oC_4 + R_o) + v_{do}.$$

(3.35)

Next, using equations (3.34) and (3.35), the stator flux linkage equations, (3.12) and (3.13), can be presented as a function of system state variables, as follows:

$$\frac{d}{dt}\psi_{qs} = C_1^*\psi_{qs} + C_2^*\omega_e\psi_{ds} + C_3^*\psi_{qr} + C_4^*\psi_{dr}\omega_{re} + C_5^*v_{qo},$$

(3.36)

$$\frac{d}{dt}\psi_{ds} = -C_2^*\omega_e\psi_{qs} + C_1^*\psi_{ds} - C_4^*\psi_{qr}\omega_{re} + C_3^*\psi_{dr} + C_5^*v_{do},$$

(3.37)

where

$$C_0 = \omega_b\frac{L_o}{x_{ls}}[1 - \frac{x_{ml}^*}{x_{ls}}] + 1, C_1^* = \frac{1}{C_0}(C_1 + C_3\frac{\omega_bL_o}{x_{ls}}\frac{x_{ml}^*}{x_{ls}} - \frac{\omega_bR_o}{x_{ls}}[1 - \frac{x_{ml}^*}{x_{ls}}]),$$

$$C_2^* = \frac{1}{C_0}(-1 - \frac{L_0\omega_b}{x_{ls}}[1 - \frac{x_{ml}^*}{x_{ls}}]), C_3^* = \frac{1}{C_0}(C_2 + \frac{\omega_bx_{ml}^*}{x_{ls}}(C_4\frac{L_o}{x_{ls}} + \frac{R_o}{x_{ls}})),$$

$$C_4^* = \frac{1}{C_0}\frac{\omega_bL_0}{x_{ls}}\frac{x_{ml}^*}{x_{ls}}, C_5^* = \frac{1}{C_0}.$$

Finally, by combining the state-equation of the mechanical shaft, electrical generator, and the MC, the overall model of the system can be described by the following eleven nonlinear equations. The derivation of the overall system model from the component's models and all the constant coefficients has been presented in Appendix G.

$$\frac{d}{dt}i_{qG}^D = -\frac{R_i}{L_i}i_{qG}^D - \frac{\omega_{grid}}{2a-1}i_{dG}^D - \frac{1}{L_i}v_{qo} + \frac{1}{L_i}v_{qG}^D,$$

(3.38)

$$\frac{d}{dt}i_{dG}^D = \omega_{grid}(2a-1)i_{qG}^D - \frac{R_i}{L_i}i_{dG}^D - \frac{1}{L_i}v_{do} + \frac{1}{L_i}v_{dG}^D,$$

(3.39)

$$\frac{d}{dt}v_{qo} = A_7\varphi_{qs} + A_7'\varphi_{ds} + A_8\varphi_{qr} + A_8'\varphi_{dr} + \frac{1}{C}i_{qG}^D - \frac{\omega_{grid}}{2a-1}v_{do}, \tag{3.40}$$

$$\frac{d}{dt}v_{do} = A_7'(2a-1)^2\varphi_{qs} + A_7(2a-1)^2\varphi_{ds} + A_8'(2a-1)^2\varphi_{qr} + A_8(2a-1)^2\varphi_{dr}$$
$$+ \frac{1}{C}i_{dG}^D + \omega_{grid}(2a-1)v_{qo}, \tag{3.41}$$

$$\frac{d}{dt}\psi_{qs} = C_1^*\psi_{qs} + C_2^*\omega_e\psi_{ds} + C_3^*\psi_{qr} + C_4^*\psi_{dr}\omega_g + C_5^*\omega_e v_{qo}, \tag{3.42}$$

$$\frac{d}{dt}\psi_{ds} = -C_2^*\omega_e\psi_{qs} + C_1^*\psi_{ds} - C_4^*\psi_{qr}\omega_g + C_3^*\psi_{dr} + C_5^*\omega_e v_{do}, \tag{3.43}$$

$$\frac{d}{dt}\psi_{qr} = C_3\psi_{qs} + C_4\psi_{qr} - (\omega_e - \omega_g)\psi_{dr}, \tag{3.44}$$

$$\frac{d}{dt}\psi_{dr} = C_3\psi_{ds} + (\omega_e - \omega_g)\psi_{qr} + C_4\psi_{dr}, \tag{3.45}$$

$$\frac{d}{dt}\omega_G = \frac{1}{J_G}[\frac{1}{n_{gear}}(K_s\Delta\theta + B(\omega_T - \frac{2\omega_g}{Pn_{gear}}) - C_5(\psi_{dr}\psi_{qs} - \psi_{qr}\psi_{ds})], \tag{3.46}$$

$$\frac{d}{dt}\theta = \omega_T - \frac{2\omega_g}{Pn_{gear}}, \tag{3.47}$$

$$\frac{d}{dt}\omega_T = \frac{1}{J_T}[\frac{1}{2\omega_T}\rho A_r C_p(\beta,\lambda)V_w^3 - (K_s\Delta\theta + B(\omega_T - \frac{2\omega_g}{PR_G}))]. \tag{3.48}$$

The power exchanged between grid and the wind turbine is an important quantity of the wind turbine system. Therefore, the grid active and reactive powers injected into the grid are chosen as the output variables for the model. The formula for the grid power based on the equations (2.73) and (2.75) can be written as follows:

$$P_{Grid} = \frac{3}{2q}V_{Gm}[\cos(\alpha_o)i_{qG}^D - \sin(\alpha_o)i_{dG}^D], \tag{3.49}$$

$$Q_{Grid} = -\frac{3}{2q}\frac{V_{Gm}}{2a-1}(\sin(\alpha_o)i_{qG}^D + \cos(\alpha_o)i_{dG}^D), \tag{3.50}$$

where $V_{Gm}$ is the peak value of the grid phase voltage.

The schematic diagram of the wind turbine system's overall dynamic model is shown in Fig. 3-13. The model is characterized by six inputs $\bar{u}$, two outputs $\bar{y}$, and eleven state variables $\bar{x}$. Out of the six inputs, $\omega_e$, $q$, $a$, and $\alpha_o$ are adjustable control variables of the MC, $\beta$ is pitch angle of the turbine

blades, and $V_W$ is the wind velocity. The active and reactive powers injected into the grid are treated as output variables for the model.
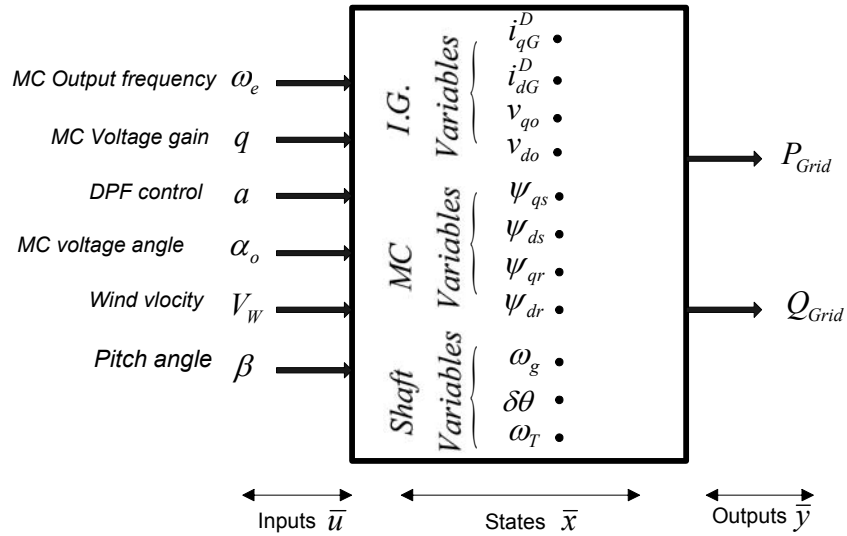


Fig. 3-13  Inputs, state variables and outputs of the overall dynamic model of wind turbine system

## 3.4 Verification of the Overall Dynamic Model

Here, the objective is to study the behavior of the system output variables, i.e., active and reactive powers injected into the utility grid, in response to variations of the input variables. In the following subsections, first the starting operation of the system will be simulated. Then, steady-state performance of the system for some input variations is investigated. Finally, the dynamic behavior of the model will be investigated by simulating its step responses. Although the realistic wind speed model was described in section 3.2.6, without loss of generality, in the following simulations the wind velocity is considered as a constant signal.

### 3.4.1 Starting the Wind Turbine System

The soft-starting procedure to reduce inrush current during the connection of the wind turbine to the grid was discussed in Chapter 1. This subsection, the system simulation starts with the wind turbine already connected to the grid [126]. The parameters of the wind turbine system are shown in Appendix L (Table L.2).

Fig. 3-14 shows the active and reactive power injected into the grid. The simulation starts with zero shaft speed and rated grid voltage. The electrical machine initially works in the motoring mode

and draws active power from the grid. When the shaft speeds up and the wind power increases, the machine switches to the generating mode and the direction of the power-flow will be changed from the generator to the grid. Table 3.2 shows the values for the model input parameters, the grid power, and the power factor at the operating point. The base values for the grid power and voltage are $S_b$=100 [kVA] and $V_{b\ (rms)}^{ll}$=4 [kV], respectively. Also, the phase-a and zoomed-in three-phase grid currents during the starting and steady-state operation are shown in Fig. 3-15.
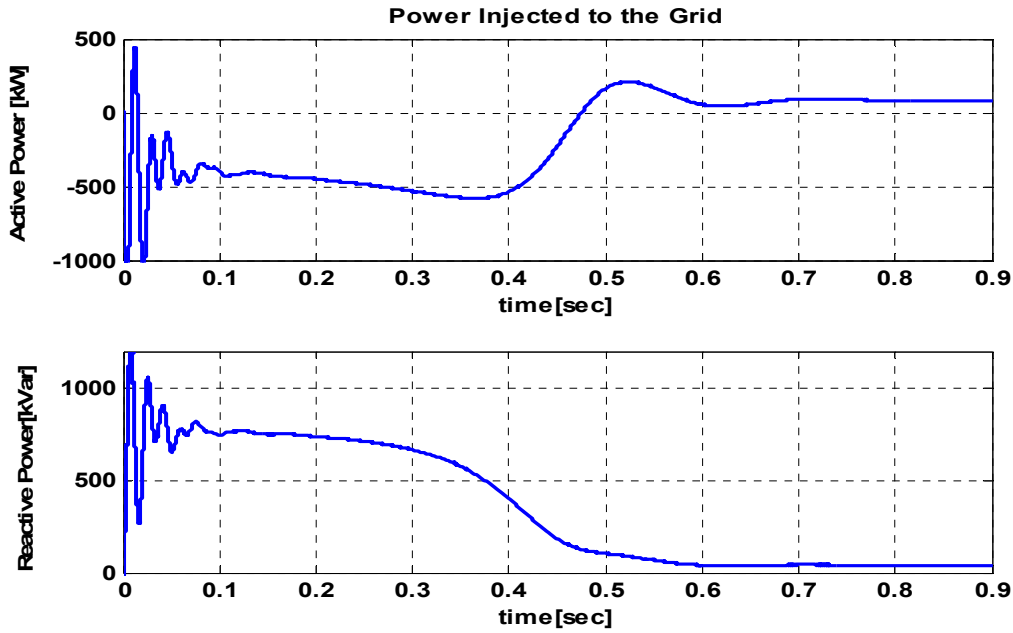


Fig. 3-14: Grid active and reactive power during the starting and the steady-state operation.

Table 3.2: Values of the input parameters and the grid power at the operating point

| Voltage Gain | Output voltage angle | MC output frequency | Pitch Angle | DPF Control | Wind Speed | Grid Power and power factor |
|---|---|---|---|---|---|---|
| $q$=0.5 | $\alpha_o$=0 | $f_e$= 6o [Hz] | $\beta$=0 | $a$=0.8 | $V_W$=10[m/s] | $P_{Grid}$= 82.76[kW] $Q_{Grid}$=40.87[kVar] $PF_{Grid}$=0.89 |
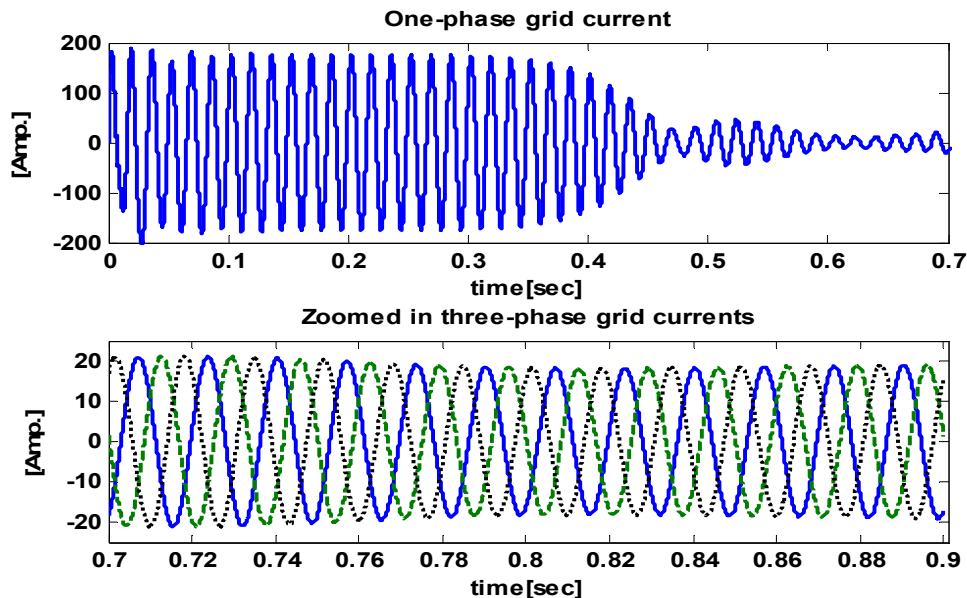
Fig. 3-15: Phase-a and three-phase grid current during the starting and steady-state operation.

## 3.4.2 Steady-State Performance of the System

The active and reactive powers injected into the grid are functions of the system inputs. Therefore, it is important to know how the grid power varies as the inputs of the system vary in their permitted ranges. In the following, the system steady-state output response to variations of the MC output frequency, voltage gain, and output voltage angle, as well as, parameter '*a*', are discussed.

Fig. 3-16 shows the steady-state grid active and reactive powers versus the MC output frequency, while other inputs of the system remain fixed at the rated values based on Table 3.1. As shown in Fig. 3-16, the active power first increases and then decreases as the frequency rises, while the reactive power decreases. The behavior of the active power verses frequency variation can be explained based on the wind turbine's power-verses-speed curve and the electrical generator power-verses-frequency curve, which will be are discussed further detail in Chapter 5 [95]. In addition, increasing the MC output frequency raises the consumption of the system reactive power, hence the reactive power injected to the grid will be decreased.

Fig. 3-17 shows the steady-state grid active and reactive power versus the MC gain voltage. The gain voltage variation has a significant effect on the grid reactive power and a minor effect on the grid active power [95].
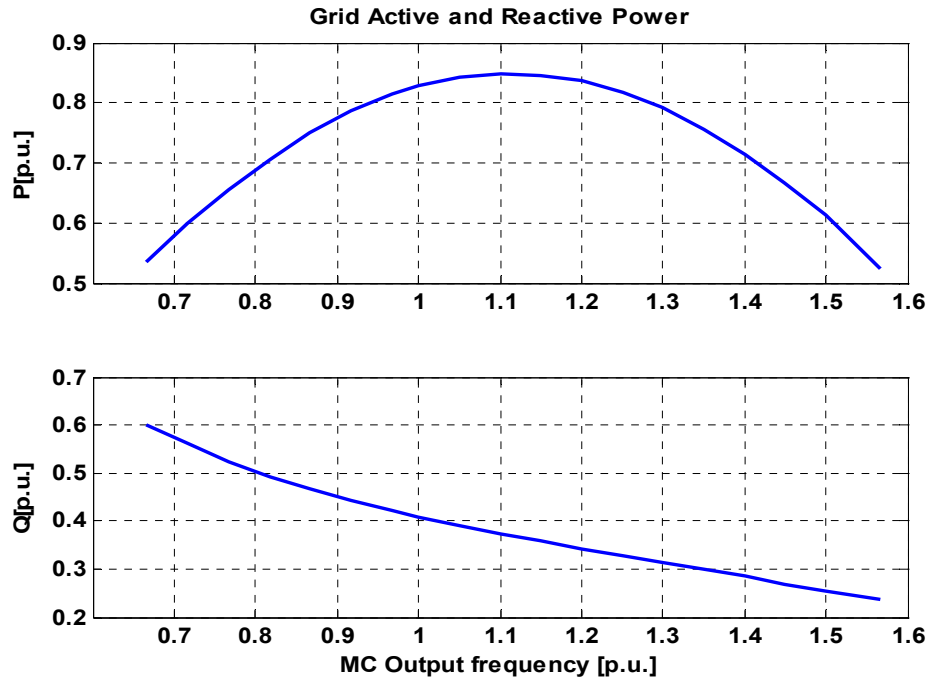
Fig. 3-16: Steady-state grid active and reactive power versus the MC output frequency
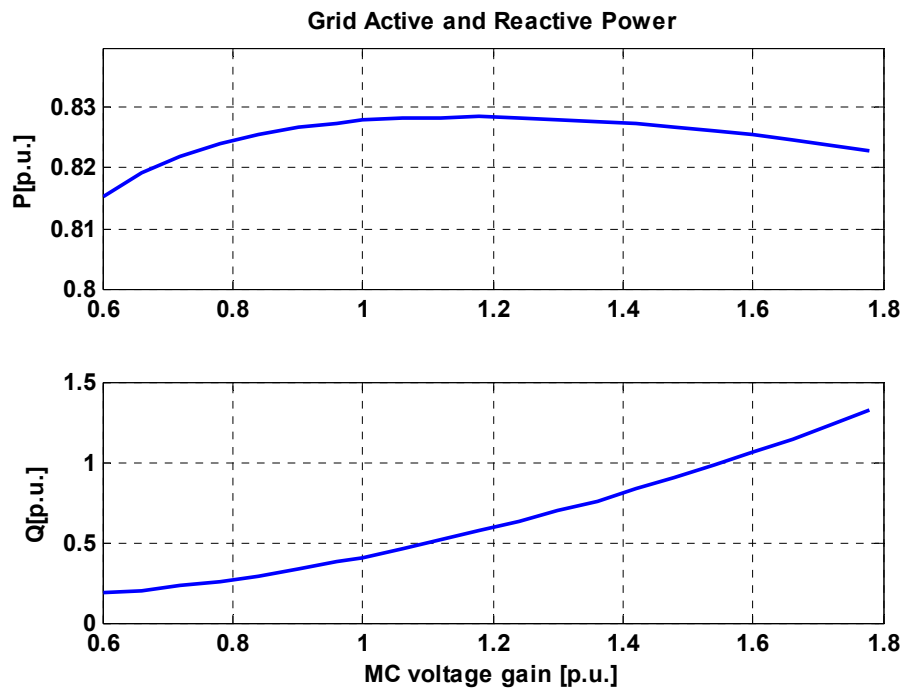


Fig. 3-17: Steady-state grid active and reactive powers versus the MC voltage gain

Fig. 3-18 shows linear variations in grid reactive power in both lagging and leading regions, corresponding to the ranges, $0 \leq a < 0.5$ and $0.5 < a \leq 1$, respectively. Note that the grid active power (not shown) is almost constant for variations of parameter '$a$'.

Fig. 3-19 shows the system outputs versus the MC output voltage angle, $\alpha_o$. Both grid active and reactive powers change dramatically with the angle $\alpha_o$. The electrical machine enters motoring mode, $P<0$, for some ranges of variations of the MC output voltage angle. The results show that $\alpha_o$ is not an appropriate input to control the system, because it causes severe variations in the system outputs and sometimes makes the machine swing between generatoring and motoring modes. Therefore, the MC output voltage angle will be kept constant at $\alpha_o = 0$ in the rest of this thesis to maintain the machine in the generatoring mode.
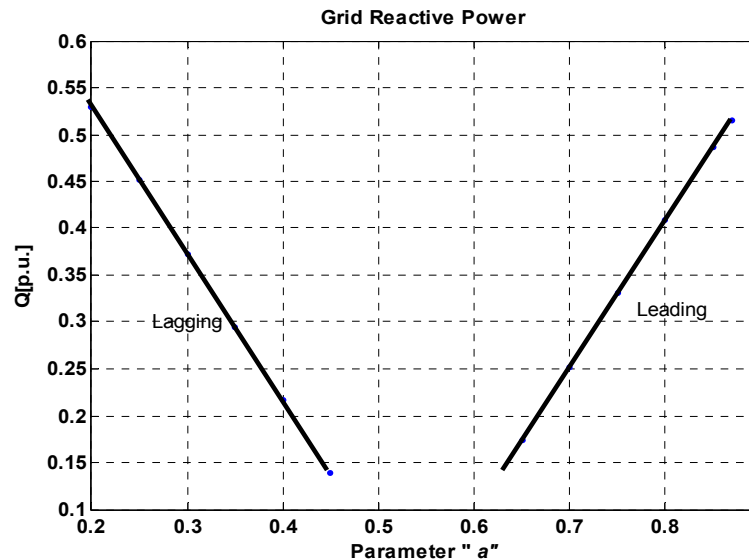


Fig. 3-18: Steady-state grid reactive power versus the parameter '$a$' in lagging and leading regions.
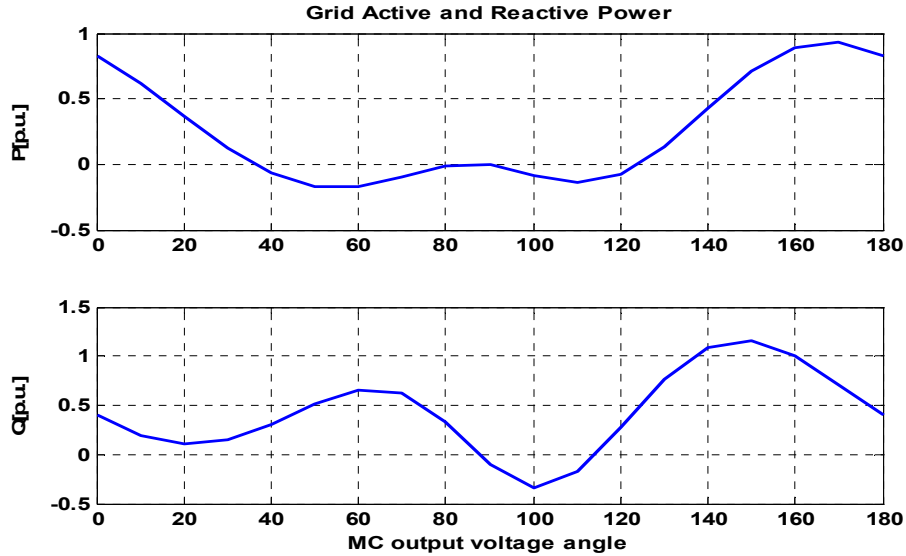
Fig. 3-19: Steady-state grid active and reactive powers versus the MC output voltage angle ($\alpha_o$).

## 3.4.3 Step Response of the System

In this section, the dynamic behavior of the system model, shown in Fig. 3-13, is investigated by simulating its step responses to different input variables. Among the electrical input variables of the model related to the MC set-points, the focus will be on the output angular speed ($\omega_e$), voltage gain ($q$), and parameter '$a$' related to input *DPF*. The wind velocity ($V_w$) is an uncontrollable disturbance input; however, the system dynamic response to wind velocity variations is important. Note that, the pitch angle is taken to be a stall control against wind gusts. In other words, the system under study is a fixed-pitch wind turbine.

Before applying the step changes, the system operates at its steady-state operating point. The first step response is related to the MC output frequency, as shown in Fig. 3-20. In this figure, responses of the grid active and reactive powers, as well as phase-a grid current, are shown for a 5% frequency step increase, corresponding to $\Delta\omega_e=3$[Hz], at t=2 [sec.]. As shown in the figure, for 5% change in the frequency, the grid current goes up from 1[p.u.] to 5 [p.u.] in about 2 cycles. Note that, in the system under study, the MC has no direct control on the grid current. Therefore, the overcurrent problem observed in the system dynamic response should be considered in the design of the converter and the protection system. The limitation related to the overcurrent will be discussed in section 3.6.

Table 3.3 shows that the frequency increase causes an increase in the grid active power and a decrease in reactive power. As mentioned before, with respect to the operating point of the system,

increasing the frequency may increase or decrease the active power. However, in this case, the frequency increase causes the increase in consumption of the system reactive power. Note that, from the control point of view, the system response to a step change in frequency indicates that the system is of non-minimum-phase nature.
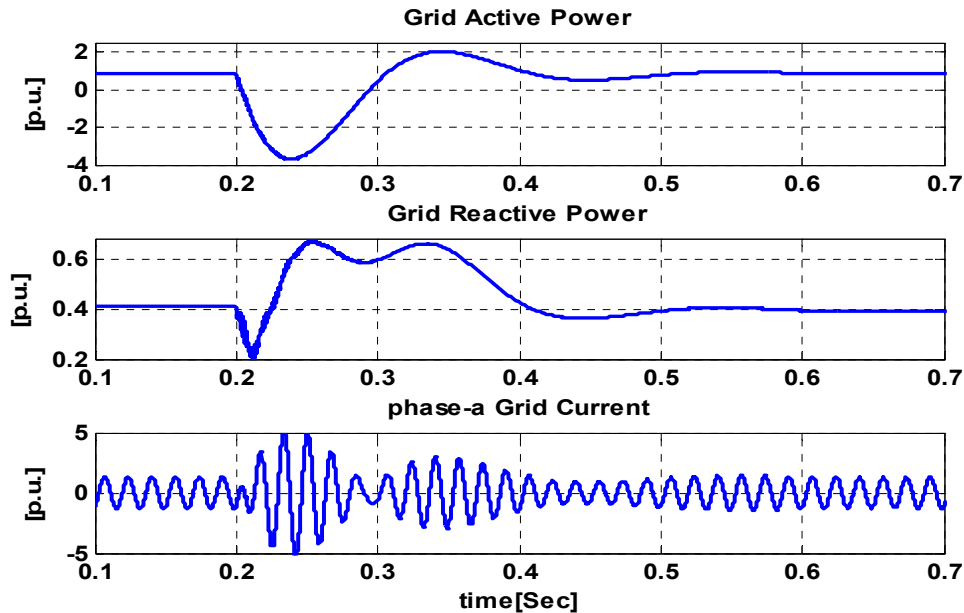


Fig. 3-20: Grid active and reactive powers and phase-a grid current responses of the dynamic wind model to 5% step increase in the MC output frequency ($\omega_e$) at t=0.2[sec.].

Fig. 3-21 shows the step response of the system to a 5% step increase in the MC voltage gain ($q$). As shown in this figure and Table 3.3, voltage gain increase results in a significant increase in grid reactive power, while active power remains almost constant, because reactive power, unlike active power, is highly dependent on the voltage magnitude.

A big step change is considered for the parameter "$a$", related to grid DPF control, as shown in Fig. 3-22. The step response of Fig. 3-22 and results in Table 3.3 reveal that the system is stable with this big step change, and also that grid reactive power is changed from the leading to the lagging state. This big change in the parameter "$a$" is applied to the system to show the capability of the system reactive power control.

Finally, the last step response is related to the wind velocity. As mentioned earlier, the wind velocity is an uncontrollable input and its step change shows the system performance for disturbance variation. The step response, illustrated in Fig. 3-23, and the results in Table 3.3, show that wind

velocity increments dramatically increase the grid active power. This occurs because of increase in the turbine mechanical power.
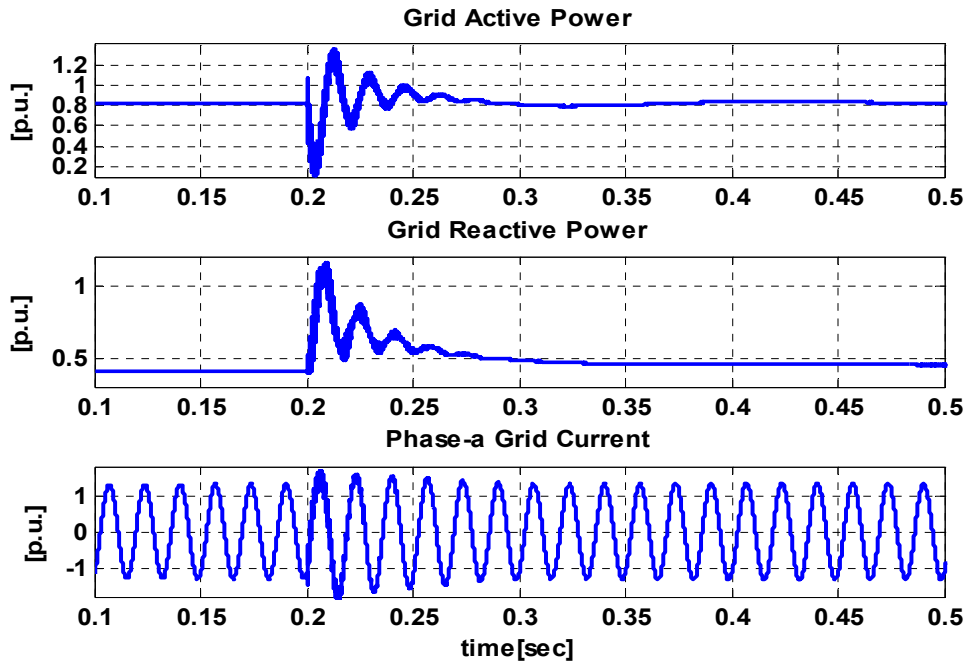


Fig. 3-21: Grid active and reactive powers and phase-a grid current responses of the dynamic wind model to 10% step increase in the MC voltage gain at t=0.2[sec.]
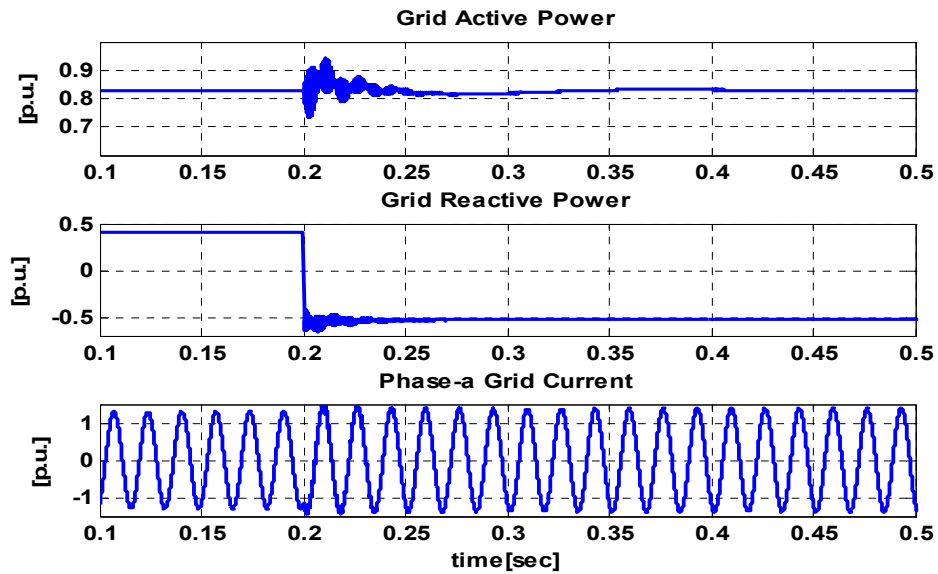


Fig. 3-22: Grid active and reactive powers and phase-a grid current responses of the dynamic wind model to 75% step decrease in the parameter "*a*" at t=0.2[sec]

86
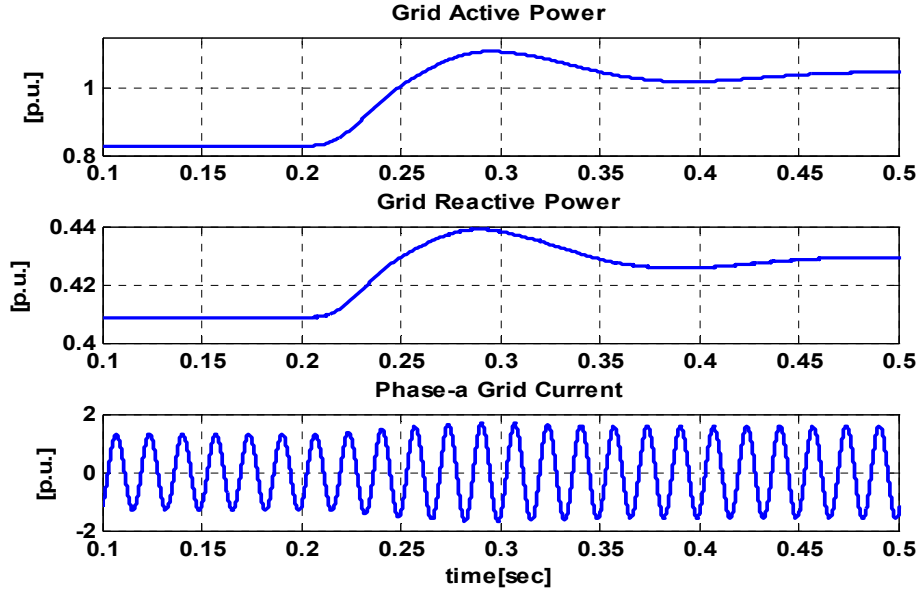
Fig. 3-23: Grid active and reactive powers and phase-a grid current responses of the dynamic wind model to 10% step increase in the wind velocity at t=0.2[sec.].

Table 3.3: Variations in output variables of the wind turbine model against some input variations

|  | $\Delta f_e$ =5% | $\Delta q$ =5% | $\Delta a$ =-75% | $\Delta V_W$ =10% |
|---|---|---|---|---|
| $\Delta P_{Grid}$ | 1.82% | 0.09% | 0.05% | 25.56% |
| $\Delta Q_{Grid}$ | -4.4% | 10.12% | -229.5% | 4.82% |

## 3.5 Overall Dynamic Model and Constant V/f Strategy

As mentioned in Subsection 3.2.3.2, the terminal voltage and frequency of the induction generator are usually controlled according to the constant *V/f* strategy to avoid flux saturation. The ratio of the variation of voltage and frequency is:

$$K_{VF} = \frac{q_{rated}}{\omega_{e\_rated}} , \qquad (3.51)$$

where $K_{VF}$ is a constant parameter, and $q_{rated}$ and $\omega_{e\_rated}$ are the MC rated voltage gain and output frequency, respectively.

To take into account the constant *V/f* strategy in the overall dynamic model, shown in Fig. 3-13, the model should be modified based on the equation (3.51). The modified model nonlinear dynamic equations are given in Appendix H.

### 3.5.1 Verification of the Overall Dynamic Model with Constant *V/f* Strategy

The steady-state and dynamic behaviors of the model with constant *V/f* strategy for the input variations must be the same as the results shown in the previous section, except for the MC frequency output. Therefore, the output response of the new model is verified only for the MC frequency change. Because of the constant *V/f* strategy, a change in the frequency is proportional to a change in the MC voltage gain whose magnitude can be determined based on the equation (3.51).

Fig. 3-24 shows the steady-state grid active and reactive powers verses the MC output frequency. During frequency increase, grid active power increases and then decreases, while reactive power increases with an almost constant slope. Increasing the frequency corresponds to increase in the voltage gain and the resulting increase in reactive power.
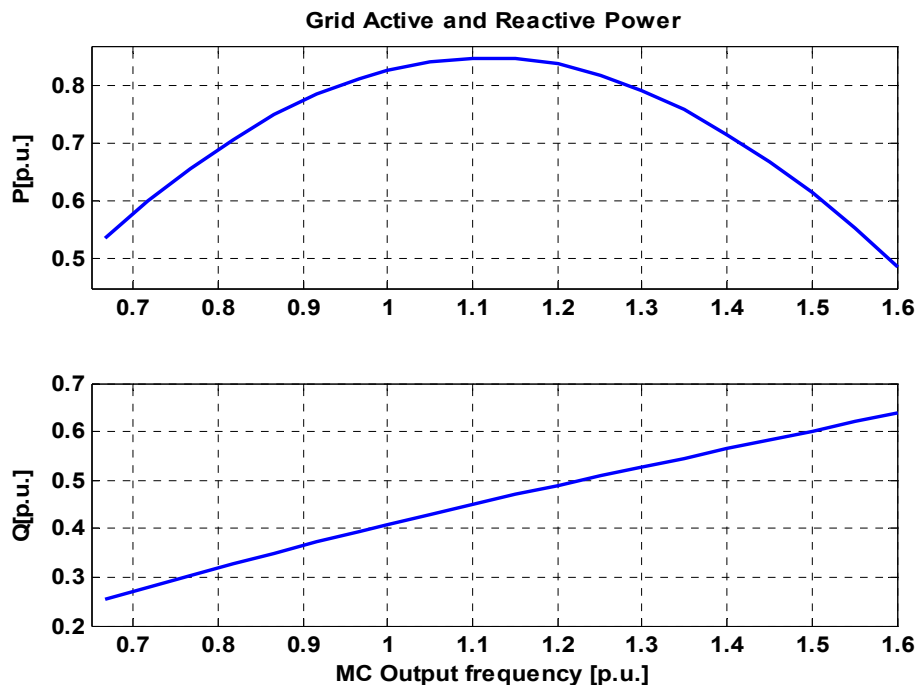


Fig. 3-24: Steady-state grid active and reactive powers versus the MC output frequency with constant *V/f* strategy

For the dynamic response, consistent with the previous simulation, a 5% step-increase is applied at t=2 [sec.] to the MC set-point frequency. Fig. 3-25 illustrates the step response of the grid power and

phase-a current. In addition, Table 3.4 shows the steady-state changes of the grid active and reactive powers for the applied step change.

The dynamic and steady-state results, Fig. 3-25 and Table 3.4, can be interpreted by considering the results of step change in frequency and the voltage gain, Fig. 3-20, Fig. 3-21 and Table 3.3, and coupling effects between the grid active and reactive power. As a result, changes in frequency affect both active and reactive power, but the magnitude of these effects depends on to the system operating point.
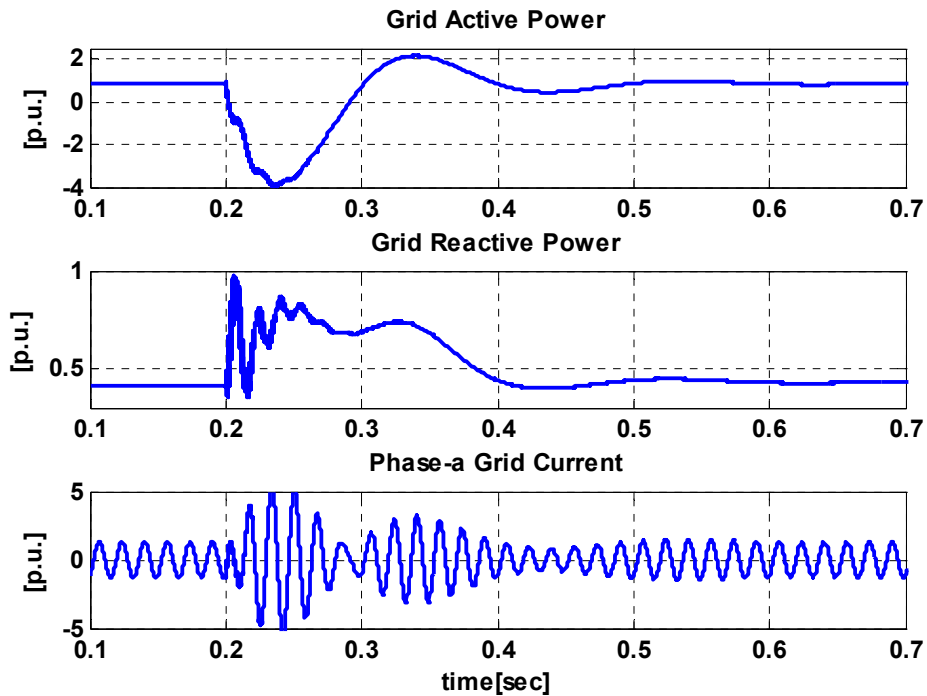


Fig. 3-25: Grid active and reactive powers and phase-a grid current responses of the dynamic wind model with constant *V/f* strategy to 5% step-increase in the MC output frequency at t=0.2[sec.]

Table 3.4: Variations of output variables of the wind turbine model with constant *V/f* strategy for step change in frequency and voltage gain

|  | $\Delta f_e$ =5% |
|---|---|
| $\Delta P_{Grid}$ | 1.82% |
| $\Delta Q_{Grid}$ | 5.12% |

## 3.6 Limitations of the variables changes

The allowable range of variation of system variables are determined by the ratings of system components. As shown in Figs. 3-20 and 3-25, in response to a small step change in the generator terminal frequency in the open-loop system, the grid current rises from 1 [p.u.] to 5 [p.u.] over 2 cycles. Devices such as MC switches cannot tolerate currents of five times their rated values in transients lasting 2 cycles. Sizing the devices based on the maximum transient current is not economical either. In actual wind turbine systems, such large over-currents can be avoided by applying changes in the control variables in the form of a ramp function instead of a step function. In the closed-loop system, there are no step changes in the wind velocity (Fig. 3-12), and as a result, no step changes in the control variables occur.

Fig. 3-26 shows a 5% ramp-increase in the MC frequency at t=0.2 [sec]. Comparing the grid current in this figure with that in Fig. 3-25 shows that the maximum transient current has been limited to 1.6 [p.u.]. This allows for sizing the system component more economically. Note that there are no limitations in using step-change for other inputs. For example, in Fig. 3-22 a step-change in the parameter a results in no significant transient current.
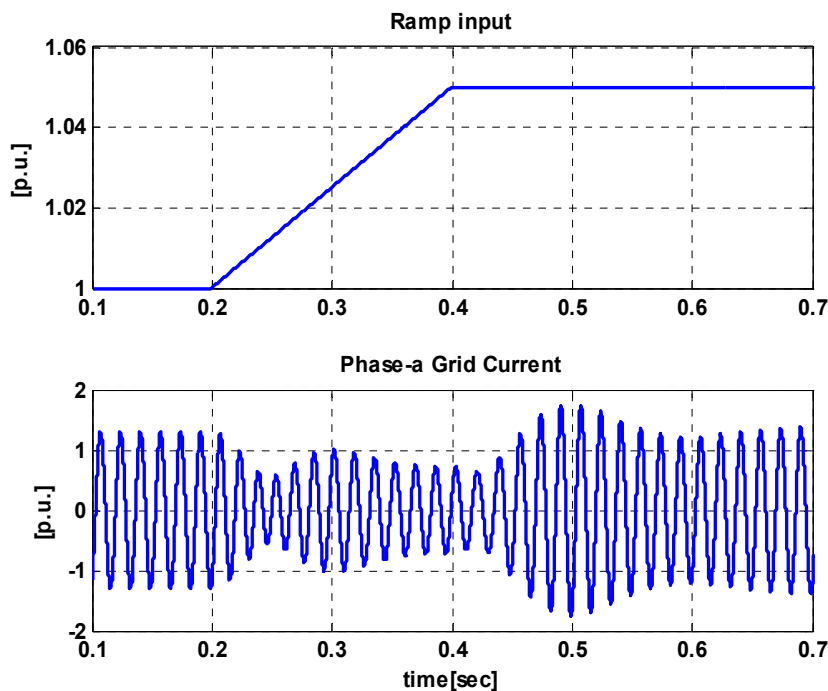


Fig. 3-26: Phase-a grid current response of the dynamic model with constant *V/f* strategy to a 5% ramp-increase in the MC output frequency at t=0.2 [sec].

90

## 3.7 Linearized Model of the Wind Turbine System

The nonlinear state-space model of the wind turbine system (with constant *V/f* strategy) presented in section 3.5, contains eleven nonlinear equations. The sources of nonlinearity are the turbine torque equation (3.2), induction machine equations (3.12)-(3.16), and the MC equation (2.58).

In the next sections, a small-signal model is used to systematically study local stability, controllability, and observability. The small-signal model is developed by linearizing the eleven nonlinear equations (Appendix H) around an operating point. The linearized model, is described by the following state-space equations:

$$\frac{d}{dt}\Delta \overline{X} = A\Delta \overline{X} + B\Delta \overline{U},$$

(3.52)

$$\Delta \overline{Y} = C\Delta \overline{X} + D\Delta \overline{U},$$

where

$$\Delta \overline{X} = [\Delta i_{qG}^{D} \quad \Delta i_{dG}^{D} \quad \Delta v_{qo} \quad \Delta v_{do} \quad \Delta \Psi_{qs} \quad \Delta \Psi_{ds} \quad \Delta \Psi_{qr} \quad \Delta \Psi_{dr} \quad \Delta \omega_{g} \quad \Delta(\delta\theta) \quad \Delta \omega_{T}]^{T},$$

$$\Delta \overline{U} = [\Delta \omega_{e} \quad \Delta q \quad \Delta a \quad \Delta \alpha_{o} \quad \Delta V_{W} \quad \Delta \beta]^{T}, \text{ and } \Delta \overline{Y} = [\Delta P_{Grid} \quad \Delta Q_{Grid}]^{T}.$$

In equation (3.52), *A, B, C,* and *D* are the Jacobian matrices, calculated at the operating point. The detailed linearization of the nonlinear equations is presented in Appendix I. This linearization results in the matrices *A, B, C,* and *D* as follows:

$$A = \begin{bmatrix}
-\dfrac{R_i}{L_i} & -\dfrac{\omega_{gird}}{2a^0-1} & -\dfrac{1}{L_i} & 0 & 0 & 0 & 0 & 0 & 0 & 0 & 0 \\[2mm]
\omega_{grid}(2a^0-1) & -\dfrac{R_i}{L_i} & 0 & -\dfrac{1}{L_i} & 0 & 0 & 0 & 0 & 0 & 0 & 0 \\[2mm]
\dfrac{1}{C} & 0 & 0 & -\dfrac{\omega_{grid}}{2a^0-1} & a_{3,5} & a_{3,6} & a_{3,7} & a_{3,8} & 0 & 0 & 0 \\[2mm]
0 & \dfrac{1}{C} & \omega_{grid}(2a^0-1) & 0 & a_{4,5} & a_{4,6} & a_{4,7} & a_{4,8} & 0 & 0 & 0 \\[2mm]
0 & 0 & C_5^*\omega_e^0 & 0 & C_1^* & C_2^*\omega_e^0 & C_3^* & C_4^*\omega_g^0 & C_4^*\varphi_{dr}^0 & 0 & 0 \\[2mm]
0 & 0 & 0 & C_5^*\omega_e^0 & -C_2^*\omega_e^0 & C_1^* & -C_4^*\omega_g^0 & C_3^* & -C_4^*\varphi_{qr}^0 & 0 & 0 \\[2mm]
0 & 0 & 0 & 0 & C_3 & 0 & C_4 & \omega_g^0-\omega_e^0 & \varphi_{dr}^0 & 0 & 0 \\[2mm]
0 & 0 & 0 & 0 & 0 & C_3 & \omega_e^0-\omega_g^0 & C_4 & -\varphi_{qr}^0 & 0 & 0 \\[2mm]
0 & 0 & 0 & 0 & a_{9,5} & a_{9,6} & a_{9,7} & a_{9,8} & -\dfrac{2B}{PJ_Gn_{gear}^2} & \dfrac{K_s}{J_Gn_{gear}} & \dfrac{B}{J_Gn_{gear}} \\[3mm]
0 & 0 & 0 & 0 & 0 & 0 & 0 & 0 & -\dfrac{2}{Pn_{gear}} & 0 & 1 \\[3mm]
0 & 0 & 0 & 0 & 0 & 0 & 0 & 0 & K_7 & K_5 & a_{11,11}
\end{bmatrix}$$

$$B = \begin{bmatrix} \dfrac{V_M K_{VF}\cos(\alpha_o^0)}{L_i} & \left(\dfrac{2\omega_i i_{dG}^D}{(2a-1)^2}\right)^0 & -\dfrac{V_M K_{VF}(\sin(\alpha_o)\omega_e)^0}{L_i} & 0 & 0 \\[2mm] -\dfrac{V_M K_{VF}\sin(\alpha_o^0)}{L_i} & 2\omega_{grid}(i_{qG}^D)^0 & -\dfrac{V_M K_{VF}(\cos(\alpha_o)\omega_e)^0}{L_i} & 0 & 0 \\[2mm] b_{3,1} & \dfrac{2\omega_{grid}v_{do}^0}{(2a^0-1)^2} & b_{3,3} & 0 & 0 \\[2mm] b_{4,1} & b_{4,2} & b_{4,3} & 0 & 0 \\[2mm] C_2^*\psi_{ds}^0 + C_5^* v_{qo}^0 & 0 & 0 & 0 & 0 \\[2mm] -C_2^*\psi_{qs}^0 + C_5^* v_{do}^0 & 0 & 0 & 0 & 0 \\[2mm] -\psi_{dr}^0 & 0 & 0 & 0 & 0 \\[2mm] \psi_{qr}^0 & 0 & 0 & 0 & 0 \\[2mm] b_{9,1} & 0 & 0 & 0 & 0 \\[2mm] 0 & 0 & 0 & 0 & 0 \\[2mm] 0 & 0 & 0 & b_{11,4} & b_{11,5} \end{bmatrix},$$

$$C = \dfrac{3V_{Gm}}{2K_{VF}\omega_e^0} \begin{bmatrix} \cos\alpha_o^0 & -\sin\alpha_o^0 & 0 & 0 & 0 & 0 & 0 & 0 & 0 & 0 & 0 \\[2mm] \left(\dfrac{-\sin\alpha_o}{2a-1}\right)^0 & \left(\dfrac{-\cos\alpha_o}{2a-1}\right)^0 & 0 & 0 & 0 & 0 & 0 & 0 & 0 & 0 & 0 \end{bmatrix},$$

$$D = -\dfrac{3V_{Gm}}{2K_{VF}\omega_e^0} \begin{bmatrix} \left(\dfrac{i_{qG}^D\cos\alpha_o - i_{dG}^D\sin\alpha_o}{\omega_e}\right)^0 & 0 & (i_{qG}^D\sin\alpha_o + i_{dG}^D\cos\alpha_o)^0 & 0 & 0 \\[3mm] -\left(\dfrac{i_{qG}^D\sin\alpha_o + i_{dG}^D\cos\alpha_o}{\omega_e(2a-1)}\right)^0 & -2\left(\dfrac{i_{qG}^D\sin\alpha_o + i_{dG}^D\cos\alpha_o}{(2a-1)^2}\right)^0 & \left(\dfrac{\cos(\alpha_o)i_{qG}^D - \sin(\alpha_o)i_{dG}^D}{2a-1}\right)^0 & 0 & 0 \end{bmatrix}.$$

The constant parameters in the above matrices are given in Appendix I. Also, the superscript "0" indicates the variable value at the operating point.

The small-signal model of the wind turbine system is illustrated schematically in Fig. 3-27.
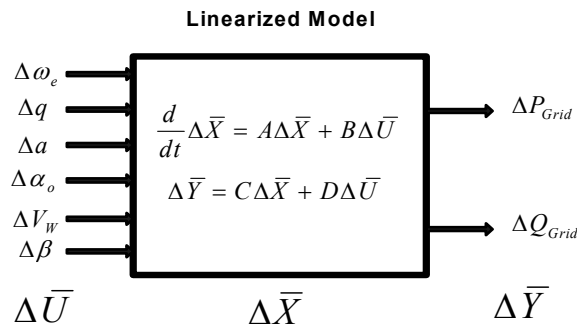


Fig. 3-27: Small-signal model of the wind turbine system

92

## 3.8 Linearized Model Performance Evaluation

In order to evaluate the linearization error at an operating point, the linearized model responses to step changes in some inputs are compared with those of the nonlinear model.

The numerical values in the Jacobian matrices *A, B, C,* and *D* at the operating point are shown in Appendix I. The operating point is given in Table 3.5.

Table 3.5: Input, state and output variables at the operating point for linearization

| $\omega_e^0 = 2\pi 60 [rad/s]$ | $q^0 = 0.5$ | $a^0 = 0.8$ | $\alpha_o^0 = 0$ | $V_W^0 = 10[m/s]$ |
|---|---|---|---|---|
| $\beta^0 = 0$ | $(i_{qG}^D)^0 = -8.45[A]$ | $(i_{dG}^D)^0 = 2.5[A]$ | $v_{qo}^0 = 1632.3[V]$ | $v_{do}^0 = -2.16[V]$ |
| $\Psi_{qs}^0 = 26.45[Wb]$ | $\Psi_{ds}^0 = 1632.5[Wb]$ | $\Psi_{qr}^0 = 109.5[Wb]$ | $\Psi_{dr}^0 = 1591.1[Wb]$ | $\omega_g^0 = 378.5[rad/s]$ |
| $\delta\theta^0 = 0.004[rad]$ | $\omega_T^0 = 9.45[rad]$ | $P_{Grid}^0 = 82.79[kW]$ | $Q_{Grid}^0 = 40.88[kW]$ | |

Fig. 3-28 shows the system response to a step increase of 1 Hz (6.28 *rad/sec*) in the MC output frequency for linearized and nonlinear models. In the next simulation, the system response to a 10% step change in parameter '*a*' for linearized and nonlinear models is obtained (see Fig. 3-29). Fig. 3-30 provides the response of the system to a 5% step increase in wind velocity for linearized and nonlinear models.
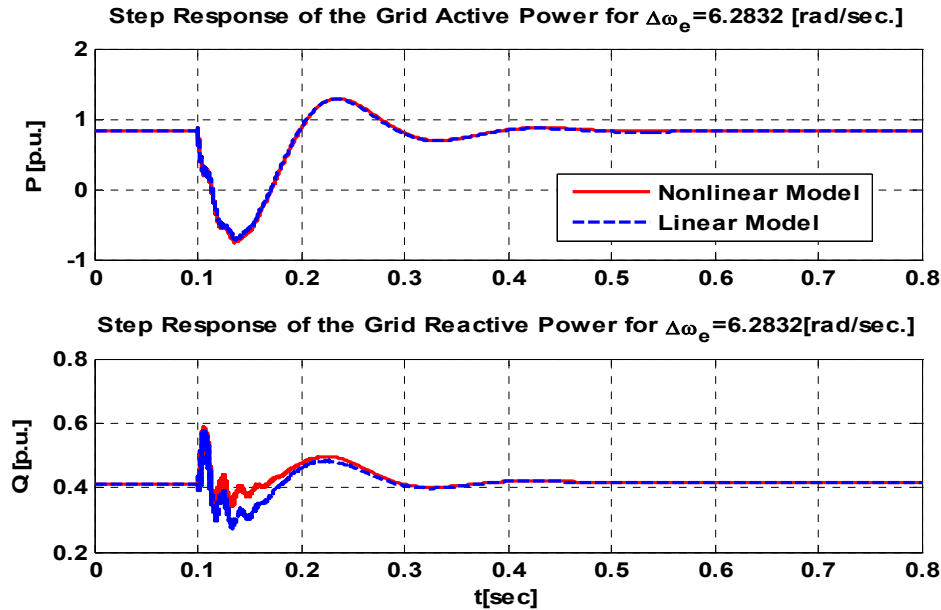


Fig. 3-28: System response to a step change in the MC output frequency with nonlinear and linearized models

(a)



(b)
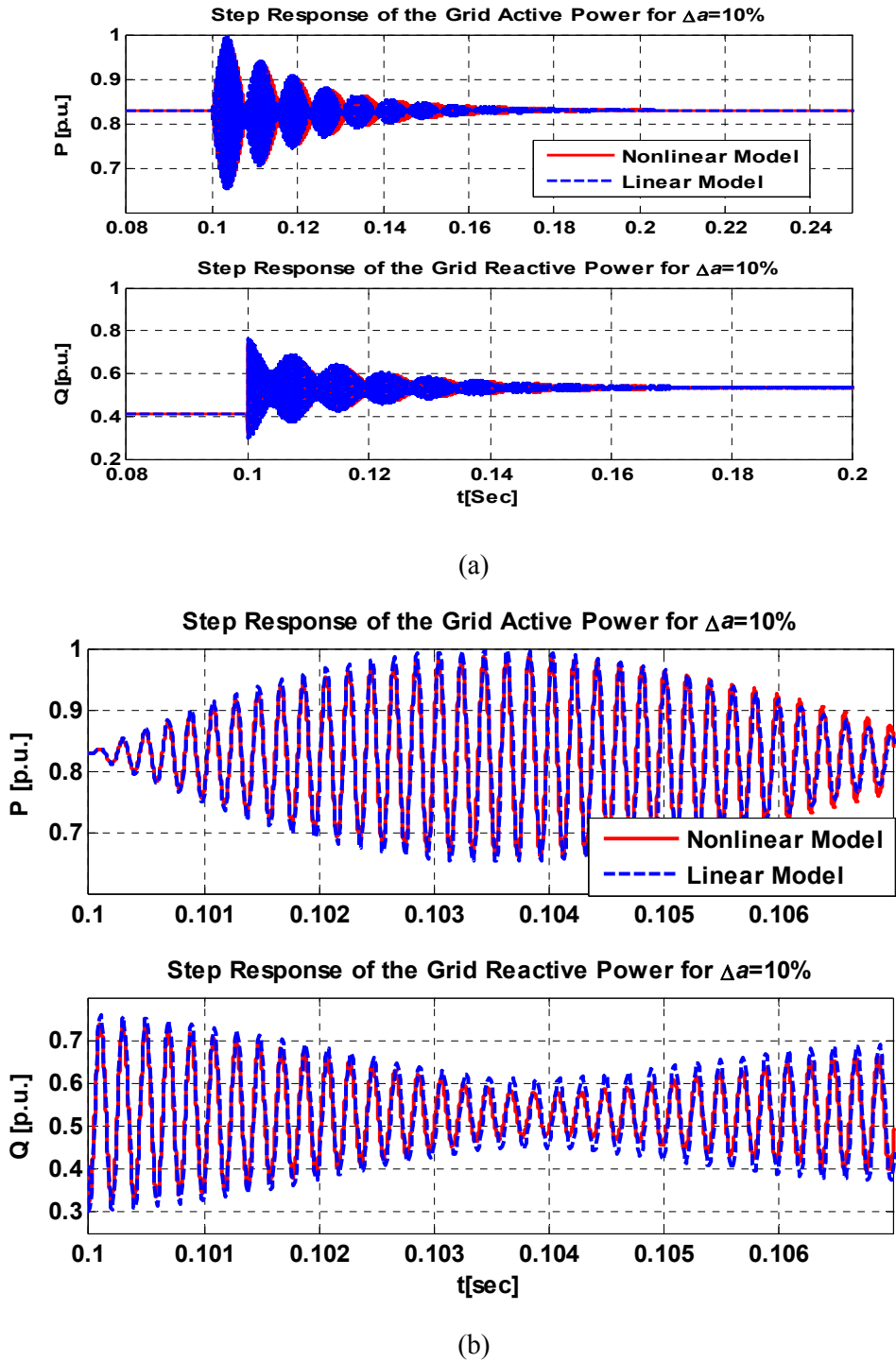
Fig. 3-29: System response to a step change in parameter *a* of the MC with nonlinear and linear models, (a) Zoomed out view (b) Zoomed in view
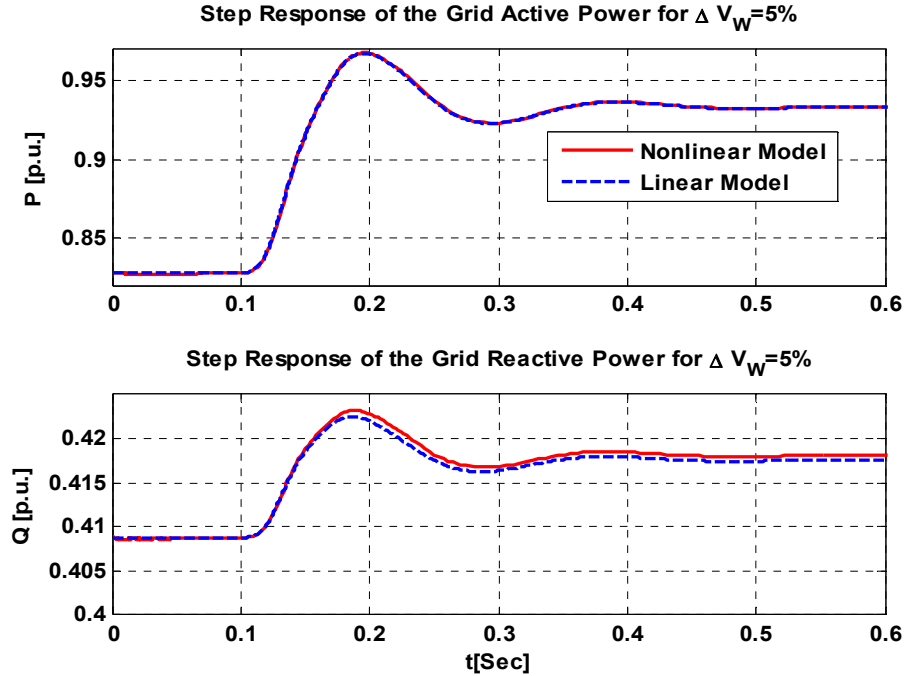
Fig. 3-30: System response to a step change in the wind velocity with nonlinear and linear models

The simulation results reveal that the small-signal linear model is an accurate approximation of the nonlinear model.

## 3.9 Local Stability Evaluation

Different methods to verify the local stability are pointed out in the literature [127][128]. A common method is to check the eigenvalues of the linearized system. When the real parts of all eigenvalues of the linearized system are negative, the nonlinear system is locally stable around the steady-state operating point [129] .

The eigenvalues of the small-signal model linearized around the operating point (Table 3.5) are shown in Table 3.6. The real parts of all eigenvalues are negative; therefore, the linearized small-signal model is asymptotically stable at the steady-state operating point.

Table 3.6 Eigenvalues of the linearized system at the operating point

| Eigenvalues | |
|---|---|
| $-12.205 \pm 32.232i$ | $-49.646 \pm 32400i$ |
| $-25.237$ | $-49.764 \pm 31574i$ |
| $-28.126 \pm 140.2i$ | $-50.91 \pm 372.8i$ |

95

## 3.10 Controllability and Observability

Controllability and obeservability are important properties of a system to be controlled. The fundamental controllability issue is associated with the question of whether the system states can be controlled in a time interval with a bounded input. Observability describes the ability to determine the system states with output measurements in a time interval.

The well-known theoretical method for testing controllability/observability is to check if the controllability /observability matrix has a full rank. This technique is normally not appropriate for numerical reasons.

### 3.10.1 Gramian method

One alternative method for testing controllability and observability of continuous and linear-time-invariant systems  starts with solving the Lyapunov equation [127]

$$AW_C + W_C A^T = -BB^T ,$$  (3.53)

where $W_c$ is named controllability Gramian.

Similarly, to test observability, the observability Gramian $Wo$ is computed as

$$A^T W_o + W_o A = -C^T C .$$  (3.54)

The system is controllable and observable if $W_c$ and $W_o$ are full-rank matrices.

In order to check the rank of the matrices, the singular value decomposition (SVD) method can be applied. Based on the SVD theorem, every $n{\times}$p matrix $X$ can be decomposed into a product of three matrices $R, S,$ and $Q$, so that [127][130]

$$X = RSQ^T ,$$  (3.55)

where    $R = (r_1,...,r_n) \in \Re^{n \times n}$    and    $Q = (q_1,...,q_p) \in \Re^{p \times p}$    are    orthogonal    matrices, $S = diag(\sigma_1,...,\sigma_q) \in \Re^{n \times p}$ , and $\sigma_1 \geq \sigma_2 \geq ... \geq \sigma_q \geq 0$ $(q = \min(n,p))$ are singular values of matrix X.

In the linearized model of the system, the SVD of  $W_c$ and $W_o$ at the operating point are shown in Table 3.7. Based on Table 3.7, all singular values of the matrices $W_c$ and $W_o$  are non-zero, and therefore, the system is completely controllable and observable. However, the singular values of $W_c$ and $W_o$ are distributed in wide ranges, the evidence of an ill-conditioned system. To show this fact, an index called condition-number can be used. The condition number is defined as

*Condition number = $\sigma_{max} / \sigma_{min}$ .*

The condition number reveals the size of the numerical error that is likely to be introduced by matrix computations. While a large condition number denotes an ill-conditioned system, a number close to one indicates a well-conditioned system. For example, the condition-number for the singular values of $W_c$ is $2.0913 \times 10^{16}$; therefore, this large number implies the matrix is ill-conditioned and close to rank deficiency.

## 3.11 Balanced Realization

This section is dedicated to converting the linearized model to a balanced realization model. A balanced realization has a coordinate system such that its controllability and observability matrices are diagonal and equal. The balanced realization tends to have less numerical errors than other realizations. In addition, a balanced realization divides the system into strongly- and weakly-controllable parts. Therefore, the system order will be decreased by canceling the weakly-controllable part of the system [131].

In the following, a balanced realization, based on the Gramian method, is presented. The Gramian method is used to find a transformation matrix to convert the state-space model to an appropriate coordinate system in which the chosen system Gramian matrices are diagonal and equal.

The state coordinate transformation matrix $T$ that transforms the linear model given by (3.52), with controllability and observability Gramian matrices $W_c$ and $W_o$, to the equivalent balanced model, is as follows:

Table 3.7: Singular values of Gramian matrices $W_c$ and $W_o$

| Singular Values of $W_C$ | Singular Values of $W_o$ |
|---|---|
| $8.3711 \times 10^{12}$ | $3.6331 \times 10^{10}$ |
| $3.477 \times 10^{12}$ | $4.9801 \times 10^{7}$ |
| $8.7259 \times 10^{9}$ | $1.3011 \times 10^{6}$ |
| $3.7327 \times 10^{9}$ | $4.6593 \times 10^{5}$ |
| $5.2685 \times 10^{8}$ | $3.0967 \times 10^{5}$ |
| $4.0851 \times 10^{8}$ | 8475.3 |
| $3.2792 \times 10^{7}$ | 6736.1 |
| 45146 | 5385.4 |
| 571.31 | 3222.1 |
| 8.3934 | 1312.5 |
| $4.0028 \times 10^{-4}$ | 471.21 |

$$\frac{d}{dt}\Delta \bar{X}_b = A_b \Delta \bar{X}_b + B_b \Delta \bar{U},$$
$$\Delta \bar{Y} = C_b \Delta \bar{X}_b + D_b \Delta \bar{U},$$

(3.56)

where $\Delta \bar{X}_b = T\Delta \bar{X}$, $A_b = TAT^{-1}$, $B_b = TB$, $C_b = CT^{-1}$, and $D_b = D$.

In addition, the Gramian matrices $W_c$ and $W_o$, should be transformed to new matrices as follows [127][129]:

$$W_c^b = TW_c T^T,$$
$$W_o^b = T^T W_o T^{-1}.$$

(3.57)

For the linearized system under study, the singular values of the Gramian based on a balanced realization are illustrated in Table 3.8.

Table 3.8  The singular values of the balanced Gramian

| | |
|---|---|
| $7.2473 \times 10^7$ | $7.7641 \times 10^5$ |
| $7.245 \times 10^7$ | $3.9973 \times 10^5$ |
| $5.7771 \times 10^7$ | 4463.6 |
| $5.7692 \times 10^7$ | 2406.1 |
| $2.0583 \times 10^6$ | 1683.3 |
| $1.7187 \times 10^6$ | |

The condition number for the balanced realization is decreased to $4.3054 \times 10^4$, showing a significant decrease with respect to that of the previous case.

## 3.12 Reduced-Order Model

To reduce calculation effort during controller design, the 11$^{th}$ order model can be reduced to a lower-order model, while keeping the performance as close as possible to the original model. There are several methods for reducing the order of systems [132]. For example, one method, named direct deletion, simply omits some weakly-controllable states. This scheme gives a good approximation in the frequency domain. This technique must be modified to guarantee a close match between the steady-state responses of the reduced-order and the original systems [131]. Another method, named enforce matching DC-Gain, is based on matching the steady-state conditions in the step response. The functions for these two methods are available in Matlab's Control Toolbox.

Using Gramian balanced realization and eliminating the weakly-controllable modes, the order of the system is reduced to 9$^{th}$-order and 8$^{th}$-order. Although the order reduction is not significant, it specifies the minimum order that the system can have without considerable loss of performance compared to the original system.

In the following, the response of a step change in the MC output frequency of the reduced-order model, developed by both matching DC-Gain and direct deletion methods, are presented. The results are compared with the response of the original 11$^{th}$-order model. Fig. 3-31 shows the response of 9$^{th}$-order model, as well as the reduced model through matching DC-Gain and direct deletion methods.

The 9$^{th}$-order model is based on eliminating the last two state variables corresponding to the smallest singular values (Table 3.8). The transient and steady-state responses for the original 11$^{th}$-order model and two reduced-order models are fairly close.

An 8$^{th}$-order model can be developed by eliminating the last three state variables. Fig. 3-32 illustrates the response of 8$^{th}$-order model, reduced through both methods. In the first output response (the grid active power), two reduced model responses are close to the original one. With the second output (the grid reactive power), while the direct deletion accurately reflects the transient behavior of the original 11$^{th}$-order model, the reduced model with matching DC-Gain method guarantees only the zero steady-state error and a reasonable dynamic response.

It is worth mentioning that the reduced-order system is obtained from the balanced realization system in which the states are different from those of the original system. Therefore, comparing the states of the reduced-order system with those of the original system, to identify the omitted states, is impractical. However, one can say intuitively that the omitted states in the reduced-order model are related to the fast dynamics of the system under study.
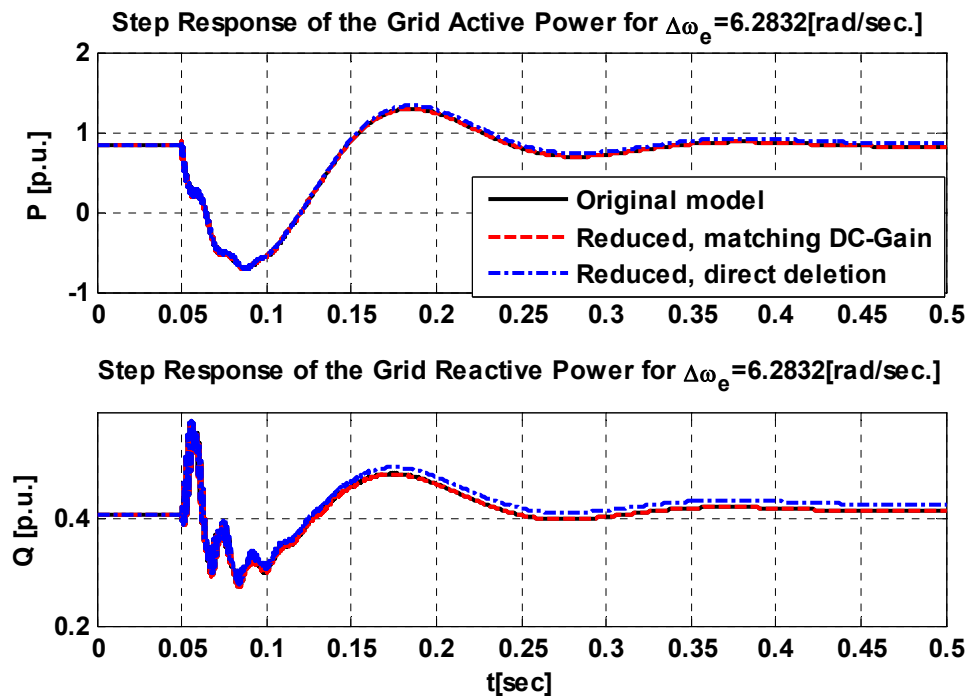


Fig. 3-31 : A comparison of the responses to step change in the MC output frequency for three linear models: Original 11$^{th}$-order, reduced 9$^{th}$-order using matching DC-Gain method and, reduced 9$^{th}$-order direct deletion method
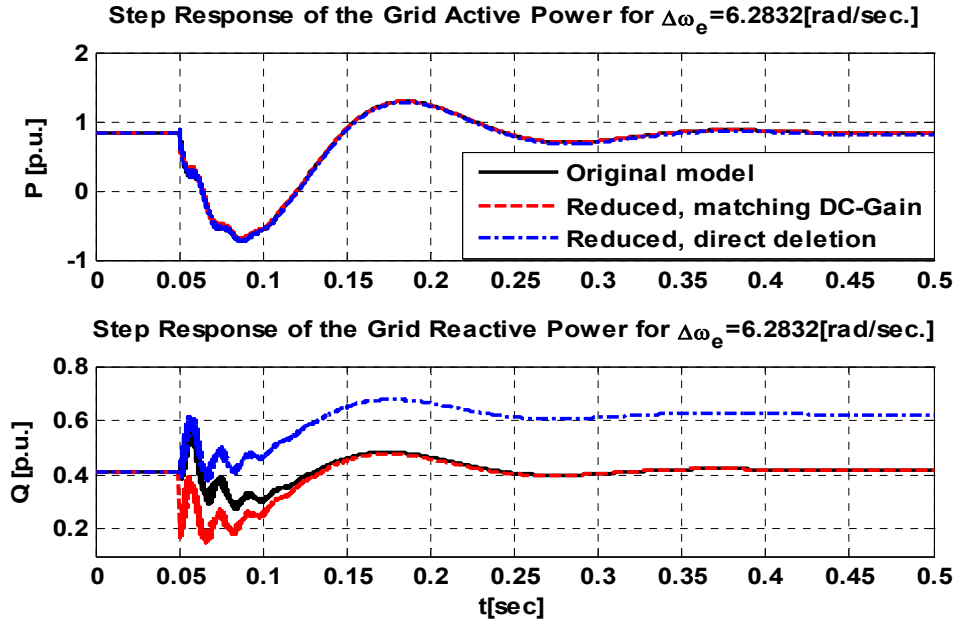
Fig. 3-32: A comparison of the responses to step change in the MC output frequency for three linear models: Original 11th-order, reduced 8th-order using matching DC-Gain method, and reduced 8th-order direct deletion method

## 3.13 Summary

In this chapter, the focus has been on developing a comprehensive dynamic mathematical model of the proposed wind turbine system to be used for controller design purposes. Detailed mathematical models of the mechanical aerodynamic conversion, drive train, and squirrel-cage induction generator are developed and combined with the MC model from Chapter 2 to enable steady-state and transient simulations of the overall system. The components of the wind turbine system are modeled by thirteen nonlinear equations: three for the turbine and shafts, six for the MC, and four for the induction machine. By combining the state equations of the system components, the overall model of the system can be described by six inputs $\bar{u}$, two outputs $\bar{y}$, and eleven state variables $\bar{x}$. Out of the six inputs, four are adjustable control variables of the MC, one is pitch angle of the turbine blades, and one is the wind velocity. The active and reactive powers injected into the grid are treated as output variables for the model. To avoid saturation of the induction machine when the stator frequency changes, a constant $V/f$ strategy is incorporated in the model and a dynamic model is developed based on the constant $V/f$ strategy. The final dynamic model with the constant $V/f$ strategy contains two controllable inputs and two outputs. The model is intended to be useful for controller design purposes.

To verify the dynamic model, first the starting operation of the system is simulated. Then steady-state performance of the system for some input variations is explored. Finally, the dynamic behaviour of the model is investigated by simulating its step response. In the starting mode, it is supposed that the machine is connected to the grid without using the soft-starting method. So, the electrical machine initially works in the motoring mode and draws active power from the grid and then the machine switches to the generating mode and the direction of the power flow will be changed from the generator to the grid.

Steady-state model performance is studied by applying changes to input variables and observing the model response. Steady-state response of the model shows the grid active and reactive power varying with the MC output frequency. But, varying the parameter 'a' affects only the grid reactive power. The results reveal that changing the parameter 'a' can change the direction of the reactive power from leading to lagging and vice versa.

Dynamic behavior of the model is investigated by simulating the step responses to some input variables, e.g., MC output frequency ($\omega_e$), voltage gain ($q$), parameter $a$ , and the wind velocity ($V_w$). The results show that the open-loop system is stable for the step changes in the inputs. In addition, from the control point of view, the step response of the system shows a type of non minimum-phase behaviour.

Moreover, a linearized model of the wind turbine system is developed around an operating point, and stability, controllability, and observability of the system are investigated. The simulation results show the local stability of the open loop system against the input variations around the operating point. The Gramian method is employed to evaluate the controllability and observability at the operating point. Using the Gramian method, a balanced realization is developed. The balanced realizations tend to have less numerical error than other realizations.

Moreover, effort was made to find a reduced-order model that has a performance as close as possible to the original model. Two reduced-order methods were used to find transformation matrices to convert the state-space model to appropriate coordinate systems in which the order of the system has been reduced from eleven to nine or from eleven to eight. The simulation results reveal that the reduced $9^{th}$-order model by DC-Gain method is an accurate approximation to the nonlinear model both in transient and steady-state performances. The reduced $8^{th}$-order model by DC-Gain method is also acceptable if there is no concern about the accuracy in dynamic response.

Overall, it can be concluded that the developed linear model is an appropriate model for design of a controller to improve the steady-state and transient performances of the system.

# Chapter 4

# Controller Design for the Wind Turbine System under Study

## 4.1 Introduction

In Chapter 3, a linear model for the proposed grid-connected wind turbine system was developed. Then, for the linearized model, the performance of the steady-state and transient responses was evaluated. In this chapter, a closed-loop feedback controller based on the linear model is designed. Based on the stability analysis in Chapter 3, the open-loop system is stable; therefore, the closed-loop controller design objective is to track a class of desired references. In addition, the controller designed in this chapter will be complemented by the maximum power point tracking algorithm in Chapter 5.

Two control design methods are adopted for design of closed-loop controller: a state-feedback controller and an output-feedback controller.

The state-feedback controller is designed based on the Linear Quadratic (LQ) method. A genetic algorithm is used to determine the weighting matrices of the LQ method to locate the closed-loop eigenvalues as close as to the desired possible values. Then, an estimation method is implemented as an observer block in the state-feedback controller. The observer estimates the states by measuring the system output and input.

Other controller design methods for MIMO systems are based on transfer function. Two controllers based on the transfer function techniques are developed for the wind turbine system.

First, a simple approach, based on ignoring the cross-channel interactions at a certain frequency, is adopted. Second, a sequential loop closure (SLC) method is used to design a MIMO controller without ignoring the cross-channel interactions.

In the next section, the equations of the state-feedback closed-loop system are derived. Section 4.3 is dedicated to LQ method for the state-feedback controller design. In section 4.4, the genetic algorithm is employed to place the closed-loop system eigenvalues to the desired region in the s-plane. The observer design stages for the state-feedback controller are presented in section 4.5. Two controllers using transfer function techniques are designed in section 4.6. Finally, in the last section, the linear controller designed based on SLC method is used in the closed-loop nonlinear system and the simulation results are compared with those of the wind turbine linear model.

## 4.2 Augmented System with Integrator

In this section, an integrator is added to the wind turbine system, to form the augmented system model shown in Fig. 4-1. The wind turbine linearized state-space model was presented in Chapter 3. The tracking error is defined as the deviation of the wind turbine system output from the corresponding reference signal. In Fig. 4-1, the wind turbine model has the input vector $\bar{u} = [\omega_e \ a]^T$, the state vector $\bar{x}$ contains eleven variables, the output vector is $\bar{y} = [P \ Q]^T$, the output reference is $\bar{y}_r = [P_{ref} \ Q_{ref}]^T$, and the tracking error is defined as: $\bar{z} = \bar{y} - \bar{y}_r$. Note that the closed-loop system references can be determined based on desired active and reactive powers delivered to the grid. For example, the active power reference will be obtained based on the maximum power tracking algorithm presented in Chapter 5. In general, an integrator can be added in series with the plant to overcome the problem of steady-state error. In other words, adding the integral action guarantees zero steady-state error in a closed-loop stable system.
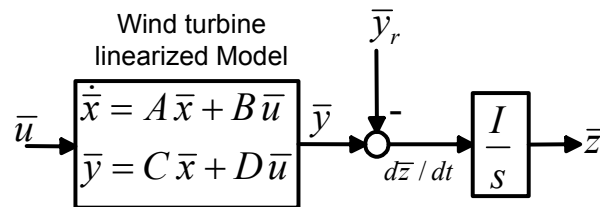


Fig. 4-1 The wind turbine linearized state-space model augmented by an integrator

The state-space model of the wind turbine model augmented by the integrator is as follows:

$$\frac{d}{dt}\tilde{x} = \tilde{A}\tilde{x} + \tilde{B}\overline{u} + \tilde{B}_r\overline{y}_r,$$

(4.1)

$$\overline{y} = \tilde{C}\tilde{x} + D\overline{u},$$

where, $\tilde{x} = \begin{bmatrix} \overline{x} \\ \overline{z} \end{bmatrix}$, $\tilde{A} = \begin{bmatrix} A & 0 \\ C & 0 \end{bmatrix}$, $\tilde{B} = \begin{bmatrix} B \\ D \end{bmatrix}$, $\tilde{B}_r = \begin{bmatrix} 0 \\ -I \end{bmatrix}$, $\tilde{C} = \begin{bmatrix} C & 0 \end{bmatrix}$, and $I$ is an identity matrix.

## 4.2.1 Closed-loop state-space equations

Fig. 4-2 shows the closed-loop system with regular state-feedback. In the closed-loop system, it is assumed that the state vector $\tilde{x}$ is measurable. The matrix $K=[K_1 \ K_2]$ is a constant matrix which is designed to achieve proper performance.

Adding the state-feedback equation to the augmented plant equations results in the closed-loop state-space model

$$\frac{d}{dt}\tilde{x} = \tilde{A}_C\tilde{x} + \tilde{B}_C\overline{y}_r,$$

(4.2)

$$\overline{y} = \tilde{C}_C\tilde{x},$$

where $\tilde{A}_C = \begin{bmatrix} A - BK_1 & -BK_2 \\ C - DK_1 & -DK_2 \end{bmatrix}$, $\tilde{B}_C = \begin{bmatrix} 0 \\ -I \end{bmatrix}$, $\tilde{C}_C = \begin{bmatrix} C - DK_1 & -DK_2 \end{bmatrix}$.

The input signal $\overline{u}$ in the closed-loop system is

$$\overline{u} = -[K_1 \ K_2]\tilde{x} = -K\tilde{x}.$$

(4.3)
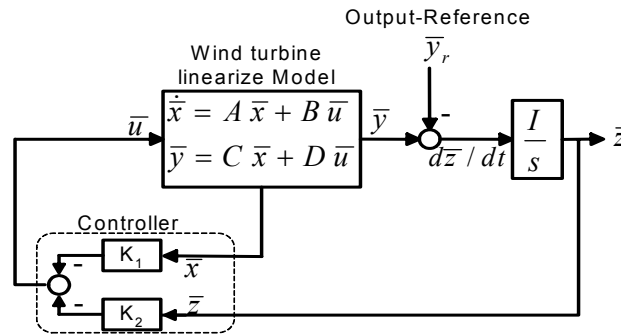


Fig. 4-2: The wind turbine closed-loop system with state-feedback

## 4.3 LQ method for State-Feedback Controller Design

The aim of the controller design is to determine the gain of the controller, i.e., $K = [K_1\ K_2]$, to make the augmented system stable and result in a proper overshoot/undershoot and settling time of the closed-loop time domain responses. The system stability and performance are related to the locations of the closed-loop poles. Theoretically, if the system is controllable, the closed-loop poles can be arbitrarily placed in the complex plane. For small order system, the classical method to choosing desired pole position can be used. However, for multi-input multi-output systems it is difficult to choice of desired pole locations [130][131][147].

An alternative approach is to determine state-feedback gains so that the closed-loop system optimizes a cost function. This approach is called Linear Quadratic (LQ). One of the advantages of the LQ approach is that the decision about the desired pole locations is replaced by a more intuitive decision involving the choice of two weighting matrices [130][133]. The LQR also guarantees a phase margin of 60 degrees for single-input, single-output systems.

The cost function, used in the design of an LQ controller, is defined as

$$J(u) = \int_0^\infty e^{2\sigma t} [\bar{x}(t)^T Q \bar{x}(t) + \bar{u}^T(t) R \bar{u}(t)] dt \,, \tag{4.4}$$

where $\sigma \geq 0$ is a real number, $\bar{x}$ is an n-dimensional sate vector, $\bar{u}$ is an r-dimensional control input vector, and $Q$ (state weighting) an $n \times n$ positive semi-definite matrix, and $R$ (input weighting) an $r \times r$ positive definite matrix. The state $\bar{x}(t)$ and input signal (control signal) $\bar{u}(t)$ are penalized by the cost function. Application of the LQ approach to optimal design involves choosing the $Q$ and $R$ matrices to provide satisfactory closed-loop performance. The satisfactory performance in the time domain response can be defined as a reasonable overshoot/undershoot and settling time.

Designing an LQ optimal controller for the system of Fig. 4-2 means determining the gain matrix $K$ in (4.3) that results in an optimal stabilizing controller. For the closed-loop feedback system, if $(\tilde{A}, \tilde{B})$ is controllable (stabilizable) and $(Q, \tilde{A})$ is observable (detectable), then the control gain, i.e., $K$ matrix, can be calculated from the formula

$$K = R^{-1} \tilde{B}^T P \,, \tag{4.5}$$

where $P$ is a unique symmetric positive semi-definite solution of the Algebraic Riccati Equation (ARE):

$$\tilde{A}^T P + P\tilde{A}^T - PHP + 2\sigma P + Q = 0,$$
$$H = \tilde{B}R^{-1}\tilde{B}^T.$$

(4.6)

By tuning $Q$ and $R$, one can specify the penalization of each element of the state vector and each control signal, and change the location of the closed-loop eigenvalues.

To achieve satisfactory performance, it is convenient to use iteration to find $Q$ and $R$. Common practice is to choose diagonal $Q$ and $R$ matrices. With a diagonal $Q$ matrix, the $i^{th}$ element of $Q$ can be assigned as a weight to penalize the $i^{th}$ component of the state matrix. Meanwhile, if it is desired to have a small control signal, the diagonal terms of the $R$ matrix must be increased. Therefore, LQ design is a trade-off between the size of the input signals and state variables.

There are an infinite number of possible selections for $Q$ and $R$. However, some methods for choosing $Q$ and $R$ as starting points of the iteration are suggested in the literature. For example, to penalize the size of the system output signals in the cost function (4.4), a common choice for $Q$ is $Q=C^T C$ [130][133][134]. Another method is using Bryson's rule [134]. Based on this rule, a first choice for matrices $Q$ and $R$ are as follows:

$$Q_{ii} = \frac{1}{\textit{Maximum acceptable value of } x_i^2} \qquad i \in \{1,2,...,l\},$$

$$R_{jj} = \frac{1}{\textit{Maximum acceptable value of } u_j^2} \qquad j \in \{1,2,...,m\},$$

(4.7)

where $l$ and $m$ are numbers of system states and inputs, respectively.

In fact, Bryson's rule scales the variables that appear in the cost function (4.4) such that the maximum acceptable value for each term is one.

## 4.3.1 Design of an LQ Controller for the Wind Turbine System

This section is dedicated to the design of an LQ controller for the wind turbine system under study [152]. In other words, the matrix $K =[K_1\ K_2]$ in the closed-loop system Fig. 4-2 is determined based on LQ controller design strategy.

The open-loop system was modeled in Chapter 3 as a state-space model with two inputs, two outputs, and eleven state variables. It is worth mentioning that the open-loop system is locally stable around the operating point, and the augmented system of Fig. 4-1 has two poles at the origin. However, the system is non-minimum-phase, because of three zeros in open-right-half-plan (ORHP), as shown in Table 4.1. Note that the operating point of the system was given in Table 3.5.

The real ORHP zeros act like delays in system response and constrain in the controller design. In other words, an ORHP zero puts an upper limit on the controller bandwidth, and the controller does not achieve arbitrarily fast tracking performance [130]. In addition, in the presence of an ORHP zero, the step response necessarily has an undershoot, whose magnitude tends to infinity as the settling time tends to zero [130][135].

Table 4.1: Zeros of the system at the operating point

| | |
|---|---|
| $-1.9334 \times 10^5$ | $-55.211 \pm 131.52i$ |
| $-34114$ | $-19.997 \pm 261.6i$ |
| $33247$ | $-25.90$ |
| $45.761 \pm 8153.9i$ | $-1.053$ |

In the following controller design, a reduced $9^{th}$-order model is used. The augmented system is completely controllable, satisfying our first LQ requirement. The LQ method is used to design the state-feedback integral controller so that the following performance goals are satisfied:

- the step response settling time is less than 5 seconds,

- the step-response steady-state error is zero, and

- the overshoot or undershoot is less than 20%.

Accordingly, the starting elements of the $Q$ and $R$ matrices are chosen based on (4.7) and some trial and error as:

$$Q = 10 \times diag\left\{1 \quad 1 \quad 1 \quad 1 \quad 1 \quad 1 \quad 1 \quad 1 \quad 1 \quad 1 \times 10^{-2} \quad 2.4 \times 10^{-4}\right\},$$

$$R = \begin{bmatrix} 1.759 \times 10^{-6} & 0 \\ 0 & 1 \end{bmatrix}.$$

With the $Q$ shown above, the augmented system is observable, satisfying the second LQ requirement.

## 4.3.2 Evaluation of the Closed-loop System with LQ Controller

To evaluate the LQ controller performance, the system step response, as well as the location of the closed-loop eigenvalues, will be considered.

The system responses when a step change is applied to each channel of the reference signals, i.e., step change in the active and reactive power references, are shown Fig. 4-3 and Fig. 4-4,

respectively. As these figures illustrate, the first channel settling time is large, $t_s>5$ sec. Note that the integrator resulted in a zero steady-state error in step response. Also, the system has an undershoot, that appears in responses to step change in the reactive power reference, as shown in Fig. 4-4.
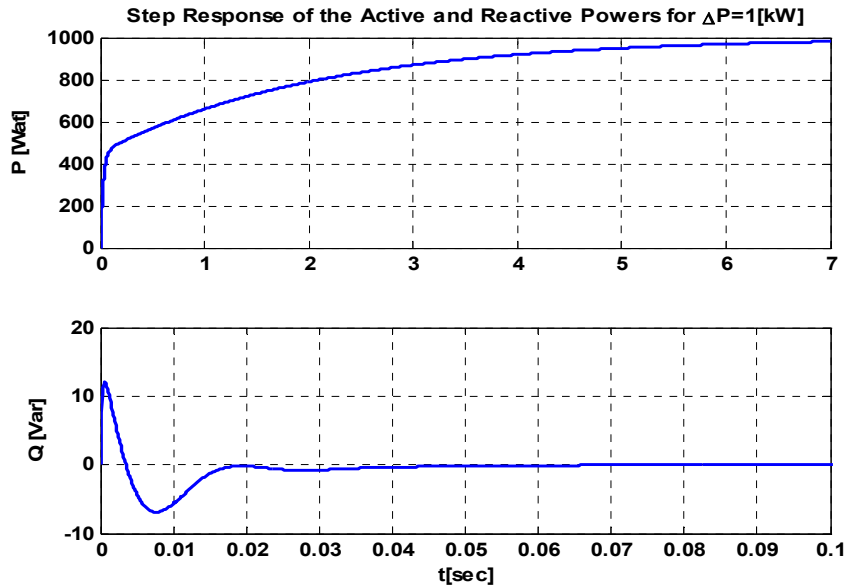


Fig. 4-3: System (linearized model) with LQ controller: step response of the active and reactive powers to a 1- kW step change in active power reference
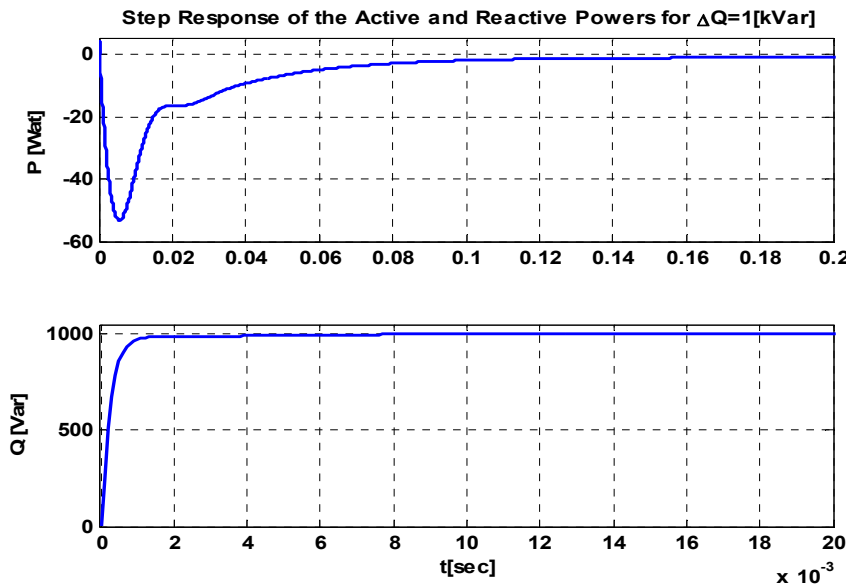


Fig. 4-4: System (linearized model) with LQ controller: step response of the active and reactive powers to a 1-kVar step change in reactive power reference

Table 4.2 shows the eigenvalues of the closed-loop system with the LQ controller. The system is stable, but the eigenvalue -0.48017 results in a large settling time and a slow closed-loop system. In addition, two pairs of eigenvalues -7719 ± 30125i and -159.91±288.18i have small damping ratio.

Table 4.2: Closed-loop system Eigenvalues with LQ controller at the operating point

| | |
|---|---|
| $-3.739 \times 10^6$ | $-159.91 \pm 288.18i$ |
| $-3.5234 \times 10^5$ | -38.451 |
| -32384 | -26.814 |
| $-7719 \pm 30125i$ | -0.48017 |
| -4308.6 | |

## 4.4 Eigenvalue Placement of an LQ Optimal System

The time and frequency responses of a closed-loop control system depend on the location of the system eigenvalues in the s-plane. In the previous section, the LQ optimal method was employed to design a controller. As mentioned, the LQ method requires choosing the positive semi-definite $Q$ and positive definite $R$ matrices in order to provide satisfactory closed-loop performance. For a high-order system, the number of $Q$ and $R$ elements is large, and finding the best weighting matrices by trial and error to achieve a desired transient performance is difficult.

In general, the objective of designing a feedback controller such that the closed-loop system has a desired transient performance can be achieved by clustering the eigenvalues of the closed-loop system in a specified stable region of the s-plane. Some methods have been presented in the literature for determining the weighting matrices, $Q$ and $R$, to locate the closed-loop eigenvalues as close to the desired values as possible [138]-[142]. In [138], a sequential method which selects the weighting matrix $Q$ in order to determine the real parts of the closed-loop eigenvalues has been proposed. Another sequential design via a root-locus technique is given in [139]. An inverse approach to place some of closed-loop eigenvalues exactly at specified points is developed by Sugimoto in [140].

In this section, first a direct approach for clustering of the closed-loop eigenvalues of an LQ optimal system will be presented. To overcome the limitation of the direct approach, another method, based on a genetic algorithm, is employed.

### 4.4.1 Boundary of the LQ optimal Closed-Loop Eigenvalues

In this subsection, a computer-aided method for the clustering of closed-loop eigenvalues in the LQ optimal method is presented. This method is based on the results presented in [141][142]. While in [141], with given $Q$ and $R$, the closed-loop eigenvalue region is determined, in [142] a reverse approach is adopted to find the best weighting matrices, $Q$ and $R$, to locate the eigenvalues in a desired region in the left-half s-plane.

By an LQ optimal controller, the closed-loop eigenvalues are bounded by two half circles of radii $r_{min}$ and $r_{max}$, and centered at $-\alpha \leq 0$, where $\alpha=0$ is the imaginary axis. The imaginary parts are bounded by two lines parallel to the real axis [141]. This region is shown in Fig. 4-5 and can be stated mathematically as follows:

$$\left\{ (x,y) : r_{\min}^2 \leq (x+\alpha)^2 + y^2 \leq r_{\max}^2 \right\} \cap \left\{ (x,y) := -\beta \leq y \leq \beta \right\}. \tag{4.8}$$
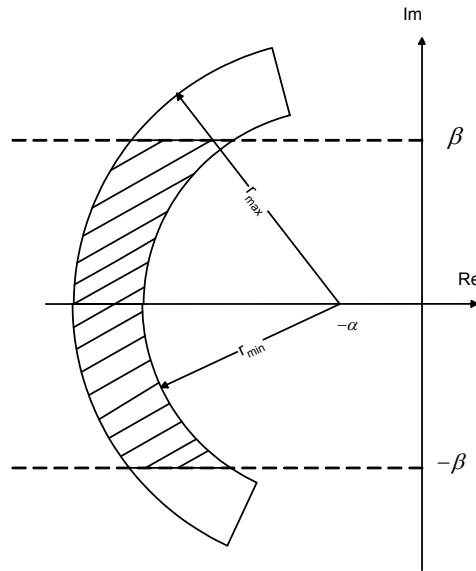


Fig. 4-5: Region of location of LQ optimal closed-loop eigenvalues

For an LQ optimal closed-loop system, with cost function given by (4.4) and control gain given by (4.5), it can be proven that the parameters of region (4.8) are as follows [141]:

$$\beta = eig_{\max}(jZ_0), \tag{4.9}$$

where *eig* represents all the eigenvalues of a matrix, and $Z_0$ is given by: $Z_0 = \dfrac{1}{2}(\tilde{A}^T - Q\tilde{A}Q^{-1})$ if in the Riccati equation (4.6), $Q > 0 \quad and \quad H \geq 0$ .

111

In addition the radii $r_{min}$ and $r_{max}$ can be determined as

$$r^2_{min} = eig_{min}(W),$$
(4.10)
$$r^2_{man} = eig_{max}(W),$$

where $eig(W)$ represents all the eigenvalues a constant $n \times n$ matrix $W$, and $n$ is order of the closed-loop system [142]. If $Q>0$ and $H\geq0$, then $W$ is given by:

$$W = ((\tilde{A} + \sigma I)Q^{-1}(\tilde{A} + \sigma I)^T + H)Q.$$
(4.11)

In a reverse approach, if a region's bounds are specified by two half circles of radii $r_{min}$ and $r_{max}$ only, it is possible to develop a method to determine the weighting matrix $Q$ by using (4.10) and (4.11). To accomplish this goal, first matrix $W$ should be chosen. Clearly, there are an infinite number of possible selections for $W$. One simple method is placing the value $r^2_{min}$ and $r^2_{max}$ directly on the diagonal of $W$. All the off-diagonal elements are equal to zero. Then, matrix $R$ must be selected such that the resulting $H$ matrix is at least positive semi-definite. A solution for equation (4.11) is presented in [142] based on solving a discrete algebraic Lyapunov matrix equation. However, this method cannot be developed for systems of high order (higher than two), since finding an appropriate $W$, resulting in a positive semi-definite $Q$, is not practical.

## 4.4.2 Eigenvalue Placement Using a Genetic Algorithm Approach

In this subsection, a genetic algorithm (GA) is deployed to place the closed-loop eigenvalues of the LQ system in a specified region in the left-half s-plane. GA is a well-known search method to find near-optimal solutions and has been employed in optimal control problems [143][144]. GA can be employed to search for the best weighting matrices corresponding to the desired eigenvalues [145]. In contrast to the previous method, GA has no system order constraint.

To implement GA, a genetic representation of feasible solutions, namely chromosomes, and a fitness function to evaluate the candidate solutions are required. For LQ optimal problems, the chromosome contains information about the weighting matrices. In this study, for simplicity, diagonal weighting matrices are considered to be

$$Q = diag\{q_1, ......, q_l\},$$
(4.12)
$$R = diag\{r_1, ........, r_m\}.$$

A chromosome based on the weighting matrix information is shown in Fig. 4-6.
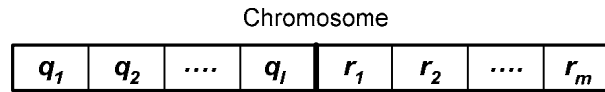
Fig. 4-6: Schematic diagram of the chromosome representation of *Q* and *R* matrices

The algorithm begins by establishing an initial population of chromosomes. Then, Riccati equation (4.6) is solved for each chromosome in the population to determine the closed-loop eigenvalues. The fitness function for each chromosome in the population can be defined as follows:

$$fit(i) = \frac{1}{\sum_{j=1}^{n_e} d_j} \quad , \qquad i = 1,...n_p ,$$

(4.13)

where $d_j$ is the minimum distance of the $j^{th}$ eigenvalue from the desired region in the s-plan, $n_e$ is the number of closed-loop eigenvalues, and $n_p$ is the population number.

The initial population should be improved through several iterations. In each iteration, three operators, *selection*, *crossover*, and *mutation*, are performed to generate a new population.

The selection operator, also known as 'roulette wheel selection', chooses the best chromosome of the current generation, so that the chromosome with largest fitness value has higher probability of selection in the next generation, although this selection operator gives a chance for weak solutions (low fitness value) to be selected, hoping that they can generate some good solutions (high fitness value) in the crossover operation.

The crossover operation is to generate new individuals from the ones chosen by selection operator. A crossover between two individuals is performed by selecting a point on the chromosomes of the two individuals and swapping the chromosomes beyond that point. Fig. 4-7 shows the crossover operation that is performed on two chromosomes.
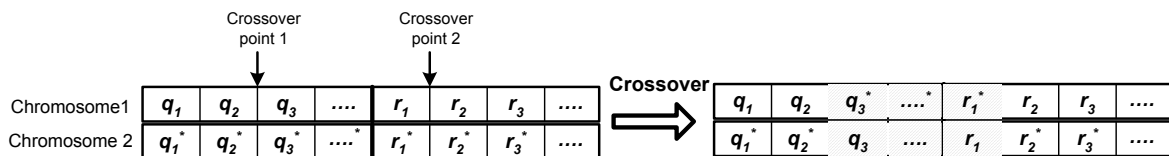


Fig. 4-7: Crossover operation on two chromosomes to make two new chromosome

A mutation operator probabilistically changes an arbitrary element of a chromosome to a new value. Mutation avoids local optima by generating new individuals which may not be similar to the current individuals. Fig. 4-8 shows an example of a mutation operator, where the second element of the chromosome is chosen to change.



Fig. 4-8: Mutation operator on one element of a chromosome

## 4.4.3 Applying GA to LQ Optimal Controller for the Wind Turbine System

In section 4.3.1, an LQ optimal controller was designed that could not satisfy the condition of the transient response. In this subsection, it is tried to tune the LQ controller so that the closed-loop eigenvalues of the system occur at the desired locations of the s-plane. Fig. 4-9 illustrates the region of the desired eigenvalues in this study.
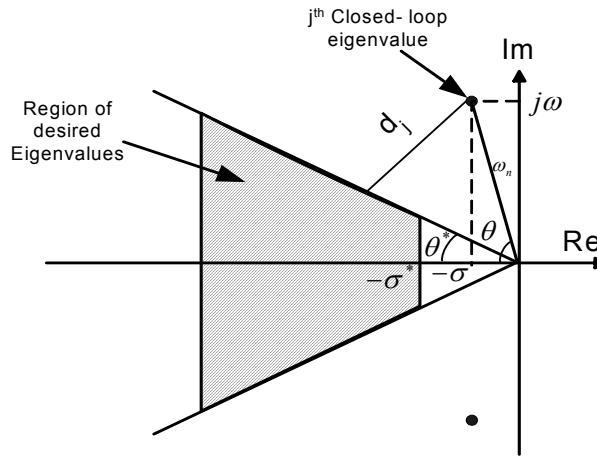


Fig. 4-9: Region of desired closed-loop eigenvalues clustering for GA approach

Consider a pair of stable complex poles with real part $-\sigma$ (rate of decay) and imaginary part $\pm j\omega$, i.e., $P_{1,2}=-\sigma\pm j\omega$. The damping ratio for these poles, $\zeta =cos(\theta),$ will determine how fast the response, related to these poles, decays toward steady state. Acceptable values for damping ratio and real part are defined as $\zeta^{*}=cos(\theta^{*})$, and $-\sigma^{*}$, respectively. A desired closed-loop region in the s-plane should have $\zeta\geq \zeta^{*}$ and $\sigma\geq \sigma^{*}$. Therefore, the desired region can be described mathematically as follows:

$$\left\{(x,y): -\theta^* \le \tan(\frac{y}{x}) \le \theta^*\right\} \cap \left\{(x,y): x \le -\sigma^*\right\}. \tag{4.14}$$

In the following simulations, as a not very conservative design, the region of desired closed-loop eigenvalues is defined based on $\zeta^*=0.6$ and $\sigma^*=1.2$.

As mentioned before, in the LQ design, the locations of closed-loop eigenvalues depend on the values of the weighting matrices. A chromosome is represented by a $1\times13$ vector, containing the eleven diagonal elements of the $Q$ matrix and the two diagonal elements of the $R$ matrix, generated with a random uniform distribution. The population contains seventy chromosomes. An acceptable chromosome should satisfy the condition for solving the Riccati equation (4.6). The closed-loop eigenvalues corresponding to acceptable chromosomes can be determined, and then the fitness function for each chromosome is calculated based on fitness index (4.13). The crossover and mutation operators use uniform distributions to choose the crossover points and mutation elements, respectively, using the probability of the crossover and mutation equal to 0.8 and 0.07, respectively.

Fig. 4-10 illustrates the error index of each generation. This index for each chromosome corresponds to the total distance of the closed-loop eigenvalues from the desired region in the s-plane, i.e., $\sum_{j=1}^{n_e} d_j$ in equation (4.13). The best weighting matrices obtained are as follows:

$$Q = 10^5 diag\{9.1 \quad 9.97 \quad 9.99 \quad 9.74 \quad 0.58 \quad 0.27 \quad 1.03 \quad 2.48 \quad 0.43 \quad 0.011 \quad 6.7\},$$
$$R = diag\{0.108 \quad 16.7\},$$

and the resulting closed-loop eigenvalues are shown in Table 4.3. The minimum damping ratio for the resulting eigenvalues ($\zeta$=0.66) is larger than optimal damping ration ($\zeta^*$) and the absolute value of the real part of the eigenvalue closest to the imaginary axis (1.45) is larger than the absolute value of the optimal real part ($\sigma^*$). Therefore, all closed-loop eigenvalues are in the desired region.

To evaluate the time domain response of the system with the LQ controller modified by GA, the system response to step changes in the active and reactive power references are shown in Fig. 4-11 and Fig. 4-12, respectively. The corresponding input control signals for the step change are also illustrated in the each figure.
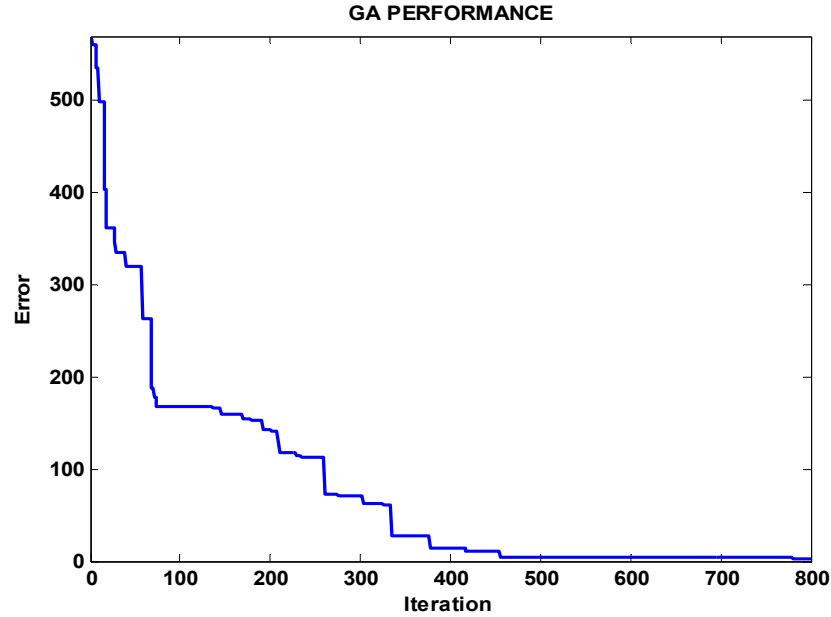
**GA PERFORMANCE**



Fig. 4-10: Minimum performance index of each generation in the GA

Table 4.3: Closed-loop system Eigenvalues at the operating point with GA-LQ optimal controller

| | |
|---|---|
| $-3.8744 \times 10^7$ | -263.89 |
| $-2.1717 \times 10^6$ | $-152.42 \pm 178.5i$ |
| $-17356 \pm 20486i$ | -25.92 |
| -32268 | -1.45 |
| -25415 | |

As seen from Fig. 4-11 and Fig. 4-12, the controller has good performance, i.e., the system outputs have, settling time of less than 5 seconds, with zero steady-state errors. The control signals in Fig. 4-3 (b) show that the frequency control signal $\omega_e$ strongly affects the active power, while the input displacement power factor signal $a$ is almost constant during real power change. On the other hand, the output reactive power variation, illustrated in Fig. 4-4 (b), is more sensitive to the variations of parameter $a$.
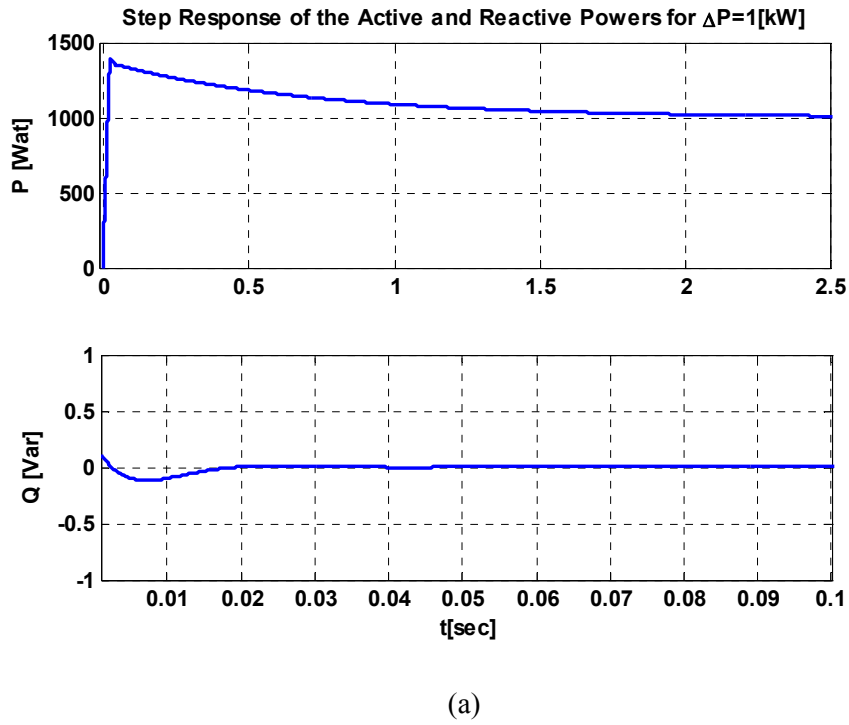
(a)
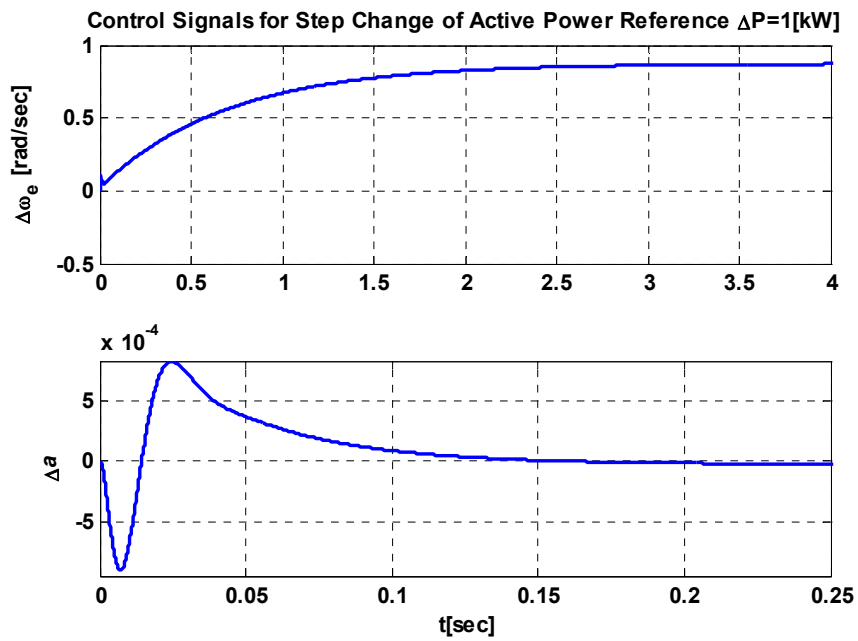


(b)

Fig. 4-11: System (linearized model) with LQ-GA controller: (a) step response of active and reactive powers to a  1-kW step change in active power reference (b) control signals
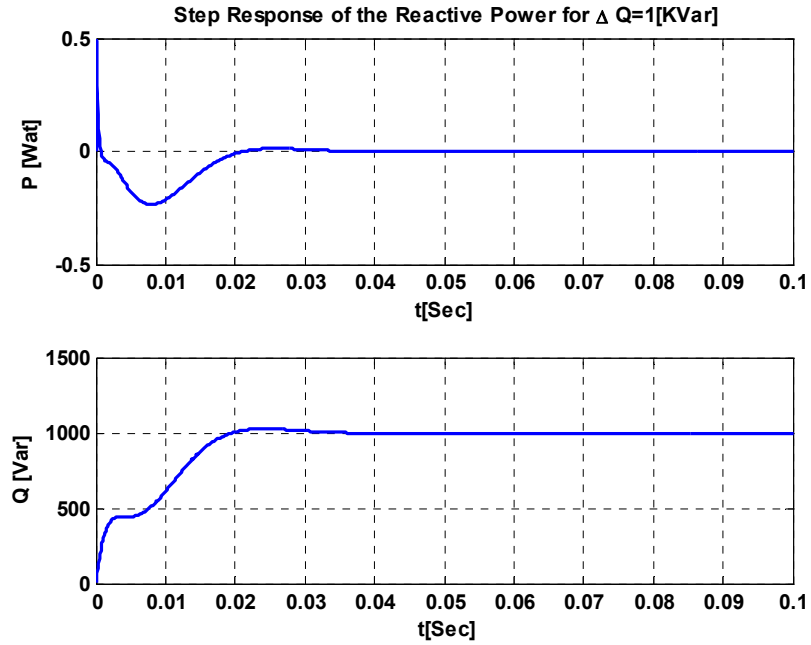
(a)
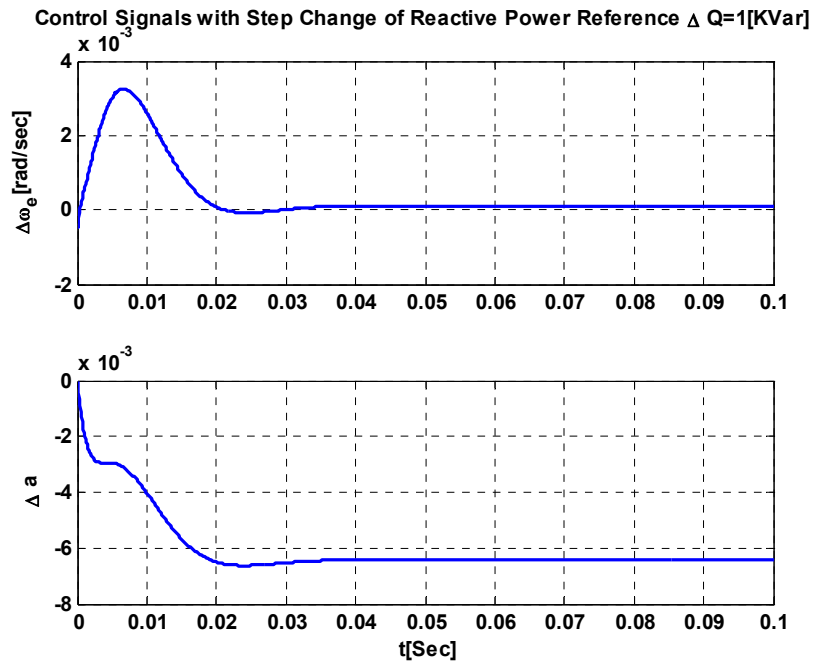


(b)

Fig. 4-12: System  (linearized model) with LQ-GA controller: (a) step response of active and
reactive powers to a  1- kVar step change in reactive power reference (b) control signals

## 4.5 Observer-based State-Feedback Controller with integral Control

In practice, sometimes it is impossible or impractical to measure some or all of the state variables. In this case, unmeasurable states can be estimated using estimation methods. The estimated states can be used in a state-feedback controller if the estimation error approaches zero or is reasonably small. The estimation method, which is implemented as an observer block, can be a part of the state-feedback controller. The observer estimates the states by measuring the output and input variables. In other words, the inputs of the observer block are the system input and output vectors, $\bar{u}$ and $\bar{y}$, respectively, and its output is the estimated state variable vector, $\hat{x}$, as shown in Fig. 4-13.

System

$$\bar{u} \quad \begin{array}{|l|} \dot{\bar{x}} = A\bar{x} + B\bar{u} \quad \bar{y} \\ \bar{y} = C\bar{x} + D\bar{u} \end{array}$$
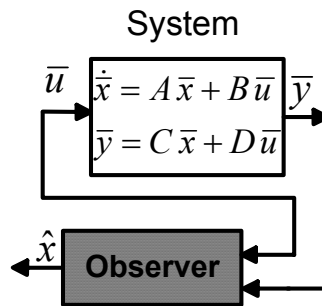
$$\hat{x} \quad \boxed{\textbf{Observer}}$$

Fig. 4-13: The observer in the state-feedback

There are a number of different observer methods in the literature, but a straightforward observer based on the Luenberger observer is adopted for this study [130][133]. The Luenberger observer and the closed-loop equations for the system based on the observer are given in Appendix J.

### 4.5.1 Design of an Optimal Observer for the Wind Turbine System

This subsection deals with the design of an optimal observer for the wind system under study to estimate the state vector. To evaluate the observer, the performance of the closed-loop system with an observer should be compared to that without an observer, which was given in section 4.3.2.

The LQ state-feedback controller developed in the previous section can be used in this section. This means that the optimal observer can be added to the control loop with the estimated states used instead of the actual states. The closed-loop observer-based state-feedback scheme with integral control is shown in Fig. 4-14.
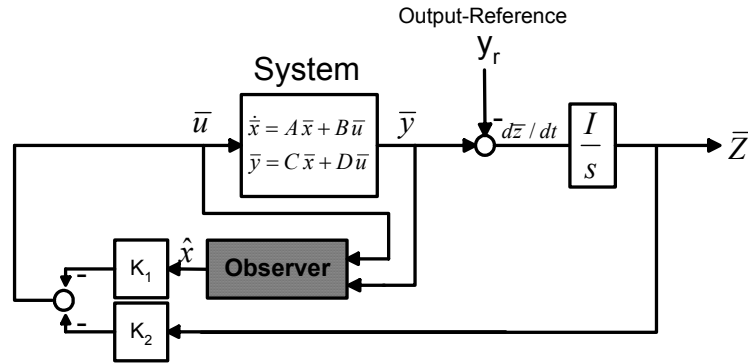
Fig. 4-14: The closed-loop observer-based system with integral control

The following criteria are considered in the optimal observer design procedure:

(a) the observer should not cause a great change in the transient response,

(b) the observer should be robust and have no noise amplification problem, and

(c) the observer should not decrease the system gain and phase margins significantly.

The transient response of the system with observer contains an additional transient as the observer estimation error decays to zero. For a fast error decay, the poles of the observer should be far enough from the origin in the left-half s-plane. However, to avoid the robustness problem and noise amplification, the observer poles should not be placed very far in the left-half s-plane.

The design of the optimal observer using LQ method is started by choosing the weighting matrices $Q_{fic}$ and $R_{fic}$. Note that from the design point of view, since the design of observer deals with fictitious control signals, there will not be any limitation on the size of weighting matrices [130]. Choosing the weighting matrices in design of the optimal observer using the LQ method is done after some trial and error to satisfy the design criteria as much as possible.

In the following, the transient behavior of the system including observer is evaluated. Note that in order to show the additional transients caused by the observer, a reasonable initial condition error (0.05) is considered for the observer. This observer error should decay to zero; however, the observer causes extra transients because it needs some time to bring the estimation error to zero.

The responses to step changes in the active and reactive power references are shown in Fig. 4-15 and Fig. 4-16, respectively. The corresponding input control signals for the step change are also illustrated in each figure. The simulation results show that the observer affects the system transients. However, the observer does not affect the steady-state (tracking) response.

The step responses shown in Fig. 4-15 and Fig. 4-16 cannot reveal the effect of the observer in the system. A better way of showing the observer's effect is measuring the phase-margin and gain-margin and comparing them with the phase-margin and gain-margin of the system without observer. In order to measure the phase and gain margins, applying the normal definition to each of the scalar transfer functions is not correct. Also, there is more than one way to apply frequency-domain methods to MIMO systems, and consequently, there is no unique definition for gain and phase margins for MIMO systems.

An index for the gain and phase margins in MIMO systems is the multi-loop margin [137][146]. This index represents the largest range for gain and phase variations in each channel, which results in a stable closed-loop system. The method of calculating this index is fully described in [146], and it has become a standard command in Matlab.

Table 4.4 compares the multi-loop indices for the system with observer and that without observer.

Table 4.4: Multi-loop gain and phase margins for the wind turbine system without and with observer

|  | Multi-Loop Gain Margin | Multi-Loop Phase Margin |
|---|---|---|
| System without observer | [0.0073   136.97] | [-89.16   89.16] |
| System with observer | [0.5  1.86] | [-33  33] |

As shown in Table 4.4, the gain and phase margins are dramatically decreased when the observer is added to the system. In fact, the observer increases the bandwidth of the controller. Recall from the previous section that the system has some zeros in the right-half plane; therefore, the high-bandwidth controller causes a big undershoot and decreases the phase-margin.
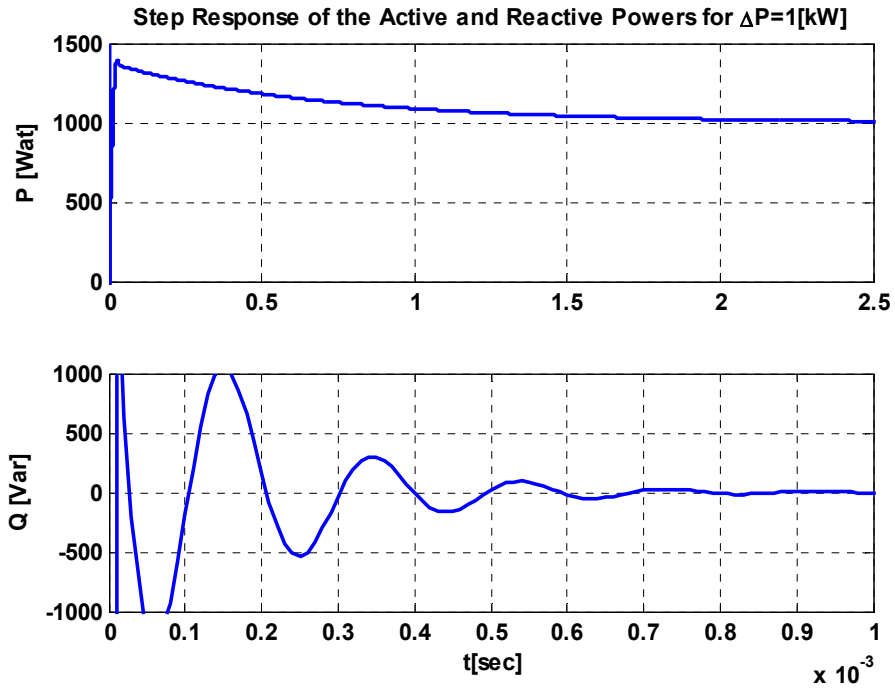
(a)
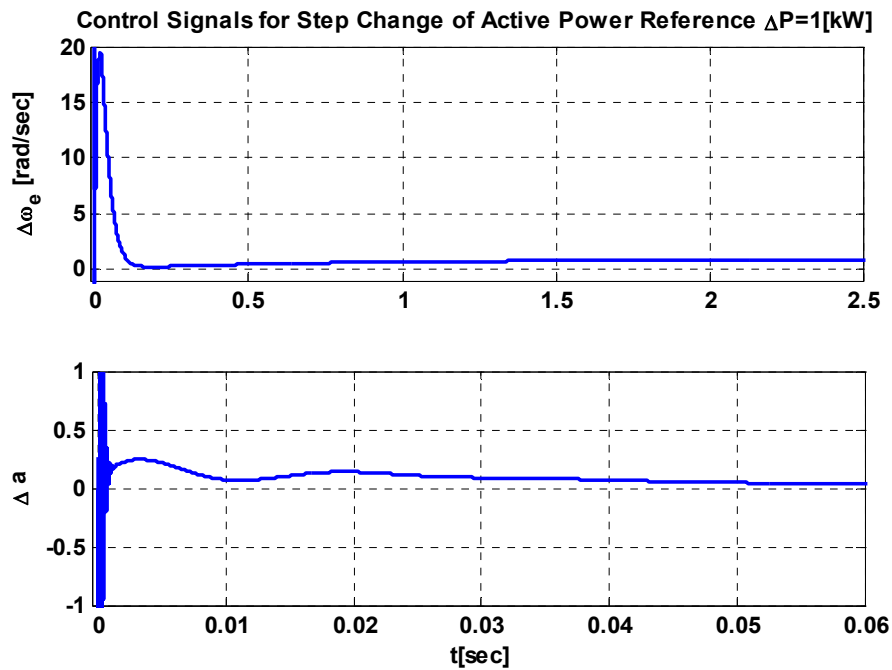


(b)

Fig. 4-15: System with observer, step response to 1 KW step change in active power (a) active and reactive power responses (b) control signals
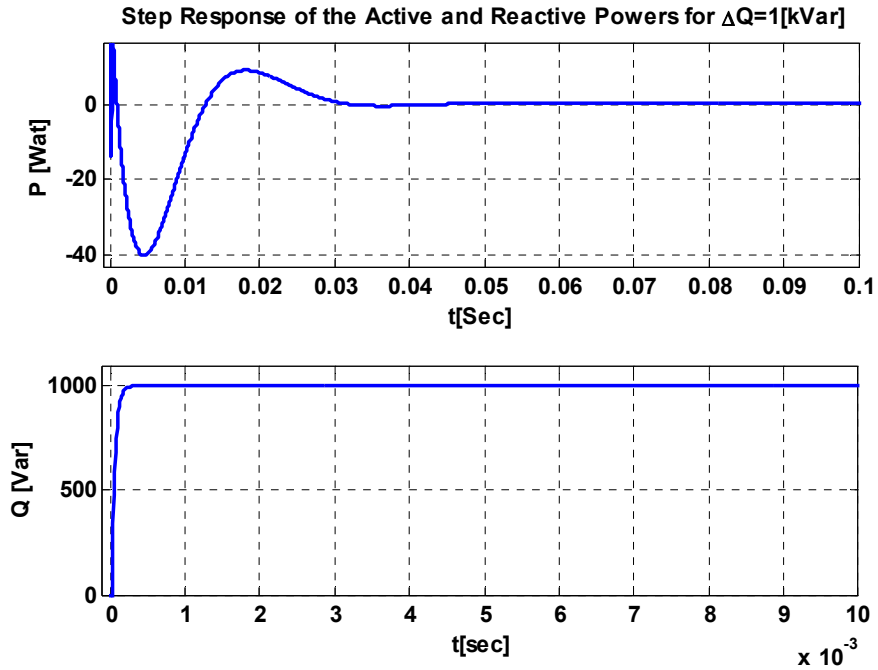
(a)
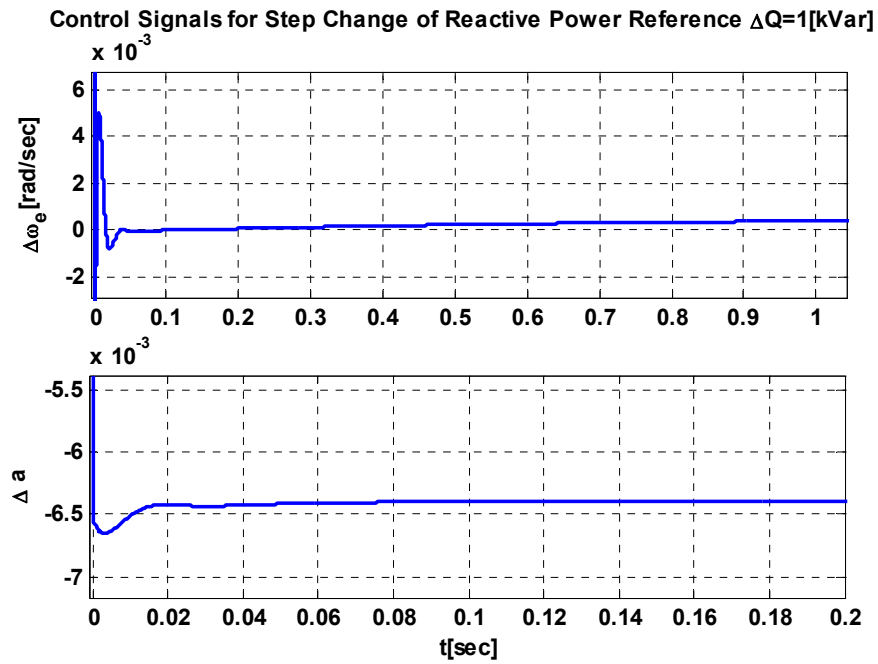


(b)

Fig. 4-16: System with observer, step response to a 1-KW step change in reactive power (a) active and reactive power responses (b) control signals

## 4.6 Design of a Controller Using Transfer Function Techniques

Some controller design methods for MIMO systems deal with transfer function tools [130][147]-[150]. In contrast to state-space controller design techniques, using transfer function techniques is not very systematic. The controller design methods based on transfer functions can be divided in two categories [130]: methods based on decoupling the MIMO system and applying the usual controller design techniques for SISO systems, and methods extending the SISO controller design techniques directly to the MIMO systems.

In this section, a controller is designed for the wind turbine system based on transfer function techniques. First, a simple approach, based on ignoring the cross-channel interactions at a certain frequency, is adopted. Second, a sequential loop closure method is used to design a MIMO controller without ignoring the cross-channel interactions.

### 4.6.1 Design of a Decoupling Controller

If cross-channel interactions can be ignored, the resulting controller consists of independent feedback controllers (diagonal controller) [130][147]. Fig. 4-17 illustrates a 2×2 system, with transfer function matrix G(s), given by (4.15).

$$G(s) = \begin{bmatrix} G_{11} & G_{12} \\ G_{21} & G_{22} \end{bmatrix}. \tag{4.15}$$

If the subsystems are weakly coupled, ignoring the interactions during the design process is reasonable. The controller design of subsystems is not a complicated task. A diagonal controller *C(s)* for the system is as follows:

$$C(s) = \begin{bmatrix} C_{11}(s) & 0 \\ 0 & C_{22}(s) \end{bmatrix}. \tag{4.16}$$
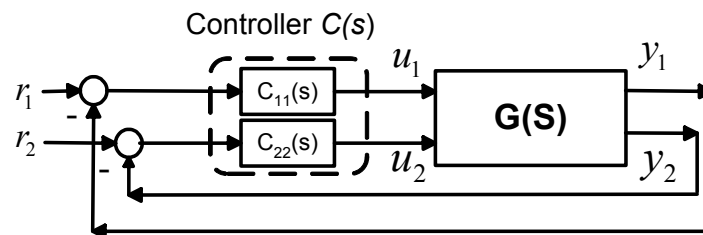


Fig. 4-17: Decentralized diagonal control of a 2×2 system

Ignoring the cross-channel terms and using decoupled control may limit the control performance [148]. One can prove theoretically that with decoupled control, perfect control of all outputs can be attained if the system has no right-half plane zeros that limit the use of high-gain feedback [149]. However, for a MIMO system with finite bandwidth, there is a performance loss with decoupled control. Moreover, interaction corresponding to off-diagonal terms may lead to instability.

The MIMO wind turbine system under study is not decoupled, and also has right-half plane zeros. Therefore, ignoring the cross-channel interactions and then designing the SISO controller for each channel yield a low-performance controller.

## 4.6.2 Reducing cross-channel interactions

In this approach, the cross-channel interaction is decreased at only one frequency. In other words, this approach decouples the system at a chosen frequency rather than at all frequencies and the resulting system is not completely decoupled. In order to have a decoupled system at steady-state, the DC conditions should be considered for applying this approach.

The method begins with applying a gain matrix $W(s)$ to the system. The resulting system is called the augmented system, as shown in Fig. 4-18.
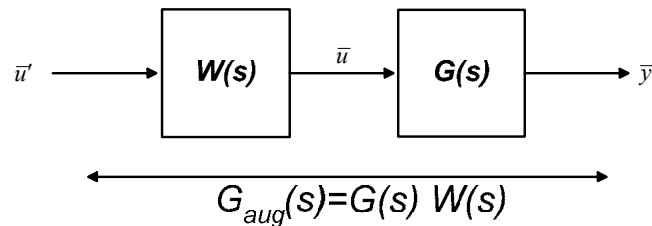


Fig. 4-18: Reducing cross-channel interaction; by applying a matrix W(S) to the system

The augmented system is defined as:

$$G_{aug}(s) = G(s)W(s).$$
(4.17)

To decouple the augmented system near DC, the system transfer function at zero frequency should be invertible, so that $W(s)$ matrix can be obtained for zero frequency as follows:

$$W(0) = inv(G(0)),$$
(4.18)

where *inv(G(0))* is the inverse of the system transfer function matrix at zero frequency. The augmented system with the diagonal $\overline{C}(s)$ controller is shown in Fig. 4-19.
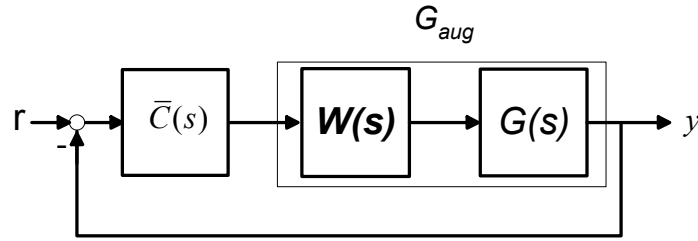


Fig. 4-19: Closed-loop controller for decoupled system and diagonal controller

The final controller for the system can be obtained by combining the controller and DC-gain matrix as follows:

$$C_{final}(s) = W(0)\overline{C}(s). \tag{4.19}$$

### 4.6.3 Applying the reduced cross-channel interactions approach to the wind turbine system

To decouple the system under study, first one needs to compute the matrix *W(0)*, equation (4.18), and obtain the augmented system. The transfer function of the open-loop wind turbine system, *G(s)*, is given in Appendix K. The Bode plots of all augmented system channels are shown in Fig. 4-20. This plot shows that the augmented system at DC is an identity matrix, which verifies that the augmented system is perfectly decoupled at steady-state. Therefore, ignoring the cross-channel interaction is reasonable for the augmented system.

In the next stage, one has to design a diagonal controller $\overline{C}$ for the new diagonal system, i.e., two SISO controllers for each channel. The controller $\overline{C}$ is as follows:

$$\overline{C}(s) = \begin{bmatrix} \overline{C}_{11}(s) & 0 \\ 0 & \overline{C}_{22}(s) \end{bmatrix}. \tag{4.20}$$

To design these two controllers, the SISOTOOL package is used. The objective of controller design strategy is achieving arbitrarily good tracking, i.e., reasonable overshoot or undershoot and settling time for the step response. Note that the system has some right-half plane zeros, which impose an upper limit on the control loop bandwidth. In other words, a low-bandwidth controller has to be used to achieve reasonable tracking performance [135].
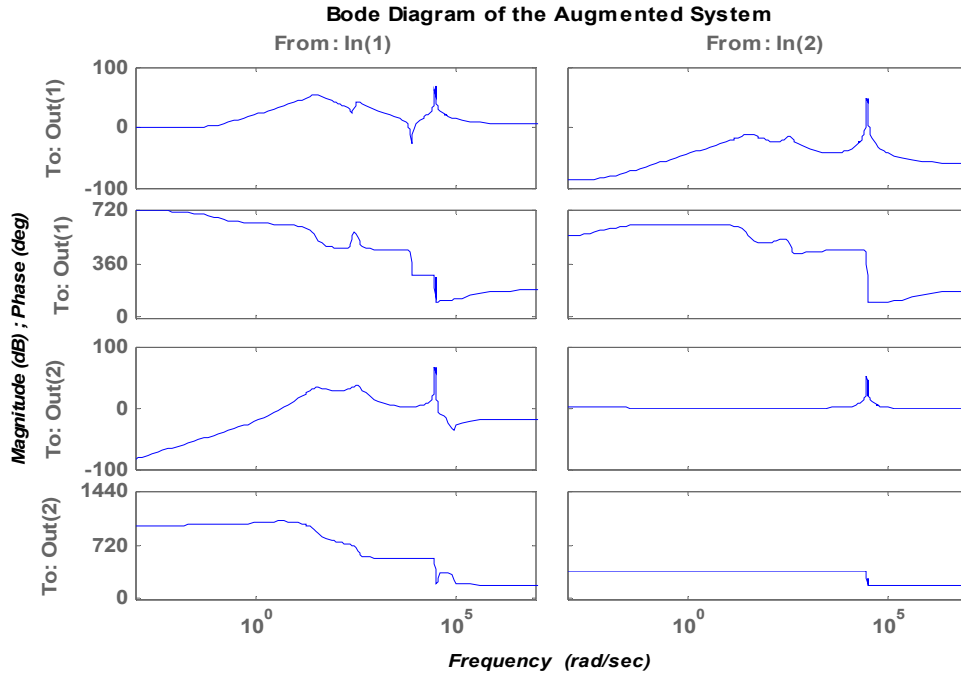
Fig. 4-20: Bode diagram of the augmented system in decoupled DC-gain approach

The first controller $\overline{C}_{11}$ is designed for the first element of the augmented transfer function, i.e., $G_{aug11}$. A typical set of objectives for $\overline{C}_{11}$ are as follows: the step response undershoot less than 100%, settling time less than 20s, and zero steady-state error. Note that for this system, it is possible to design a controller to bring the settling time to zero, but the step response undershoot magnitude tends to go to infinity; hence, it is impossible to achieve arbitrarily good tracking.

The following controller is designed for the transfer function $G_{aug11}$ :

$$\overline{C}_{11}(s) = \frac{0.0611(1+0.41s)}{s(1+1.25s)} . \tag{4.21}$$

The corresponding root locus, bode diagram and step response of the closed-loop $G_{aug11}$ system with controller $\overline{C}_{11}$ is shown in Fig. 4-21. The performance results show that the system meets the design conditions.

To design the controller $\overline{C}_{22}$ , the transfer function $G_{aug22}$ should be considered. The controller $C_{22}$ is designed to achieve a good performance. One can design a controller with a reasonable

bandwidth to achieve an overshoot less than 10% and settling time less than 1 sec. For this purpose, the controller is designed with the following transfer function:

$$\overline{C}_{22}(s) = \frac{5.8(1+0.019s)}{s(1+0.15s)} . \tag{4.22}$$

Fig. 4-22 shows the root locus, Bode diagram and step response of the closed-loop system $G_{aug22}$ with controller $C_{22}$. The simulation result illustrates that the controller satisfies the design conditions.

The final controller for the main system $G(s)$ can be derived using equations (4.18)-(4.22). To check the performance of the MIMO system with the final controller design, first the stability of the closed-loop system should be checked. While the controller $\overline{C}(s)$ is perfectly designed for the augmented system, the final controller $C_{final}(s)$ results in an unstable closed-loop system. This instability occurs consequently to the cross-channel interactions. To decrease the effect of cross-channel interactions, the controller bandwidth in each channel should be decreased. By trial and error and reducing the gain of the controller $\overline{C}(s)$, it is possible to make the closed-loop system stable. However, reducing the controller gain will increase the system settling time. The final controller, ending up with a stable MIMO closed-loop system is as follows:

$$C_{final}(s) = \begin{bmatrix} \dfrac{-5.5 \times 10^{-6}(s+2.439)}{s(s+0.833)} & \dfrac{3.9 \times 10^{-9}(s+2.439)}{s(s+0.833)} \\ \dfrac{-9 \times 10^{-7}(s+52.63)}{s(s+6.67)} & \dfrac{-1.084 \times 10^{-6}(s+52.63)}{s(s+6.67)} \end{bmatrix} . \tag{4.23}$$

The final closed-loop MIMO step responses are shown in Fig. 4-23. As indicated, the closed-loop system is stable with zero steady-state error. However, we have a sizable settling time in channel one and its cross-channel coupling (from input-1 to output-2), may not be acceptable.
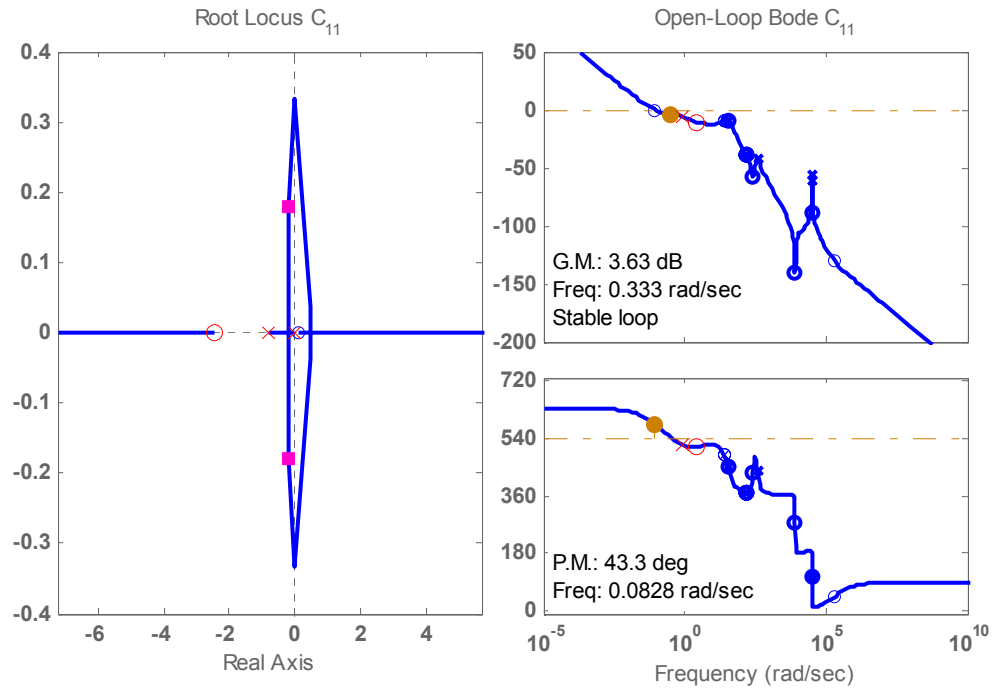
(a)
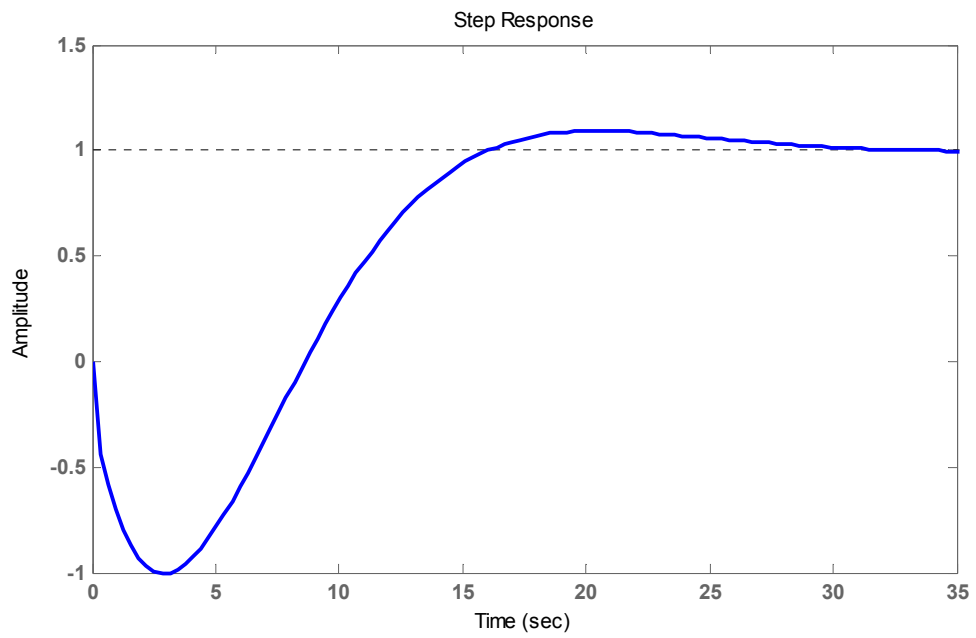


(b)

Fig. 4-21: Closed-loop $G_{aug11}$ system with controller $C_{11}$, (a) root locus and bode diagram, (b) step response
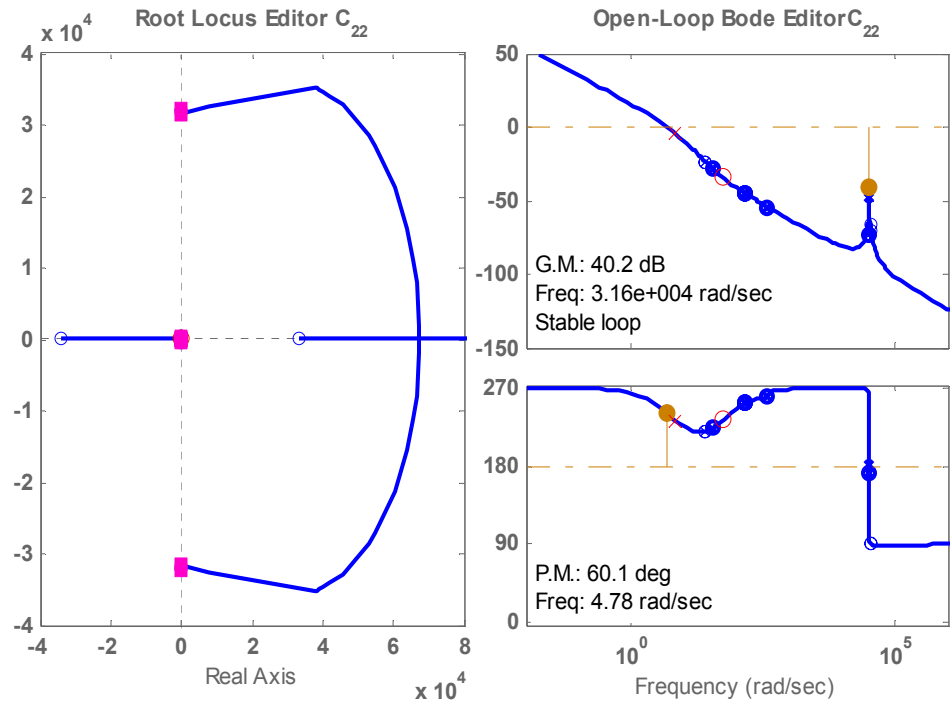
(a)
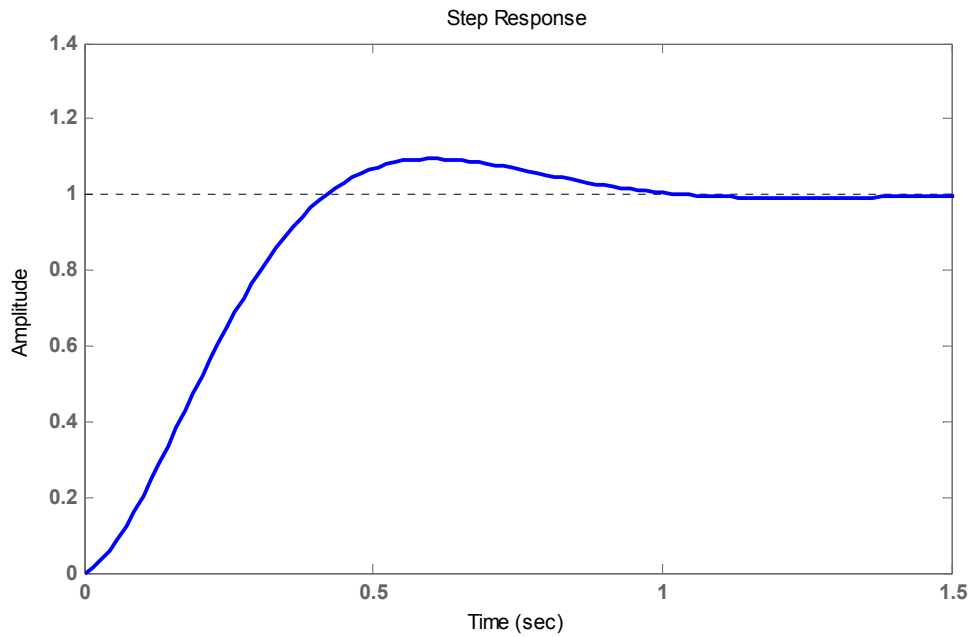


(b)

Fig. 4-22: Closed-loop $G_{aug}(2,2)$ system with controller $C_2$, (a) root locus and bode diagram, (b) step response
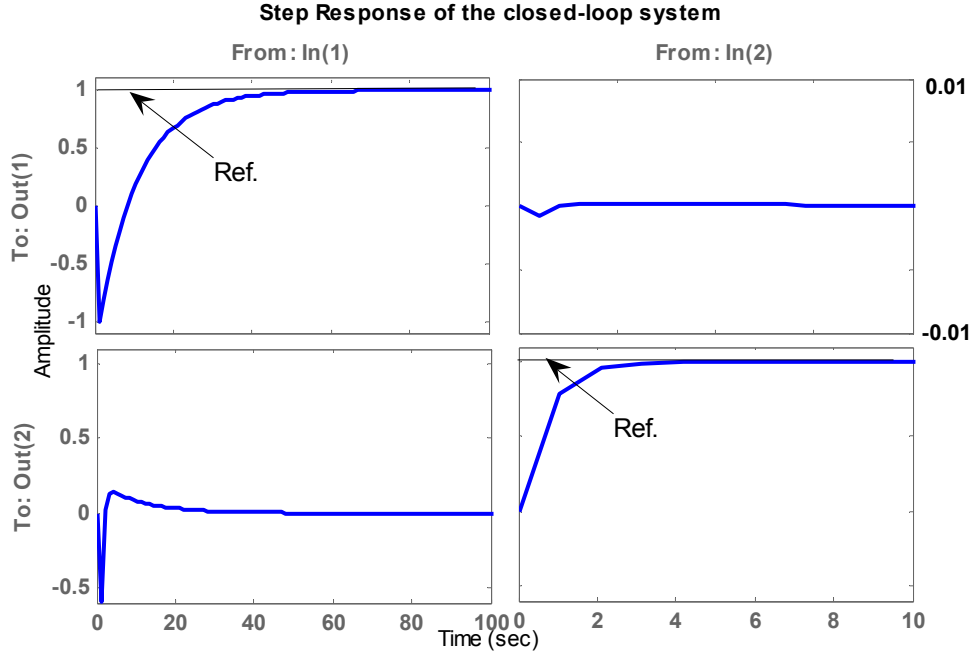
Fig. 4-23: Step response of the closed-loop MIMO system with the final controller designed with DC-decoupling approach

## 4.6.4 Sequential Loop Closure Approach (SLC)

In special cases when the transfer function of the system has a triangular structure, SISO techniques can be used to design the controller for an MIMO system, sequentially [130][147][150]. Although the wind turbine system under study has non-triangular structure, in the next subsection we will show by ignoring a weak cross-channel coupling the transfer function of the system can be converted to triangular form.

The SLC controller design begins with designing an SISO controller for the channel that has no cross-channel interactions with other channels. Then, the design will continue to the next channel while taking into account the effect of the previously-designed channel as a disturbance. For example, consider that the system has a 2×2 upper triangular structure as follows:

$$\begin{bmatrix} y_1 \\ y_2 \end{bmatrix} = \begin{bmatrix} T_{11} & T_{12} \\ 0 & T_{22} \end{bmatrix} \begin{bmatrix} u_1 \\ u_2 \end{bmatrix}. \tag{4.24}$$

A schematic of implementing the SLC structure for a 2×2 upper-triangular system is shown in Fig. 4-24. One can design controller $C_{22}$ for the second channel so that the closed-loop system containing $T_{22}$ and $C_{22}$ has a good performance. In the next stage, the controller $C_{11}$ is designed

for the first channel ($T_{11}$) by considering the effect of the second cross-channel coupling as a disturbance. The strategy for designing the controller $C_{11}$ is to have a good performance and a good disturbance rejection for the first channel closed-loop system. With a good disturbance rejection, the second closed-loop system has no serious effect on the first closed-loop performance. Note that the stability of the cross-channel transfer function $T_{12}$ is a necessary condition for the final controller.
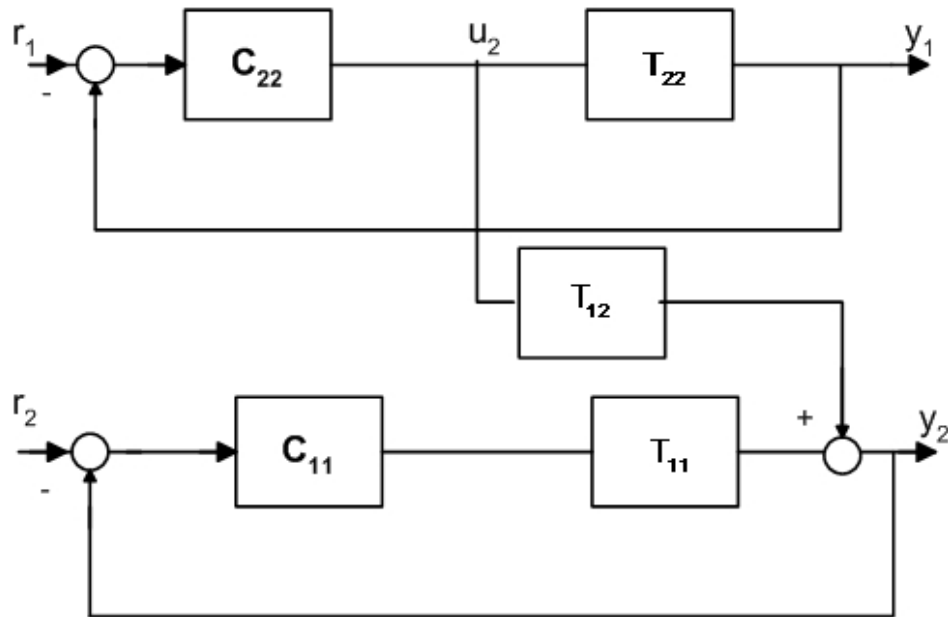


Fig. 4-24: Sequential loop closure structure for a 2×2 upper-triangular system [130][150]

## 4.6.5 Applying the SLC approach to the wind turbine system

The wind turbine system under study has non-triangular structure. In the first stage of SLC method, the system transfer function is converted to a triangular form. One possible method is to ignore a weak cross-channel coupling. Fig. 4-25 illustrates the open-loop step responses of the wind turbine system under study. It can be recognized from the step response that the second input has no strong interaction with the first output, while there is a strong coupling between second output and the first input. This fact was confirmed in the previous simulations; for example, see Fig. 4-23. The reason for this weak coupling is that the second input is a parameter for tuning the output reactive power and has no significant effect on the first output, i.e., output active power.
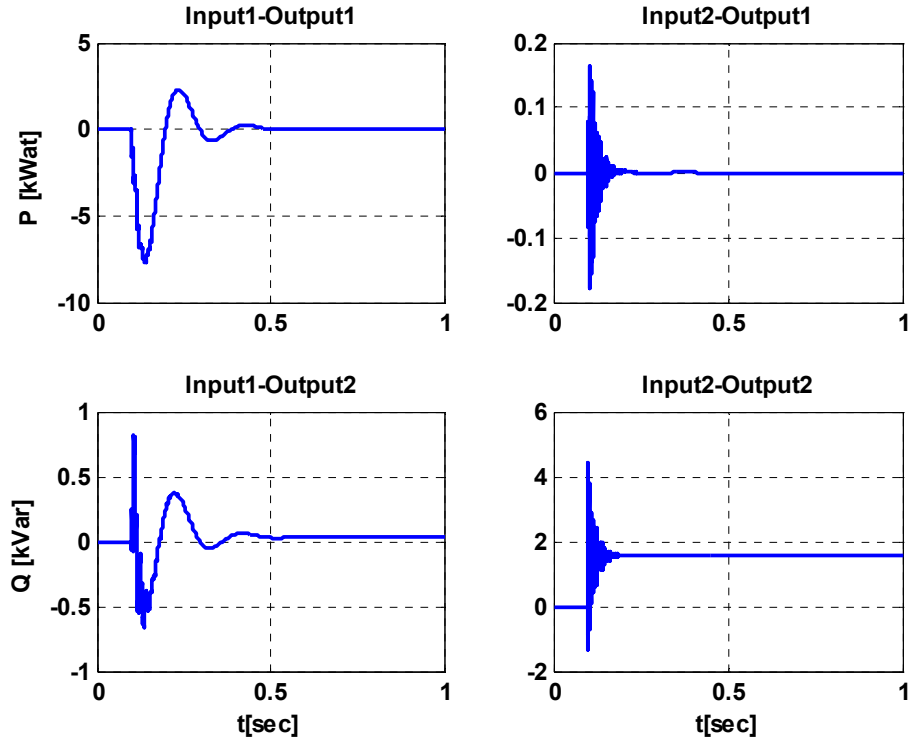
Fig. 4-25: Open-loop step response of the wind turbine system

By ignoring the input2-output1 cross-channel the new system structure is triangular. However, for simplicity, one can re-order the inputs and outputs to change the system transfer function to upper triangular form, as follows:

$$\begin{bmatrix} y_2 \\ y_1 \end{bmatrix} = \begin{bmatrix} G_{22} & G_{12} \\ G_{21} \approx 0 & G_{11} \end{bmatrix} \begin{bmatrix} u_2 \\ u_1 \end{bmatrix}.$$
(4.25)

The SLC controller design starts with focusing on the first channel transfer function, $G_{11}$. The open-loop step response of the first channel is similar to that of a second-order system. Therefore, a convenient way to design a controller for this channel is to approximate the system by a second-order system. A second-order transfer function can be found so that its step response is fairly close to the main system step response. An approximated second-order transfer function for the first channel is obtained as

$$G_{11-apr} = \frac{N_1 s + N_2}{D_1 s^2 + D_2 s + D_3},$$
(4.26)

where $N_1 = -12.47 \times 10^5$, $N_2 = 1.155 \times 10^5$, $D_1 = 1$, $D_2 = 23.2$, and $D_3 = 1153$.

133

Fig. 4-26 compares the open loop step responses of the main transfer function ($G_{11}$) with the second-order approximated transfer function $G_{11\text{-}apr}$. As shown in this figure, second-order system is a good approximation for the main system.

**Step Response of the input1-Output1**
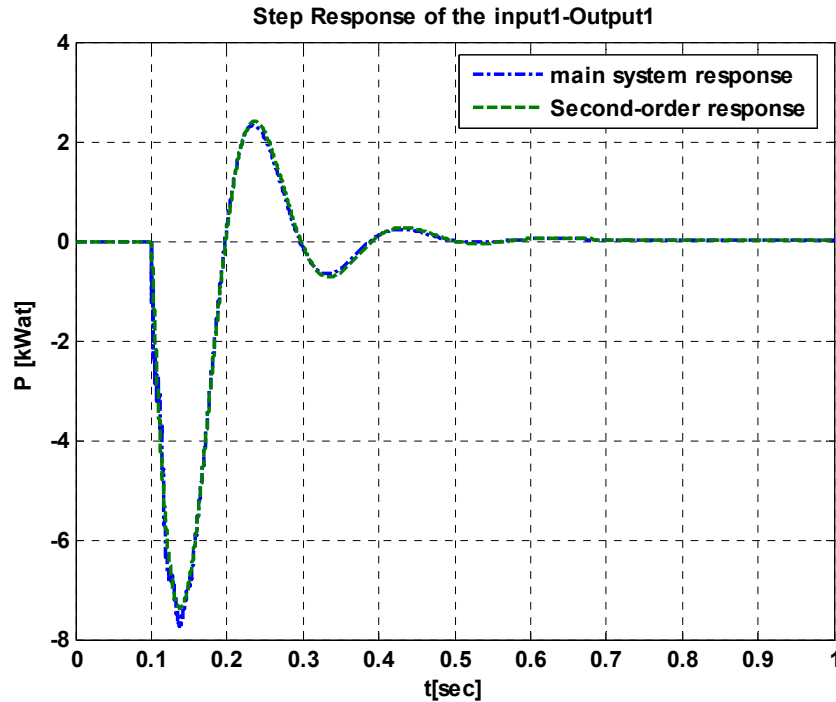


Fig. 4-26: A comparison of the step response of the first-channel of main system ($G_{11}$) and second-order approximation ($G_{11\text{-}apr}$)

### 4.6.5.1 Design of a controller for the first loop

In this subsection, a closed-loop controller is designed for the SISO transfer function $G_{11\text{-}apr}$. For the second-order system designing a Proportional-Integral (PI) controller is a suitable choice. The PI controller will increase the order of the system and adds a zero to the system as well; so, it will eliminate the steady-state step error [151]. The closed-loop system has the form shown in Fig. 4-27.
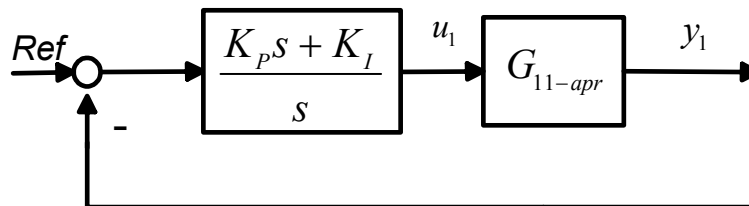


Fig. 4-27: Closed-loop with PI controller for the $G_{11\text{-}apr}$

134

The transfer function of the PI controller is

$$C_{11} = \frac{K_p s + K_I}{s}.$$  (4.27)

The aim of the design is to tune the two gains $K_p$ and $K_I$ to satisfy transient response specifications. In the first step, the stability region of the system is found when a PI controller is present. The Routh-Herwitz method is adopted to look for the values of $K_p$ and $K_I$ that make the system stable. The characteristic polynomial for the closed-loop system of Fig. 4-27 is

$$\Delta(s) = (K_p s + K_I)(N_1 s + N_2) + s(s^2 + D_2 s + D_3).$$  (4.28)

Using the above characteristic polynomial, the stable region, with $K_p$ and $K_I$ varying, can be found as shown in Fig. 4-28. The following conditions are considered for the design of a PI controller ($K_p$ and $K_I$ should be chosen form the stable region):

- zero steady-state error for a step reference, and

- damping ratio $\xi$=0.7 and damping frequency $\omega_n$=1.

The integral term in the PI controller satisfies the first requirement. To tune the two gains $K_p$ and $K_I$ to satisfy the second specification, the root locus technique is used to place the system complex eigenvalues with $\xi$=0.7 and $\omega_n$=1, as shown in Fig. 4-29. The gains $K_p$=6.31×10$^{-4}$ and $K_I$=-8.13×10$^{-4}$ put the closed-loop complex eigenvalues in the desired place. Fig. 4-30 shows the step response with the designed PI controller. As shown in this figure, the response has an acceptable overshoot (10%) and settling time (less than 10 sec), but it has a big undershoot. To decrease the system undershoot, the bandwidth of the PI controller must be decreased. By tuning the PI controller gain, one can decrease the response undershoot. However, it causes the response settling time to increase, as shown in Fig. 4-30. Therefore, the choice of values of $K_p$ and $K_I$ is a trade-off between the undershoot and settling time.
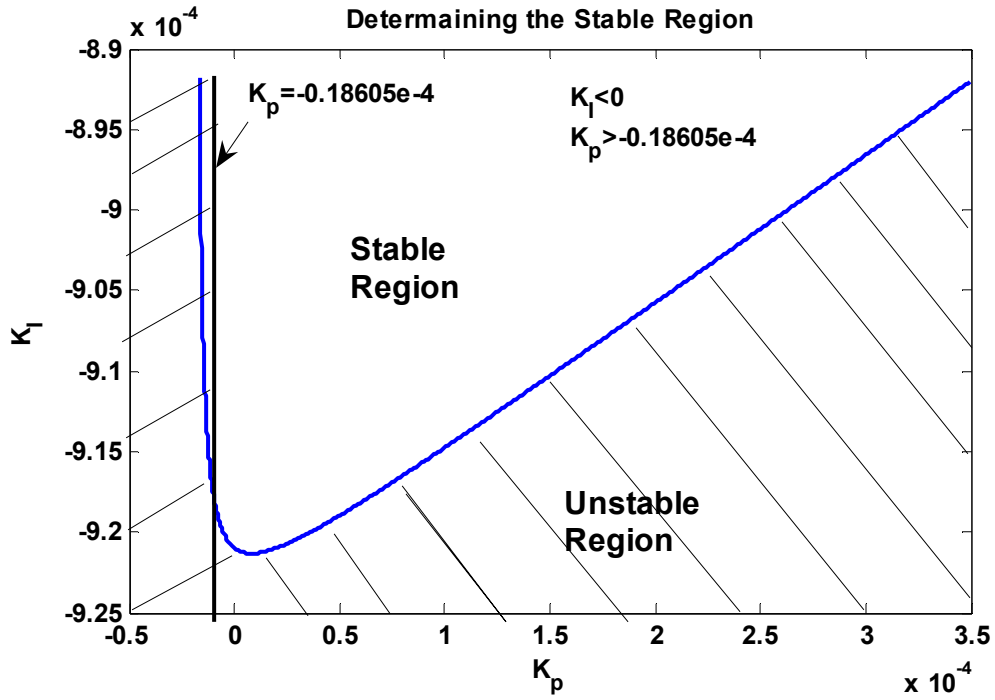
Fig. 4-28: The stable region with varying *Kp* and $K_I$ for the closed-loop system of $G_{11\text{-}apr}$ and PI controller
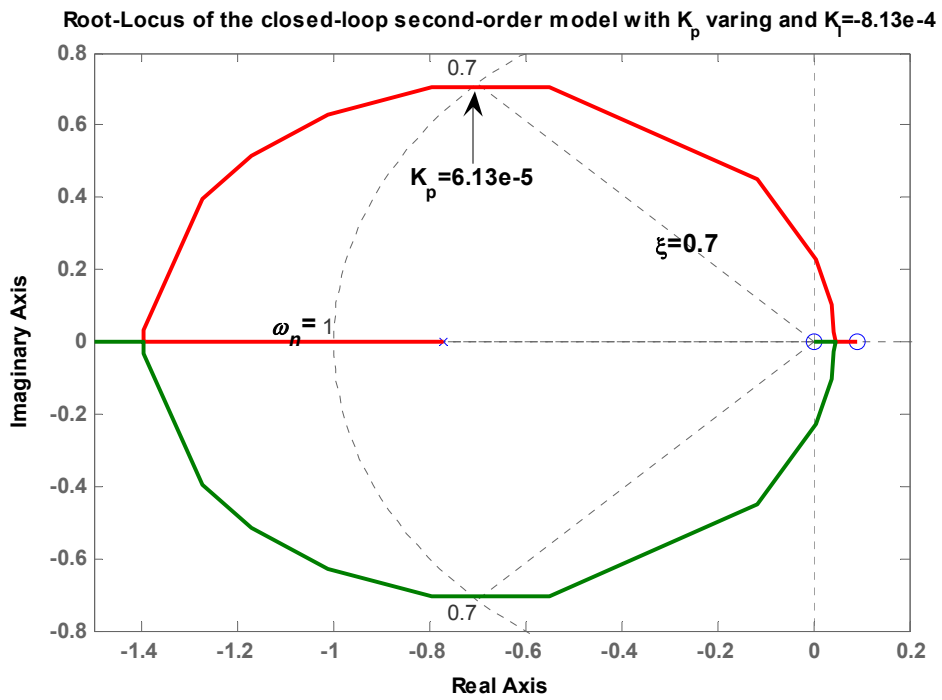


Fig. 4-29: Root locus of the closed-loop system to tune the PI controller parameters

136
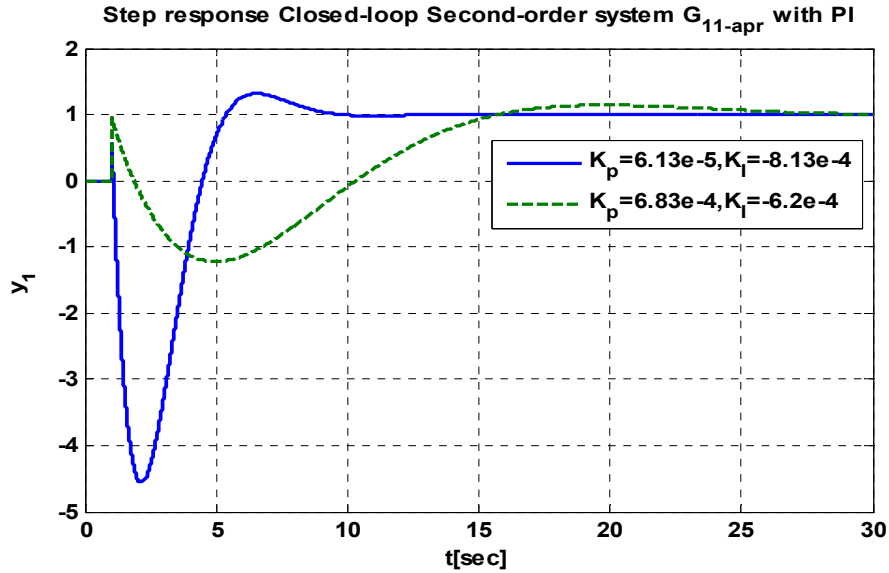
Fig. 4-30: Step response of the closed-loop second-order system $G_{11\text{-}apr}$ with PI controller

### 4.6.5.2 Designing the second channel controller

In the next stage of the SLC method, the focus will be on designing $C_{22}$ controller for the transfer function $G_{22}$. As mentioned before, the influence of the first feedback loop must be considered as a disturbance for this feedback loop (Fig. 4-24). The objective in designing $C_{22}$ is to have a good tracking performance and disturbance rejection. To achieve this, the controller must have a high gain at the frequencies that tracking the reference and rejecting the disturbance are desired. However, a high-gain controller magnifies the sensor noise and causes poor stability robustness at the frequencies with lots of uncertainty [130][149][150]. Tracking and disturbance rejection should be considered at low frequencies and noise rejection and stability robustness at high frequencies [130].

The $C_{22}$ controller is designed in the SISOTOOL toolbox environment. Note that the transfer function $G_{22}$ has a zero in the right-half plane that imposes an upper limit on the control loop bandwidth. The $C_{22}$ controller includes an integrator to get perfect steady-state step tracking and a zero to cancel out a stable dynamic. The transfer function of controller $C_{22}$ is

$$C_{22} = \frac{40s - 3920}{s(s^2 + 16900s + 1.94 \times 10^8)} . \tag{4.29}$$

The root locus, Bode diagram, and step response of the system with the designed controller are shown in Fig. 4-31. The system step response has a settling time less than 1.4 s and no overshoot.

(a)



(b)
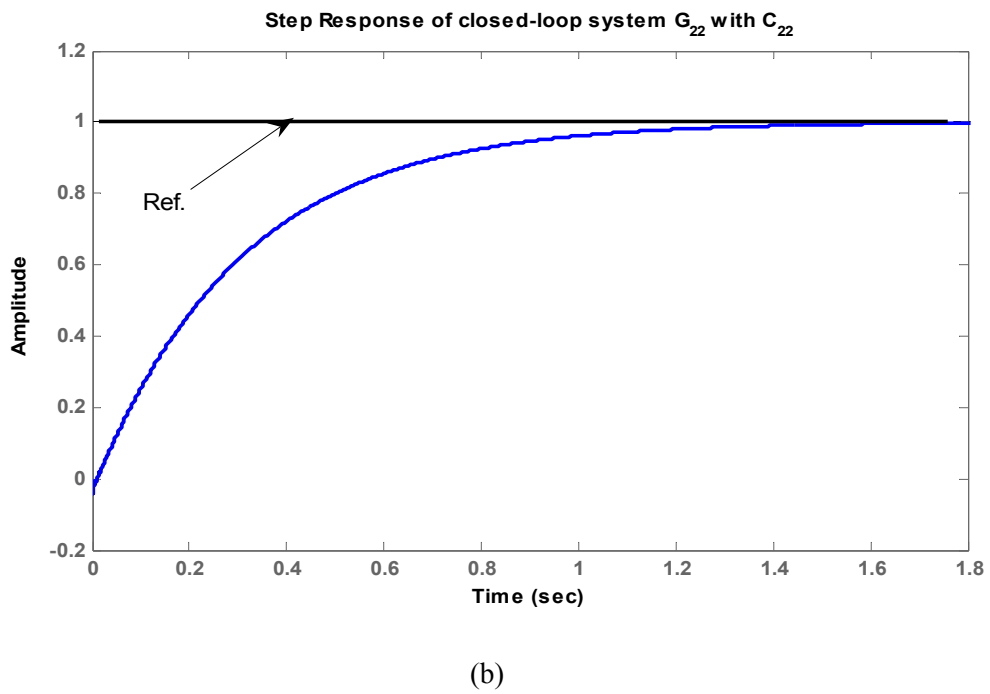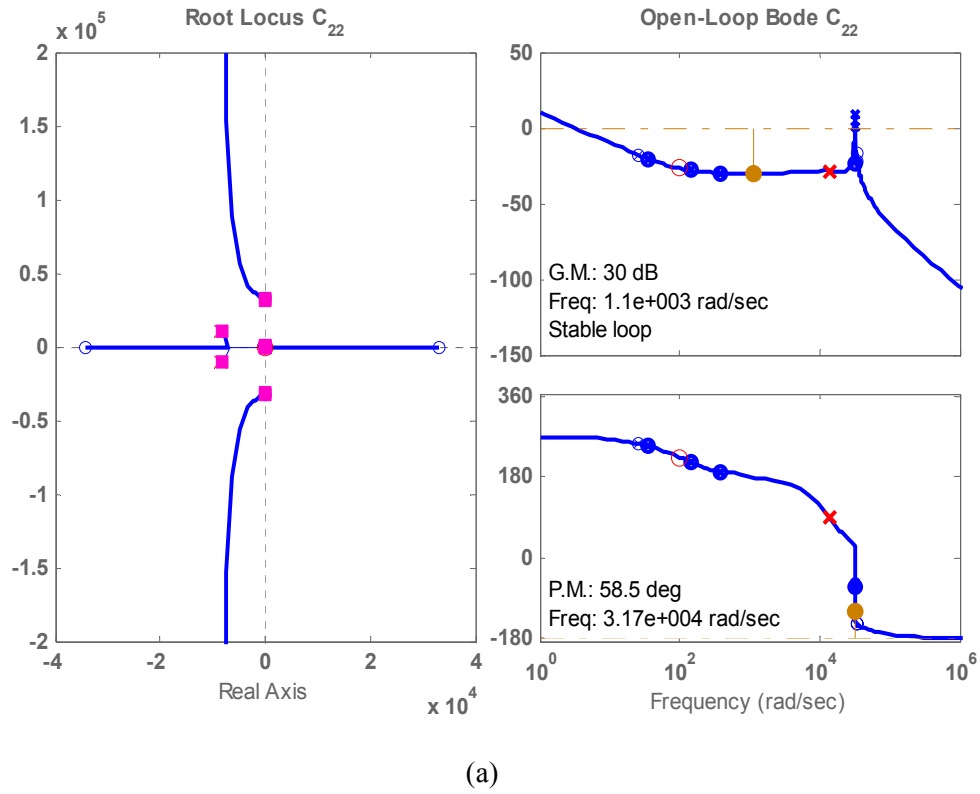
Fig. 4-31: Closed-loop $G_{22}$ system with controller $C_{22}$, (a) root locus and bode diagram, (b) step response

Fig. 4-32 illustrates the Bode plot of the second loop gain, i.e., $L_{22}=G_{22}\times C_{22}$. The figure reveals that the second closed-loop system has a high gain at low frequency for good tracking and disturbance rejection and low gain at high frequency for stability robustness and sensor noise rejection.
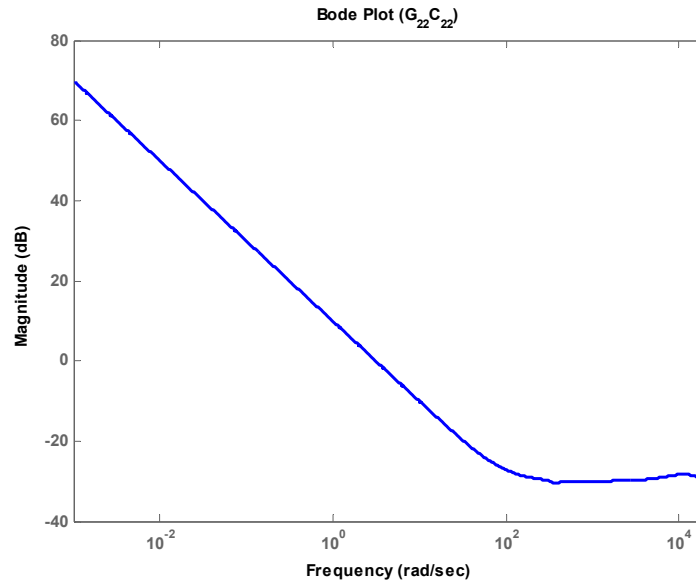


Fig. 4-32: Bode plot of the loop gain of the system $G_{22}$ and controller $C_{22}$

In order to verify the MIMO closed-loop system performance with the controller designed by SLC method, the Singular Value Decomposition (SVD) index, that was defined in the pervious chapter, is employed to find the maximum and minimum of the system loop gain. The large/small SVD means large/small gain of a system. The SVD of the MIMO closed-loop system loop gain is illustrated in Fig. 4-33. The system has a large SVD at low frequencies and a small SVD at high frequencies. Therefore, the MIMO closed-loop system has a good tracking and disturbance rejection at low frequency and good sensor noise rejection and stability robustness at high frequency.
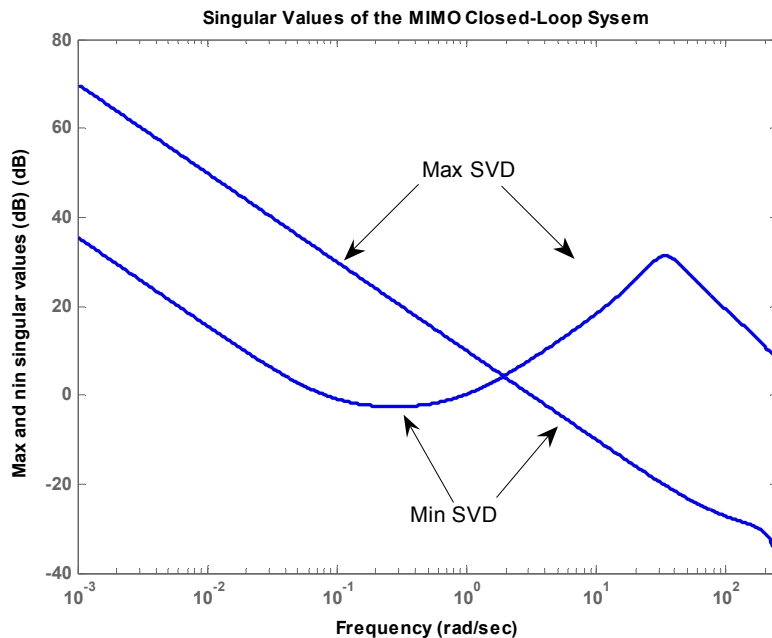
Fig. 4-33: SVD of the MIMO closed-loop system loop gain with SLC controller

### 4.6.6 Closed-Loop Wind Turbine Nonlinear Model with the SLC Controller

The linear controller designed with SLC is used to control the wind turbine system under study. The linear and nonlinear system models are used in the simulations to follow. Fig. 4-34 shows the schematic diagram of implementation of the closed-loop system in the Simulink/Matlab environment. The closed-loop system responses to the step changes in the active and reactive power references are shown in Fig. 4-35. The figure reveals a small discrepancy between the linear and nonlinear model responses. Before applying the step change at t=1sec, the system is in steady-state at the operating point. The step change is applied to the output active and reactive power references at t=1 and 40 sec, respectively. The corresponding input control signals are also illustrated in Fig. 4-36. As seen in Fig. 4-35, the system outputs follow the references with zero steady-state errors. The control signals in Fig. 4-36 show that the frequency control signal strongly affects the active power, while the input power factor signal is almost constant during real power changes. On the other hand, the output reactive power variation is more sensitive to the variations of input power factor control signal.
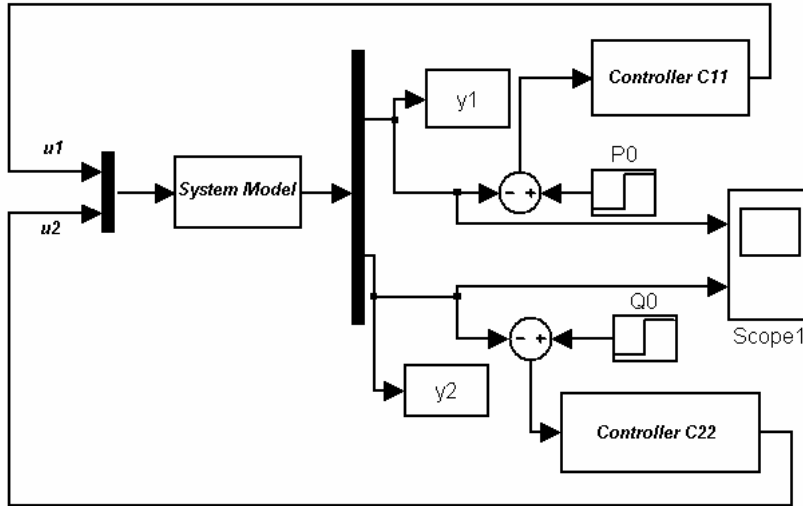
Fig. 4-34: Block diagram of the closed-loop system in the Simulink/Matlab
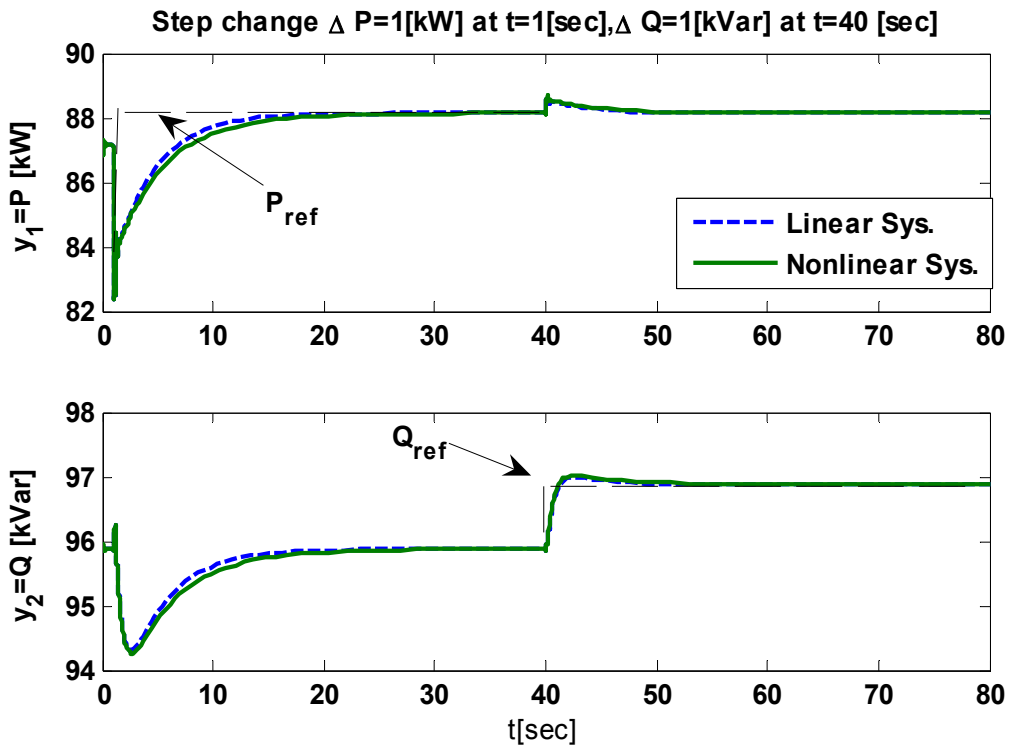


Fig. 4-35: Comparison of the linear and nonlinear closed-loop system responses to step changes in references
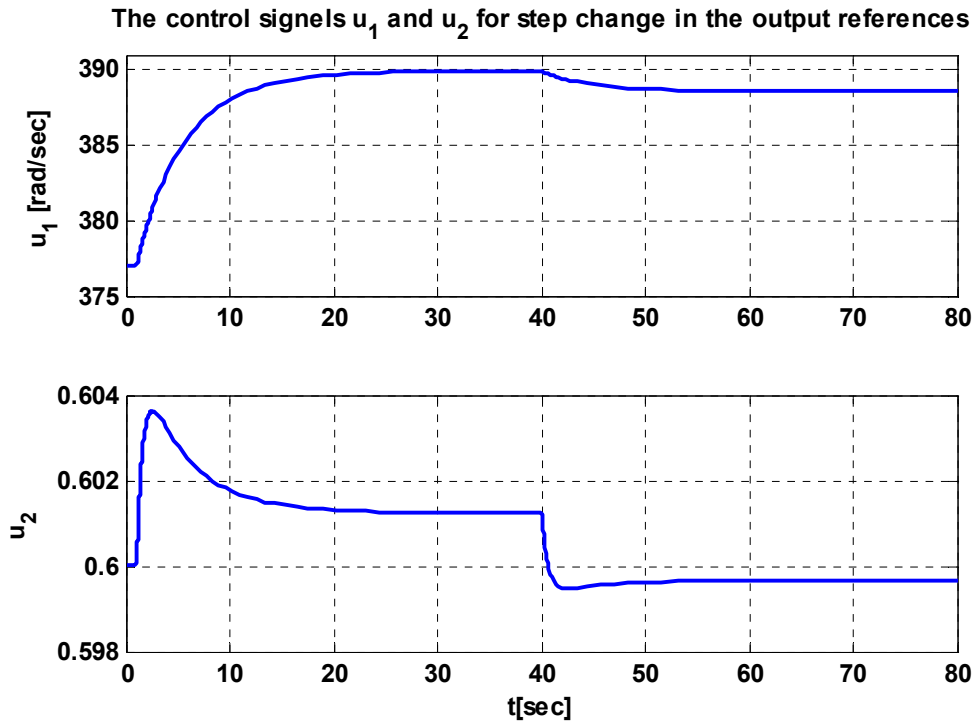
Fig. 4-36: The control signals variations when step changes are applied to the output references

## 4.7 Summary

A closed-loop feedback controller, based on the linear model, is designed. The open-loop system is locally stable around the operating point, and the controller design objective is to track a class of desired active and reactive powers delivered to the grid. Two control design methods are adopted for the wind turbine system: a state-feedback controller and an output-feedback controller.

In the state-feedback controller, since the goal is to achieve zero steady-state error for the family of step reference signals, first an integrator is added after the system. The combination of the system with the integrator forms the augmented plant. Then, the state-feedback controller is designed based on the LQ method. The LQ method is proved to be simple and effective for adjusting the parameters of the closed-loop controller. The LQ method involves choosing weighting matrices that minimize a cost function and provide satisfactory closed-loop performance. The closed-loop performance depends on the location of the system eigenvalues in the s-plane, and the locations of the eigenvalues are dependent on the weighting matrices in the LQ method. For a high-order system, the number of $Q$ and $R$ elements is large, and finding the best weighting matrices by trial and error to achieve a desired transient performance is difficult.

A genetic algorithm (GA) is used to determine the weighting matrices of the LQ method to locate the closed-loop eigenvalues as close to the desired values as possible. The simulation results reveal that the system with the closed-loop controller, designed by LQ and GA methods, can satisfy the design constraints.

The state-feedback controller needs to measure all state variables. However, it is impractical to measure all state variables in the system under study. Therefore, an observer is designed and used in the state-feedback loop. The observer estimates the states by measuring the output and input variables. The inputs of the observer block are the system input and output vectors, and its output is the estimated state variables. The simulation results show that the observer affects the system transients, but it has no effect on the steady-state (tracking) response. However, the gain and phase margins are dramatically decreased when the observer is added to the system. In fact, the observer increases the bandwidth of the controller. Because the system has some zeros in the right-half plane,  the high-bandwidth controller causes a big undershoot and decreases the phase-margin.

Two other controllers based on the transfer function techniques are developed for the wind turbine system.

First, a simple approach, based on decoupling the system at DC, is adopted. The controller is carefully designed for the system, but the final controller results in an unstable closed-loop system. This instability occurs consequent to the cross-channel interactions. To decrease the effect of cross-channel interactions, the controller bandwidth in each channel should be decreased. The closed-loop system becomes stable by trial and error and reducing the gain of the controller. However, reducing the controller gain increases the system settling time.

Second, a sequential loop closure method is used to design a MIMO controller without ignoring the cross-channel interactions at a certain frequency. By ignoring a weak cross-channel coupling, the transfer function of the system under study can be converted to a triangular form. The SLC controller design begins with designing an SISO controller for the channel that has no cross-channel interactions with other channels. Then, the design will continue to the next channel while taking into account the effect of the previously-designed channel as a disturbance. For simplicity in controller design, the first channel transfer function is approximated by a second-order system. A PI controller is designed for the second-order system to satisfy the design conditions. The second loop controller is designed so that the closed-loop system has a high gain at low frequencies which yields good tracking and disturbance rejection. Also, the closed-loop with second loop controllers has low gain at high frequencies which yields stability robustness and sensor noise rejection. The SVD index reveals that the final MIMO closed-loop system with the SLC controller has a good tracking and disturbance rejection as well as a reasonable sensor noise rejection and stability robustness.

Finally, the controller based on the SLC method is used in the closed-loop nonlinear MIMO system. The simulation results are compared with those of the wind turbine linear model. The results indicate that the system outputs follow the references with zero steady-state errors, and there is a small discrepancy between the linear and nonlinear model responses. In addition, the control signals show that the frequency control signal strongly affects the active power, while the input power factor control signal is almost constant during real power changes. On the other hand, the output reactive power variation is more sensitive to the variations of input power factor control signal.

# Chapter 5

# Maximum Power Point Tracking Control for the Proposed Wind Turbine System

## 5.1 Introduction

This chapter focuses on the maximum wind power extraction algorithm, or Maximum Power Point Tracking (MPPT) control, for the proposed wind energy conversion system. At a given wind velocity, the mechanical power available from a wind turbine is a function of its shaft speed. To maximize the power captured from the wind, the shaft speed has to be controlled. In order to track maximum power, the matrix converter (MC) adjusts the induction generator terminal frequency, and thus, the turbine shaft speed. The MC also adjusts the reactive power transfer at the grid interface towards voltage regulation or power factor correction. A MPPT algorithm is integrated in the closed-loop control system designed in the previous chapter, to control the MC in order to capture maximum wind power.

In the next section, the concept of the MPPT in the wind energy conversion systems is presented. Three existing maximum wind power extraction methods, Perturbation and Observation (P&O), Wind Speed Measuring (WSM), and Power Signal Feedback (PSF), are reviewed in Section 5.3. In Section 5.4, the implementation of P&O method for the proposed

wind turbine system is introduced. Section 5.5, presents power signal feedback method, called sensor-less PSF, for the wind turbine system under study. The claims made for the capabilities of the proposed scheme are supported by analysis and simulation results.

## 5.2 Maximum Power Tracking Concept

In this section, the concept of Maximum Power Point Tracking (MPPT) is presented. The variable-speed wind turbine (VSWT) was introduced in Chapter 1. At a given wind velocity, the mechanical power available from a wind turbine is a function of its shaft speed. To maximize the power captured from the wind, the shaft speed has to be controlled by a variable-speed method. As mentioned in Chapter 1, the variable-speed wind turbine (VSWT) provides more energy output, lower mechanical stress, and less power fluctuations, compared to the constant-speed turbine.

The equations of the wind turbine mechanical power and mechanical torque were given in Chapter 3 (see equations (3.1) and (3.2)). The wind turbine mechanical output power, $P_T$ is affected by the ratio of the turbine shaft speed and the wind velocity, i.e., tip-speed-ratio ($\lambda=R\omega_T/V_W$). As a result of variations in wind velocity, the turbine shaft speed $\omega_T$ (or generator shaft speed $\omega_g$), and wind turbine power $P_T$ will change. Fig. 5-1 shows a family of typical $P_T$ versus $\omega_r$ curves for different wind velocities for a typical system. As seen in this figure, different power curves have different maximum power, $P_{max}$ (or optimal power, $P_{opt}$).
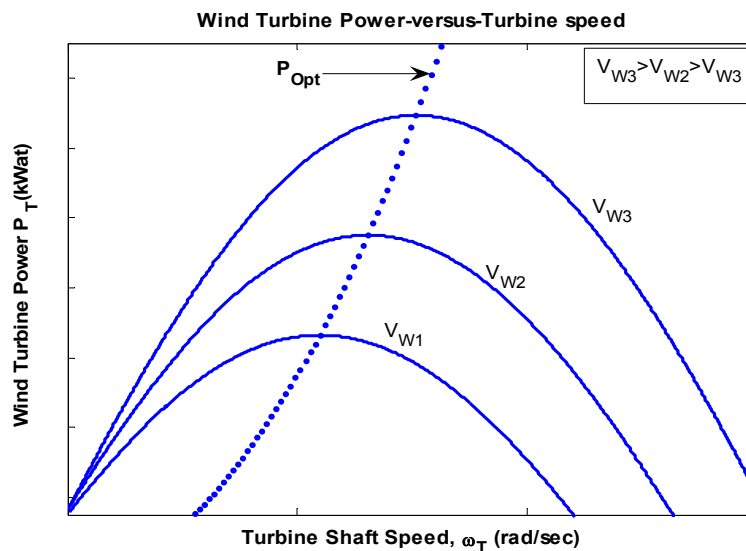


Fig. 5-1: Wind turbine mechanical output power versus shaft speed

In Fig. 5-1, the shaft speed $\omega_{P_{max}}$ corresponding to the maximum power is obtained from the following equation:

$$\frac{\partial P_T}{\partial \omega_{P_{max}}} = 0 \tag{5.1}$$

Substituting equation (3.1) and (3.4) from Chapter 3 in (5.1), yields:

$$\omega_{P_{max}} = \frac{V_w}{R}\left(\left(\frac{15 - 0.3\beta}{\pi}\right)\cos^{-1}(\frac{0.00184\beta(15 - 0.3\beta)}{\pi 0.5\rho^2 V_W^2(0.44 - 0.0167\beta)}) + 3\right) \tag{5.2}$$

From (3.1) and (5.2) the maximum mechanical output power formula is:

$$P_{max} = P_T(\omega_{P_{max}}) \tag{5.3}$$

From mechanical design point of view, wind turbines are designed to operate at maximum power for an average wind speed. However, it is clear that wind speed dose not stay at an average level all the time. At lower wind speeds, tip speed ratio ($\lambda$) is increased (with constant rotor speed), and accordingly, the power coefficient $C_p$ decreases (equation (3.4)). As a consequence, the wind turbine is not operating under optimal conditions (where $Cp$ is low) most of the time. Optimal operating conditions can be achieved by employing a MPPT method. Implementing a MPPT method depends on wind turbine structure; however, these methods can be roughly classified into three types [153]-[155]. In the following section, different MPPT methods are discussed.

## 5.3 Maximum Power Point Tracking Methods

A literature survey identifies three common MPPT methods namely, perturbation and observation (P&O) [106], wind speed measurement (WSM) [153], and power signal feedback (PSF) [16][154]. In the following, these three methods are briefly explained.

### 5.3.1 Perturbation and Observation Method

The Perturbation and Observation (P&O) or Hill-Climb Searching (HCS) method is based on perturbing the turbine shaft speed in small steps and observing the resulting changes in turbine mechanical power [106][154].

The concept and schematic diagram of the P&O method is shown in Fig. 5-2. If the shaft speed increment ($\Delta\omega_T$) results in a turbine power increment ($\Delta P_T$), the operating region is in the up-hill

curve, and increasing shaft speed must be continued toward maximum power point; otherwise, the turbine operating region is in the down-hill curve, so the shaft speed should be decreased by the P&O method to reach the maximum power point. To implement the P&O method, one can check the signs of $(\Delta\omega_T)$ and $(\Delta P_T/\Delta\omega_T)$. The shaft speed is incremented $(\Delta\omega_T>0)$ in small steps as long as $(\Delta P_T/\Delta\omega_T)>0$ or decremented $(\Delta\omega_T<0)$ in small steps as long as $(\Delta P_T/\Delta\omega_T)<0$. This is continued till maximum power point is reached, i.e., $(\Delta P_T/\Delta\omega_T)=0$. If incrementing shaft speed results in $(\Delta P_T/\Delta\omega_T)<0$ or decrementing shaft speed results in $(\Delta P_T/\Delta\omega_T)>0$, the direction of shaft speed change must be reversed [106].
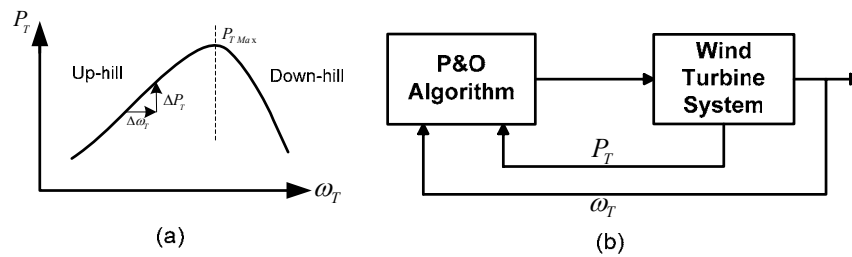


Fig. 5-2: P&O method: (a) turbine power versus shaft speed and principle of the P&O method (b) block diagram of the P&O control in wind turbine

   The superiority of P&O method to other MPPT methods is in that it does not require priori knowledge of the maximum wind turbine power at different wind velocities, and electrical machine parameters [106][153][157]. However, P&O method is suitable for systems with small inertia (small time-constant) [12][158], such as solar energy conversion systems with no inertia or low-power and low-inertia wind turbine systems [156]. For medium and large-inertia wind turbine systems, the turbine speed cannot follow changes in wind velocity; so, the P&O method (without any other controller) will not be able to control the wind turbine system properly [154].

### 5.3.2 Wind Speed Measurement Method

The aim of the turbine speed control is to maintain turbine shaft speed at optimal value, i.e., $\omega_{P_{max}}$ , so that maximum mechanical power can be captured at any given wind velocity $(V_W)$ [153][159]. In the wind speed measurement (WSM) method, both wind velocity and shaft speed $(\omega_T)$ should be measured. Also, optimal tip-speed-ratio $(\lambda_{opt})$ must be determined for the controller. The block diagram of this method is shown in Fig. 5-3.

Although this method is a simple method for implementing the MPPT, there are two drawbacks to implementing the WSM method. First, obtaining accurate value of the wind velocity is complicated and increases the cost of the system [153][160]. Second, the optimal tip-speed-ratio is dependent on the wind energy system characteristics. Therefore, the controller will require adjustment before installation in a new wind energy system [154].
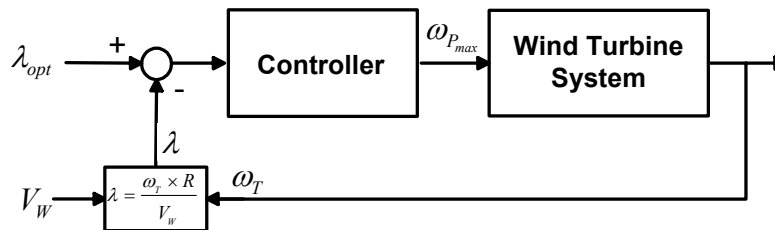


Fig. 5-3: Block diagram of a wind energy system with shaft speed control using wind WSM method

## 5.3.3 Power Signal Feedback (PSF) Control

The block diagram of a wind energy system with PSF control is shown in Fig. 5-4. In this method, the maximum power curve of the wind turbine, Fig. 5-1, should be obtained first from experimental results. Then, the data points for maximum output power and the corresponding wind turbine speed must be recorded in a lookup table[154][160]-[162].

The concept of the PSF method is illustrated in Fig. 5-5. Tracking of the maximum power curve, the dashed-curve, is the aim of the PSF method. Suppose the system is initially stable at point A with wind velocity $V_1$, shaft speed $\omega_{T1}$ and maximum output power $P_1$. If the wind velocity increases to $V_0$, the new optimum power targeted by the controller should be $P_0$. In the moment following the wind velocity change, the shaft speed is still at $\omega_{T1}$, due to inertia of the shaft. But, the turbine output power is increased to $P'_1$, while the power reference based on the lockup table is still $P_1$. The shaft will accelerate under additional turbine torque and the operating point is moved by the controller on the $P_T$-$\omega_T$ curve corresponding to $V_0$ toward point B. Eventually, the system will stabilize at point B with the new output power $P_0$. Similar to this scenario, if the system is settled down initially at point C and the wind velocity decrease to the $V_0$, the shaft decelerates toward $\omega_{T0}$.
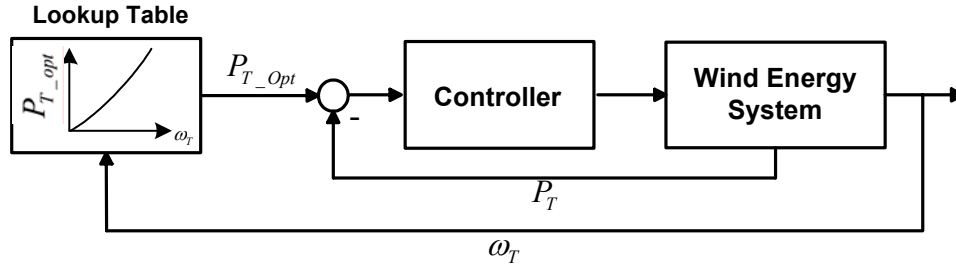
Fig. 5-4: Block diagram of a wind energy system with Power Signal Feedback control
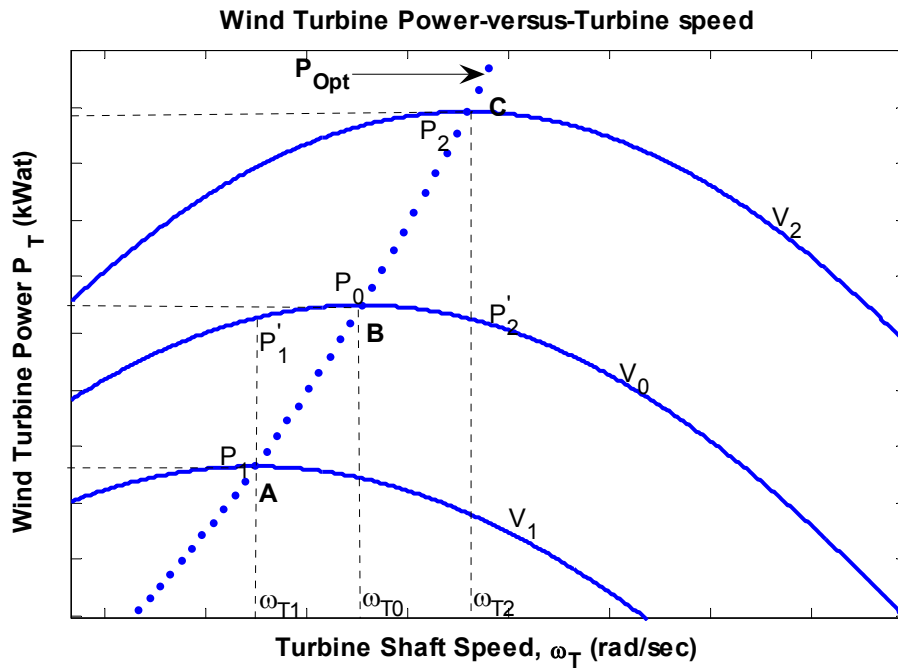


Fig. 5-5: The power signal control concept

To implement PSF control, the controller should be aware of the wind turbine maximum power versus shaft speed curve. The maximum power is tracked by the shaft speed measurement and corresponding power reference determination. No wind velocity measurement is required in this method [154][162].

Although the PSF method does not require measuring the wind velocity, a barrier is the difficulty of obtaining the maximum power curve of the wind turbine. Moreover, measuring the mechanical shaft speed and wind turbine output power is another drawback of the PSF method.

In the following, a mechanical speed-sensorless PSF method is implemented in the wind turbine system to overcome the mechanical shaft speed measurement requirement.

## 5.3.4 Mechanical Speed-Sensorless PSF method

This subsection presents a maximum power tracking approach, called sensor-less PSF method. The method has the capability of providing a power reference for the controller corresponding to maximum power point without measuring the turbine shaft speed. In other words, the method is based on PSF control, but neither wind velocity sensor nor turbine speed sensors are required. This is the significant advantage of this method. The method can be developed for all wind-turbine system including an induction-generator (I.G.) [16][163]-[165].

Fig. 5-6 shows the block diagram of a mechanical speed-sensorless PSF control system. In this method a look-up table containing induction generator synchronous speeds ($\omega_s$) corresponding to the optimal generator powers ($P_{gen-opt}$) is used. As the wind velocity keeps changing with time, the wind turbine must keep adjusting its speed to track the optimum wind turbine speed. In the following, the details of the sensorless PSF method are presented.
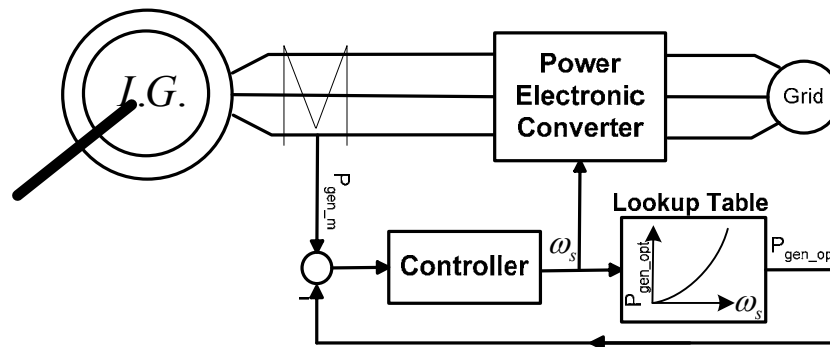


Fig. 5-6 : Block diagram of the mechanical speed-sensoreless PSF control system

In the system under study the generator is connected to the turbine through a gearbox with gear ratio $n_{gear}$. Based on the turbine power-versus-turbine shaft speed ($P_T$-versus-$\omega_T$) curves of Fig. 5-1, the torque versus shaft speed at the generator side ($T_g$-versus-$\omega_g$) characteristics are shown in Fig. 5-7. Note that in this figure, the quadratic optimal torque curve, $T_{opt}$-vesus-$\omega_g$ , is drawn based on the following formula:

$$T_{opt} = \frac{P_{max}}{\omega_{P_{max}}} .$$
(5.4)

The dynamic behavior of the turbine and induction generator can be described as follows:

$$T_T - T_c = J \frac{d\omega_g}{dt} .$$

(5.5)

where $T_C(=-T_g)$ is the induction generator counter-torque and $J$ is total shaft moment inertia (including turbine and generator shaft inertia).

**Wind Turbine Torque-versus-Turbine speed**
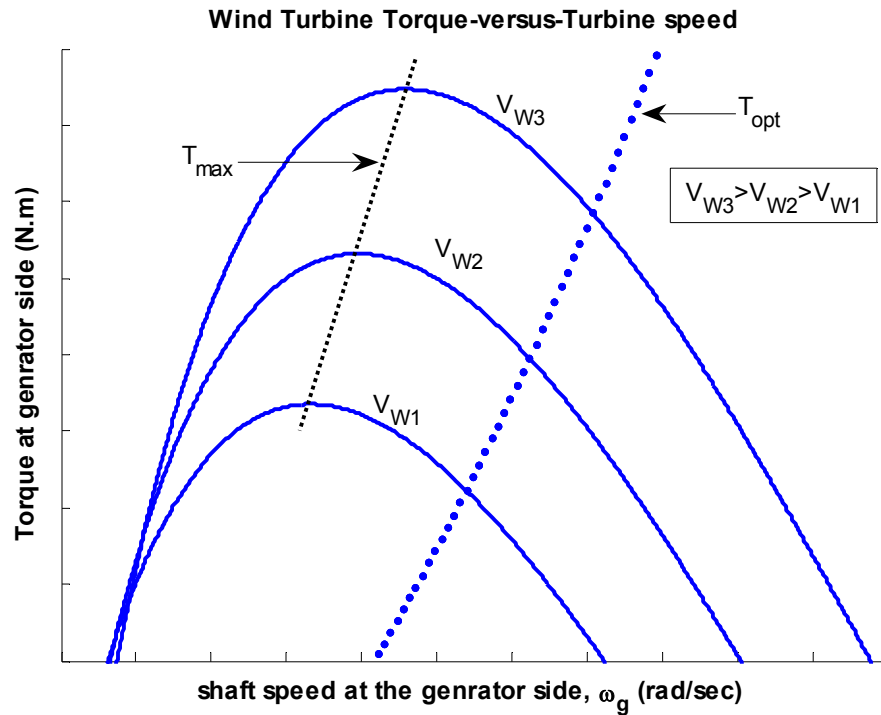


Fig. 5-7: Wind turbine torque versus shaft speed on the generator side for different wind velocites

Maximum power production for any wind velocity is achieved when the generator counter-torque equals optimal turbine torque ($T_{opt}$). The equilibrium shaft speed can be found graphically as the intersection of turbine torque-speed curve with generator torque-speed curves as illustrated in Fig. 5-8 [106]. In this figure, the $P_T$-versus-$\omega_T$ and $T_T$-versus-$\omega_T$ curves of the wind turbine, as well as a family of $T_c$-versus-$\omega_g$ curves for the induction generator for different generator synchronous speeds ($\omega_s$) are shown. Note that all curves are drawn on the same side of the gearbox. By varying the output frequency of the converter ($\omega_e$), and thus, induction generator synchronous speed ($\omega_s$), the $T_c$-versus-$\omega_g$ curve can be shifted to the right or left with respect to the wind turbine torque-speed curve to assume a wide range of possible steady-state operating points defined by the intersections of the two curves. Obviously, one of the operating points

corresponds to maximum power. To move from one operating point to another, $\omega_e$ is changed in steps (small enough to maintain generating mode) and the difference between the wind turbine torque $T_T$ and the new generator counter torque $T_c$ at the operating speed will accelerate or decelerate the shaft according to equation (5.5) until the new steady-state operating point is reached. In the following, moving towards maximum power point starting on two different sides of optimal operating point are presented [106].
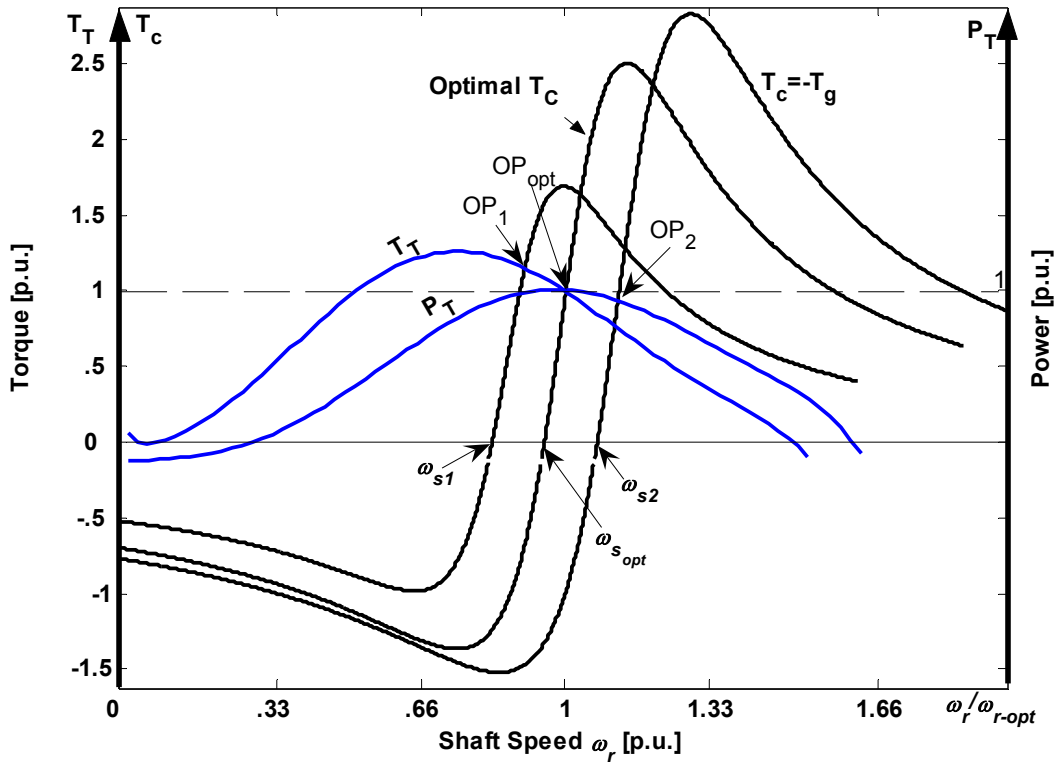


Fig. 5-8: Maximizing captured wind power by shifting $T_c$ - $\omega_r$ curve with respect to $T_T$ - $\omega_r$ curve

## A. Accelerating Shaft towards Maximum Power Point

In Fig. 5-8, $OP_{opt}$ is the operating point corresponding to maximum power captured from the wind at the wind velocity of $V_W$. At this point $P_T$ =1 [p.u.], $T_T$ =1 [p.u.], and $\omega_r = \omega_{r_{opt}}$ =1[p.u.], where $\omega_{r_{opt}}$ is the angular shaft speed corresponding to maximum power point.

Assuming the present operating point to be $OP_1$, corresponding to $\omega_{s1}$, the shaft should speed up so that the operating point $OP_{opt}$ can be assumed by the system. This can be achieved by

increasing $\omega_s$ from $\omega_{s1}$ to $\omega_{s_{opt}}$ through an increase in the induction generator terminal frequency.

The frequency adjustment is performed in steps small enough for the induction machine to keep operating as a generator throughout the transition period. This action makes $T_T$-$T_c$>$0$ and accelerates the shaft according to equation (5.5) towards maximum power point.

**B. Decelerating Shaft towards Maximum Power Point**

Assuming the present operating point to be $OP_2$, corresponding to $\omega_{s2}$, the shaft should slow down so that the system assumes the operating point $OP_{opt}$. This can be accomplished by decreasing $\omega_s$ from $\omega_{s2}$ to $\omega_{s_{opt}}$ through a decrease in the induction generator terminal frequency and voltage according to constant $V/f$ strategy, in steps small enough to restrict operation within the stable generating region. This action makes $T_T$-$T_c$<$0$ and decelerates the shaft according to equation (5.5) towards maximum power point.

**5.3.4.1 The Maximum Power Point Data in the Mechanical Sensorless PSF Method**

In the following, a formula for the optimal $P_{opt}$-versus-$\omega_s$ curve will be derived and the corresponding data of the curve will be entered in the lookup table of Fig. 5-6 [16][165].

The generator torque is a function of its terminal voltage, and $\omega_s$, and $\omega_g$, as given by equation (5.6).

$$T_G = f(V_s, \omega_s, \omega_g) . \tag{5.6}$$

As mentioned in Chapter 3, section 3.5, the induction generator voltage terminal is adjusted by the MC according to a constant $V/f$ strategy. To satisfy this strategy, the magnitude of induction generator terminal voltage should be varied linearly with synchronous frequency as follows:

$$V_s(\omega_s) = K_W \omega_s , \tag{5.7}$$

where $K_W$ is a proportionality constant. This constant can be calculated based on the constant V/f ratio, that was defined in equation (3.51), as follows:

$$K_w = k_{VF} V_{Grid-rated} , \tag{5.8}$$

where $V_{Grid-rated}$ is the grid rated voltage.

Substituting (5.7) in equation (5.6), and using the induction machine equivalent circuit in Chapter 3, Fig. 3-7, and equation (3.11), the generator torque can be written as a function of $\omega_s$ and $\omega_g$ :

$$T_g = f(\omega_g, \omega_r).$$ (5.9)

Note that, in the generating mode of the induction machine, $\omega_s < \omega_g$ and sign of $T_g$ is negative, representing a counter torque.

At the shaft speed $\omega_r$, the optimal torque corresponding to the maximum acquisition power can be found from the $T_{opt}$-versus-$\omega_r$ curve, Fig. 5-1. The system is at the maximum power point if the induction generator counter-torque is equal to $T_{opt}$ :

$$T_{opt}(\omega_g) = -T_g.$$ (5.10)

$T_g$ can be calculated using the induction machine equivalent circuit, Fig. 3-7, as follows:

$$T_g = \frac{3 r_r |I_r|^2}{\omega_s - \omega_g},$$ (5.11)

where $I_r$ is the rotor current and can be obtained from the equivalent circuit as

$$I_r = \frac{V_s(\omega_s) Z_m}{Z_s(Z_R + Z_m) + Z_m Z_r},$$ (5.12)

where $Z_s = r_s + j\omega_s L_s$ is the stator impedance, $Z_r = r_r(\omega_s/(\omega_s - \omega_r)) + j\omega_s L_r$ is the rotor impedance, and $Z_m = j\omega_s L_M$ is the magnetizing impedance.

Using equation(5.10), for a given optimal turbine torque and mechanical shaft speed ($\omega_g = \omega_{g_{opt}}$), the corresponding generator synchronous speed ($\omega_s = \omega_{s_{opt}}$) can be determined. In other words, by solving equation (5.10) it is possible to plot the $T_{opt}$–versus-$\omega_{s_{opt}}$ curve. Employing this curve, instead of $T_{opt}$–versus-$\omega_{g_{opt}}$, makes the system speed-sensorless, because there is no need to measure the mechanical speed $\omega_g$.

The lookup table in Fig. 5-6, contains the data points of $P_{gen\_opt}$-versus-$\omega_{s_{opt}}$ curve, that can be obtained easily from the $T_{opt}$-versus-$\omega_{s_{opt}}$ curve as follows.

The optimal turbine power is:

$$P_{opt}(\omega_{g_{opt}}) = T_{opt}(\omega_{g_{opt}})\omega_{g_{opt}} . \tag{5.13}$$

$P_{gen\_opt}$ can be calculated using the induction machine equivalent circuit as

$$P_{gen\_opt}(\omega_{s_{opt}}) = P_{opt}(\omega_{g_{opt}}) - P_{mech\_loss} - 3r_s I_s^2 - 3r_r I_r^2 , \tag{5.14}$$

where $P_{mech\_loss}$ represents mechanical losses, $I_s$ and $I_r$ are induction generator stator and rotor currents, and $3r_s I_s^2$ and $3r_r I_r^2$ are copper losses in the stator and the rotor, respectively. Note that the stator current can be determined as

$$I_s = I_r \frac{Z_s + Z_m}{Z_m} . \tag{5.15}$$

Finally, the amounts of $P_{gen\_opt}$-versus-$\omega_{s_{opt}}$ should be entered in the lookup table of Fig. 5-6.

The flowchart of Fig. 5-9 shows briefly the stages of finding the lookup table for implementing using the mechanical speed-sensorless PSF method.
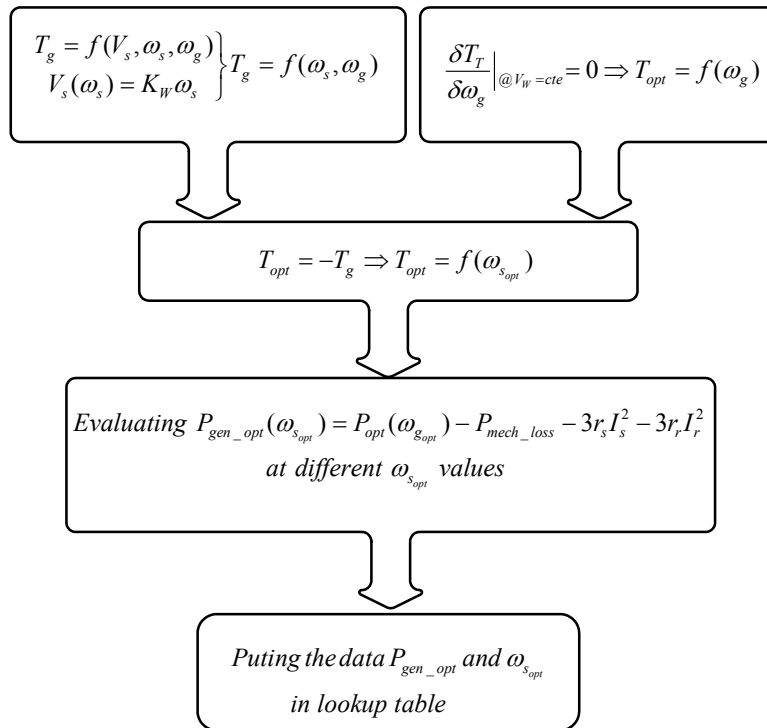


Fig. 5-9: Stages of finding the lookup table in the mechanical sensorless PSF method

## 5.4 Implementing the P&O Method for a Small Wind Turbine System including a Matrix Converter

As mentioned in the pervious section, P&O method is suitable for the wind turbines with small inertia. Therefore, other MPPT methods should be employed in the wind turbine under study. In this section, in order to evaluate the P&O method, a wind turbine system including an induction generator and an MC, with small inertia, is considered. Selected simulation results obtained from the low-power wind turbine system under study are presented in this section; the detailed explanations are given in [106]. Note that in [106], instead of a conventional MC, an improved MC topology which does not have any commutation problems was adopted for the small wind turbine system. The MC state-space dynamic model that was developed in Chapter 2 is a valid model for the improved MC.

The structure of the system is the same as in Fig. 5-6, except for the controller which is based on P&O method. The system parameters are shown in Appendix L. To assess the capability of the P&O method in tracking the maximum power point at varying wind velocity, a step change is applied to the wind velocity. The system is first operating at the wind velocity of $V_{w1}$=8m/s. At this velocity, the optimal power captured from the wind turbine is 37kW. At $t$=1.8s, the wind velocity is decreased to 6m/s. The optimal power corresponding to this velocity is 15kW. Again, at $t$=2.5s, the wind velocity is increased back to 8m/s. Fig. 5-10 illustrates successful tracking of maximum power using the P&O method following the changes made to the wind velocity. Fig. 5-11 shows the variations in the matrix converter output frequency set-point that results in the necessary changes in the induction generator terminal frequency and thus the shaft speed in attempt to track the maximum power point. It has to be noted that the magnitude of the induction generator terminal voltage has been varied with frequency according to the constant $V/f$ strategy. Also, the displacement power factor at the interface with the grid has been maintained at unity at steady-state, using matrix converter control.

As mentioned, this method does not require priori knowledge of maximum wind turbine power at different wind velocities, and induction machine parameters. Also, using this method, maximum power point can be reached irrespective of the present operating point, while maintaining the operation in the stable generating region during transitions.
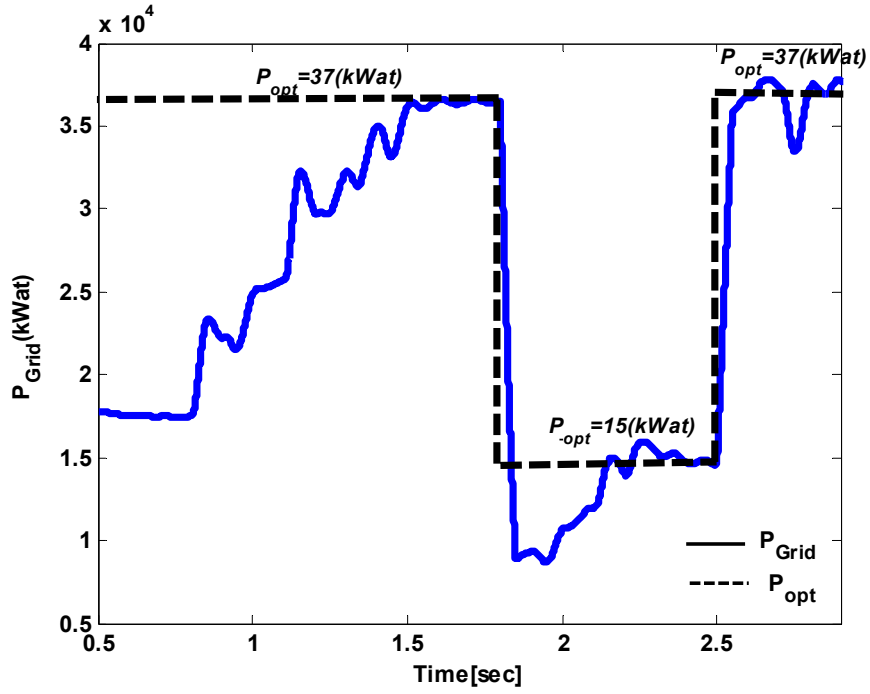
Fig. 5-10: Maximum power point tracking control at varying wind velocity with P&O method
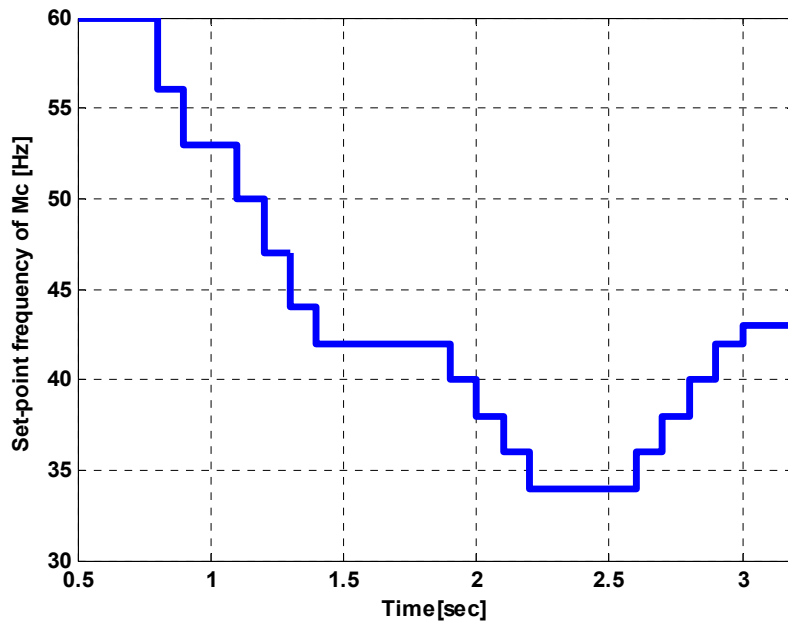


Fig. 5-11: Frequency set point variations during maximum power point tracking with P&O method

## 5.5 Implementing the Mechanical Speed-Sensorless PSF Method on the Wind Turbine System under Study

In this section, simulation results of the wind turbine system under study including the mechanical speed-sensorless power signal feedback are presented. The parameters of the wind turbine system are given in Appendix L.

To implement the mechanical speed-sensorless PSF method, based on block diagram Fig. 5-6, first, the curves $T_{opt}(\omega_g)$ (Fig. 5-7) and $T_{opt}(\omega_s , \omega_g)$ (equations (5.6) and (5.7)) should be determined. Second, the lookup table data can be obtained based on flowchart of Fig. 5-9.

In the wind turbine system, it is easier to measure the grid power instead of the power at the generator output terminals. Therefore, for implementing the speed-senseless PSF method on the system, the grid optimal power, $P_{Grid\_opt}$ , should be entered in the lookup table. The $P_{Grid\_opt}(\omega_s)$ curve can be calculated by subtracting MC active power losses from the $P_{gen\_opt}$ at each synchronous frequency. Fig. 5-12 shows the curves $P_{T\_opt}$-versus-$\omega_s$ and $P_{Grid\_opt}$-versus-$\omega_s$ for the system under study.
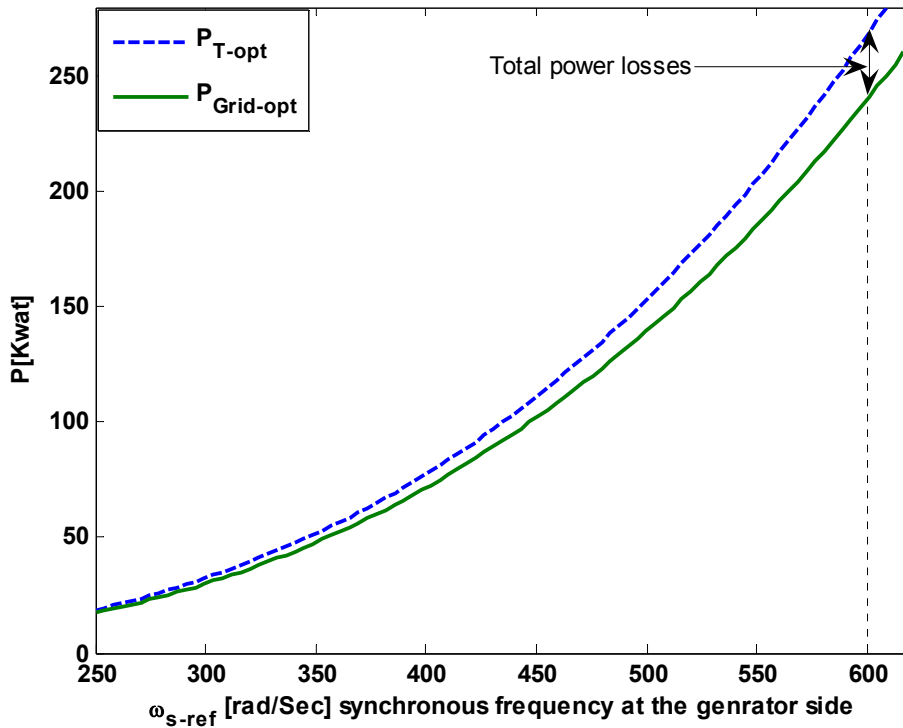


Fig. 5-12: $P_{Topt}(\omega_s)$ and $P_{Grid\_opt}(\omega_s)$ curves

The schematic diagram of the wind turbine system with the speed sensor-less PSF, in Matlab/Simulink environment, is shown in Fig. 5-13.
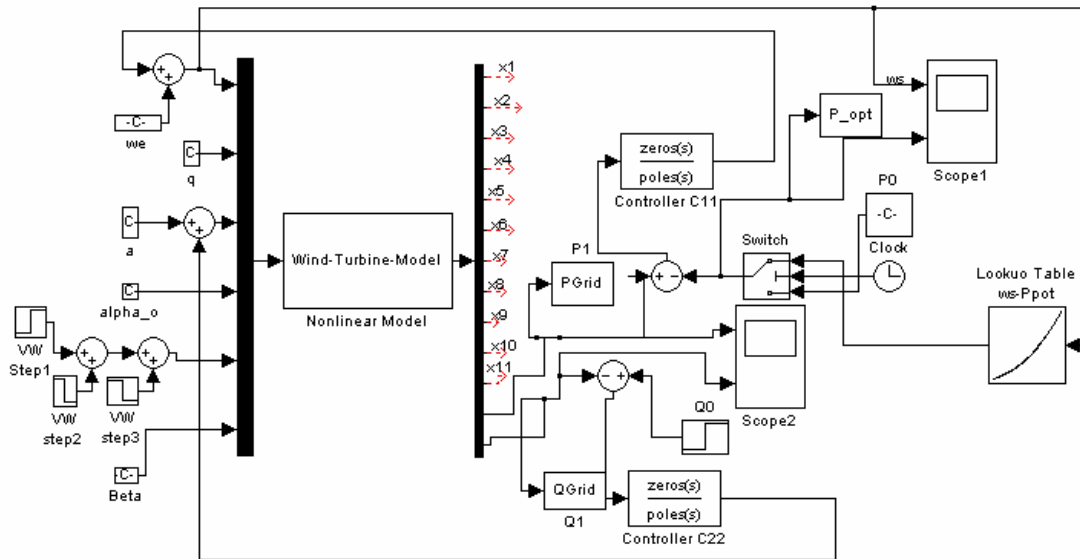


Fig. 5-13: Block diagram of the wind turbine system with the mechanical speed-sensorless PSF in Matlab/Simulink

The system is originally stable at an operating point with wind velocity of 10 m/s before applying the maximum power point tracking (MPPT) method. Table 5.1 shows the input and output parameters of the system at the operating point.

Table 5.1: Parameters of the wind turbine system at the operating point

| Voltage Gain | Output voltage angle | MC output frequency | Rotor pitch angle | Wind speed | Grid powers |
|---|---|---|---|---|---|
| $q=0.5$ | $\alpha_o=0$ | $f_{o\_MC}=60$ Hz | $\beta=0$ | $V_W=10$[m/s] | $P_{Grid}=80.82$[kWat] $Q_{Grid}=56.42$[kVar] |

In the following simulations, the mean wind velocity will be changed to verify the capability of the MPPT method used. Table 5.2 shows the maximum mechanical wind power and the grid

active power reference for three different wind velocities. The controller should follow the maximum power at each wind velocity.

Table 5.2: Maximum Power at different wind velocity

| Wind velocity [m/s] | WT Maximum Power [kWat] | Grid Maximum Power [kWat] |
|---|---|---|
| $V_W$=10 | $P_{Topt}$= 86.39 | $P_{Grid,opt}$= 84.96 |
| $V_W$=11 | $P_{Topt}$= 114.99 | $P_{Grid,opt}$= 113.11 |
| $V_W$=12 | $P_{Topt}$= 149.29 | $P_{Grid,opt}$= 146.81 |

Note that in Table 5.2, the discrepancy between the wind turbine and the grid maximum power is because of the system total losses.

Fig. 5-14 depicts the grid active power of the wind turbine system with the speed-sensorless PSF at three wind velocities. The system works at the operating point, Table 5.1, initially. The MMPT algorithm has stabilized the system at maximum power point corresponding to wind velocity equals 10 m/s. Mean wind velocity is then increased to 12 m/s at $t$=30s, decreased to 11m/s at t=60s, and finally decreased to 10 m/s at $t$=90s. The wind turbine system tracks the maximum power corresponding to different wind velocities successfully. At the same time, the grid reactive power and synchronous speed of induction generator are controlled by the MC. The reactive power of the grid is kept almost constant by the MC as shown in Fig. 5-15. Fig. 5-16 and Fig. 5-17 illustrate the electrical synchronous speed of the generator, which is adjusted by the MC, and the mechanical shaft speed of the turbine, respectively, in response to the wind velocity variations.

Also, as shown in Fig. 5-14, the settling time of the system with the MPPT method, for the step change, is about 8s. In other words, the system can track the maximum power point for the mean wind speed changes that take place at frequencies lower than approximately 1/8 Hz.
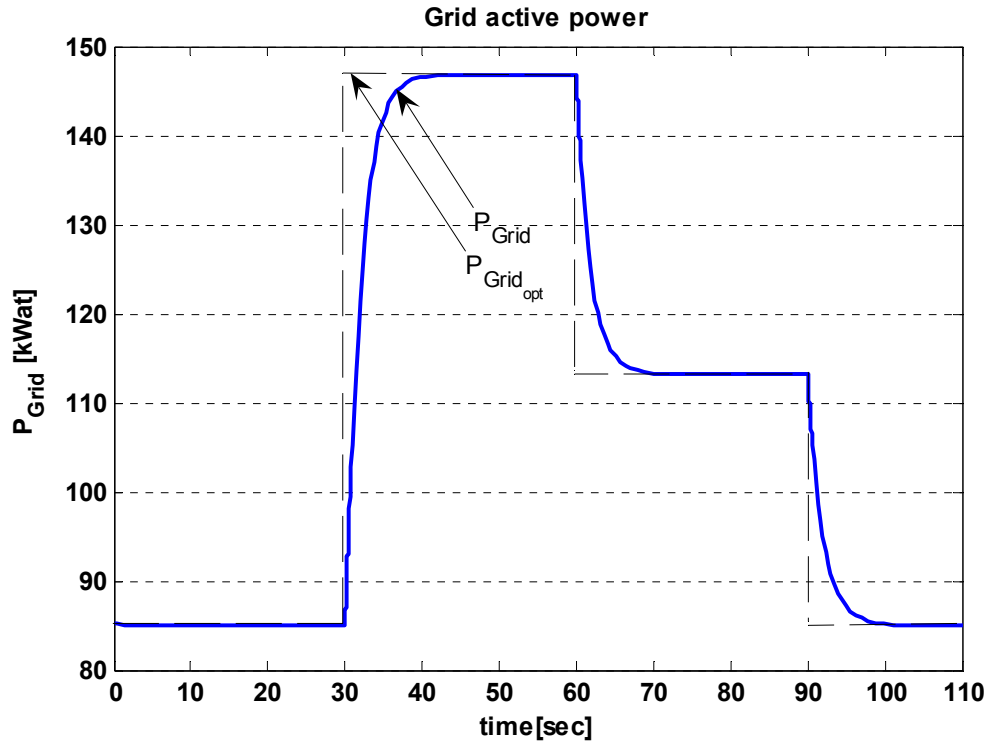
**Grid active power**



Fig. 5-14: Grid active power for the wind turbine system including speed-sensorless PSF method
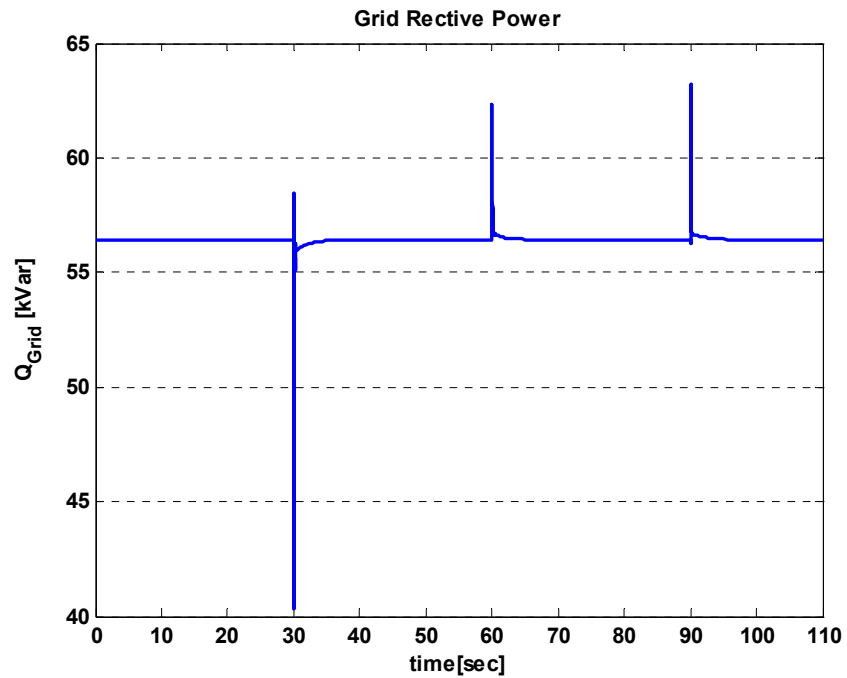
**Grid Rective Power**



Fig. 5-15: Grid reactive power for the wind turbine system including speed-sensorless PSF method

162
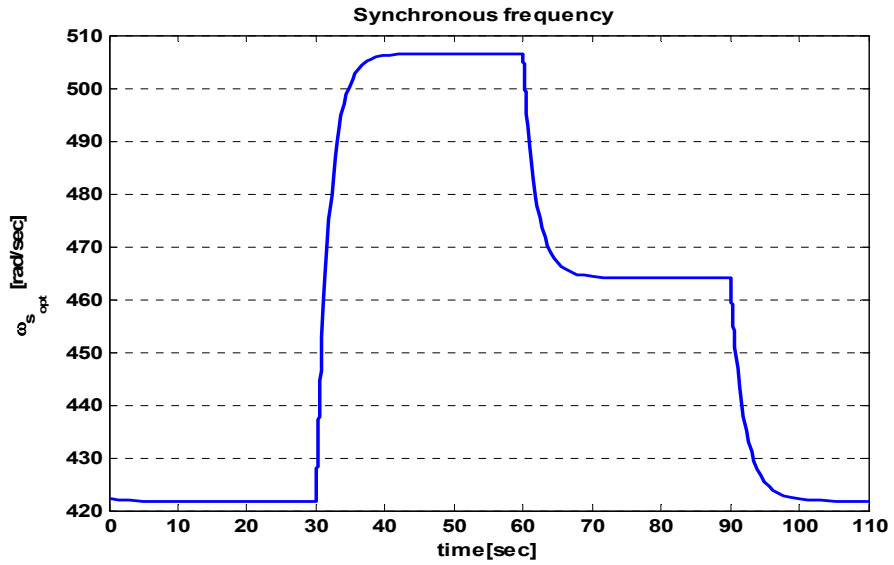
Fig. 5-16: Synchronous frequency at induction generator terminals for the wind turbine system including speed-sensorless PSF method
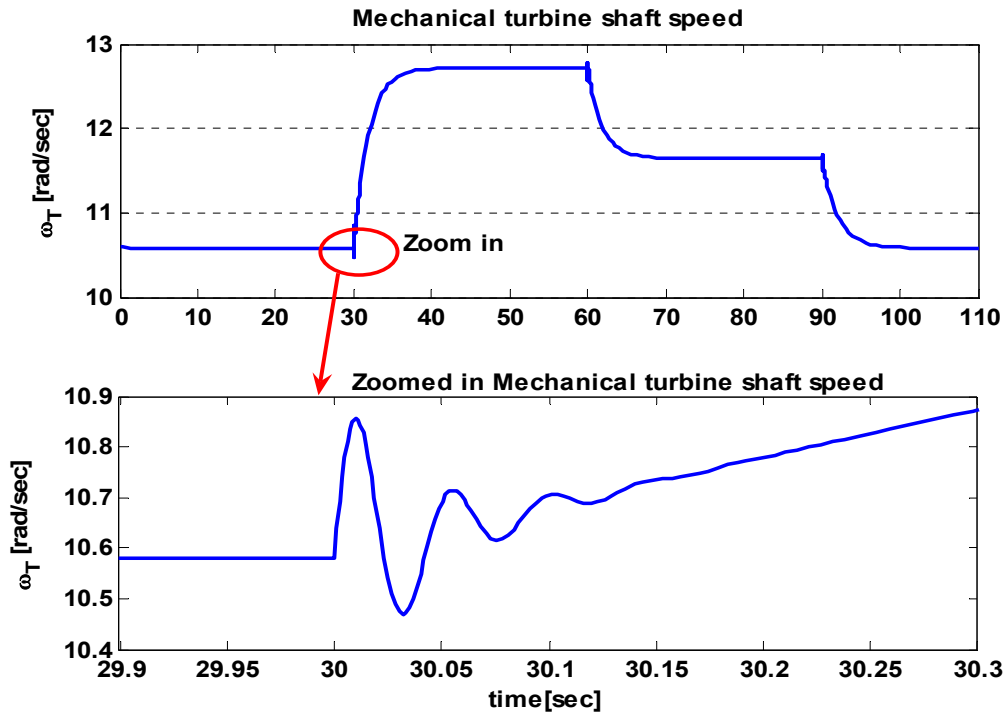


Fig. 5-17: Turbine shaft mechanical speed for the wind turbine system including speed-sensorless PSF method

Fig. 5-18 shows the range of variation of wind speed over which maximum power point can be successfully tracked. Accordingly, the minimum wind speed at which the wind turbine injects active power into the grid, is 3m/s corresponding to maximum grid power of 1.04kW. The maximum wind speed limit of the system is 22m/s corresponding to a maximum grid power of 838.82kW. Therefore, the system with the adopted MPPT method is capable of tracking the maximum power in response to a step decrease to $V_W$=3m/s and a step increase $V_W$=22m/s from the operating point ($V_W$=10m/s, $P_{Grid,opt}$=84.96kW). At wind velocities below 3m/s, the direction of the active power flow will be from the grid to the wind turbine because the electrical machine operates in motoring mode. If the wind speed exceeds 22m/s, the controller will not be able to track maximum power.
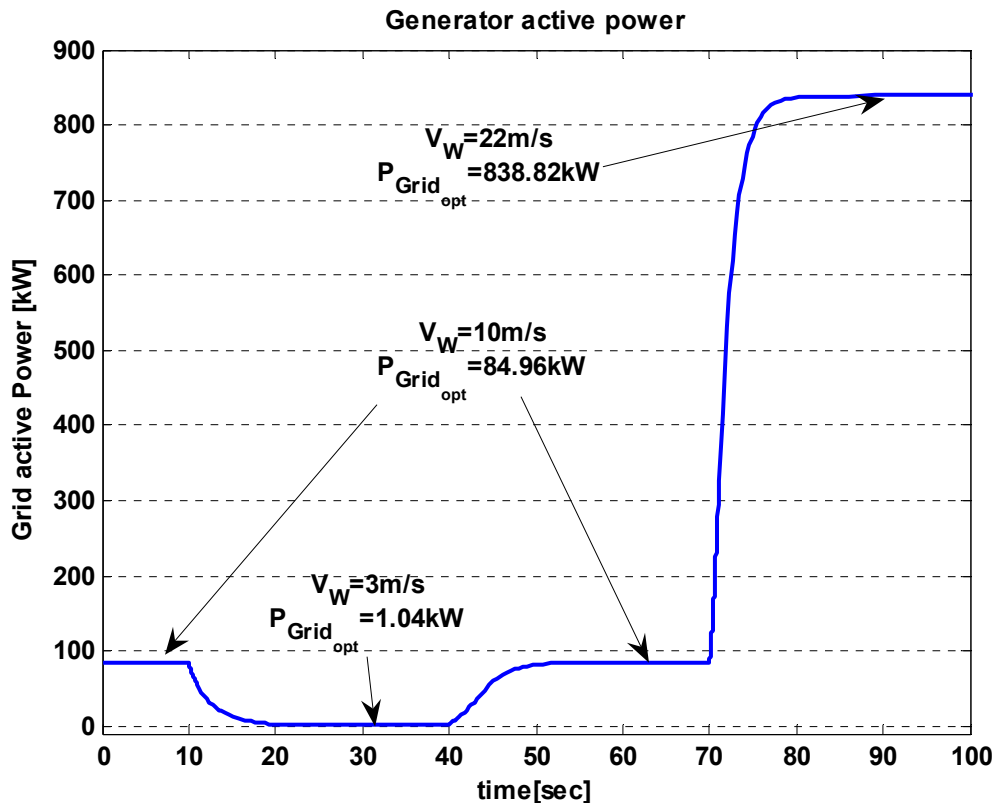


Fig. 5-18: Maximum and minimum levels of grid active power for the wind turbine system including speed-sensorless PSF method

The simulation results show that the controller including the mechanical sensorless PSF method has a high capability to track the maximum power point at different wind velocities. However, accuracy of the method depends on the data obtained for the lookup table.

## 5.5.1 Evaluation of the Mechanical Speed-sensorless PSF method with the instantaneous wind velocity

In Subsection 3.2.6, the wind velocity model was described as the wind speed average value plus a stochastic fluctuation of the wind velocity, equation (3.23). Also, the high-frequency damping phenomenon was considered in the final wind velocity model to be used in the wind turbine model, as shown in Fig. 3-12.

In the previous simulations of Section 5.5, the wind velocity was considered to be a constant signal with some step changes. In this subsection, the controller including the speed-sensorless PSF method is evaluated with an instantaneous wind velocity model. The wind velocity signal ($V_W$) and the grid active response ($P_{Grid}$), as well as the optimal synchronous speed, are depicted in Fig. 5-19. As shown in this figure, the mean value of the instantaneous wind velocity is increased from 10m/s to 11m/s at $t$=20s. In each instance, the system follows the instantaneous wind velocity variations and the controller leads the system toward the maximum power point based on the mean wind velocity. The simulation results reveal that the controller including the speed-sensorless PSF method is capable of working with the instantaneous wind velocity.
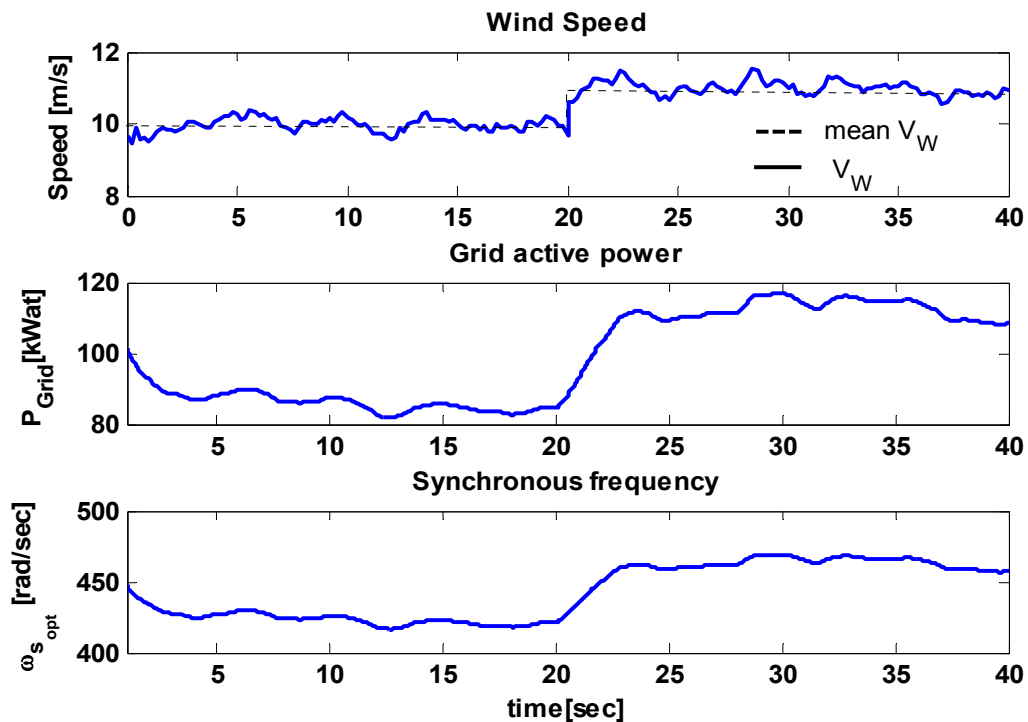


Fig. 5-19: Evaluating the system including the speed-sensorless PSF method with the instantaneous  wind model

## 5.6 Summary

This chapter presented a maximum power point tracking (MPPT) method for the proposed wind turbine system. The controller including the MPPT method controls the shaft speed to maximize the power captured from the wind. This is possible by adjusting the MC output frequency. The output voltage is adjusted according to constant *V/f* strategy. The controller also adjusts the MC variables to control the reactive power transfer at the grid interface to regulate the power factor.

The concepts of three MPPT methods, Perturbation and Observation (P&O), Wind Speed Measuring (WSM), and Power Signal Feedback (PSF) are reviewed.

The P&O method is a continuous search algorithm to track the maximum power point. The P&O method does not require prior knowledge of the maximum wind turbine power at different wind velocities, or electrical machine parameters. However, this method is suitable for wind turbine systems with very small inertia that can respond quickly to shaft speed change requests.

The wind speed measurement (WSM) method regulates the shaft speed to keep the turbine at an optimal tip-speed-ratio ($\lambda_{opt}$). In this method, both wind velocity and shaft speed ($\omega_T$) should be measured. Also, $\lambda_{opt}$ must be given to the controller. This method suffers two drawbacks: difficulty of measuring the wind velocity and dependence of $\lambda_{opt}$ on the wind turbine characteristics.

In the PSF method, the controller should be aware of the wind turbine maximum power versus shaft speed curve. In this method, the maximum power is tracked by the shaft speed measurement only and no wind velocity measurement is required. However, the difficulty of obtaining the maximum power curve of the wind turbine, and measuring the mechanical shaft speed and wind turbine output power are the drawbacks of the PSF method.

A developed power signal feedback method, called speed-sensorless PSF, is proposed for the wind turbine system under study to improve the PSF method. The method needs neither a wind velocity sensor nor a turbine speed sensor. Simulation results show successful tracking of maximum power at all wind velocities.

# Chapter 6

# Conclusions

## 6.1 Summary and conclusions

In this thesis, a wind energy conversion system including a matrix converter (MC) is proposed. A squirrel-cage induction generator (SCIG) is selected because of its low-cost, robustness and high reliability for wind turbines. The wind turbine is followed by a gearbox which steps up the shaft speed. MC interfaces the SCIG with the grid and transfers the entire power generated by the wind turbine to the grid. Also, MC controls the terminal voltage and frequency of the induction generator, based on a constant *V/f* strategy, to adjust the turbine shaft speed, and accordingly, control the active power injected into the grid to track maximum power at all wind velocities. The power factor at the interface with the grid is also controlled by MC to either ensure purely active power injection into the grid for optimal utilization of the installed wind turbine capacity or assist in regulation of voltage at the point of connection. Furthermore, the reactive power requirements of the induction generator are satisfied by MC to avoid use of self-excitation capacitors.

A dynamic model that represents the proposed system and a closed-loop controller to track the desired active and reactive powers delivered to the grid are developed. The desired power is used as the reference for the closed-loop control of the power injected into the grid. The controller uses an algorithm to derive the maximum power that can be achieved at a given wind velocity. In order to track maximum power, MC adjusts the induction generator terminal frequency, and thus the turbine shaft speed. MC adjusts the reactive power transfer at the grid interface to achieve voltage regulation or power factor correction.

Chapter 2 introduces MC and its overall dynamic model. An MC is highly controllable and allows independent control of the output voltage magnitude, frequency, and phase angle, as well as the input power factor. Compared with the DC-link AC/AC converter systems, an advantage of

the MC is elimination of the DC-link, including bulky capacitors. Furthermore, the MC structure is inherently capable of a four-quadrant operation. The developed dynamic model consists of six nonlinear equations in the same frequency frame. The final state-space *qdo* dynamic model contains six state variables and four control variables. Input and output active and reactive power formulas are developed based on the model state variables. To evaluate the MC state-space *qdo* dynamic model, first the model is simulated with Matlab/Simulink; then, the results are compared with the simulation results of a model based on the MC fundamental-frequency equivalent circuit, obtained from the PSIM simulation package. The results of the two models are fairly close. The presented state-space model is comprehensive in the sense that it includes output voltage magnitude, frequency and phase angle, as well as input displacement power factor, as control variables. The proposed model can be used effectively in modeling electrical systems including MC, for transient study, stability analysis, and systematic controller design.

Chapter 3 focuses on developing a comprehensive dynamic mathematical model of the proposed wind turbine system to be used for controller design purposes. Detailed mathematical models of the mechanical aerodynamic conversion, drive train, and squirrel-cage induction generator are developed and combined with the MC model to enable steady-state and transient simulations of the overall system. To avoid saturation of the induction machine when the stator frequency is changed, the dynamic model is modified based on the constant *V/f* strategy. Steady-state response of the model shows that the grid active and reactive power vary with the MC output frequency. But, by varying the parameter that controls the displacement power factor, only the grid reactive power is affected. Dynamic behavior of the model is investigated by simulating the step responses to selected input variables.

Moreover, a linearized model of the wind turbine system is developed around an operating point. The results show the local stability of the open loop system against the input variations around the operating point. However, the step response of the system shows a type of nonminimum-phase behaviour. The controllability and observability are evaluated at the operating point and a reduced-order model that has performance close to the original model is developed. It is concluded that the linear model is an appropriate model for the design of a controller to improve the steady-state and transient performances of the system.

Chapter 4 is dedicated to the design of a closed-loop feedback controller based on the linear model to track the desired active and reactive powers delivered to the grid. Two control design methods are adopted for the wind turbine system: a state-feedback and an output-feedback controller. In the state-feedback closed-loop system, first an integrator is added after the system

model to achieve zero steady-state error for the step response. Then, the state-feedback controller is designed based on the LQ method. The LQ method is effective for adjusting the parameters of the closed-loop controller. A genetic algorithm (GA) is used to determine the weighting matrices of the LQ method to locate the closed-loop eigenvalues as close to the desired values as possible. The simulation results reveal that the system with the closed-loop controller, designed by LQ and GA method, can satisfy the design constraints. Moreover, an observer is designed and used in the state-feedback loop. The simulation results show that the observer affects the system transients, but it has no effect on the steady-state (tracking) response. However, the gain and phase margins are dramatically decreased when the observer is added to the system.

Two other approaches to design of the controller based on transfer function techniques are adopted: DC decoupling and a sequential loop closure (SLC). The controller designed with DC decoupling approach yields a low-gain controller that causes a long settling time that is not acceptable. The simulation results with the SLC controller show good tracking and disturbance rejection, as well as reasonable sensor noise rejection and stability robustness, for both linear and nonlinear versions of the proposed model. In addition, the simulation results with SLC closed-loop controller show that the frequency control signal strongly affects the active power, while the input power factor control signal is almost constant during real power changes.

Chapter 5 presents the maximum power point tracking (MPPT) based on two methods: Perturbation and Observation (P&O), and Power Signal Feedback (PSF). The P&O method is a continuous search algorithm to track the maximum power point. The P&O method does not require prior knowledge of the maximum wind turbine power at different wind velocities and electrical machine parameters. However, this method is suitable for wind turbine systems with very small inertia, that can respond quickly to shaft speed change requests. In the PSF method, the controller should be aware of the wind turbine maximum power versus shaft speed curve. In this method, the maximum power is tracked by shaft speed measurement only, and no wind velocity measurement is required. However, the difficulty of obtaining the maximum power curve of the wind turbine, as well as measuring the mechanical shaft speed and wind turbine output power are the drawbacks of the PSF method. A developed power signal feedback method, called speed-sensorless PSF, is proposed for the wind turbine system under study to improve the PSF method. The method needs neither a wind velocity sensor nor a turbine speed sensor; but, it needs the maximum power curve of the wind turbine. Simulation results show successful tracking of maximum power at all wind velocities.

## 6.2 Contributions

The focus of this thesis is on three main issues:

- Developing a dynamic model for MC and the proposed wind energy conversion system,

- Designing a closed-loop controller for the proposed system, and

- Developing a maximum power point tracking method for the system under study.

This research is novel because it proposes the use of an MC in a wind turbine system and develops a dynamic overall model and a maximum power point tracking controller for the proposed wind turbine system.

The following outline the contributions of this thesis:

1. A wind energy conversion system based on an induction generator and a matrix converter, that has not been thoroughly investigated before, is proposed.

2. A comprehensive state-space *qdo* dynamic model is developed for the MC. The main contribution in this model is to include a control variable for input displacement power factor. The model could be used effectively in modeling electrical systems including MC, for transient study, stability analysis, and systematic controller design.

3. In the modeling of the proposed wind turbine system, the main contribution of this work is developing an overall model that considers all electrical and mechanical control variables. The model contains four control variables related to the MC and one for turbine blade pitch angle control, and considers wind velocity as a disturbance input. Another contribution in this part is to modify the dynamic model based on a constant *V/f* strategy to avoid saturation of the induction machine when the induction generator stator frequency is changed.

4. In the linearized model, the main contribution is developing a reduced-order model of the system based on the linearized model with a performance as close as possible to the original model.

5. In the closed-loop state-feedback controller design, the main contribution of this work is using the genetic algorithm (GA) in the linear-quadratic (LQ) method to satisfy the design constraints perfectly.

6. For the proposed wind turbine, an output-feedback controller is designed based on an SLC method. The main contribution of this part is adopting a simple method for designing the

controller, first by ignoring a weak cross-channel coupling, and second by approximating a channel by a second-order system and designing a PI controller. The designed controller has a good transient and tracking performance, disturbance and sensor noise rejection, and stability robustness.

7. In the maximum power point tracking controller design, the main contribution of this work is to develop a method for the proposed system which needs neither a wind velocity sensor nor a turbine shaft speed sensor. In this method, the electrical power injected to the grid is the only measurement in the closed-loop system.

## 6.3 Suggestions for Future work

To continue and complete the work presented in this dissertation, one can focus on a number of specific areas as follows:

- **Experimental Test**

A laboratory prototype of the proposed wind energy conversion system can be built and tested to verify the validity of the developed dynamic model.

- **Multilevel Matrix Converter**

A multilevel MC is scalable to higher power and voltage levels. The purpose of using multilevel MC is to improve the energy capture of the wind turbine. Studying the configuration and switching strategy of multilevel MC, and developing a dynamic model of a wind turbine system including a multilevel MC are suggested.

- **Robust Control of the Wind Turbine System**

To identify the wind turbine model parameters, the wind speed statistics should be collected at each operating point during long intervals. The developed model is subject to parameter uncertainty. In order to cope with the model uncertainties and design a controller accordingly, the techniques of linear robust control theory should be used.

- **Using Permanent Magnet (PM) Generator in the Proposed System**

The progress in the permanent magnet materials fabrication has extended the PM generator lifetime and decreased the production cost. This is a motivation for replacing the induction generator (and gearbox) with a PM generator.

- **Intelligent Maximum Power Point Tracking (MPPT) Algorithm**

An intelligent algorithm can be developed for MPPT with the following features:

- independent of the wind turbine characteristics, and thus flexible and effective, and

- trainable online to behave adaptively.

# Appendix A

# Practical Bidirectional Switch Configuration for the Matrix Converter

For many years, thyristor have been the preferred semiconductor switch in power electronic converters. To realize a bidirectional switch, two thyristors have to be connected in antiparallel.

In order to turn off the thyristor, force-commutating circuits should be used. This results in increased size and complexity of circuits. As a result of development the new generation of inherent gate-turn-off switches such as GTO, BJT, MOSFET and IGBT, as well as increasing their power ratings, these switches have become a better choice than the thyristor. In order for an MC to have capability of four-quadrant operation, bidirectional or four-quadrant switches are required.

A four-quadrant switch is capable of blocking voltages of both polarities in OFF-state and conducting currents in both directions in ON-state. Currently, there is no monolithic switch in the market with this capability. In practice, the four-quadrant switch can be realized using power diodes and gate-turn-off switches.

Fig A-1 illustrates three practical methods of realizing bidirectional switches with power diodes and insulated bipolar junction gate transistor (IGBT). Table A-1 compares the three bidirectional switch structures, i.e. diode bridge, common emitter and common collector. Among these three possible bidirectional switch structures, the common-emitter configuration has minimized stray inductance and is usually preferred in practice [97][98].
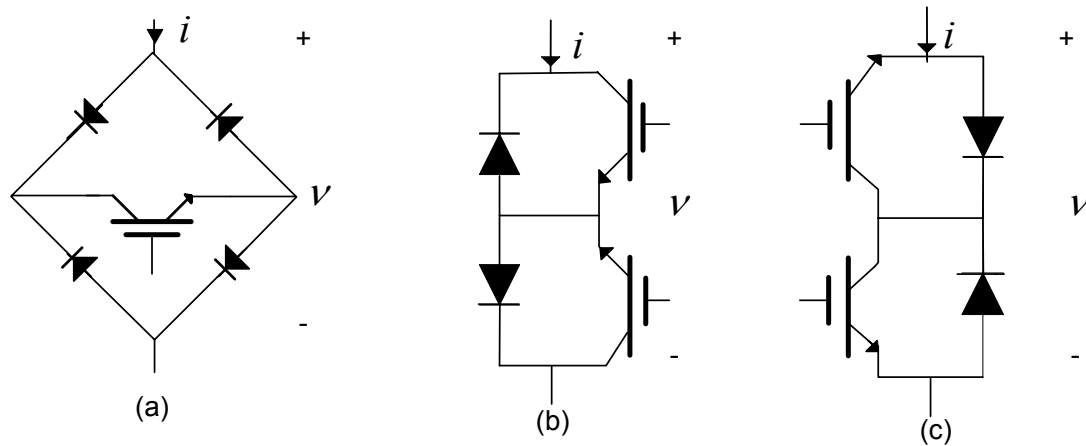
Fig. A-1: Three practical bidirectional switch configurations: (a) Diode bridge and one switch (b) Common emitter and (c) common collector

Table A-1 comparison of bidirectional switch structures [97][98]

| Structure | Number of components | Advantages | Disadvantages |
|---|---|---|---|
| **Diode Bridge and one switch** | *4 diodes*<br>*1 switch* | *One gate drive per switch cell* | *-High device losses*<br>*-No control on the direction of current by switch* |
| **Common emitter** | *2 diodes*<br>*2 switches* | *Independent control of the direction of current* | *High number of isolated power supplies for the gate drives in MC models* |
| **Common collector** | *2 diodes*<br>*2 switches* | *Reduce the number of isolated power supplies for the gate drives in MC module* | *High stray inductance* |

A MC circuit may be constructed from the bidirectional switch cell with discrete components. It is also feasible to build a MC in a package with IGBT modules. The technology has moved in the direction of developing a practical full MC power circuit in a single package. Some types of single-package MC are now commercially available.

# Appendix B

# Switch State Combinations in MC

Table B-1: 27 Switch state combinations in MC[55]

| Group | Switches 'ON' | | | $V_{AB}$ | $V_{BC}$ | $V_{CA}$ | $i_a$ | $i_b$ | $i_c$ |
|---|---|---|---|---|---|---|---|---|---|
| I | $S_{Aa}$ | $S_{Bb}$ | $S_{Cc}$ | $v_{ab}$ | $v_{bc}$ | $v_{ca}$ | $i_A$ | $i_B$ | $i_C$ |
| | $S_{Aa}$ | $S_{Bc}$ | $S_{Cb}$ | $-v_{ca}$ | $-v_{bc}$ | $-v_{ab}$ | $i_A$ | $i_C$ | $i_B$ |
| | $S_{Ab}$ | $S_{Ba}$ | $S_{Cc}$ | $-v_{ab}$ | $-v_{ca}$ | $-v_{bc}$ | $i_B$ | $i_A$ | $i_C$ |
| | $S_{Ab}$ | $S_{Bc}$ | $S_{Ca}$ | $v_{bc}$ | $v_{ca}$ | $v_{ab}$ | $i_C$ | $i_A$ | $i_B$ |
| | $S_{Ac}$ | $S_{Ba}$ | $S_{Cb}$ | $v_{ca}$ | $v_{ab}$ | $v_{bc}$ | $i_B$ | $i_C$ | $i_A$ |
| | $S_{Ac}$ | $S_{Bb}$ | $S_{Ca}$ | $-v_{bc}$ | $-v_{ab}$ | $-v_{ca}$ | $i_C$ | $i_B$ | $i_A$ |
| II-A | $S_{Aa}$ | $S_{Bc}$ | $S_{Cc}$ | $-v_{ac}$ | $0$ | $v_{ca}$ | $i_A$ | $0$ | $-i_A$ |
| | $S_{Ab}$ | $S_{Bc}$ | $S_{Cc}$ | $v_{bc}$ | $0$ | $-v_{bc}$ | $0$ | $i_A$ | $-i_A$ |
| | $S_{Ab}$ | $S_{Ba}$ | $S_{Ca}$ | $-v_{ab}$ | $0$ | $v_{ab}$ | $-i_A$ | $i_A$ | $0$ |
| | $S_{Ac}$ | $S_{Ba}$ | $S_{Ca}$ | $v_{ca}$ | $0$ | $-v_{ca}$ | $-i_A$ | $0$ | $i_A$ |
| | $S_{Ac}$ | $S_{Bb}$ | $S_{Cb}$ | $-v_{bc}$ | $0$ | $v_{bc}$ | $0$ | $-i_A$ | $i_A$ |
| | $S_{Aa}$ | $S_{Bb}$ | $S_{Cb}$ | $-v_{ab}$ | $0$ | $-v_{ab}$ | $i_A$ | $-i_A$ | $0$ |
| II-B | $S_{Ac}$ | $S_{Ba}$ | $S_{Cc}$ | $v_{ca}$ | $-v_{ca}$ | $0$ | $i_B$ | $0$ | $-i_B$ |
| | $S_{Ac}$ | $S_{Bb}$ | $S_{Cc}$ | $-v_{bc}$ | $-v_{bc}$ | $0$ | $0$ | $i_B$ | $-i_B$ |
| | $S_{Aa}$ | $S_{Bb}$ | $S_{Ca}$ | $-v_{ab}$ | $-v_{ab}$ | $0$ | $-i_B$ | $i_B$ | $0$ |
| | $S_{Aa}$ | $S_{Bc}$ | $S_{Ca}$ | $-v_{ca}$ | $v_{ca}$ | $0$ | $-i_B$ | $0$ | $i_B$ |
| | $S_{Ab}$ | $S_{Bc}$ | $S_{Cb}$ | $v_{bc}$ | $-v_{ab}$ | $0$ | $0$ | $-i_B$ | $i_B$ |
| | $S_{Ab}$ | $S_{Ba}$ | $S_{Cb}$ | $-v_{ab}$ | $v_{ab}$ | $0$ | $i_B$ | $-i_B$ | $0$ |
| II-C | $S_{Ac}$ | $S_{Bc}$ | $S_{Ca}$ | $0$ | $v_{ca}$ | $-v_{ca}$ | $i_c$ | $0$ | $-i_C$ |
| | $S_{Ac}$ | $S_{Bc}$ | $S_{Cb}$ | $0$ | $-v_{bc}$ | $-v_{bc}$ | $0$ | $i_C$ | $-i_C$ |
| | $S_{Aa}$ | $S_{Ba}$ | $S_{Cb}$ | $0$ | $-v_{ab}$ | $-v_{ab}$ | $-i_C$ | $i_C$ | $0$ |
| | $S_{Aa}$ | $S_{Ba}$ | $S_{Cc}$ | $0$ | $-v_{ca}$ | $v_{ca}$ | $-i_C$ | $0$ | $i_C$ |
| | $S_{Ab}$ | $S_{Bb}$ | $S_{Cc}$ | $0$ | $v_{bc}$ | $-v_{ab}$ | $0$ | $-i_C$ | $i_C$ |
| | $S_{Ab}$ | $S_{Bb}$ | $S_{Ca}$ | $0$ | $-v_{ab}$ | $v_{ab}$ | $i_C$ | $-i_C$ | $0$ |
| III | $S_{Aa}$ | $S_{Ba}$ | $S_{Ca}$ | $0$ | $0$ | $0$ | $0$ | $0$ | $0$ |
| | $S_{Ab}$ | $S_{Bb}$ | $S_{Cb}$ | $0$ | $0$ | $0$ | $0$ | $0$ | $0$ |
| | $S_{Ac}$ | $S_{Bc}$ | $S_{Cc}$ | $0$ | $0$ | $0$ | $0$ | $0$ | $0$ |

Based on Table B.1, the connections between input and output phases of MC can be classified in three groups with different properties, as illustrated in Table B.2.

Table B.2: Classifications of switch state combinations of Table B.1

| | Number of combinations | Special Feature |
|---|---|---|
| Group I | 6 combinations | Each output phase is connected to a different input phase |
| Group II | $3 \times 6$ combinations | Two output phases are shorted |
| Group III | 3 combinations | Three output phases are shorted |

# Appendix C

# Modulation Algorithm and SVPWM

There are two major modulation algorithms in the literature for controlling the switches in an MC, i.e., direct and indirect methods [60].

## C.1  Direct switching matrix approach

A transformation matrix $D$, whose elements are sinusoidal functions at frequency $\omega_o \pm \omega_i$, makes a direct connection between the input and output voltages and currents of MC. Thus, this method is named direct method. In this method, one can prove that the maximum voltage gain is restricted to 0.5 instead of 0.87 [60]. Improving the feasible voltage ratio to 0.87 is possible by injecting the third harmonics of the input and output frequencies into the desired output phase voltages as shown in equation (C.1).

$$\overline{v}_{ABC} = V_{om} \begin{bmatrix} \cos(\omega_o t) \\ \cos(\omega_o t - 2\pi/3) \\ \cos(\omega_o t + 2\pi/3) \end{bmatrix} + \begin{Bmatrix} -\dfrac{1}{6}\cos(3\omega_o t) + \dfrac{1}{2\sqrt{3}}\cos(3\omega_i t) \\ -\dfrac{1}{6}\cos(3\omega_o t) + \dfrac{1}{2\sqrt{3}}\cos(3\omega_i t) \\ -\dfrac{1}{6}\cos(3\omega_o t) + \dfrac{1}{2\sqrt{3}}\cos(3\omega_i t) \end{Bmatrix} \tag{C.1}$$

where $\overline{v}_{ABC}$ is the MC output voltage vector, $V_{om}$ is the peak value of MC output voltage, and $\omega_i$ and $\omega_o$ are the input and output MC frequencies, respectively. These additional injected harmonics are called common-mode voltages. Even though common-mode voltages cause nonsinusoidal output phase voltages, they have no effect on the output line-to-line voltages and allow the desired voltage gain to increase to 87% [60][65][99]. Adding the common-mode voltages makes analysis and implementing the direct switching matrix method difficult. It is worth mentioning that this method uses all combinations of the three groups in Table B.2.

**C.2 Indirect switching matrix approach**

The indirect switching matrix approach or indirect modulation is based on a simplified modulator model, making it feasible to implement classical PWM methods for MCs [55][97][99]. This method is based on the fact that the MC, and its transfer switching matrix, are considered as an imaginary two-stage transformation: rectification stage and inverter stage. In the rectification stage, a fictitious dc link with a dc voltage of constant local average will be provided. Then, the fictitious dc voltage is converted to the three-phase output voltages in inverter stage. One solution for the transformation matrix $D$ is as follows:

$$D = m. \begin{bmatrix} \cos(\omega_o t + \varphi_o) \\ \cos(\omega_o t + \varphi_o - 2\pi/3) \\ \cos(\omega_o t + \varphi_o + 2\pi/3) \end{bmatrix} \begin{bmatrix} \cos(\omega_i t - \varphi_i) \\ \cos(\omega_i t - \varphi_i - 2\pi/3) \\ \cos(\omega_i t - \varphi_i + 2\pi/3) \end{bmatrix}^T = D_I(\omega_o).D_R^T(\omega_i) \qquad (C.2)$$

In the above transformation matrix the $D_I(\omega_o)$ is the 3×1 inverter transfer matrix which is a function of output frequency, and the $D_R(\omega_i)$ is the 3×1 rectifier transfer matrix which is a function of input frequency. The concept of the indirect method is illustrated in Fig. C-1 by six imaginary switches for the rectifier part and six imaginary switches for the inverter part.
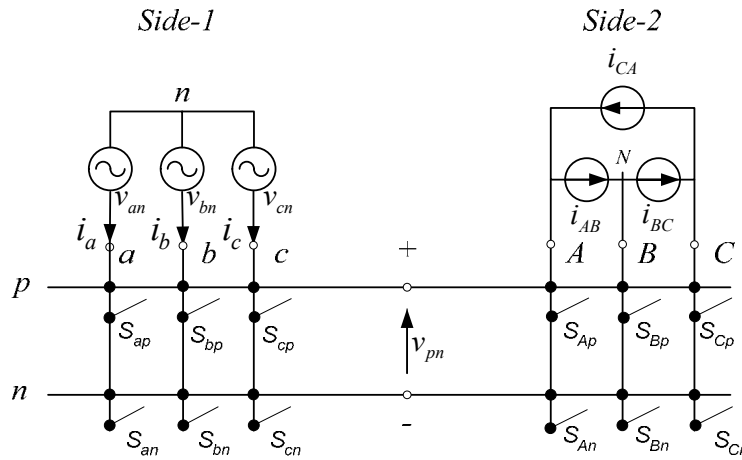


Fig. C-1: Two- stage MC with fictitious dc-link

To make the concept of fictitious dc voltage clear, one can multiply the input ac voltage vector from (3-11) by $D_R^T(\omega_i)$. Then, a constant equivalent dc voltage is obtained as follow:

Appendix C. Modulation Algorithm…

$$D_R^T(\omega_i)v_{iPh} =$$

$$\begin{bmatrix} \cos(\omega_i t + \varphi_i) & \cos(\omega_i t + \varphi_i - 2\pi/3) & \cos(\omega_i t + \varphi_i + 2\pi/3) \end{bmatrix} V_{im} \begin{bmatrix} \cos(\omega_i t) \\ \cos(\omega_i t - 2\pi/3) \\ \cos(\omega_i t + 2\pi/3) \end{bmatrix} \qquad (C.3)$$

$$= 1.5 \times V_{im} \times \cos(\varphi_i) = consta\,nt$$

Also three-phase output voltages will be produced by multiplying the constant voltage given in (C.3) and inverter transfer matrix $D_I(\omega_o)$.

It follows from Fig. C-1 that the connection between the input and output phases is possible only through the positive and negative rails of the fictitious dc link. Due to the operation of the inverter stage, one of the following two switching conditions occurs at any given time:

- Two phases of the input and output connect to the same line '$P$' or '$N$', and
- Three phases of input or output connect to the same line '$P$' or '$N$'.

These two possible conditions include all combinations of groups II and III, and none from the group I, in Table B.2. Thus this method will realized only 21 switching combinations out of the 27 combinations in total. It is unlike direct matrix transfer approach that uses all combinations.

Reference [55] shows that the maximum voltage gain with indirect method is $\sqrt{3}/2$, without necessary harmonic injection into the transfer matrix.

The indirect method is well-known method for implementing PWM techniques in MC, like general voltage source and current source converters, and it does not have the complexity of direct approach. In the next section, a systematic PWM method based on indirect switching matrix approach is reviewed.

## C.3 Space Vector Pulse width Modulation Technique

The space vector-based pulse width modulation (SVPWM) technique is a well known method in control of DC/AC converters [100]. The SVPWM offers a number of useful features, especially in realistic implementation, such as:

- voltages or currents can be represented in two-dimension reference frames instated of three-dimensional *abc* frames,
- reducing the number of switching in each cycle,
- better output waveforms compared with conventional PWM methods,

- controllable $PF_{in}$ (input Power Factor) regardless of the $PF_{out}$ (load power factor),

- extending easily to multilevel inverters by inserting additional switching states, and

- SVPWM is a digital modulation technique and is easy to implement with digital controller, while PWM is an inherently analogue technique.

SVPWM can be applied to MC in the same way that it is applied to DC/AC converter, but is more complex in this case [55][60][62]. Based on the indirect matrix switching approach, the SVPWM can be simultaneously applied to both output voltage at the inverter part and input current at the rectifier part. In the following sections, the SVPWM procedures for both voltage- source inverter and current- source rectifier are reviewed. Then, the steps for controlling the output voltages and inputs currents are discussed.

## C.5  SVPWM for controlling output voltages of voltage source inverter

Fig. C-2 illustrates the voltage source inverter (VSI) part of the MC circuit of Fig. C-1, with fictitious dc-link voltage, $V_{dc}$ .
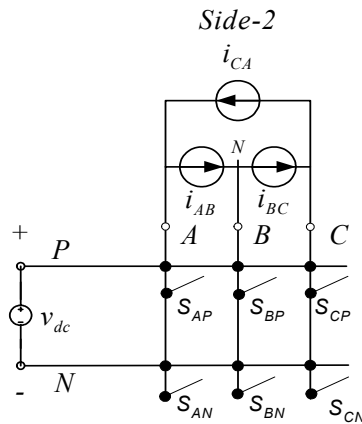


Fig. C-2: Voltage-source inverter with fictitious dc-link voltage, $V_{dc}$

Eight possible switching states that can be considered for the six switches of VSI, as shown in Fig. C-3. The combinations (7) and (8) make zero output voltage.
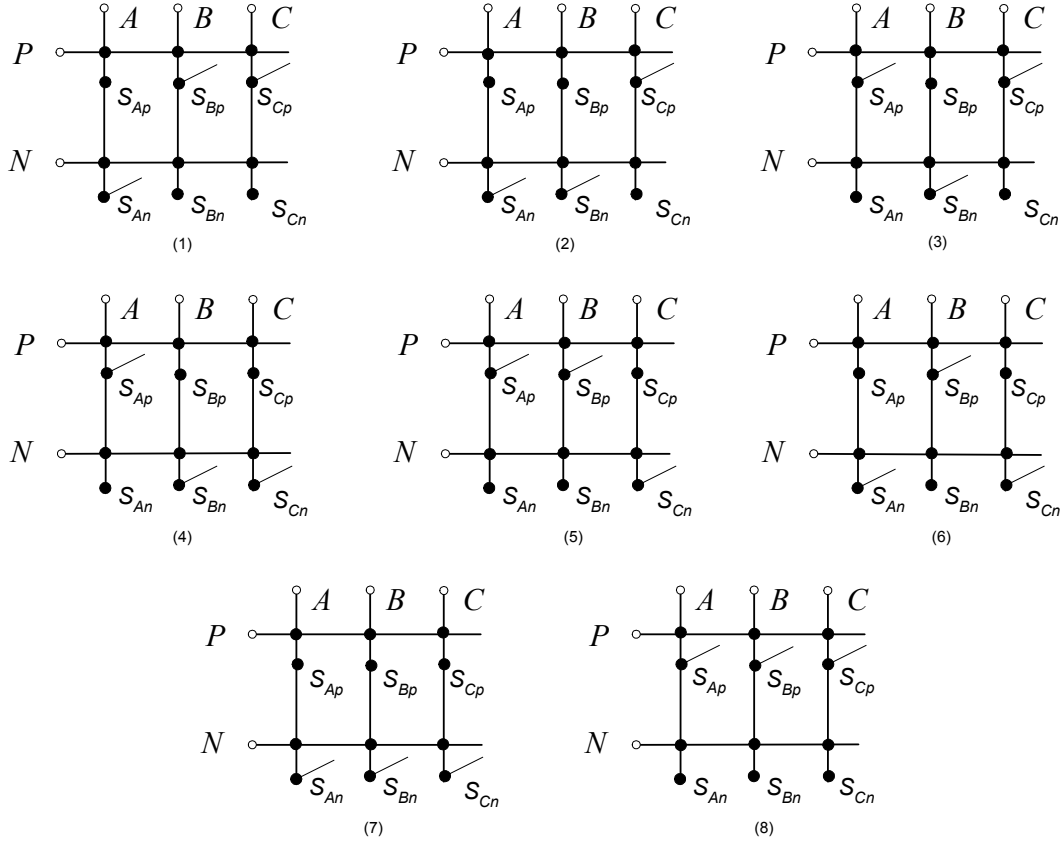
Fig. C-3: Eight possible switching states for the six switches of VSI

The desired three-phase output ac voltages $v_{AB}$, $v_{BC}$ and $v_{CA}$ are a set of quantized values in *abc* coordinate at each state. These voltages can be transferred to a fixed two-dimensional *dq*-frame as follows [101]:

$$\begin{bmatrix} V_{oq} \\ V_{od} \end{bmatrix} = \frac{2}{3} \begin{bmatrix} 1 & \cos(\frac{2\pi}{3}) & \cos(-\frac{2\pi}{3}) \\ 0 & \sin(\frac{2\pi}{3}) & \sin(-\frac{2\pi}{3}) \end{bmatrix} \begin{bmatrix} v_{AB} \\ v_{BC} \\ v_{CA} \end{bmatrix} \tag{C.4}$$

In complex form, the space vector of the desired quantized output line voltages can be defined by:

$$V_{oL} = \frac{2}{3}(v_{AB} + v_{BC}e^{j\frac{2\pi}{3}} + v_{CA}e^{-j\frac{2\pi}{3}}) \tag{C.5}$$

This transformation can be used for any of the three-phase quantities in *abc*-frame, i.e., voltages or currents related to the voltage or current source converters.

By calculating the switching state vector for allowed output voltages of the voltage-source inverter in each switching state, six non-zero space switching voltage vectors, $\vec{V}_1, \vec{V}_2, ..., \vec{V}_6$, will result, as illustrated in Fig C-4. These vectors can form a hexagon centered at the origin of the *dq* frame. The remaining two zero voltage space voltage vectors, $\vec{V}_0$ & $\vec{V}_7$, are located at the origin of the frame.
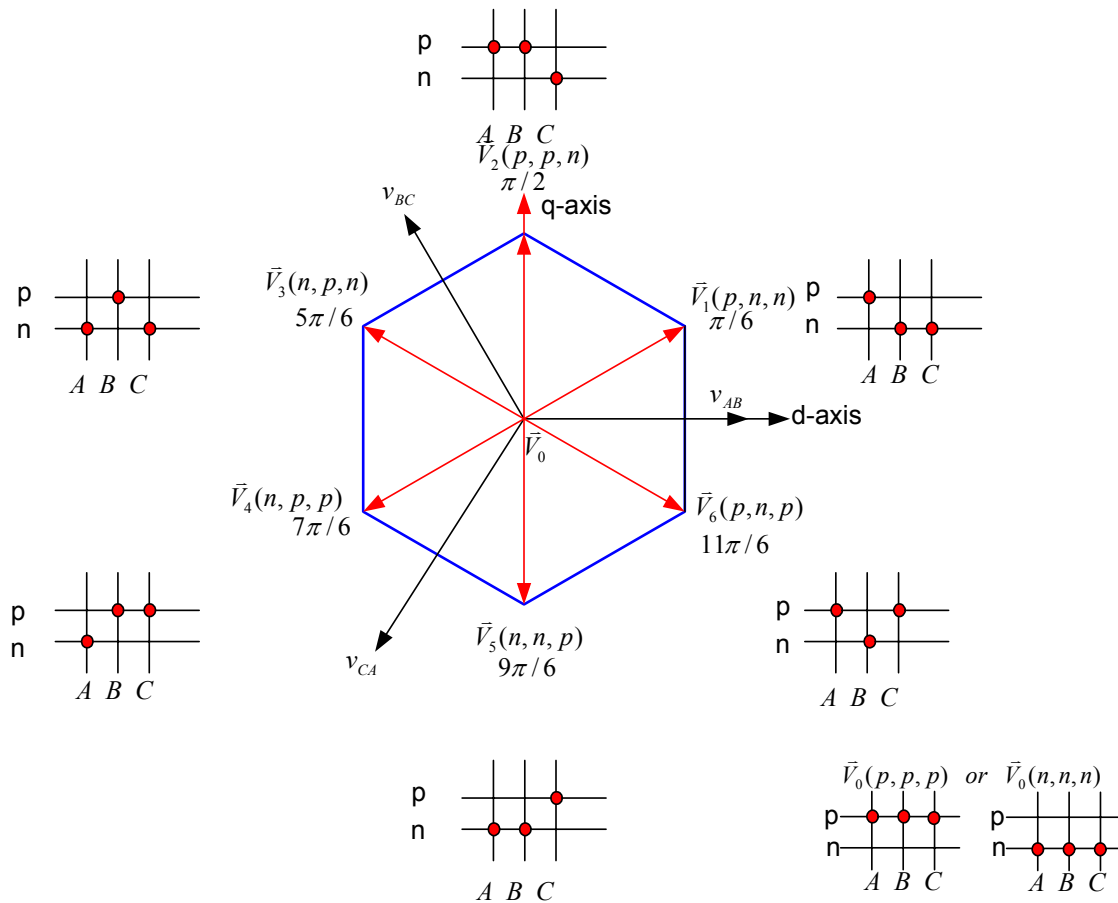


Fig. C-4:Output voltage space vector in complex plane

The continuous desired output voltages, $v_{AB}(t)$, $v_{BC}(t)$ and $v_{CA}(t)$ can be represented by a space vector given by (C.6).

182

Appendix C. Modulation Algorithm...

$$V_{oL\_ref} = \sqrt{3}V_{om}e^{j(\omega_o t + \varphi_o)} \tag{C.6}$$

This reference vector should be synthesized using the two active vectors adjacent to the reference vector and a zero vector. Fig. C-5 illustrates an example of how $\vec{V}_{ol\_ref}$ can be synthesized when it is located in sector 1, between non-zero vectors $\vec{V}_1$ and $\vec{V}_6$
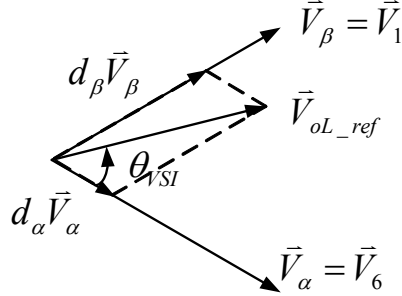


Fig. C-5: $\vec{V}_{oL\_ref}$ synthesis using vectors $\vec{V}_1$ and $\vec{V}_6$

During each switching period, $T_s$, the $V_{oL\_ref}$ is calculated by choosing the time $T_\alpha$ spent in vector $\vec{V}_\alpha$, and time $T_\beta$ spent in vector $\vec{V}_\beta$. The rest of the time $T_0$ is dedication to a zero vector. These three time periods can be stated by duty cycles using trigonometric identities as

$$\begin{cases} T_\alpha = m_v \ sin(\dfrac{\pi}{3} - \theta_{VSI}).T_s = d_\alpha T_s \\ T_\beta = m_v \ sin(\theta_{VSI}).T_s = d_\beta T_s \\ T_{0v} = d_{0v} T_s = T_s - (T_\alpha + T_\beta) \end{cases} \Rightarrow \begin{cases} d_\alpha = m_v \ sin(\dfrac{\pi}{3} - \theta_{VSI}) \\ d_\beta = m_v \ sin(\theta_{VSI}) \\ d_{0v} = 1 - (d_\alpha + d_\beta) \end{cases}, \tag{C.7}$$

where $0 \leq m_v \leq 1$ is the modulation index of voltage source inverter, and $\theta_{SVI}$ the angle between the reference vector and the closest clockwise state vector.

There are several methods for distributing the time periods $(T_\alpha, T_\beta, T_0)$ during a switching period in space vector modulation. One possible way is shown in Fig. C-6.
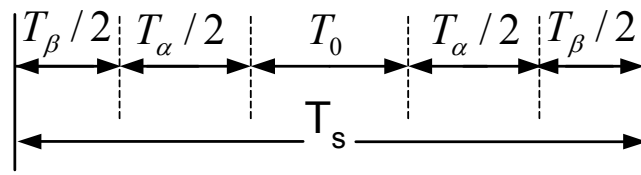
Fig. C-6: A possible method of distributing the time periods during one switching period

## C.6  SVPWM for control input currents of Current-Source Rectifier

The first part of indirect MC of Fig. C-1, with a fictitious dc-link current, $I_{dc}$, can be considered as a current-source rectifier. The implementation of SVPWM for the current-source rectifier is very similar to that of the voltage-source inverter. It is necessary to replace $\theta_{VSI}$ with input space vector angle current $\theta_{CSR}$ and subscripts $\alpha$ and $\beta$ in duty cycles with subscripts $\mu$ and $\gamma$, respectively. Also, there is a similar hexagon for input currents of current-source rectifier, as shown in Fig. C-7. Furthermore the duty cycles for the current-source rectifier are as follows:

$$
\begin{cases}
T_\mu = m_c \ sin(\dfrac{\pi}{3} - \theta_{CSR})T_s = d_\mu T_s \\
T_\gamma = m_c \ sin(\theta_{CSR})T_s = d_\gamma T_s \\
T_{0c} = d_{0c} T_s = T_s - (T_\mu + T_\gamma)
\end{cases}
\Rightarrow
\begin{cases}
d_\mu = m_c \ sin(\dfrac{\pi}{3} - \theta_{CSR}) \\
d_\gamma = m_c \ sin(\theta_{CSR}) \\
d_{0c} = 1 - (d_\mu + d_\gamma)
\end{cases}
, \qquad (C.8)
$$

where $0 \le m_c \le 1$ is the modulation index of the current-source rectifier.
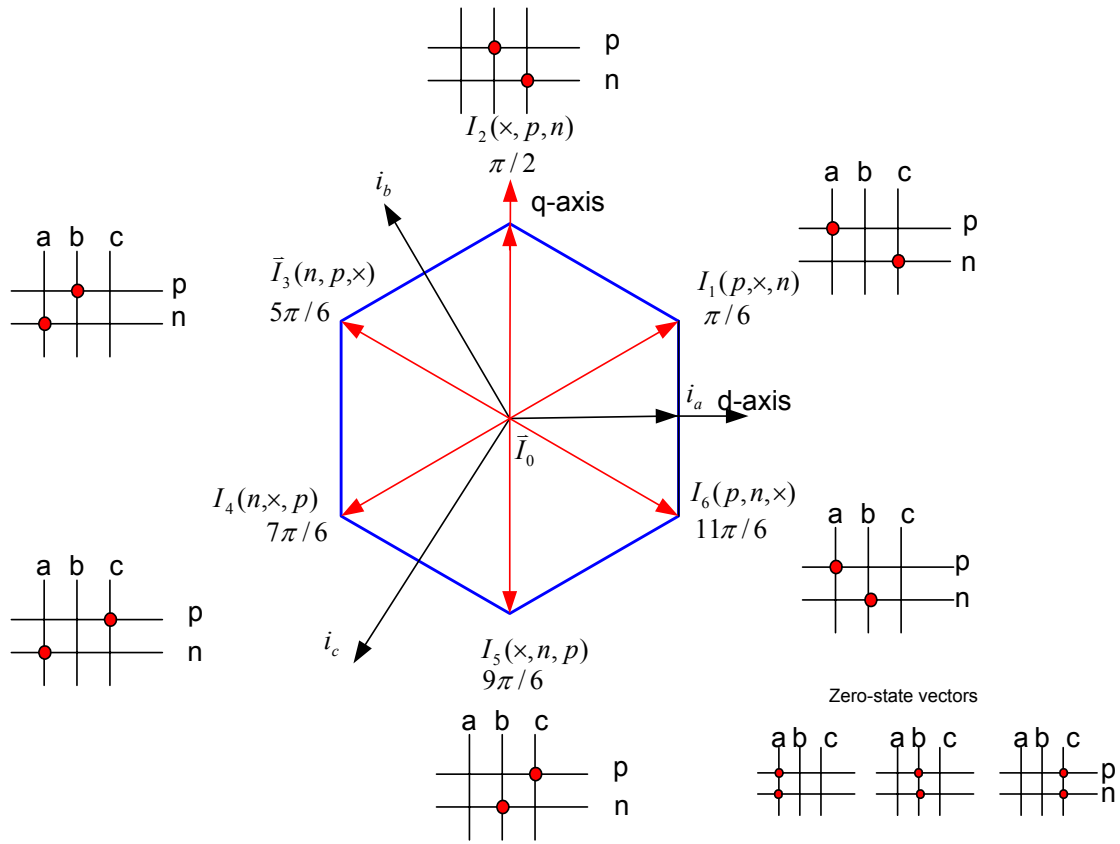
Fig. C-7: Input current space vector in complex plane

**C.7  SVPWM for Output Voltages and Input Currents in the Matrix Converter**

In the MC with indirect method, it is supposed to have supposes a target constant voltage space vector, for the inverter part, and a constant current space vector, for the rectifier part. Each converter has a hexagon which contains six $60°$ sectors. In total, 6×6 combinations can be considered in each sequence. For each converter there are three duty cycles based on (C.6) and (C.7). In [55] it is proved that the modulation process in the MC is performed by using five combined duty cycles as follows:

$$d_{\alpha\mu} = d_{\alpha} \times d_{\mu} = \frac{T_{\alpha\mu}}{T_s} = m \ sin(\frac{\pi}{3} - \theta_{VSI}) \ sin(\frac{\pi}{3} - \theta_{CSR}),$$

$$d_{\beta\mu} = d_{\beta} \times d_{\mu} = \frac{T_{\beta\mu}}{T_s} = m \ sin(\theta_{VSI}) \ sin(\frac{\pi}{3} - \theta_{CSR}),$$

$$d_{\beta\gamma} = d_{\beta} \times d_{\gamma} = \frac{T_{\beta\gamma}}{T_s} = m \ sin(\theta_{VSI}) \ sin(\frac{\pi}{3} - \theta_{CSR}), \tag{C.9}$$

$$d_{\alpha\gamma} = d_{\alpha} \times d_{\gamma} = \frac{T_{\alpha\gamma}}{T_s} = m \ sin(\frac{\pi}{3} - \theta_{VSI}) \ sin(\theta_{CSR}),$$

$$d_0 = \frac{T_0}{T_s} = 1 - (d_{\alpha\mu} + d_{\beta\mu} + d_{\beta\gamma} + d_{\alpha\gamma}),$$

where $m = m_v \times m_c$ is the modulation index, and the $d_0$ is the duty ratio corresponding to zero states, given in Table B.1.

There are different combinations for ordering the time segments corresponding to duty ratios given by equation (C.9) in each switching cycle. Fig. C-8 shows a distribution, among the possible combinations, that has minimum change of state of switches during a switching cycle as well as symmetrical switching around the zero-voltage interval.
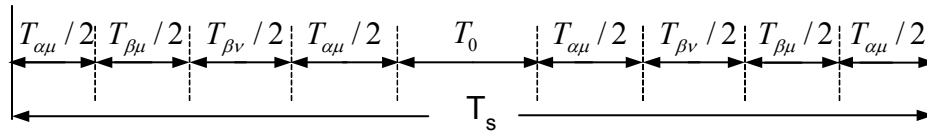


Fig. C-8: A distribution of duty cycles of switches during a switching cycle

Based on six segments in the desired output voltage space vector hexagon of Fig C-4 and six segments in the desired input current space vector hexagon of Fig C-7, as well as four duty cycles for

186

Appendix C. Modulation Algorithm…

each switching cycle ($T_s$), in total there are 6×6×4=144 combinations of switches in the MC, as shows in Fig. C-9.

According to the above discussions space vector modulation-based control of 3-phase to 3-phase MC has to perform in each switching cycle, $T_s$, as follows:

A. Based on the 3-phase desired output voltages, the phase angle of the desired output voltage space vector of output voltages (equation (C.5)), i.e., $\theta_{VSI}$ , should be determined.

B. By $\theta_{VSI}$ , the output voltage operational segment based on hexagon of Fig. C.4 will be determined.

C. With this operational segment, the duty cycles, $d_\alpha$ and $d_\beta$ can be determined.

D. For desired input currents and by doing the same procedure outlined in (A) to (C), and considering Fig. C-7 and (C.8), the duty cycles $d_\mu$ and $d_\gamma$ can be determined.

E. The combined duty cycles of the MC are based on (C.9), and therefore the switching times can be calculated.

F. The calculated switching times will be converted to switching pulses for MC switching based on Fig. C-9.

G. After completing a switching cycle, the stages (A) to (F) will be repeated for a new set of desired output voltages and input currents.
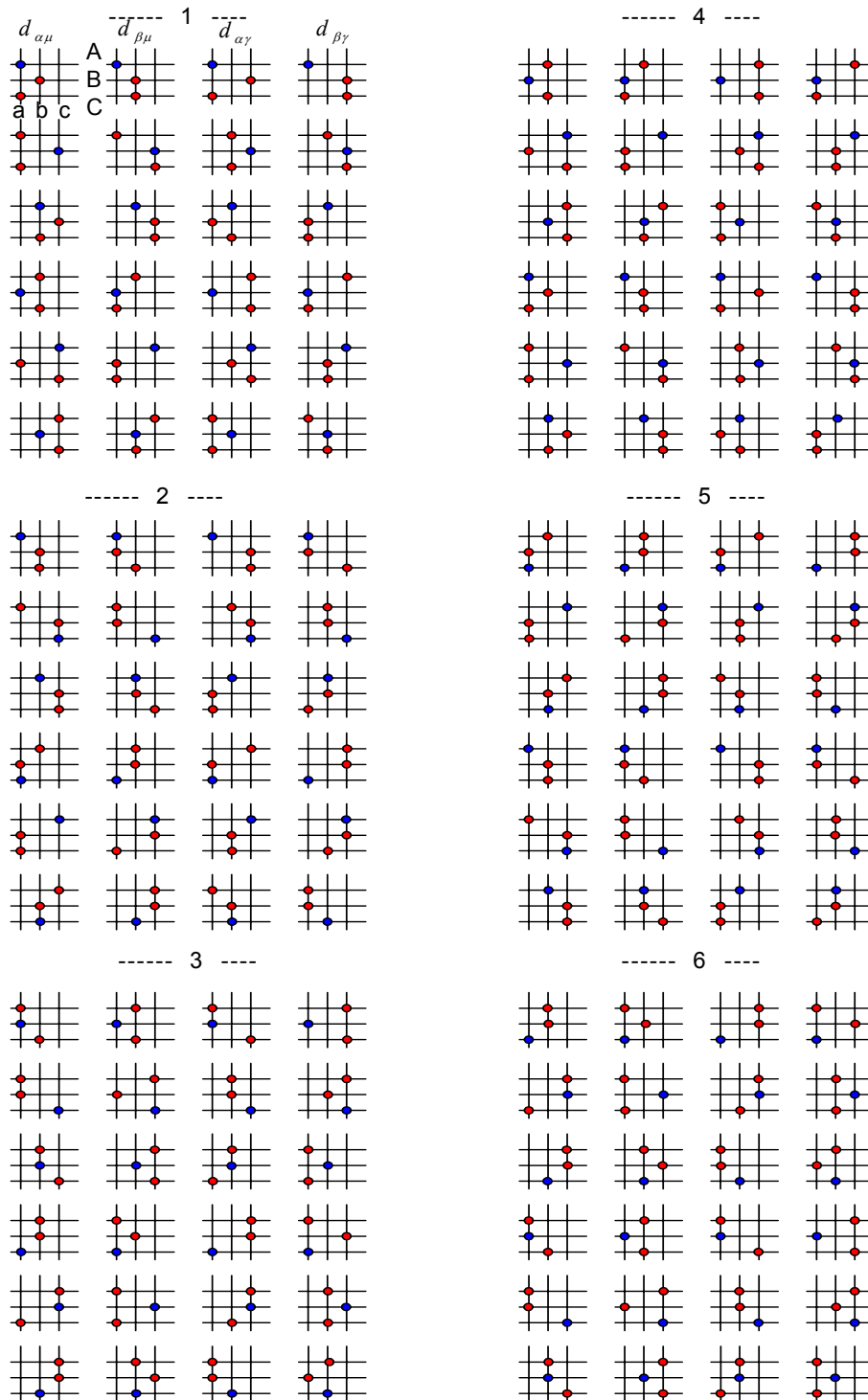
Fig. C-9: 144 combinations of switch states in MC

# Appendix D

# A Comparison Between PWM and SVPWM Techniques

In order to compare the performances of the PWM and SVPWM modulation techniques, these methods are applied to a DC/AC converter as shown in the Fig. 3-26. As illustrated in Fig D-1, an induction motor is connected to the ac terminals of the converter. In Fig. D-1(a) the conventional PWM method is implemented by an analogue circuit, while in Fig. D-1(b), the SVPWM method is implemented digitally (using a routine in a DLL block). The inputs of the DLL block are the desired output frequency, magnitude of the output voltage, the switching frequency and the input displacement angle.

The comparison is done under the same conditions for the input power supply and mechanical Load.

The line-to-line output terminal voltage and output line current for the PWM and SVPWM methods are shown in Fig. D-2 (a) and Fig. D-2 (b), respectively. Furthermore, Fig. D-3 and Table D.1 illustrate the harmonic spectrum and Total Harmonic Distortions (THD) for the two methods. Fig. D-4 compares the number of switchings under these methods.

Based on these simulation results, SVPWM technique shows the following advantages over PWM technique:

- Lower harmonic distortion
- Fewer number of switchings

Having these advantages in mind, the SVPWM technique will be chosen as the method of modulation for matrix converter, although implementation of SVPWM is more complex than conventional PWM.

189

Fig. D-1: Block diagrams of a DC/AC converter controlled under methods (a) PWM and (b) SVPWM

Fig.D-2: Line-to-Line output voltage ($V_{AB}$) and output current ($i_A$) of the converter with (a) PWM method, (b) SVPWM method
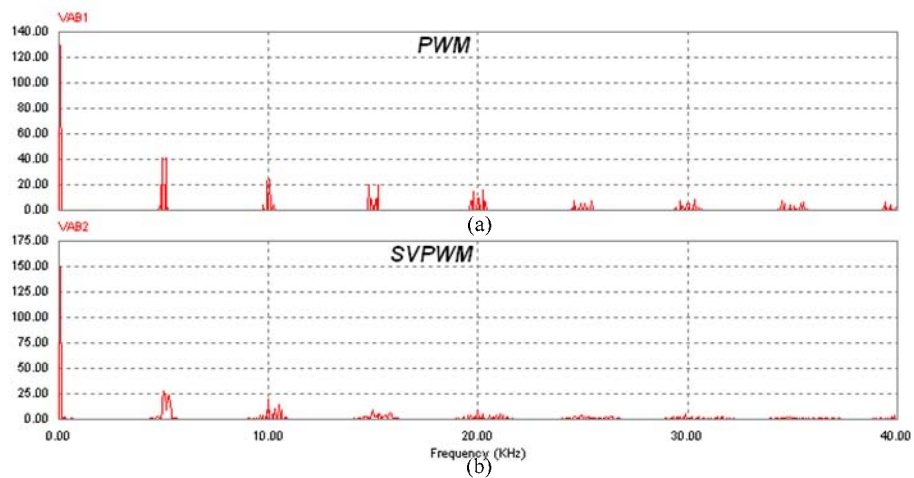


Fig. D-3: A comparison of Harmonic spectrums for (a) PWM method and (b) SVPWM method

191

Table D.1:  A comparison of  number of switching per period and output voltage THDs for PWM
SVPWM methods

| Method | Number of Switchings (in a period) | THD% |
|--------|-----------------------------------|------|
| PWM | 600 | 69 |
| SVPWM | 320 | 50 |
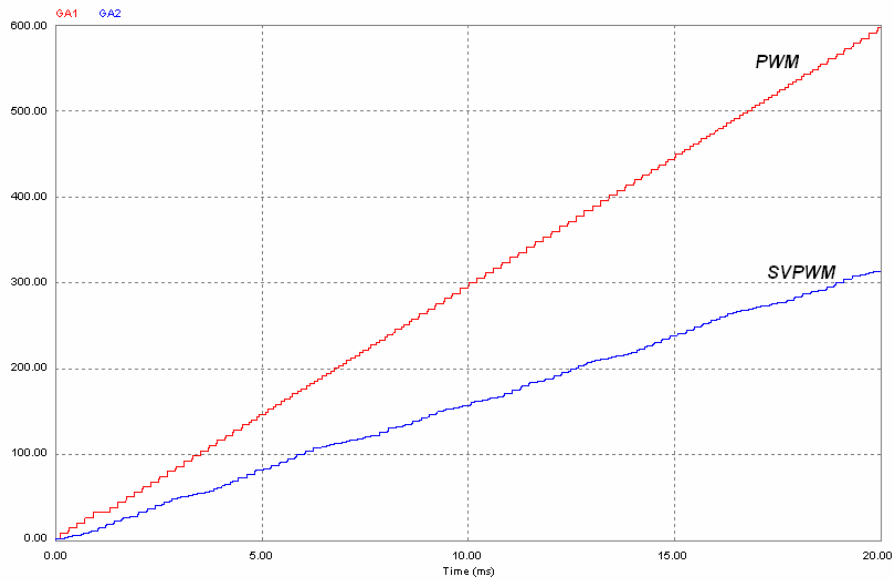


Fig. D-4: A comparison of the number of switchings of PWM and SVPWM methods

# Appendix E

# Safe Commutation in MC and Indirect MC Topology

### E.1 Safe Commutation in Switching Sequence of a MC

Due to the commutation problems in bidirectional switches, safe commutation between an out-going and an in-coming switch cannot be achieved in one step only, and multi-step switching is mandatory. A reliable approach in this case is the four-step commutation method. This technique lets the load current be transferred from one switch to another switch without causing an input source line-to-line short circuit or an inductive load current open circuit. The principal concept of four-step technique can be explained by connecting two phases of a 3-phase balanced source to one phase of the load through two bi-directional switches, as shown in Fig. E-1 [60].
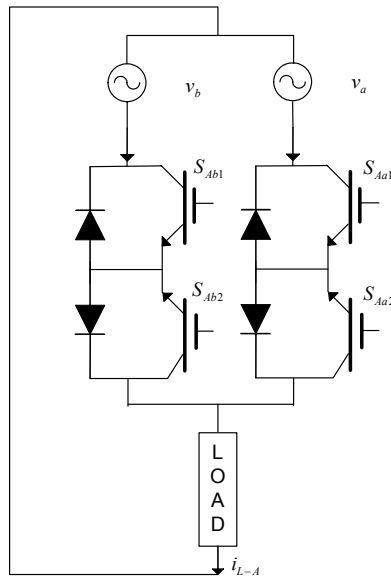


Fig. E-1: Two-phase to single-phase MC for principal concept of four-step technique

It is supposed that in the initial state, the direction of the load current is as shown and the right switches, $S_{Aa1}$ and $S_{Aa2}$ are on. Thus, the load current is passing through the bidirectional switch $S_{Aa}$. If the load current is to be commutated to the left source ($v_b$), the switches $S_{Ab1}$ and $S_{Ab2}$ are required to turn on. With ideal switches, it is only necessary to turn off the outgoing bidirectional switch $S_{Aa}$ and

gate the incoming bidirectional switch $S_{Ab}$. It means that the commutation will be done in one step, as shown in Fig. E-2(a). However, in real switches, the commutation between these two switches involves changing the switch states of four devices, based on the direction of the current [47]. In this method, in the first stage, according to the direction of the current, the device that is not conducting, in this case $S_{Aa2}$, will be turned off. In the next stage, the devise $S_{Ab1}$ is gated to undertake the current in the specified direction. Therefore, the load current will be completely transferred to this incoming device after turning off the outgoing device $S_{Aa1}$. The four-step commutation method will be completed by turning on the device $S_{Ab2}$ as it permits the current reversals capability in incoming bidirectional switch, $S_{Ab}$. The timing of the four-step method is shown in Fig. E-2(b). It is worth noting that the time delay, $T_d$, between switching depends on device characteristics.
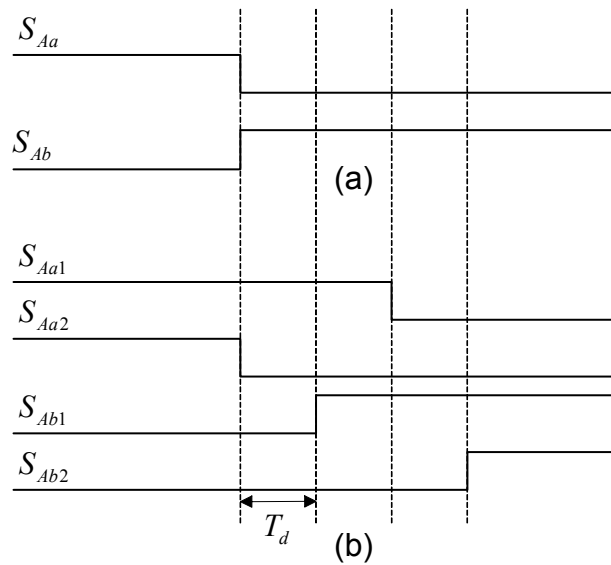


Fig. E-2: Timing diagram (a) Ideal switches (b) Four-step method

The application of the four-step method in the three-phase MC is more complex than in the previous example. In the three-phase MC, each phase of the output has three bidirectional switches to connect to the three phases of the input. Therefore, for each output line, six devices go through switch state change sequentially. For these six devices, there are 15 valid state combinations, as listed in Table E.1. The first three states are the initial states before the commutation commences or the last state after commutation is finished. When an output terminal is switched from one of the three input phases to another, it means switching between one of the three first states. For implementing the four-step method, four intermediate states or transient states, out of states 4 to 15 in Table E.1, are

194

required. The choice of the intermediate states depends on the direction of the current and desired input phase as well as the original input phase to which an output was connected. According to Table E.1 and also two possible directions for current in each state, there are 12 switching path, as shown in Fig. E-3 [102].

Table E.1: State combinations for the six devices in one output phase of MC with four-step method

| State | $S_{aA1}$ | $S_{aA2}$ | $S_{bA1}$ | $S_{bA2}$ | $S_{cA1}$ | $S_{cA2}$ |
|-------|-----|-----|-----|-----|-----|-----|
| 1 | on | on | off | off | off | Off |
| 2 | off | off | on | on | off | Off |
| 3 | off | off | off | off | on | On |
| 4 | on | off | off | off | off | Off |
| 5 | off | on | off | off | off | Off |
| 6 | off | off | on | off | off | Off |
| 7 | off | off | off | on | off | Off |
| 8 | off | off | off | off | on | off |
| 9 | off | off | off | off | off | on |
| 10 | on | off | on | off | off | off |
| 11 | off | on | off | on | off | off |
| 12 | off | off | on | off | on | off |
| 13 | off | off | off | on | off | on |
| 14 | on | off | off | off | on | off |
| 15 | off | on | off | off | off | on |

The four-step commutation method in MC can be realized in two ways: (1) writing the SVPWM code in a microcontroller or a DSP, and (2) using discrete circuit components.

In [102], a logic circuit is proposed as a better alternative to the microcontroller/DSP method or other discrete component-based circuits. The overall circuit configuration of the logic circuit is shown in Fig. E-4. This circuit uses only a few logic gates, and is simple, inexpensive, easy to understand and easy to realize by FPGA (field programmable Gate Array) or other programmable devices.

1,2,3 initial or end State, other states transition states
_____ positive current path
------- negative current path
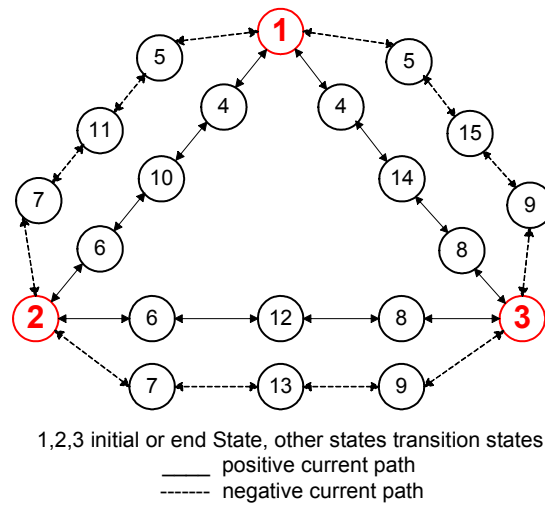
Fig. E-3: 12-path switching for the six devices in one output phase of MC with four-step method
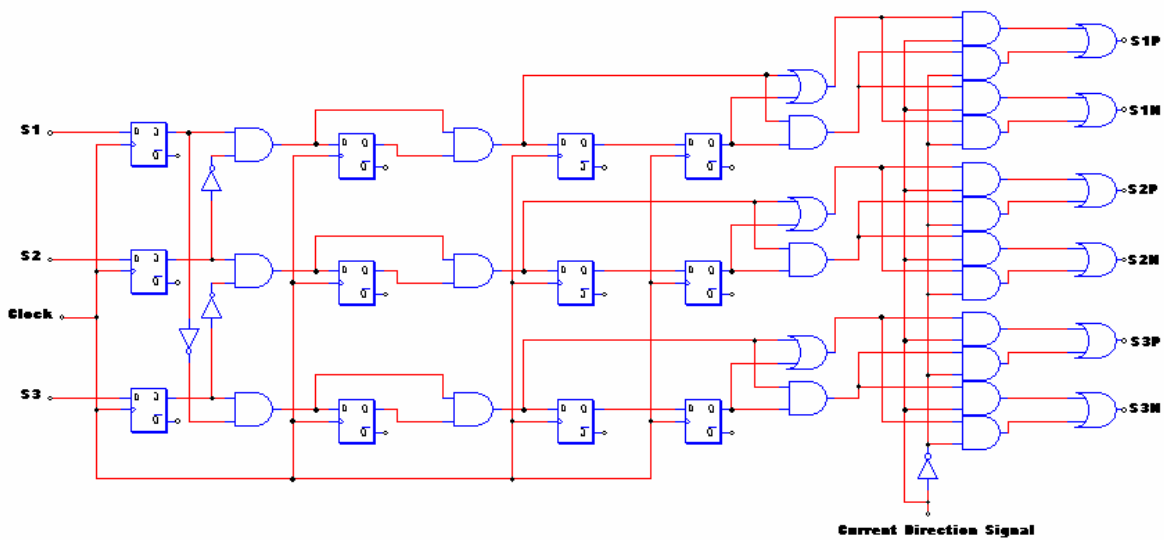


Fig. E-4: A logic circuit for realization of four-step method

## E.2 Indirect Matrix Converter Topology

As mentioned in the pervious section, a serious drawback attributed to the conventional MC topology is the commutation problems. Some solutions, such as the four-step switching method for safe operation of the switches, require complicated switching strategies, impairing the elegance of the topology. This is a serious problem that can limit the application of MCs in industry. In this section, a novel topology of MC with advantages over the conventional MC will be introduced [59][103]. This topology is known as the indirect MC (IMC).

196

The indirect MC is composed of two separate parts, the rectifier stage and the inverter stage. This is based on the concept of fictitious dc-link used in the indirect modulation method for controlling the conventional MC. It is also similar to the traditional AC/DC/AC converter after eliminating the DC capacitor [103][104]. In the indirect MC topology, the rectifier and inverter parts are realized by 12 switches. Note that, there is no energy storage element between the line-side and load-side converters. Fig. E-5 shows the schematic diagram of the IMC topology.
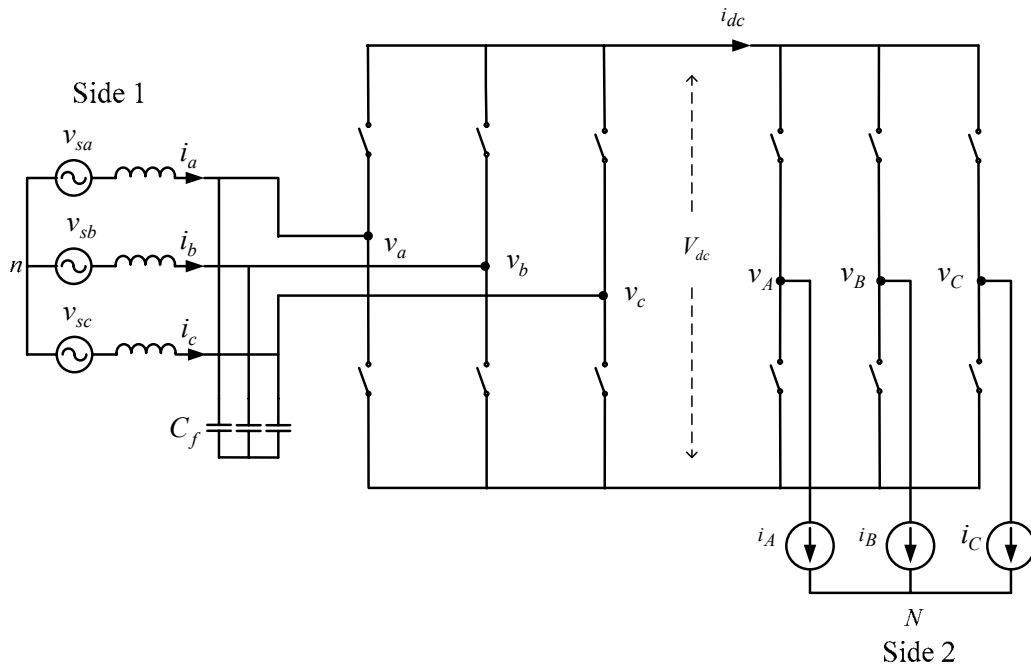


Fig. E-5: Schematic diagram of the indirect matrix converter topology

In this structure, the inverter is fed by a rectifier which is able to operate with positive and negative dc current and voltage, as required by the inverter. The dc-link voltage can be considered as both a voltage source and current source. A stiff voltage and current characteristic can be provided by input voltage source and inductive load, respectively. However, for compensation of the ripple in input current, filter capacitors are added.

The lack of commutation problems is the important advantage of this new topology. The reason for this feature can be explained as follows.

There is a real dc-link between rectifier and inverter in the indirect MC. When a current commutation in the rectifier side is requested, it is possible to connect three output phases in the

197

inverter side to the positive or negative bus.  This causes a zero current in the dc-link as well as the rectifier side. Therefore, all switches on the rectifier side turn on and turn off at the instant of zero current;  this means soft switching. Thus, the commutation problems associated with the conventional MC are absolutely avoided. Also, all load-side switches commutate like a conventional DC/AC inverter.

## E.3  Choosing the Type and Number of Switches

By controlling the polarity of dc voltage in such a way that dc-link voltage is always positive, it is possible to use unidirectional switches in the inverter part as shown in Fig. E-6. It is worth noting that with negative dc voltage a short circuit will happen in the inverter legs in this configuration. Therefore, the inverter side is the same as the traditional inverter. But the rectifier has all bidirectional switches unlike the conventional rectifier. Thus, the number of switches in this new configuration will be 18: 12 switches for the rectifier part and 6 switches for the inverter part.

   Even thought unidirectional switches are used on the rectifier side, this new structure of the MC has the potential to work in four quadrants. However, some researchers have shown that the number of switches can be reduced, under certain conditions, to 9 unidirectional switches in an ultra sparse MC (USMC) topology, resulting in a reduction in the cost [59][105].

## E.4  Modulation Algorithm

   In the IMC topology, there are two converters that are separated by the dc-link. From the modulation point of view, this separation has some distinguished merits. This feature reduces the complexity of the control method. For controlling these two converters, the space vector PWM (SVPWM) as well as conventional PWM methods can be applied to both rectifier and inverter. The PWM method is a simple method in comparison with SVPWM method, and it can be implemented by analog devices, but SVPWM has better performance especially in inverter. In [58], a PWM method for the rectifier side and a SVPWM for the inverter side are used.
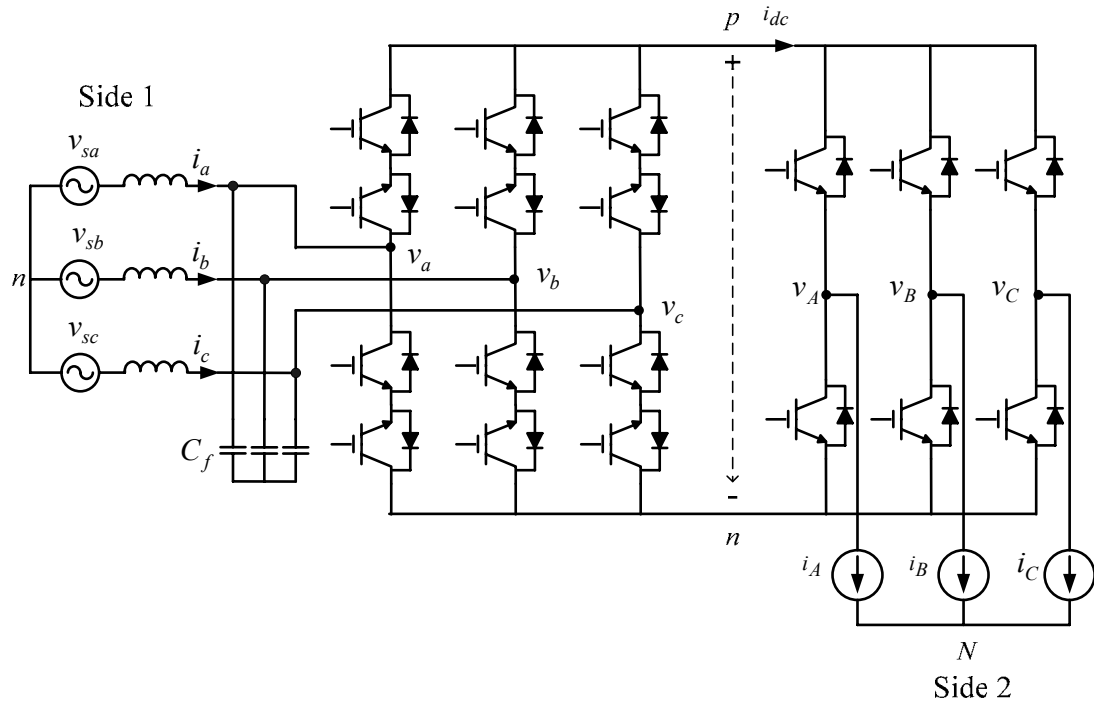
Fig.E-6: IMC with 12 bidirectional switches on the rectifier side and 6 switches unidirectional in the inverter part

Briefly, the indirect MC topology has the following advantages:

- Since all the switches at the line-side turn on and turn off at zero current and also all load side switches commutate like a conventional DC/AC inverter, the commutation problems associated with the bidirectional switches in the conventional MC topology have been solved.
- It has the same performance as the conventional MC such as unity input power factor and close-to-sinusoidal waveforms containing switching harmonics only.
- No bulky capacitor is needed in the dc-link.
- The control method is simple because of separated converters and the possibility of using a PWM algorithm instead of SVPWM algorithm.
- Due to soft switching on the rectifier side, it is expected to have higher efficiency than the conventional MC.

# Appendix F

# Calculating the term $(K_0 D) D^T (K_0)^{-1}$

In order to calculate the term $(K_0 D) D^T (K_0)^{-1}$, one can write :

$$
(K_0 D) D^T (K_0)^{-1} = ((K_0 D)_1 + (K_0 D)_2)(D_1 + D_2)^T (K_0)^{-1}
$$
$$
= \{(K_0 D)_1 (D_1)^T + (K_0 D)_2 (D_1)^T + (K_0 D)_1 (D_2)^T + (K_0 D)_2 (D_2)^T\}(K_0)^{-1}.
$$

(F.1)

From equation (2.12) and definition of $K_0$,

$$
(K_o D)_1 = \frac{2}{3} q \cos(\alpha_o) \begin{bmatrix} \cos(\omega_i t) & \cos(\omega_i t - \frac{2\pi}{3}) & \cos(\omega_i t + \frac{2\pi}{3}) \\ (2a-1)\sin(\omega_i t) & (2a-1)\sin(\omega_i t - \frac{2\pi}{3}) & (2a-1)\sin(\omega_i t + \frac{2\pi}{3}) \\ \frac{1}{2q\cos(\alpha_o)} & \frac{1}{2q\cos(\alpha_o)} & \frac{1}{2q\cos(\alpha_o)} \end{bmatrix}.
$$

(F.2)

$$
(K_o D)_2 = \frac{2}{3} q \sin(\alpha_o) \begin{bmatrix} (2a-1)\sin(\omega_i t) & (2a-1)\sin(\omega_i t - \frac{2\pi}{3}) & (2a-1)\sin(\omega_i t + \frac{2\pi}{3}) \\ -\cos(\omega_i t) & -\cos(\omega_i t - \frac{2\pi}{3}) & -\cos(\omega_i t + \frac{2\pi}{3}) \\ 0 & 0 & 0 \end{bmatrix}.
$$

(F.3)

The four terms of right-hand-side of equation (F.1) can be determined as follows:

**1**- Determining $(K_0 D)_1 (D_1)^T$ :

$$
D_1 = \frac{a}{3} \begin{bmatrix} 1+2q\cos(\theta_{s1}) & 1+2q\cos(\theta_{s1}-2\pi/3) & 1+2q\cos(\theta_{s1}+2\pi/3) \\ 1+2q\cos(\theta_{s1}+2\pi/3) & 1+2q\cos(\theta_{s1}) & 1+2q\cos(\theta_{s1}-2\pi/3) \\ 1+2q\cos(\theta_{s1}-2\pi/3) & 1+2q\cos(\theta_{s1}+2\pi/3) & 1+2q\cos(\theta_{s1}) \end{bmatrix}
$$
$$
= \frac{a}{3}(2q \begin{bmatrix} \cos(\theta_{s1}) & \cos(\theta_{s1}-2\pi/3) & \cos(\theta_{s1}+2\pi/3) \\ \cos(\theta_{s1}+2\pi/3) & \cos(\theta_{s1}) & \cos(\theta_{s1}-2\pi/3) \\ \cos(\theta_{s1}-2\pi/3) & \cos(\theta_{s1}+2\pi/3) & \cos(\theta_{s1}) \end{bmatrix} + \begin{bmatrix} 1 & 1 & 1 \\ 1 & 1 & 1 \\ 1 & 1 & 1 \end{bmatrix}) = \frac{a}{3}(2qD_{11} + Ones).
$$

(F.4)

200

Appendix F. Calculating the term $(K_0 D) D^T (K_0)^{-1}$

where and $\theta_{s1} = \omega_i t - (\omega_o t + \alpha_o)$. From (F.2) and (F.4), one can get,

$$(K_0 D)_1 (\frac{a}{3}(2qD_{11}))^T = \frac{2}{3}q\frac{a}{3}(2q)\cos(\alpha_o) \times$$

$$\begin{bmatrix} \cos\omega_i t & \cos(\omega_i t - \frac{2\pi}{3}) & \cos(\omega_i t + \frac{2\pi}{3}) \\ A_1\sin\omega_i t & A_1\sin(\omega_i t - \frac{2\pi}{3}) & A_1\sin(\omega_i t + \frac{2\pi}{3}) \\ B_1 & B_1 & B_1 \end{bmatrix} \begin{bmatrix} \cos(\theta_{s1}) & \cos(\theta_{s1} + 2\pi/3) & \cos(\theta_{s1} - 2\pi/3) \\ \cos(\theta_{s1} - 2\pi/3) & \cos(\theta_{s1}) & \cos(\theta_{s1} + 2\pi/3) \\ \cos(\theta_{s1} + 2\pi/3) & \cos(\theta_{s1} - 2\pi/3) & \cos(\theta_{s1}) \end{bmatrix}, \quad \text{(F.5)}$$

where $A_1 = (2a - 1)$ and $B_1 = \dfrac{1}{2q\cos(\alpha_o)}$. Thus, from (F.4) and (F.5), one can write:

$$(K_0 D)_1 (D_1)^T = \begin{bmatrix} K_1\cos(\omega_o t + \alpha_o) & K_1\cos(\omega_o t + \alpha_o - \frac{2\pi}{3}) & K_1\cos(\omega_o t + \alpha_o + \frac{2\pi}{3}) \\ A_1 K_1\sin(\omega_o t + \alpha_o) & A_1 K_1\sin(\omega_o t + \alpha_o - \frac{2\pi}{3}) & A_1 K_1\sin(\omega_o t + \alpha_o + \frac{2\pi}{3}) \\ \frac{a}{3} & \frac{a}{3} & \frac{a}{3} \end{bmatrix}, \quad \text{(F.6)}$$

where $K_1 = \dfrac{3}{2}(\dfrac{2}{3}q\dfrac{a}{3}(2q))\cos(\alpha_o) = \dfrac{2}{3}aq^2\cos(\alpha_o)$.

**2- Determining $(K_0 D)_2 (D_1)^T$**

Comparing the terms $(K_0 D)_1$ and $(K_0 D)_2$, one can find easily the term $(K_0 D)_2 (D_1)^T$ from equation (F.6) as follows:

$$(K_0 D)_2 (D_1)^T = \begin{bmatrix} A_1 K_2\sin(\omega_o t + \alpha_o) & A_1 K_2\sin(\omega_o t + \alpha_o - \frac{2\pi}{3}) & A_1 K_2\sin(\omega_o t + \alpha_o + \frac{2\pi}{3}) \\ -K_2\cos(\omega_o t + \alpha_o) & -K_2\cos(\omega_o t + \alpha_o - \frac{2\pi}{3}) & -K_2\cos(\omega_o t + \alpha_o + \frac{2\pi}{3}) \\ 0 & 0 & 0 \end{bmatrix}, \quad \text{(F.7)}$$

where $K_2 = \dfrac{3}{2}(\dfrac{2}{3}q\dfrac{a}{3}(2q))\sin(\alpha_o) = \dfrac{2}{3}aq^2\sin(\alpha_o)$.

**3-Determaining $(K_0 D)_1 (D_2)^T$ :**

Appendix F. Calculating the term $(K_0D)D^T(K_0)^{-1}$

$$D_2 = \frac{1-a}{3}\begin{bmatrix} 1+2q\cos(\theta_{s2}) & 1+2q\cos(\theta_{s2}-2\pi/3) & 1+2q\cos(\theta_{s2}+2\pi/3) \\ 1+2q\cos(\theta_{s2}-2\pi/3) & 1+2q\cos(\theta_{s2}+2\pi/3) & 1+2q\cos(\theta_{s2}) \\ 1+2q\cos(\theta_{s2}+2\pi/3) & 1+2q\cos(\theta_{s2}) & 1+2q\cos(\theta_{s2}-2\pi/3) \end{bmatrix}$$

$$= \frac{1-a}{3}(2q\begin{bmatrix} \cos(\theta_{s2}) & \cos(\theta_{s2}-2\pi/3) & \cos(\theta_{s2}+2\pi/3) \\ \cos(\theta_{s2}-2\pi/3) & \cos(\theta_{s2}+2\pi/3) & \cos(\theta_{s2}) \\ \cos(\theta_{s2}+2\pi/3) & \cos(\theta_{s2}) & \cos(\theta_{s2}-2\pi/3) \end{bmatrix} + \begin{bmatrix} 1 & 1 & 1 \\ 1 & 1 & 1 \\ 1 & 1 & 1 \end{bmatrix}) = \frac{1-a}{3}(2qD_{22} + Ones).$$

(F.8)

where $\theta_{s2} = \omega_i t + (\omega_o t + \alpha_o)$. From (F.2) and (F.8), one can get:

$$(K_0D)_1(\frac{1-a}{3}(2qD_{22}))^T = \frac{2}{3}q\frac{1-a}{3}(2q)\cos(\alpha_o)$$

$$\begin{bmatrix} \cos\omega_i t & \cos(\omega_i t - \frac{2\pi}{3}) & \cos(\omega_i t + \frac{2\pi}{3}) \\ A_1\sin\omega_i t & A_1\sin(\omega_i t - \frac{2\pi}{3}) & A_1\sin(\omega_i t + \frac{2\pi}{3}) \\ B_1 & B_1 & B_1 \end{bmatrix}\begin{bmatrix} \cos(\theta_{s2}) & \cos(\theta_{s2}-2\pi/3) & \cos(\theta_{s2}+2\pi/3) \\ \cos(\theta_{s2}-2\pi/3) & \cos(\theta_{s2}+2\pi/3) & \cos(\theta_{s2}) \\ \cos(\theta_{s2}+2\pi/3) & \cos(\theta_{s2}) & \cos(\theta_{s2}-2\pi/3) \end{bmatrix},$$

(F.9)

where $B_1 = \dfrac{1}{2q\cos(\alpha_o)}$. Thus from (F.8) and (F.9) one can write:

$$(K_0D)_1(D_2)^T = \begin{bmatrix} K_1'\cos(\omega_o t + \alpha_o) & K_1'\cos(\omega_o t + \alpha_o - \frac{2\pi}{3}) & K_1'\cos(\omega_o t + \alpha_o + \frac{2\pi}{3}) \\ -A_1K_1'\sin(\omega_o t + \alpha_o) & -A_1K_1'\sin(\omega_o t + \alpha_o - \frac{2\pi}{3}) & -A_1K_1'\sin(\omega_o t + \alpha_o + \frac{2\pi}{3}) \\ \frac{1-a}{3} & \frac{1-a}{3} & \frac{1-a}{3} \end{bmatrix},$$ (F.10)

where $K_1' = \frac{3}{2}(\frac{2}{3}q\frac{1-a}{3}(2q))\cos(\alpha_o) = \frac{2}{3}(1-a)q^2\cos(\alpha_o)$.

**4**-Determaining $(K_0D)_2(D_2)^T$

Comparing the terms $(K_0D)_1$ and $(K_0D)_2$, one can find easily the term $(K_0D)_2(D_2)^T$ from equation (F.10) as follows:

Appendix F. Calculating the term $(K_0D)D^T(K_0)^{-1}$

$$(K_0D)_2(D_2)^T = \begin{bmatrix} -A_1K_2'\sin(\omega_o t + \alpha_o) & -A_1K_2'\sin(\omega_o t + \alpha_o - \dfrac{2\pi}{3}) & -A_1K_2'\sin(\omega_o t + \alpha_o + \dfrac{2\pi}{3}) \\ -K_2'\cos(\omega_o t + \alpha_o) & -K_2'\cos(\omega_o t + \alpha_o - \dfrac{2\pi}{3}) & -K_2'\cos(\omega_o t + \alpha_o + \dfrac{2\pi}{3}) \\ 0 & 0 & 0 \end{bmatrix}, \quad \text{(F.11)}$$

where $K_2' = \dfrac{3}{2}(\dfrac{2}{3}q\dfrac{1-a}{3}(2q))\sin(\alpha_o) = \dfrac{2}{3}(1-a)q^2\sin(\alpha_o)$.

From (F.6) and (F.10),

$$(K_0D)_1(D)^T = (K_0D)_1(D_1 + D_2)^T$$

$$= \frac{2}{3}q^2\cos(\alpha_o)\begin{bmatrix} \cos(\omega_o t + \alpha_o) & \cos(\omega_o t + \alpha_o - \dfrac{2\pi}{3}) & \cos(\omega_o t + \alpha_o + \dfrac{2\pi}{3}) \\ (2a-1)^2\sin(\omega_o t + \alpha_o) & (2a-1)^2\sin(\omega_o t + \alpha_o - \dfrac{2\pi}{3}) & (2a-1)^2\sin(\omega_o t + \alpha_o + \dfrac{2\pi}{3}) \\ \dfrac{1}{2q^2\cos(\alpha_o)} & \dfrac{1}{2q^2\cos(\alpha_o)} & \dfrac{1}{2q^2\cos(\alpha_o)} \end{bmatrix}. \quad \text{(F.12)}$$

From (F.7) and (F.11),

$$(K_0D)_2(D)^T = (K_0D)_2(D_1 + D_2)^T$$

$$= \frac{2}{3}q^2\sin(\alpha_o)\begin{bmatrix} (2a-1)^2\sin(\omega_o t + \alpha_o) & (2a-1)^2\sin(\omega_o t + \alpha_o - \dfrac{2\pi}{3}) & (2a-1)^2\sin(\omega_o t + \alpha_o + \dfrac{2\pi}{3}) \\ -\cos(\omega_o t + \alpha_o) & -\cos(\omega_o t + \alpha_o - \dfrac{2\pi}{3}) & -\cos(\omega_o t + \alpha_o + \dfrac{2\pi}{3}) \\ 0 & 0 & 0 \end{bmatrix}. \quad \text{(F.13)}$$

Therefore, from (F.12) and (F.13), the term $((K_0D)_1 + (K_0D)_2)(D_1 + D_2)^T$ can be calculated.

**5-** Calculation the term $(K_0D)D^T(K_0)^{-1}$

One can write: $(K_0D)D^T(K_0)^{-1} = ((K_0D)D^T)_1(K_0)^{-1} + ((K_0D)D^T)_2(K_0)^{-1}$. Also we have :

Appendix F. Calculating the term $(K_0 D) D^T (K_0)^{-1}$

$$(K_o)^{-1} = \begin{bmatrix} \cos \omega_o t & \sin \omega_o t & 1 \\ \cos(\omega_o t - \dfrac{2\pi}{3}) & \sin(\omega_o t - \dfrac{2\pi}{3}) & 1 \\ \cos(\omega_o t + \dfrac{2\pi}{3}) & \sin(\omega_o t + \dfrac{2\pi}{3}) & 1 \end{bmatrix}. \tag{F.14}$$

Finally, from (F.12), (F.13) and (F.14), one can get:

$$(K_0 D) D^T (K_0)^{-1} = q^2 \cos(\alpha_o) \begin{bmatrix} \cos(\alpha_o) & \sin(\alpha_o) & 0 \\ (2a-1)^2 \sin(\alpha_o) & (2a-1)^2 \cos(\alpha_o) & 0 \\ 0 & 0 & \dfrac{1}{q^2 \cos(\alpha_o)} \end{bmatrix}. \tag{F.15}$$

# Appendix G

# Overall Dynamic Model Equations of the Wind Turbine System

The overall dynamic model of the system contains equations of the MC, induction generator, and wind turbine as follows:

**G.1 State equations of the Matrix Converter system**

The overall state-space-*qdo* dynamic model of the balanced three-phase MC system, shown in Fig. 4.1 is given by equations (2.49), (2.51), and (2.57) which are repeated here:

$$\frac{d}{dt}(i_{qO}) = -\frac{R_o}{L_o}i_{qO} - \omega_o i_{dO} + \frac{1}{L_o}(v_{qO} - v_{q\_out}),$$
(G.1)

$$\frac{d}{dt}(i_{dO}) = \omega_o i_{qO} - \frac{R_o}{L_o}i_{dO} + \frac{1}{L_o}(v_{dO} - v_{d\_out}),$$
(G.2)

$$\frac{d}{dt}(i_{qi}^D) = -\frac{R_i}{L_i}i_{qi}^D - \frac{\omega_i}{2a-1}i_{di}^D - \frac{1}{L_i}v_{qO} + \frac{1}{L_i}v_{q\_in}^D,$$
(G.3)

$$\frac{d}{dt}(i_{di}^D) = \omega_i(2a-1)i_{qi}^D - \frac{R_i}{L_i}i_{di}^D - \frac{1}{L_i}v_{dO} + \frac{1}{L_i}v_{d\_in}^D,$$
(G.4)

$$\frac{d}{dt}v_{qo} = -\frac{q^2\cos^2(\alpha_o)}{C}i_{qO} - \frac{q^2\cos(\alpha_o)\sin(\alpha_o)}{C}i_{dO} + \frac{1}{C}i_{qi}^D - \frac{\omega_i}{2a-1}v_{dO},$$
(G.5)

$$\frac{d}{dt}v_{do} = -\frac{q^2(2a-1)^2\cos(\alpha_o)\sin(\alpha_o)}{C}i_{qO}$$
$$- \frac{q^2(2a-1)^2\cos^2(\alpha_o)}{C}i_{qO} + \frac{1}{C}i_{dG}^D + \omega_i(2a-1)v_{qO}.$$
(G.6)

**G.2  State Equations of Induction Generator**

From equations  (3.12)-(3.16), one can write:

Appendix G. Overall Dynamic Model Equations…

$$\frac{d\psi_{qs}}{dt} = C_1\psi_{qs} - \omega_e\psi_{ds} + C_2\psi_{qr} + \omega_b v_{qs},$$ (G.7)

$$\frac{d\psi_{ds}}{dt} = \omega_e\psi_{qs} + C_1\psi_{ds} + C_2\psi_{dr} + \omega_b v_{ds},$$ (G.8)

$$\frac{d\psi_{qr}}{dt} = C_3\psi_{qs} + C_4\psi_{qr} - (\omega_e - \omega_{re})\psi_{dr},$$ (G.9)

$$\frac{d\psi_{dr}}{dt} = C_3\psi_{ds} + (\omega_e - \omega_{re})\psi_{qr} + C_4\psi_{dr},$$ (G.10)

where:

$$C_1 = \omega_b \frac{r_s}{x_{ls}}\left(\frac{x^*_{ml}}{x_{ls}} - 1\right), C_2 = \omega_b \frac{r_s}{x_{ls}}\frac{x^*_{ml}}{x_{lr}}, C_3 = \omega_b \frac{r_r}{x_{lr}}\frac{x^*_{ml}}{x_{ls}}, C_4 = \omega_b \frac{r_r}{x_{lr}}\left(\frac{x^*_{ml}}{x_{lr}} - 1\right),$$

$$x^*_{ml} = (x_m^{-1} + x_{ls}^{-1} + x_{lr}^{-1})^{-1}.$$

In addition, the electromechanical torque of the machine can be written as follows:

$$T_e = \frac{3}{2}\left(\frac{p}{2}\right)\frac{1}{\omega_b}(\psi_{ds}i_{qs} - \psi_{qs}i_{ds}) = C_5(\psi_{dr}\psi_{qs} - \psi_{qr}\psi_{ds}),$$ (G.11)

where $C_5 = \frac{3}{2}\frac{P}{2}\frac{1}{\omega_b}\frac{x^*_{ml}}{x_{ls}x_{lr}}.$

## G.3 Rotor and Shaft State Equations of the Wind Turbine

From equations (3.6)-(3.8), one gets:

$$\frac{d}{dt}\omega_T = \frac{1}{J_T}[T_T - (K_s\delta\theta + B\delta\omega)],$$ (G.12)

$$\frac{d}{dt}\delta\theta = \omega_T - \frac{\omega_g}{n_{gear}},$$ (G.13)

$$\frac{d}{dt}\omega_g = \frac{1}{J_G}[\frac{1}{n_{gear}}(K_s\delta\theta + B\delta\omega) - T_e],$$ (G.14)

where

Appendix G. Overall Dynamic Model Equations…

$$T_T = \frac{1}{2\omega_T} \rho A_r C_p(\beta, \lambda) V_w^3 \text{ is the turbine mechanical torque,}$$

$$C_p(\lambda, \beta) = (0.44 - 0.0167\beta) \sin[(\frac{\pi(-3+\lambda)}{15-0.3\beta})] - 0.00184(-3+\lambda)\beta,$$

$\delta\theta = \theta_T - \theta_g / n_{gear}$, $\delta\omega = \omega_T - \omega_g / n_{gear}$, and $T_e$ is the generator electromechanical torque.

## G.4  Complete Dynamic Model Equations

At the input and output terminals of the MC, one can write:

$$v_{qs} = v_{q\_out}, \ v_{ds} = v_{d\_out}, \tag{G.15}$$

$$i_{qs} = i_{qo}, \ i_{ds} = i_{do}, \ i_{qi}^D = i_{qG}^D, \ i_{di}^D = i_{dG}^D, \tag{G.16}$$

$$\omega_e = \omega_o, \ \omega_i = \omega_{grid}, \ \omega_g = \frac{2}{P}\omega_{re}, \tag{G.17}$$

$$v_{qG} = v_{q\_in}, \ v_{dG} = v_{d\_in}. \tag{G.18}$$

In equations (G.7) and (G.8), the generator terminal voltages, $v_{qs}$ and $v_{ds}$, should be stated in terms of state variables and inputs variables. Note that, for the overall system, the grid voltage, $v_{qG}$ and $v_{dG}$, are the input variables.

From equation (G.1) and (G.2), the generator voltage can be written as follow:

$$v_{qs} = v_{q\_out} = -L_o \frac{d}{dt} i_{qs} - R_o i_{qs} - L_0 \omega_e i_{ds} + v_{qo}, \tag{G.19}$$

$$v_{ds} = v_{d\_out} = -L_o \frac{d}{dt} i_{ds} + L_o \omega_e i_{qs} - R_o i_{ds} + v_{do}. \tag{G.20}$$

The generator stator current equations, in the *dqo* frame, can be obtained from the flux equation equations as follows:

$$i_{qs} = \frac{1}{x_{ls}}[\psi_{qs}(1 - \frac{x_{ml}^*}{x_{ls}}) - \frac{x_{ml}^*}{x_{lr}}\psi_{qr}], \tag{G.21}$$

Appendix G. Overall Dynamic Model Equations…

$$i_{ds} = \frac{1}{x_{ls}}[\psi_{ds}(1 - \frac{x_{ml}^*}{x_{ls}}) - \frac{x_{ml}^*}{x_{lr}}\psi_{dr}].$$
(G.22)

Substituting the generator currents, equations (G.21) and (G.22), and their derivations in equations (G.19) and (G.20), and using equations (G.9) and (G.10), the generator terminal voltage can be written as a function of the state variables of the system, as follows:

$$v_{qs} = \frac{d}{dt}(\psi_{qs})\frac{-L_o}{x_{ls}}[1 - \frac{x_{ml}^*}{x_{ls}}] + \psi_{qs}(C_3\frac{L_o}{x_{ls}}\frac{x_{ml}^*}{x_{ls}} - \frac{R_o}{x_{ls}}[1 - \frac{x_{ml}^*}{x_{ls}}]) - \psi_{ds}\frac{L_0\omega_e}{x_{ls}}[1 - \frac{x_{ml}^*}{x_{ls}}]$$
$$+ \psi_{qr}\frac{x_{ml}^*}{x_{ls}}(C_4\frac{L_o}{x_{ls}} + \frac{R_o}{x_{ls}}) + \psi_{dr}\frac{L_0}{x_{ls}}\frac{x_{ml}^*}{x_{ls}}\omega_{re} + v_{qo},$$
(G.23)

$$v_{ds} = \frac{d}{dt}(\psi_{ds})\frac{-L_o}{x_{ls}}[1 - \frac{x_{ml}^*}{x_{ls}}] + \psi_{qs}(\frac{L_o\omega_e}{x_{ls}}[1 - \frac{x_{ml}^*}{x_{ls}}]) + \psi_{ds}(\frac{L_o}{x_{ls}}\frac{x_{ml}^*}{x_{ls}}C_3 - \frac{R_o}{x_{ls}}[1 - \frac{x_{ml}^*}{x_{ls}}])$$
$$- \psi_{qr}\frac{L_o x_{ml}^*}{x_{ls}x_{ls}}\omega_{re} + \psi_{dr}\frac{x_{ml}^*}{x_{ls}x_{ls}}(L_oC_4 + R_o) + v_{do}.$$
(G.24)

Now, using equations (G.23), (G.24) and (G.17), the stator flux state-equations, (G.7) and (G.8), can be stated as a function of states variables of the system, as follows:

$$\frac{d}{dt}\psi_{qs} = C_1^*\psi_{qs} + C_2^*\omega_e\psi_{ds} + C_3^*\psi_{qr} + C_4^*\psi_{dr}\omega_g + C_5^*\omega_e v_{qo},$$
(G.25)

$$\frac{d}{dt}\psi_{ds} = -C_2^*\omega_e\psi_{qs} + C_1^*\psi_{ds} - C_4^*\psi_{qr}\omega_g + C_3^*\psi_{dr} + C_5^*\omega_e v_{do},$$
(G.26)

where

$$C_0 = \omega_b\frac{L_o}{x_{ls}}[1 - \frac{x_{ml}^*}{x_{ls}}] + 1, \quad C_1^* = \frac{1}{C_0}(C_1 + C_3\frac{\omega_b L_o}{x_{ls}}\frac{x_{ml}^*}{x_{ls}} - \frac{\omega_b R_o}{x_{ls}}[1 - \frac{x_{ml}^*}{x_{ls}}]),$$

$$C_2^* = \frac{1}{C_0}(-1 - \frac{L_0\omega_b}{x_{ls}}[1 - \frac{x_{ml}^*}{x_{ls}}]), \quad C_3^* = \frac{1}{C_0}(C_2 + \frac{\omega_b x_{ml}^*}{x_{ls}}(C_4\frac{L_o}{x_{ls}} + \frac{R_o}{x_{ls}})), \quad C_4^* = \frac{1}{C_0}\frac{\omega_b L_0}{x_{ls}}\frac{x_{ml}^*}{x_{ls}}, \quad C_5^* = \frac{1}{C_0}.$$

It is worth mentioning that, upon the assumption of $\omega_e = \omega_b$ the above coefficients are independent of the frequency variations.

Finally, in following the output voltage state equations of the MC are rewritten. Substituting equations (G.16), (G.21) and (G.22) in equations (G.5) and (G.6), one gets:

208

Appendix G. Overall Dynamic Model Equations…

$$\frac{d}{dt}v_{qo} = A_7\psi_{qs} + A_7'\psi_{ds} + A_8\psi_{qr} + A_8'\psi_{dr} + \frac{1}{C}i_{qG}^D - \frac{\omega_{grid}}{2a-1}v_{do},$$  (G.27)

$$\frac{d}{dt}v_{do} = A_7'(2a-1)^2\psi_{qs} + A_7(2a-1)^2\psi_{ds} + A_8'(2a-1)^2\psi_{qr} + A_8(2a-1)^2\psi_{dr}$$

$$+ \frac{1}{C}i_{dG}^D + \omega_{grid}(2a-1)v_{qo},$$  (G.28)

where:

$$A_7 = -\frac{q^2\cos^2(\alpha_o)}{Cx_{LS}}(1-\frac{x_{ml}^*}{x_{LS}}), \qquad A_7' = -\frac{q^2\cos(\alpha_o)\sin(\alpha_o)}{Cx_{LS}}(1-\frac{x_{ml}^*}{x_{LS}}), \qquad A_8 = \frac{q^2\cos^2(\alpha_o)}{Cx_{LS}}\frac{x_{ml}^*}{x_{LS}},$$

$$A_8' = \frac{q^2\cos(\alpha_o)\sin(\alpha_o)}{Cx_{LS}}\frac{x_{ml}^*}{x_{LS}}.$$

Substituting equation (G.11) in (G.14), the generator shaft speed state equation becomes:

$$\frac{d}{dt}\omega_g = \frac{1}{J_G}[\frac{1}{n_{gear}}(K_s\Delta\theta + B(\omega_T - \frac{2\omega_G}{Pn_{gear}}) - C_5(\psi_{dr}\psi_{qs} - \psi_{qr}\psi_{ds})].$$  (G.29)

Also, the wind turbine shaft speed from equations (G.12) and turbine torque definition is:

$$\frac{d}{dt}\omega_T = \frac{1}{J_T}[\frac{1}{2\omega_T}\rho A_r C_p(\beta,\lambda)V_w^3 - (K_s\Delta\theta + B(\omega_T - \frac{2\omega_G}{PR_G}))].$$  (G.30)

Eventually, the complete dynamic model of the wind turbine system can be summarized in the form of eleven state-equations, as follows:

$$\frac{d}{dt}i_{qG}^D = -\frac{R_i}{L_i}i_{qG}^D - \frac{\omega_{grid}}{2a-1}i_{dG}^D - \frac{1}{L_i}v_{qo} + \frac{1}{L_i}v_{qG}^D,$$  (G.31)

$$\frac{d}{dt}i_{dG}^D = \omega_{grid}(2a-1)i_{qG}^D - \frac{R_i}{L_i}i_{dG}^D - \frac{1}{L_i}v_{do} + \frac{1}{L_i}v_{dG}^D,$$  (G.32)

Appendix G. Overall Dynamic Model Equations…

$$\frac{d}{dt}v_{qo} = A_7\psi_{qs} + A_7'\psi_{ds} + A_8\psi_{qr} + A_8'\psi_{dr} + \frac{1}{C}i_{qG}^D - \frac{\omega_{grid}}{2a-1}v_{do} ,$$

(G.33)

$$\frac{d}{dt}v_{do} = A_7'(2a-1)^2\psi_{qs} + A_7(2a-1)^2\psi_{ds} + A_8'(2a-1)^2\psi_{qr} + A_8(2a-1)^2\psi_{dr}$$

$$+ \frac{1}{C}i_{dG}^D + \omega_{grid}(2a-1)v_{qo} ,$$

(G.34)

$$\frac{d}{dt}\psi_{qs} = C_1^*\psi_{qs} + C_2^*\omega_e\psi_{ds} + C_3^*\psi_{qr} + C_4^*\psi_{dr}\omega_g + C_5^*\omega_e v_{qo} ,$$

(G.35)

$$\frac{d}{dt}\psi_{ds} = -C_2^*\omega_e\psi_{qs} + C_1^*\psi_{ds} - C_4^*\psi_{qr}\omega_g + C_3^*\psi_{dr} + C_5^*\omega_e v_{do} ,$$

(G.36)

$$\frac{d}{dt}\varphi_{qr} = C_3\psi_{qs} + C_4\psi_{qr} - (\omega_e - \omega_g)\psi_{dr} ,$$

(G.37)

$$\frac{d}{dt}\varphi_{dr} = C_3\psi_{ds} + (\omega_e - \omega_g)\psi_{qr} + C_4\psi_{dr} ,$$

(G.38)

$$\frac{d}{dt}\omega_G = \frac{1}{J_G}[\frac{1}{n_{gear}}(K_s\Delta\theta + B(\omega_T - \frac{2\omega_g}{Pn_{gear}}) - C_5(\psi_{dr}\psi_{qs} - \psi_{qr}\psi_{ds})] ,$$

(G.39)

$$\frac{d}{dt}\theta = \omega_T - \frac{2\omega_g}{Pn_{gear}} ,$$

(G.40)

$$\frac{d}{dt}\omega_T = \frac{1}{J_T}[\frac{1}{2\omega_T}\rho A_r C_p(\beta,\lambda)V_w^3 - (K_s\Delta\theta + B(\omega_T - \frac{2\omega_g}{PR_G}))] .$$

(G.41)

Note that in the state equations the grid voltage in *qdo* frame transferred to output side of the MC, based on equation (5-8), can be rewritten as follows:

$$\bar{v}_{qdoG}^D = qV_{Gm}\begin{bmatrix} \cos(\alpha_o) \\ -\sin(\alpha_o) \\ 0 \end{bmatrix} .$$

(G.42)

# Appendix H

# Incorporating Constant *V/f* strategy in the Overall Dynamic Model Equations

The speed control of the induction generator is commonly performed based on the constant *V/f* strategy. In other words, variation of the terminal frequency of the induction generator (synchronous speed) should be related to the terminal voltage of induction generator. In the following, first grid terminal voltage in *qdo* frame is determined, and then, the state equations are rewritten.

The voltages $v_{qG}^D$ and $v_{dG}^D$, i.e., the grid voltages in the *dqo*-D frame, are obtained as follows:

$$\bar{v}_{qdoG}^D = (K_O D)\bar{v}_{abcG}, \tag{H.1}$$

where $\bar{v}_{abcG} = V_M \begin{bmatrix} \cos(\omega_i t + \alpha_i) \\ \cos(\omega_i t + \alpha_i - 2\pi/3) \\ \cos(\omega_i t + \alpha_i + 2\pi/3) \end{bmatrix}$ and

$K_o D =$

$$\frac{2}{3}q\cos(\alpha_o)\begin{bmatrix} \cos(\omega_i t) & \cos(\omega_i t - \frac{2\pi}{3}) & \cos(\omega_i t + \frac{2\pi}{3}) \\ (2a-1)\sin(\omega_i t) & (2a-1)\sin(\omega_i t - \frac{2\pi}{3}) & (2a-1)\sin(\omega_i t + \frac{2\pi}{3}) \\ \frac{1}{2q\cos(\alpha_o)} & \frac{1}{2q\cos(\alpha_o)} & \frac{1}{2q\cos(\alpha_o)} \end{bmatrix} +$$

$$\frac{2}{3}q\sin(\alpha_o)\begin{bmatrix} (2a-1)\sin(\omega_i t) & (2a-1)\sin(\omega_i t - \frac{2\pi}{3}) & (2a-1)\sin(\omega_i t + \frac{2\pi}{3}) \\ -\cos(\omega_i t) & -\cos(\omega_i t - \frac{2\pi}{3}) & -\cos(\omega_i t + \frac{2\pi}{3}) \\ 0 & 0 & 0 \end{bmatrix}.$$

Substituting the equations for $\bar{v}_{qdoG}^D$ and $K_0 D$ in (H.1), one gets:

Appendix H. Incorporating Constant V/f...

$$\bar{v}_{qdoG}^{D} = V_M \frac{2}{3} q \left[ \frac{3}{2} \cos(\alpha_o) \begin{bmatrix} \cos(\alpha_i) \\ (2a-1)\sin(-\alpha_i) \\ 0 \end{bmatrix} + \frac{3}{2} \sin(\alpha_o) \begin{bmatrix} (2a-1)\sin(-\alpha_i) \\ -\cos(\alpha_i) \\ 0 \end{bmatrix} \right]$$

$$= V_M q \left[ \begin{matrix} \cos(\alpha_o)\cos(\alpha_i) - (2a-1)\sin(\alpha_o)\sin(\alpha_i) \\ -\sin(\alpha_o)\cos(\alpha_i) - (2a-1)\cos(\alpha_o)\sin(\alpha_i) \\ 0 \end{matrix} \right].$$

(H.2)

Taking the phase angle of the input voltage as a reference and equal to zero, i.e., $\alpha_i = 0$, equation (H.2) can be rewritten as follows :

$$\bar{v}_{qdoG}^{D} = V_M q \begin{bmatrix} \cos(\alpha_o) \\ -\sin(\alpha_o) \\ 0 \end{bmatrix}$$

(H.3)

In order to take into account the constant *V/f* strategy in the equations, one can write:

$$K_{VF} = \frac{q_{rated}}{\omega_{e\_rated}}$$

(H.4)

where $K_{VF}$ is a constant parameter, and $q_{rated}$ and $\omega_{e\_rated}$ are the MC rated voltage gain and output frequency, respectively.

Subsisting (H.4) in (H.3):

$$v_{qdoG}^{D} = V_M K_{VF} \omega_e \begin{bmatrix} \cos(\alpha_o) \\ -\sin(\alpha_o) \\ 0 \end{bmatrix}$$

(H.5)

Subsisting (H.5) in equations (G.31) and (G.32) results in :

$$\frac{d}{dt} i_{qG}^{D} = -\frac{R_i}{L_i} i_{qG}^{D} - \frac{\omega_{grid}}{2a-1} i_{dG}^{D} - \frac{1}{L_i} v_{qo} + \frac{V_M K_{VF} \cos(\alpha_o)}{L_i} \omega_e$$

(H.6)

$$\frac{d}{dt} i_{dG}^{D} = \omega_{grid}(2a-1) i_{qG}^{D} - \frac{R_i}{L_i} i_{dG}^{D} - \frac{1}{L_i} v_{do} - \frac{V_M K_{VF} \sin(\alpha_o)}{L_i} \omega_e$$

(H.7)

Appendix H. Incorporating Constant V/f…

In order to take into account the constant *V/f* strategy for other equations, the only minor changes are related to the coefficients of equations (G.33) and (G.34) as follows:

$$A_7 = \frac{q^2 \cos^2(\alpha_o)}{Cx_{LS}}(\frac{x_{ml}^*}{x_{LS}} - 1) = \frac{(K_{VF}\omega_e)^2 \cos^2(\alpha_o)}{C\omega_e L_S}(\frac{x_{ml}^*}{x_{LS}} - 1)$$

$$= \frac{(K_{VF})^2}{CL_S}(\frac{x_{ml}^*}{x_{LS}} - 1)\omega_e \cos^2(\alpha_o) = A_{7\_1}\omega_e \cos^2(\alpha_o),$$

where $L_s = \dfrac{x_{LS}}{\omega_e}$ and $A_{7\_1} = \dfrac{(K_{VF})^2}{CL_S}(\dfrac{x_{ml}^*}{x_{LS}} - 1)$.

$$A_7' = -\frac{q^2 \cos(\alpha_o)\sin(\alpha_o)}{Cx_{LS}}(1 - \frac{x_{ml}^*}{x_{LS}}) = \frac{1}{2}A_{7\_1}\omega_e \sin(2\alpha_o).$$

$$A_8 = \frac{(K_{VF}\omega_e)^2 \cos^2(\alpha_o)}{C\omega_e L_S}(\frac{x_{ml}^*}{x_{LS}}) = \frac{(K_{VF})^2}{CL_S}(\frac{x_{ml}^*}{x_{LS}})\omega_e \cos^2(\alpha_o) = A_{8\_1}\omega_e \cos^2(\alpha_o),$$

where $A_{8\_1} = \dfrac{(K_{VF})^2}{CL_S}(\dfrac{x_{ml}^*}{x_{LS}})$.

$$A_8' = \frac{q^2 \cos(\alpha_o)\sin(\alpha_o)}{Cx_{LS}}\frac{x_{ml}^*}{x_{LS}} = \frac{1}{2}A_{8\_1}\omega_e \sin(2\alpha_o).$$

Finally, the overall equations of the nonlinear model with the constant *V/f* strategy are as follows:

$$\frac{d}{dt}i_{qG}^D = -\frac{R_i}{L_i}i_{qG}^D - \frac{\omega_{grid}}{2a-1}i_{dG}^D - \frac{1}{L_i}v_{qo} + \frac{V_M K_{VF}\cos(\alpha_o)}{L_i}\omega_e, \tag{H.8}$$

$$\frac{d}{dt}i_{dG}^D = \omega_i(2a-1)i_{qG}^D - \frac{R_i}{L_i}i_{dG}^D - \frac{1}{L_i}v_{do} - \frac{V_M K_{VF}\sin(\alpha_o)}{L_i}\omega_e, \tag{H.9}$$

Appendix H. Incorporating Constant V/f…

$$\frac{d}{dt}v_{qo} = \omega_e\{A_{7\_1}[\cos^2(\alpha_o)\psi_{qs} + \frac{1}{2}\sin(2\alpha_o)\psi_{ds}]$$
$$+ A_{8\_1}[\cos^2(\alpha_o)\psi_{qr} + \frac{1}{2}\sin(2\alpha_o)\psi_{dr}]\} + \frac{1}{C}i_{qG}^D - \frac{\omega_i}{2a-1}v_{do},$$

(H.10)

$$\frac{d}{dt}v_{do} = (2a-1)^2\omega_e\{A_{7\_1}[\frac{1}{2}\sin(2\alpha_o)\psi_{qs} + \cos^2(\alpha_o)\psi_{ds}]$$
$$+ A_{8\_1}[\frac{1}{2}\sin(2\alpha_o)\psi_{qr} + \cos^2(\alpha_o)\psi_{dr}]\} + \frac{1}{C}i_{dG}^D + \omega_i(2a-1)v_{qo},$$

(H.11)

$$\frac{d}{dt}\varphi_{qs} = C_1^*\psi_{qs} + C_2^*\psi_{ds} + C_3^*\psi_{qr} + C_4^*\psi_{dr}\omega_r + C_5^*v_{qo},$$

(H.12)

$$\frac{d}{dt}\varphi_{ds} = -C_2^*\psi_{qs} + C_1^*\psi_{ds} - C_4^*\psi_{qr}\omega_r + C_3^*\psi_{dr} + C_5^*v_{do},$$

(H.13)

$$\frac{d}{dt}\varphi_{qr} = C_3\psi_{qs} + C_4\psi_{qr} - (\omega_e - \omega_r)\psi_{dr},$$

(H.14)

$$\frac{d}{dt}\varphi_{dr} = C_3\psi_{ds} + (\omega_e - \omega_r)\psi_{qr} + C_4\psi_{dr},$$

(H.15)

$$\frac{d}{dt}\omega_r = C_6[-C_5(\psi_{dr}\psi_{qs} - \psi_{qr}\psi_{ds}) + \frac{1}{R_G}(K_s\Delta\theta + B(\omega_T - \frac{2\omega_r}{PR_G}))],$$

(H.16)

$$\frac{d}{dt}\Delta\theta = \omega_T - \frac{2\omega_r}{PR_G},$$

(H.17)

$$\frac{d}{dt}\omega_T = \frac{1}{J_T}[\frac{(0.5\pi\rho R^2 V_W^3)}{\omega_T}((0.44 - 0.0167\beta)\sin[\frac{\pi(\frac{R\omega_T}{V_W} - 3)}{15 - 0.3\beta}] -$$
$$0.00184(\frac{R\omega_T}{V_W} - 3).\beta) - (K_s\Delta\theta + B(\omega_T - \frac{2\omega_r}{PR_G})]$$

(H.18)

# Appendix I

# Linearized Model Of the Wind Turbine System

## I.1 Linearization the Nonlinear equations

The linearized equations based on the eleven nonlinear equations (H.8)-(H.18) are as follows:

$$
\frac{d}{dt}\Delta i_{qG}^D = -\frac{R_i}{L_i}\Delta i_{qG}^D - \frac{\omega_{grid}}{2a^0-1}\Delta i_{dG}^D - \frac{1}{L_i}\Delta v_{qo} + \frac{V_{Gm}K_{VF}\cos(\alpha_o^0)}{L_i}\Delta\omega_e
$$
$$
+ (\frac{2\omega_i i_{dG}^D}{(2a-1)^2})^0\Delta a - \frac{V_{Gm}K_{VF}(\sin(\alpha_o)\omega_e)^0}{L_i}\Delta\alpha_o \tag{I.1}
$$

$$
\frac{d}{dt}\Delta i_{dG}^D = \omega_{grid}(2a-1)^0\Delta i_{qG}^D - \frac{R_i}{L_i}\Delta i_{dG}^D - \frac{1}{L_i}\Delta v_{do}
$$
$$
- \frac{V_{Gm}K_{VF}\sin(\alpha_o^0)}{L_i}\Delta\omega_e + 2\omega_{grid}(i_{qG}^D)^0\Delta a - \frac{V_{Gm}K_{VF}(\cos(\alpha_o)\omega_e)^0}{L_i}\Delta\alpha_0 \tag{I.2}
$$

$$
\frac{d}{dt}\Delta v_{qo} = \frac{1}{C}\Delta i_{qG}^D - \frac{\omega_{grid}}{2a^0-1}\Delta v_{do} + a_{3,5}\Delta\psi_{qs} + a_{3,6}\Delta\psi_{ds} + a_{3,7}\Delta\psi_{qr}
$$
$$
+ a_{3,8}\Delta\psi_{dr} + b_{3,1}\Delta\omega_e + \frac{2\omega_{grid}v_{do}^0}{(2a^0-1)^2}\Delta a + b_{3,3}\Delta\alpha_o \tag{I.3}
$$

$$
\frac{d}{dt}\Delta v_{do} = \frac{1}{C}\Delta i_{dG}^D + \omega_{grid}(2a-1)^0\Delta v_{qo} + a_{4,5}\Delta\psi_{qs} + a_{4,6}\Delta\psi_{ds} + a_{4,7}\Delta\psi_{qr} + a_{4,8}\Delta\psi_{dr}
$$
$$
+ b_{4,1}\Delta\omega_e + b_{4,2}\Delta a + b_{4,3}\Delta\alpha_o \tag{I.4}
$$

$$
\frac{d}{dt}\Delta\psi_{qs} = C_1^*\Delta\psi_{qs} + C_2^*\omega_e\Delta\psi_{ds} + C_3^*\Delta\psi_{qr} + C_4^*\omega_g^0\Delta\psi_{dr}
$$
$$
+ C_4^*\psi_{dr}^o\Delta\omega_g + C_5^*\omega_e^0\Delta v_{qo} + (C_2^*\psi_{ds}^0 + C_5^*v_{qo}^0)\Delta\omega_e \tag{I.5}
$$

$$
\frac{d}{dt}\psi_{ds} = -C_2^*\omega_e\Delta\psi_{qs} + C_1^*\Delta\psi_{ds} - C_4^*\omega_g^0\Delta\psi_{qr}
$$
$$
+ C_3^*\Delta\psi_{dr} + C_5^*\omega_e^0\Delta v_{do} - C_4^*\psi_{qr}^0\Delta\omega_g + (-C_2^*\psi_{qs}^0 + C_5^*v_{do}^0)\Delta\omega_e \tag{I.6}
$$

Appendix I. Linearized Model…

$$\frac{d}{dt}\Delta\psi_{qr} = C_3\Delta\psi_{qs} + C_4\Delta\psi_{qr} - \omega_e^0\Delta\psi_{dr} + \omega_g^0\Delta\psi_{dr} + \psi_{dr}^0\Delta\omega_g - \psi_{dr}^0\Delta\omega_e, \tag{I.7}$$

$$\frac{d}{dt}\Delta\psi_{dr} = C_3\Delta\psi_{ds} + (\omega_e^0 - \omega_g^0)\Delta\psi_{qr} + C_4\Delta\psi_{dr} - \psi_{qr}^0\Delta\omega_g + \psi_{qr}^0\Delta\omega_e, \tag{I.8}$$

$$\frac{d}{dt}\Delta\omega_g = a_{9,5}\Delta\psi_{qs} + a_{9,6}\Delta\psi_{ds} + a_{9,7}\Delta\psi_{qr} + a_{9,8}\Delta\psi_{dr} - \frac{2B}{PJ_G n_{gear}^2}\Delta\omega_g$$
$$+ \frac{K_s}{J_G n_{gear}}\Delta(\delta\theta) + \frac{B}{J_G n_{gear}}\Delta\omega_T + b_{9,1}\Delta\omega_e \tag{I.9}$$

$$\frac{d}{dt}\Delta(\delta\theta) = \Delta\omega_T - \frac{2}{Pn_{gear}}\Delta\omega_g, \tag{I.10}$$

$$\frac{d}{dt}\Delta\omega_T = K_7\Delta\omega_g + K_5\Delta(\delta\theta) + a_{11,11}\Delta\omega_T + b_{11,4}\Delta V_W + b_{11,5}\Delta\beta, \tag{I.11}$$

where

$$K_1^0 = (\frac{V_W}{\omega_T})^0, \ K_2^0 = \frac{\pi}{15 - 0.3\beta^0}((\frac{R\omega_T}{V_W})^0 - 3), \ K_3^0 = K_1 + K_2\beta^0, \ K_4^0 = -R\frac{\pi V_W^0}{15 - 0.3\beta^0},$$

$$K_6^0 = V_W^0, \ \ K_7^0 = K_1^0(K_6^0)^2\frac{0.3\pi}{(15 - 0.3\beta^0)^2}(\frac{R}{K_1^0} - 3),$$

$$a_{3,5} = A_{7\_1}(\omega_e\cos^2(\alpha_o))^0, \ a_{3,6} = \frac{1}{2}A_{7\_1}(\omega_e\sin(2\alpha_o))^0, \ a_{3,7} = A_{8\_1}(\omega_e\cos^2(\alpha_o))^0,$$

$$a_{3,8} = \frac{1}{2}A_{8\_1}(\omega_e\sin(2\alpha_o))^0, \ a_{4,5} = \frac{1}{2}A_{7\_1}((2a-1)^2\omega_e\sin(2\alpha_o))^0,$$

$$a_{4,6} = A_{7\_1}((2a-1)^2\omega_e\cos^2(\alpha_o))^0, \ a_{4,7} = \frac{1}{2}A_{8\_1}((2a-1)^2\omega_e\sin(2\alpha_o))^0,$$

$$a_{4,8} = A_{8\_1}((2a-1)^2\omega_e\cos^2(\alpha_o))^0, \ a_{9,5} = \frac{-C_6}{J_G(\omega_e^2)^0}\psi_{dr}^0, \ a_{9,6} = \frac{C_6}{J_G(\omega_e^2)^0}\psi_{qr}^0,$$

$$a_{9,7} = \frac{C_6}{J_G(\omega_e^2)^0}\psi_{ds}^0, \ a_{9,8} = -\frac{C_6}{J_G(\omega_e^2)^0}\psi_{qs}^0,$$

$$a_{11,11} = (-(K_1^0)^2 K_6^0\sin(K_2^0) - K_1^0 K_4^0\cos(K_2^0))K_3^0 - (K_1^0)^2 K_5^0 K_6^0 K_4 + K_6,$$

$$b_{3,1} = \{A_7^*[\cos^2(\alpha_o)\varphi_{qs} + \frac{1}{2}\sin(2\alpha_o)\psi_{ds}] + A_8^*[\cos^2(\alpha_o)\psi_{qr} + \frac{1}{2}\sin(2\alpha_o)\psi_{dr}]\}^0,$$

$$b_{3,3} = \{\omega_e\{A_7^*[-\sin(2\alpha_o)\psi_{qs} + \cos(2\alpha_o)\psi_{ds}] + A_8^*[-2\sin(\alpha_o)\psi_{qr} + \cos(2\alpha_o)\psi_{dr}]\}\}^0,$$

216

Appendix I. Linearized Model…

$$b_{4,1} = \{(2a-1)^2\{A_7^*[\frac{1}{2}\sin(2\alpha_o)\psi_{qs} + \cos^2(\alpha_o)\psi_{ds}] + A_8^*[\frac{1}{2}\sin(2\alpha_o)\psi_{qr} + \cos^2(\alpha_o)\psi_{dr}]\}\}^0,$$

$$b_{4,2} = \{4(2a-1)\omega_e\{A_7^*[\frac{1}{2}\sin(2\alpha_o)\psi_{qs} + \cos^2(\alpha_o)\psi_{ds}] + A_8^*[\frac{1}{2}\sin(2\alpha_o)\psi_{qr} + \cos^2(\alpha_o)\psi_{dr}]\}\}^0,$$

$$b_{4,3} = \{(2a-1)^2\omega_e\{A_7^*[\cos(2\alpha_o)\psi_{qs} - \sin(2\alpha_o)\psi_{ds}] + A_8^*[\cos(2\alpha_o)\psi_{qr} - \cos(2\alpha_o)\psi_{dr}]\}\}^0,$$

$$b_{9,1} = \frac{2C_6}{(\omega_e^3)^0}(\psi_{dr}^0\psi_{qs}^0 - \psi_{qr}^0\psi_{ds}^0),$$

$$b_{11,4} = \{(3K_1^0K_6^0\sin(K_2^0) + K_4^0\cos(K_2^0))K_3^0 + 2K_5^0K_6^0K_3 + 3K_1^0K_5^0K_6^0K_4\},$$

$$b_{11,5} = \{K_7^0K_3^0\cos(K_2^0) + K_1^0(K_6^0)^2K_2\sin(K_2^0) + (K_6^0)^2K_3 + K_1^0(K_6^0)^2K_4\}.$$

## I.2 Output equations of the small-signal model

The output of small-signal model contains the grid real and reactive powers, i.e., $\Delta P_{Grid}$ and $\Delta Q_{Grid}$ that can be derived based on the nonlinear equations (3.49) and (3.50), as follows:

$$\Delta P_{Grid} = \frac{3V_{Gm}}{2K_{VF}\omega_e^0}\{\cos(\alpha_o^0)\Delta i_{qG}^D - \sin(\alpha_o^0)\Delta i_{dG}^D - (\sin(\alpha_o)i_{qG}^D + \cos(\alpha_o)i_{dG}^D)^0\Delta\alpha_o$$
$$- \frac{1}{\omega_e^0}(\cos(\alpha_o)i_{qG}^D - \sin(\alpha_o)i_{dG}^D)^0\Delta\omega_e\}, \tag{I.12}$$

$$\Delta Q_{Grid} = -\frac{3V_{Gm}}{2K_{VF}}(\frac{1}{(2a-1)\omega_e})^0\{\sin(\alpha_o^0)\Delta i_{qG}^D + \cos(\alpha_o^0)\Delta i_{dG}^D$$
$$+ (\cos(\alpha_o)i_{qG}^D - \sin(\alpha_o)i_{dG}^D)^0\Delta\alpha_o \tag{I.13}$$
$$+ (\sin(\alpha_o)i_{qG}^D + \cos(\alpha_o)i_{dG}^D)^0(\frac{-2}{(2a^0-1)}\Delta a - \frac{1}{\omega_e^0}\Delta\omega_e)\}.$$

## I.3  Numerical values of the Jacobian matrices

The numerical values of the Jacobian matrices A, B, C, and D at the operating point are:

A=

| -100 | -628.32 | -1000 | 0 | 0 | 0 | 0 | 0 | 0 | 0 | 0 |
|---|---|---|---|---|---|---|---|---|---|---|
| 226.19 | -100 | 0 | -1000 | 0 | 0 | 0 | 0 | 0 | 0 | 0 |
| 1e6 | 0 | 0 | -628.32 | -1.0479e5 | 0 | 1.025e5 | 0 | 0 | 0 | 0 |
| 0 | 1e6 | 226.19 | 0 | 0 | -37726 | 0 | 36902 | 0 | 0 | 0 |
| 0 | 0 | 325.55 | 0 | -45.54 | -376.99 | 44.375 | 50.528 | 212.38 | 0 | 0 |
| 0 | 0 | 0 | 325.55 | 376.99 | -45.54 | -50.528 | 44.375 | -14.612 | 0 | 0 |
| 0 | 0 | 0 | 0 | 28.905 | 0 | -29.551 | 1.5489 | 1591.1 | 0 | 0 |
| 0 | 0 | 0 | 0 | 0 | 28.905 | -1.5489 | -29.551 | -109.47 | 0 | 0 |
| 0 | 0 | 0 | 0 | 0.87472 | -0.060182 | -0.89748 | 0.014545 | -1.0531 | 16849 | 42.123 |
| 0 | 0 | 0 | 0 | 0 | 0 | 0 | 0 | -0.025 | 0 | 1 |
| 0 | 0 | 0 | 0 | 0 | 0 | 0 | 0 | 1.25 | -20000 | -55.302 |

B=

| 4331.6 | 5243.1 | 0 | 0 | 0 |
|---|---|---|---|---|
| 0 | -6371.2 | -9.798e5 | 0 | 0 |
| 22411 | -4527.5 | -7.9796e6 | 0 | 0 |
| -7619.9 | -1.792e7 | 3.0415e6 | 0 | 0 |
| -222.94 | 0 | 0 | 0 | 0 |
| 24.59 | 0 | 0 | 0 | 0 |
| -1591.1 | 0 | 0 | 0 | 0 |
| 109.47 | 0 | 0 | 0 | 0 |
| 0.39844 | 0 | 0 | 0 | 0 |
| 0 | 0 | 0 | 0 | 0 |
| 0 | 0 | 0 | 22.848 | -5.3188 |

C=

| 9798 | 0 | 0 | 0 | 0 | 0 | 0 | 0 | 0 | 0 | 0 |
|---|---|---|---|---|---|---|---|---|---|---|
| 0 | -16330 | 0 | 0 | 0 | 0 | 0 | 0 | 0 | 0 | 0 |

D=

| 219.62 | 0 | -24528 | 0 | 0 |
|---|---|---|---|---|
| 108.44 | 1.3627e5 | 1.3799e5 | 0 | 0 |

# Appendix J

# Luenberger Observer Construction

The block diagram of the Luenberger observer is shown in Fig. J-1. The observer is fundamentally a copy of the plant, so that it has the same input and almost the same differential equations. First, the actual measured output $\overline{y}$ is compared to the estimated output $\hat{y}$, and then, using the observer gain $L$, the estimated states $\hat{x}$ is produced so that this state vector tends to the actual state vector $\overline{x}$.
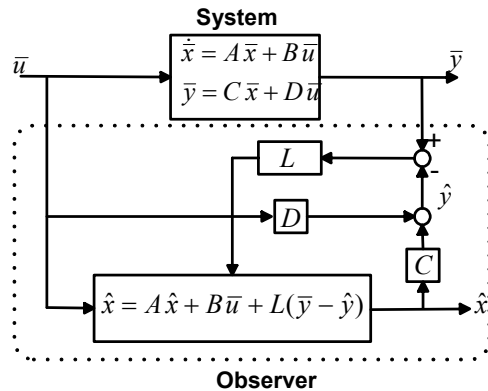


Fig. J-1: The closed-loop feedback system with optimal observer augmented

The observer state-space equations are as follows:

$$\dot{\hat{x}} = A\hat{x} + L(\overline{y} - \hat{y}) + B\overline{u},$$
$$\hat{y} = C\hat{x} + D\overline{u}. \tag{J.1}$$

The state-estimator or observer error is:

$$\overline{e} = \overline{x} - \hat{x}. \tag{J.2}$$

Appendix J. Luenberger Observer

In general, the observer is called asymptotically stable if the observer error converges to zero, for any initial condition $e(0)$, when $t \to \infty$ [136]. For a Luenberger observer, one can prove that observer error dynamics is [130][131]:

$$\dot{e} = \dot{\tilde{x}} - \dot{\hat{x}} = (A - LC)e(t).$$  \hfill (J.3)

Therefore, the Luenberger observer is asymptotically stable if and only if the eigenvalues of $A$-$LC$ are all in the left-half plane. Moreover, arbitrary observer error dynamics can be assigned if and only if $(A^T, C^T)$ is controllable.

In practice, the methods such as pole placement or LQ can be used to find the observer gain $L$ so that the observer is asymptotically stable with desired dynamics. Since the observer dynamics should be much faster than the system itself, we need the eigenvalues of $A$-$LC$ to be farther to the left than those of $A$-$BK$ [130][131].

**J-1 Closed-Loop Equations for the System Based on Observer**

In this subsection, equations of the closed-loop system, comprised of the augmented system together with the state feedback controller, Fig. 4-2, are modified to include the Luenberger observer equations. The closed-loop observer-based state-feedback with integral control scheme is shown in Fig. 4-14.

In this system, the controller contains the following three dynamics:

- The state-feedback equations using the estimated state $\hat{x}$:

$$\bar{u} = -K \begin{bmatrix} \hat{x} \\ \bar{z} \end{bmatrix} = -\begin{bmatrix} K_1 & K_2 \end{bmatrix} \begin{bmatrix} \hat{x} \\ \bar{z} \end{bmatrix} = -K_1 \hat{x} - K_2 \bar{z}.$$  \hfill (J.4)

- The integrator equations:

$$\dot{\bar{z}} = \bar{y} - \bar{y}_r.$$  \hfill (J.5)

- The observer equations:

$$\dot{\hat{x}} = A\hat{x} + L(y - \hat{y}) - BK\hat{x} = (A - BK)\hat{x} + L(y - \hat{y}),$$  \hfill (J.6)

where $\hat{y} = (C - DK)\hat{x}$.

Appendix J. Luenberger Observer

Although the closed-loop system state vector is $\begin{bmatrix} \bar{x} & \bar{z} & \hat{x} \end{bmatrix}^T$, choosing the states representation $\begin{bmatrix} \bar{x} & \bar{z} & \bar{e} \end{bmatrix}^T$ is more practical in the implementation of the state-space model. Therefore, the state-space equations are:

$$\dot{\bar{x}} = A\bar{x} + B\bar{u} = (A - BK_1)\bar{x} - BK_2\bar{z} + BK_1\bar{e} , \tag{J.7}$$

$$\dot{\bar{z}} = \bar{y} - \bar{y}_r = (C - DK_1)\bar{x} - (DK_2)\bar{z} + (DK_1)\bar{e} - \bar{y}_r , \tag{J.8}$$

$$\dot{\bar{e}} = \dot{\bar{x}} - \dot{\hat{x}} = (A - LC)\bar{e} . \tag{J.9}$$

Finally, the output equation is:

$$\bar{y} = C\bar{x} + D\bar{u} = (C - DK_1)\bar{x} - (DK_2)\bar{z} + (DK_1)\bar{e} . \tag{J.10}$$

**J-2 Optimal Observer**

This subsection is dedicated to the use of LQ method to design an optimal observer. The system with a Luenberger observer, equations (J.7)-(J.10), is considered. To use the LQ method to find an optimal observer, the observer dynamic equation should be rewritten as an LQ problem to design the observer gain L in an optimal way. One can prove that the observer error dynamics, equation (J.9), is the same as that of the following fictitious error [130]:

$$\dot{e}_{fic} = A^T e_{fic} + C^T u_{fic} , \tag{J.11}$$

$$u_{fic} = -L^T e_{fic} . \tag{J.12}$$

Equations (J.11) and (J.12) are in the form of a fictitious system and controller; so, it is possible to use the LQ method to design the optimal controller, and get the optimal gain $L^T$ for the system of (J.11). To find the optimal controller, the following requirements should be satisfied:

- $(A^T, C^T)$ is controllable (stabilizable)

- $(Q_{fic}, A^T)$ is observable (detectable)

where $Q_{fic}$ is the penalty weighting matrix of the fictitious error. As with the previous explanation for the LQ method, the design of the optimal observer is possible by solving the corresponding ARE, equation (4.6). Then, the observer gain $L$ matrix can be calculated from the following formula:

$$L = P_{fic} C^T R_{fic}^{-1}, \tag{J.13}$$

where $P_{fic}$ is a unique symmetrical positive semi-definite solution of the ARE, and $R_{fic}$ the penalty weighting matrix of the fictitious control signals.

# Appendix K

# Transfer Function of the Wind Turbine System

$$G(s) = \begin{bmatrix} G_{11} & G_{12} \\ G_{21} & G_{22} \end{bmatrix}$$

$G_{11}=$

219.62 (s+1.935e5)(s+25.48)(s-0.08957) $(s^2+56.24s+2.042e^4)$ $(s^2 +49.24s+6.833e^4)(s^2-90.57s+6.649e^7)(s^2+112.5s + 1.01e^9)$

_____

(s+25.24)$(s^2 + 24.41s+ 188)(s^2 + 56.25s + 2.045e^4)(s^2 +101.8s+1.416e^5)$ $(s^2+99.53s + 9.969e^8)$ $(s^2 + 99.29s+1.05e^9)$

$G_{12}=$

51371893.8(s+5.784e$^4$)(s-5.613e$^4$)(s-2003)(s+27.08)$(s^2+1.954s+14.44)(s^2+56.24s+2.04e4)(s^2 +2142s+2.829e^6)$

_____

(s+25.24) $(s^2 +24.41s+1188)$ $(s^2+56.25s+2.045e^4)$ $(s^2+101.8s +1.416e^5)$ $(s^2+99.53s +9.969e^8)$ $(s^2 +99.29s +1.05e^9)$

$G_{21}=$

108.44(s-4992)(s+1.084e$^4$)(s-48.88)(s-6.062)(s+5.299)$(s^2 +56.19s +2.044e^4)$ $(s^2-3726s+7.169e^7)(s^2-1718s + 7.597e^8)$

_____

(s+25.24) $(s^2+ 24.41s + 1188)$ $(s^2+56.25s+2.045e^4)$ $(s^2+101.8s+1.416e^5)(s^2+99.53s+9.969e^8)$ $(s^2+99.29s + 1.05e^9)$

$G_{22}=$

136270 (s+3.413e$^4$) (s-3.326e$^4$) (s+25.71) $(s^2+24.55s +1193)$ $(s^2+56.25s+2.045e^4)$ $(s^2+92.35s+1.417e^5)$ $(s^2+99.19s+1.034e^9)$

_____

(s+25.24) $(s^2 + 24.41s +1188)$ $(s^2 + 56.25s + 2.045e^4)$ $(s^2 + 101.8s + 1.416e^5)$ $(s^2+99.53s + 9.969e^8)$ $(s^2 + 99.29s + 1.05e^9)$

# Appendix L

# Parameters of the system under study

Table L.1: Parameters of the small wind turbine system

| Induction Generator [123] | Wind Turbine System | Matrix Converter | Grid*(Infinite Bus)* |
|---|---|---|---|
| $V_{rated}$=400[V] | $J_T$=10 [kg.m$^2$] | $R_i$=$R_o$=0.0001[Ω] | $V_G$=400[V] |
| $f_{rated}$=60[Hz], P=6[Poles] | $n_{gear}$=20 | $L_i$=$L_o$=.01 [mH] | $f_G$=60[Hz] |
| $r_s$=0.294, $r_r$=0.156 [Ω] | $\rho_{air}$ =1.25[kg/m$^3$] | C=0.001[mF] | |
| $L_s$=1.39, $L_r$=0.74 [mH], $L_M$=41 [mH] | R=10 [m] | 0<q≤0.87 | |
| J=0.4[Kg.m$^2$], $P_{mech\_loss}$=1%$P_{rated}$ | | 0≤a≤1 | |

Table L.2: Parameters of the system under study

| Induction Generator [96] | Wind Turbine System | Matrix Converter | Grid*(Infinite Bus)* |
|---|---|---|---|
| 500[hp], 2.3[KV], 1773[rpm] | $J_T$=100 [kg.m$^2$] | $R_i$=$R_o$=0.1[Ω] | $V_G$=4[KV][*] |
| $T_B$=1.98×10$^3$[N.m], $I_{B(abc)}$=93.6[A] | $K_s$=2×10$^6$ [Nm/rad] | $L_i$=$L_o$=1 [mH] | $f_G$=60[Hz] |
| $r_s$=0.262, $r_r$=0.187 [Ω] | B=5×10$^3$ [Nm/rad/s] | C=0.1[mF] | |
| $X_{ls}$=1.206, $X_{lr}$=1.206, $X_M$=54.02 [Ω] | $n_{gear}$=20 | 0<q≤0.87 | |
| J=11.06[Kg.m$^2$] | $\rho_{air}$ =1.25[kg/m$^3$] | 0≤a≤1 | |
| P=4[Poles], $P_{mech\_loss}$=1%$P_{rated}$ | R=10 [m] | | |

[*]Note that the voltage rating has not been chosen based on the data of a practical wind turbine system. High voltage levels make the size of the generator impractical due to the high insulation strength requirements.

# Bibliography

[1]     BTM Consults internet homepage, available at http://www.btm.dk/, March 2007.

[2]     CanWEA, *Canadian wind energy association*, available at www.canwea.ca/, February, 2007.

[3]     Donna Cansfield (Ontario Energy Minister), *Address of Onatrio's Largest Wind Farm Officially opens*, , available at aimpowergren.com, April, 2006.

[4]     L. Surugiu, and I. Paraschivoiu, "Environmental, social, and economical aspects of wind energy," *AIAA-2000-3008 Environmental, Social and Economical Aspects of Wind Energy*, $35^{th}$ *Intersociety*, vol.2, pp. 1167-1174.

[5]      S. Krohn, *The wind energy pioneer - Poul la Cour,* Published by The Danish Wind Turbine Manufacturers Association, available at: http://webasp.ac-aix-marseille.fr/rsi/bilan/action_0405 /13LduRempart/Doc/Doc_page/windpower.pdf, February, 2008.

[6]      R. Hoffmann and P. Mutschler, "The Influence of Control Strategies on the Energy Capture of Wind Turbines, " *Application of Electrical Energy*, Piscataway, NJ, USA, 2000, pp. 886-893

[7]     P. Migliore, J. van Dam, and A. Huskey, "Acoustic Tests of Small Wind Turbinesat," available at        http://www.wind.appstate.edu/reports/NRELAcousticTestsofSmallWindTurbines.pdf, February, 2007.

[8]     L. H. Hansen, L. Helle, F. Blaabjerg, E. Ritchie, S. Munk- Nielsen, H. Bindner, P. Sørensen, and B. Bak-Jensen, "Conceptual survey of Generators and Power Electronics for Wind Turbines, " *Risø National Laboratory*, Roskilde, Denmark December 2001.

[9]     O. Carlson, J. Hylander, and K. Thorborg, "Survey of variable speed operation of wind turbines," *In European Union Wind Energy Conf., Goeteborg, Sweden*, May 1996, pp. 406-409.

[10]    M. Idan, D. Lior, and G. Shaviv, "A robust controller for a novel variable speed wind turbine transmission, " *Journal of Solar Energy Engineering*, November 1998, pp.120:247-252.

[11]     S. Bhowmik and R. Spee, "Wind speed estimation based variable speed wind power generation," *Industrial Electronics Society, 1998. IECON '98, Proc. of the 24th Annual Conf. of the IEEE* , vol. 2, 31 Aug.-4 Sept. 1998 pp.596 – 601.

Bibliography

[12]   M. G. Simoes, B. K. Bose, and R. J. Spiegel, "Fuzzy logic based intelligent control of a variable speed cage machine wind generation system, " *IEEE Tran. On Power Electronics*, vol.: 12, Issue: 1, pp. 87 – 95, Jan. 1997.

[13]   Q. Wang and L. Chang, "An intelligent maximum power extraction algorithm for inverter-based variable speed wind turbine systems, " *IEEE Trans. Power Electronics*, vol. 19, Issue: 5, pp. 1242 – 1249, Sept. 2004.

[14]   A. Miller, E. Muljadi, and D.S. Zinger, "A variable speed wind turbine power control," *IEEE Trans. on Energy Conversion*, vol. 12, Issue: 2, pp. 181 – 186, June 1997.

[15]   Xu Longya and C. Wei, "Torque and reactive power control of a doubly fed induction machine by position sensorless scheme, " *IEEE Trans. on Industry Applications*, vol. 31, Issue 3, pp. 636 – 642, May-June 1995.

[16]   W. Lu and B. T. Ooi*,* "Multiterminal LVDC system for optimal acquisition of power in wind-farm using induction generators," *IEEE Trans. On Power Electronics*, vol. 17, NO. 4, pp. 558-563, JULY 2002.

[17]   J.L. Rodriguez-Amenedo, S. Arnalte, and J.C. Burgos, "Automatic generation control of a wind farm with variable speed wind turbines," *IEEE Trans. On Energy Conversion*, vol 17, Issue 2, pp. 279 – 284, June 2002.

[18]   D. Seyoum and M.F. Rahman, "The dynamic characteristics of an isolated self-excited induction generator driven by a wind turbine," *Rec. in Proc. IAS Conf., Industry Applications Conf., Annual Meeting,* vol. 2, Oct. 2002, pp. 731 – 738.

[19]   F. Blaabjerg, Zhe Chen, and S.B. Kjaer, "Power electronics as efficient interface in dispersed power generation systems," *IEEE Trans. on Power Electronics*, vol. 19, Issue: 5 , pp.1184 – 1194, Sept. 2004.

[20]   L.L. Freries, *Wind Energy Conversion Systems* , Prentice Hall,1990.

[21]   S.Heier, *Grid Integration of Wind Energy Conversion Systems*, Chapter 1, John Wiley & Sons Ltd, 1998.

[22]   J.F. Manwell, J.G. McGowan, A.L. Rogers, *Wind Energy Explained, Theory, Design and Application*, Wiley, 2002.

[23]   S. Mathew, *Wind Energy Fundamentals, Resource Analysis, and Economics*, Springer, 2006.

[24]   P.G. Casielles, J. Sanz, and J. Pascual, "Control system for a wind turbine driven self excited asynchronous generator," *in Proc. Mediterranean Electrotechnical Integrating Research,*

Bibliography

*Industry and Education in Energy and Communication Engineering, MELECON '89 Conf.*, April 1989, pp. 95 – 98.

[25]   D.A. Torrey, "Variable-reluctance generators in wind-energy systems, " Rec. in *IEEE PESC '93, Power Electronics Specialists Conf.*, June *1993*, pp. 561 – 567.

[26]   J. Matevosyan, *Wind power in areas with limited export capability*, Licentiate Thesis Royal Institute of Technology Department of Electrical Engineering Stockholm, 2004.

[27]   A.J.G. Westlake, J.R. Bumby, and E. Spooner, "Damping the power-angle oscillations of a permanent-magnet synchronous generator with particular reference to wind turbine applications," *in IEE Proc. Electric Power Applications*, vol. 143, Issue: 3, May 1996, pp. 269–280.

[28]   S. Grabic, N. Celanovic, V. Katie, "Series converter stabilized wind turbine with permanent magnet synchronous generator," *in IEEE Conf. PESC 04, Power Electronics Specialists Conference*, vol. 1, June 2004, pp. 464 – 468.

[29]   L. Dambrosio, and B. Fortunato, "One step ahead adaptive control technique for a wind turbine-synchronous generator system," *in Proc. IECEC-97, Intersociety Energy Conversion Engineering Conference*, vol. 3, July 1997, pp. 1970 – 1975.

[30]   D.S .Zinger, E. Muljadi, "Annualized wind energy improvement using variable speeds," *IEEE Trans. on Industry Applications* , vol. 33 , Issue: 6 , pp. 1444 – 1447 Nov.-Dec. 1997.

[31]   P. Bauer, S.W.H. De Haan, and M.R.Dubois, "Wind energy and Offshore Windparks: State of the Art and Trends," *EPE-PEMC Dubrovnik & Cavat*, 2002, pp 1-15.

[32]   P. Bauer, S.W.H. De Haan, C.R. Meyl, and J.T.G. Pierik, "Evaluation of electrical systems for offshore wind farms," *Rec. in IEEE Industry Applications Conf.,* vol.3, Oct. 2000, pp. 1416–1423.

[33]   E. Bogalecka and Z. Krzeminski, "Control systems of doubly-fed induction machine supplied by current controlled voltage source inverter, " *in Sixth International Conf. on Electrical Machines and Drives, Conf. Publ. No. 376*, Sep 1993, pp. 168 – 172.

[34]   C. Knowles-Spittle, B.A.T. Al Zahawi, and N.D. MacIsaac, "Simulation and analysis of 1.4 MW static Scherbius drive with sinusoidal current converters in the rotor circuit," *in Proc. IEE Seventh International Conf. on Power Electronics and Variable Speed Drives, Conf. Publ. No. 456*, Sept. 1998, pp. 617 – 621.

Bibliography

[35]    R. Pena, J.C. Clare, and G.M. Asher, "A doubly fed induction generator using back-to-back PWM converters supplying an isolated load from a variable speed wind turbine, " *Electric Power Applications, IEE Proc.*, vol. 143, Issue: 5, Sept. 1996, pp. 380 – 387.

[36]    T. Yifan and Xu Longya, " A flexible active and reactive power control strategy for a variable speed constant frequency generating system," *IEEE Trans. on Power Electronics,* vol. 10 , Issue: 4 , pp. 472 – 478, July 1995.

[37]    Wen-Song Chienand and  Ying-Yu Tzou, "Analysis and design on the reduction of DC-link electrolytic capacitor for AC/DC/AC converter applied to AC motor drives, " *in Proc. IEEE PESC 98, Power Electronics Specialists Conf.,* vol. 1, May 1998, pp. 275 – 279.

[38]    J.S. Kim and S. K., Sul*,* "New control scheme for AC-DC-AC converter without DC link electrolytic capacitor, " *in IEEE Proc. PESC '93, Power Electronics Specialists Conference, 1993,* June 1993, pp. 300 – 306.

[39]    K. Siyoung, S. Seung-Ki, and T.A. Lipo, "AC to AC power conversion based on matrix converter topology with unidirectional switches," *in Proc. APEC '98, Applied Power Electronics Conf. and Exposition, 1998,* vol. 1, Feb. 1998, pp. 301 – 307.

[40]    M. Salo and H. Tuusa*,* "A high performance PWM current source inverter fed induction motor drive with a novel motor current control method," *in Proc. IEEE PESC 99, Power Electronics Specialists Conference, 1999,* vol. 1 , 27 June-1 July 1999, pp. 506 – 511.

[41]    M. Venturini, "A new sine wave in sine wave out, conversion technique which eliminates reactive elements, " *in Proc. POWERCON 7,* 1980, pp. E3_1–E3_15.

[42]     M. Venturini and A. Alesina, "The generalized transformer: A new bidirectional sinusoidal waveform frequency converter with continuously adjustable input power factor, " *in Proc. IEEE PESC'80,* 1980, pp. 242–252.

[43]    J. Rodriguez, "A new control technique for AC–AC converters," *in Proc IFAC Control in Power Electronics and Electrical Drives Conf.,* Lausanne, Switzerland, 1983, pp. 203–208.

[44]    D.H. Shin, G.-H. Cho, and S.-B. Park, "Improved PWM method of forced commutated cycloconvertors, " *in IEE Proc. Electric Power Applications,* Proc. B, vol. 136,  Issue 3,  May 1989, pp.121 – 126.

[45]    Y. H. Kim and M. Ehsani, "Control of force-commutated direct frequency changers," *in Conf. Industry Applications,* 1990, pp. 1163 – 1170.

[46]    N. Burany, "Safe control of four-quadrant switches," *in Conf. Rec. Industry Applications,* Oct. 1989, pp.1190 – 1194.

228

Bibliography

[47] L. Huber, D. Borojevic, and N. Burany, "Electric Analysis, design and implementation of the space-vector modulator for forced-commutated cycloconvertors," *in Proc. B, IEE Power Applications*, vol. 139, Issue 2, March 1992, pp. 103 – 113.

[48] M. Ziegler and W. Hofmann, "Semi natural two steps commutation strategy for matrix converters," *Rec. 29th Annual Power Electronics Specialists IEEE Conf., PESC 98,* vol. 1, May 1998, pp. 727 – 731.

[49] R. Teichmann and j. Oyama, "ARCP soft-switching technique in matrix converters," *IEEE Trans. On Industrial Electronics*, vol. 49, Issue 2, pp. 353 – 361, April 2002.

[50] J. Rodriguez, "A new control technique for AC–AC converters," *in Proc. IFAC Control in Power Electronics and Electrical Drives Conf.*, Lausanne, Switzerland, 1983, pp. 203–208.

[51] J. Oyama, T. Higuchi, E. Yamada, T. Koga, and T. Lipo, "New control strategy for matrix converter, " *in Proc. IEEE PESC'89, 1989*, pp. 360–367.

[52] P. D. Ziogas, S. I. Khan, and M. H. Rashid, "Analysis and design of forced commutated cycloconverter structures with improved transfer characteristics, " *IEEE Trans. Ind. Electronics*, vol. IE-33, pp. 271–280, Aug. 1986.

[53] P. Ziogas, S. Khan, and M. Rashid, "Some improved forced commutated cycloconverter structures, " *IEEE Trans. Ind. Applicat.*, vol. 1A-21, pp. 1242–1253, Sept./Oct. 1985.

[54] A. Alesina and M. G. B. Venturini, "Analysis and design of optimum amplitude nine-switch direct AC–AC converters, " *IEEE Trans. Power Electron.,* vol. 4, pp. 101–112, Jan. 1989.

[55] L. Huber and D. Borojevic, "Space vector modulated three phase to three phase matrix converter with input power factor correction," *IEEE Trans. Ind. Applicat.,* vol. 31, pp. 1234–1246, Nov./Dec. 1995.

[56] H. Hotate and K. Masuse, "Basic characteristics of matrix-converter-controlled by space vector modulation considering input voltage conditions" *in Conf. IPEMC 2004, the 4th International Power Electronics and Motion Control,* vol. 2, Aug. 2004 pp. 719 – 723.

[57] C. Wang and Q. Lu, "Analysis of naturally sampled space vector modulation PWM in over modulation region," *in Conf. IPEMC 2004, the 4th International Power Electronics and Motion Control Conf.,* vol. 2, Aug. 2004, pp. 694 – 698.

[58] L. Wei, T.A. Lipo, "A novel matrix converter topology with simple commutation," *Rec. in Conf. Thirty-Sixth IAS 2001, Industry Applications IEEE Conference Annual Meeting,* vol. 3, Sept. 2001, pp. 1749 – 1754.

Bibliography

[59]  Lixiang Wei, T.A. Lipo, Ho Chan, "Matrix converter topologies with reduced number of switches," *In Conf. PESC02, Power Electronics Specialists Conference*, vol. 1, June 2002, pp. 57 – 63.

[60]  P.W. Wheeler, J. Rodriguez, J. C. Clare, L. Empringham, A. Weinstein, "Matrix converters: a technology review, " *IEEE Trans. on Industrial Electronics* vol. 49, Issue 2, pp. 276 - 288 April 2002

[61]  C. Klumpner, P. Nielsen, I. Boldea, F. Blaabjerg, "A new matrix converter motor (MCM) for industry applications*," IEEE Trans. on Industrial Electronics,* vol. 49, Issue 2, pp. 325-335. April 2002

[62]   D. Casadei, G. Serra, A. Tani, and L. Zarri, "Matrix converter modulation strategies: A new general approach based on space-vector representation of the switch state," *IEEE Trans. On Industrial Electronics*, vol. 49, pp. 370–381, Apr. 2002.

[63]  O. Simon, J. Mahlein, M. N. Muenzer, and M. Bruckmarm, " Modern solutions for industrial matrix-converter applications," *IEEE Trans. On Industrial Electronics*, vol. 49, Issue 2, pp. 401-406, April 2002

[64]  L. Wei, Y. Matsushita, and T.A. Lipo, " Investigation of dual-bridge matrix converter operating under unbalanced source voltages," *in Conf. PESC '03, Power Electronics Specialist Conf.*, vol. 3, June 2003, pp. 1293 – 1298.

[65]  F. Blaabjerg, D. Casadei, C. Klumpner, and M. Matteini, "Comparison of two current modulation strategies for matrix converters under unbalanced input voltage conditions," *IEEE Trans. on Industrial Electronics*, vol. 49, Issue 2, pp :289 – 296, April 2002.

[66]  P.W. Wheeler, J.C. Clare, M. Apap, L. Empringham, C. Whitley, and G. Towers, "Power supply loss ride-through and device voltage drop compensation in a matrix converter permanent magnet motor drive for an aircraft actuator" *in Conf. PESC 04, Power Electronics Specialists Conf.,* vol. 1, June 2004, pp.149 – 154.

[67]  C. Klumpner, and F. Blaabjerg, "Experimental evaluation of ride-through capabilities for a matrix converter under short power interruptions," *IEEE Tran. on Industrial Electronics*, vol. 49, Issue 2, pp. 315 – 324, April 2002.

[68]  J. Adamek, W. Hofmann, and M. Ziegler, "Fast commutation process and demand of bidirectional switches in matrix converters, " *in Conf. PESC '03, Power Electronics Specialist Conf.* vol. 3, June 2003, pp. 1281 – 1286.

Bibliography

[69]  R. Sittig, A. Krysiak, and St. Chmielus, "Monolithic bidirectional switches promise superior characteristics, " *in Conf. PESC 04, Power Electronics Specialists Conference*, vol. 4, June 2004, pp. 2977 – 2982.

[70]  Kang Jun-Koo, H. Hara, E. Yamamoto, E. Watanabe, and J. Oyama, "Input harmonics damping for high power quality applications of matrix converter," *Rec. in 38th IAS Annual Meeting, Industry Applications Conf.,* vol. 3,  Oct. 2003, pp. 1498 – 1503.

[71]  S. Ferreira Pinto, and J. Fernando Silva, "Input filter design for sliding mode controlled matrix converters," *in Conf.  PESC '01, Power Electronics Specialists Conference*, vol. 2, June 2001, pp. 648 – 653.

[72]  D. Casadei, G. Serra, A. Tani, and L. Zarri, "Effects of input voltage measurement on stability of matrix converter drive system," *in Proc. IEE Electric Power Applications*, vol. 151, Issue 4, July 2004, pp. 487 – 497.

[73]  D. Casadei, G. Serra, A. Tani, L. Zarri, "Stability analysis of electrical drives fed by matrix converters, " *in Proc. IEEE ISIE 2002, International Symposium on Industrial Electronics*, vol. 4, July 2002, pp. 1108 – 1113.

[74]  L. Helle, K.B. Larsen, A. H. Jorgensen, S. Munk-Nielsen, F. Blaabjerg, "Evaluation of modulation schemes for three-phase to three-phase matrix converters," *IEEE Transactions on Industrial Electronics*, vol. 51, issue 1,  Feb. 2004 pp.158 – 171.

[75]  M. Aten, C. Whitley, G. Towers, P. Wheeler, J. Clare, K. Bradley, "Dynamic performance of a matrix converter driven electro-mechanical actuator for an aircraft rudder," *in Proc. second International Conference on Power Electronics, Machines and Drives, PEMD 2004*, vol. 1, April 2004, pp. 326 – 331.

[76]  B. Ooi and M. Kazerani, "Elimination of the waveform distortions in the voltage-source-converter type matrix converter," *in Conf. Rec. IEEE-IAS Annu. Meeting*, vol. 3, 1995, pp. 2500–2504.

[77]  P. Nielsen, *The matrix converter for an induction motor drive*,  Ph.D. dissertation, Inst. Energy Technol., Aalborg Univ., Aalborg East, Denmark, 1996.

[78]  P. W. Wheeler and D. A. Grant, "A low loss matrix converter for AC variable-speed drives," *in Proc. EPE Conf.*, vol. 5, 1993, pp. 27–32.

[79]  A.M. Hava, R. J. Kerkman, T.A. Lipo, "A high performance generalized discontinuous PWM algorithm, " *in Proc. PEC'97*, vol. 2, 1997, pp. 886–894.

Bibliography

[80]    P. Nielsen, F. Blaabjerg, and J. K. Pedersen, "Space vector modulated matrix converter with minimized number of switchings and a feed forward compensation of input voltage unbalance, " *in Proc. PEDES'96*, vol. 2, 1996, pp. 833–839.

[81]    J.Wu, P.Dong, J.M. Yang, and Y.R. Chen, "A Novel Model of Wind Energy Conversion System," *in Proc. DRPT2004, IEEE International Conf. on Electric Utility Deregulation and Power Technologies* , April 2004 Hong Kong, pp. 804-809.

[82]    R., Teodorescu and F. Blaabjerg, "Flexible control of small wind turbines with grid failure detection operating in stand-alone and grid-connected mode," *IEEE Trans. on Power Electronics* vol. 19, Issue 5, pp. 1323 – 1332, Sept. 2004.

[83]    T. Satish, K. K. Mohapatra, N. Mohan, "Speed Sensor-less Direct Power Control of a Matrix Converter Fed Induction Generator for Variable Speed Wind Turbines," *in Proc. Power Electronics, Drives and Energy Systems,* PEDES'06, Dec 2006,  pp. 1-6.

[84]    S. F. Pinto, L. Aparicio, P. Esteves, "Direct Controlled Matrix Converters in Variable Speed Wind Energy Generation Systems Power Engineering," *in Proc. Energy and Electrical Drives, POWERENG 2007,* April 2007, pp. 654 – 659.

[85]    Huang Keyuan, He Yikang, "Investigation of a matrix converter-excited brushless doubly-fed machine wind-power generation system," *in Proc. Power Electronics and Drive Systems, PEDS 2003,* Nov. 2003, Vol. 1, pp. 743 – 748.

[86]    Qi Wang, Xiaohu Chen, Yanchao Ji, "Control for Maximal Wind Energy Tracing in Matrix Converter AC Excited Brushless Doubly-Fed Wind Power Generation System," *in Proc. IEEE Industrial Electronics, IECON 2006,* Nov. 2006, pp. 718 – 723.

[87]    L. Zhang, C. Watthanasarn, "A matrix converter excited doubly-fed induction machine as a wind power generator," *in Proc. Power Electronics and Variable Speed Drives,* Sept. 1998, pp. 532 – 537.

[88]    D. Aouzellag, K. Ghedamsi, E.M. Berkouk, "Network Power Flow Control of Variable Speed Wind Turbine," *in Proc. Power Engineering, Energy and Electrical Drives, POWERENG 2007,* April 2007, pp. 435 – 439.

[89]    L. Zhang, C. Watthanasarn, W. Shepherd, "Application of a matrix converter for the power control of a variable-speed wind-turbine driving a doubly-fed induction generator," *in Proc. Industrial Electronics, Control and Instrumentation, IECON 97.* Vol. 2*,* Nov. 1997, pp. 906-911.

Bibliography

[90]  M. Kazerani, *Dynamic Matrix Converter Theory Development and Application*, Ph.D. thesis, Department of Electrical Eng., McGill University, Canada, 1995.

[91]  B.T. Ooi and M. Kazerani, "Application of dyadic matrix converter theory in conceptual design of dual field vector and displacement factor controls", *in Proc. IEEE Industry Applications Society Annual Meeting,* Vol. 2, Oct. 1994, pp. 903-910.

[92]  H. Nikkhajoei, A. Tabesh, and R. Iravani, "Dynamic model of a matrix converter for controller design and system studies", *IEEE Trans. on Power Delivery*, Vol. 21, Issue 2, Apr. 2006, pp. 744 – 754.

[93]  A. Alesina and M. Venturini, "Solid-state power conversion: A Fourier analysis approach to generalized transformer synthesis", *IEEE Trans. on Circuits and Systems*, Vol. 28, Issue 4, Apr. 1981, pp. 319 – 330.

[94]  S.M. Barakati, M. Kazerani, J.D. Aplevich, "An overall model for a matrix converter," *Accepted in IEEE International symposium on Industrial Electronics, ISIE08*, June 2008, pp.

[95]  S. M. Barakati, M. Kazerani, and J.D. Aplevich "A Dynamic Model for a Wind Turbine System Including a Matrix Converter, " *in Proc. IASTED, PES2007*, January 2006, pp. 1-8.

[96]  P. C. Krause, O Wasynczuk , S. D. Sudhoff, *Analysis of electric machinery*, IEEE Press, 1994.

[97]  L. Neft and C.D. Shauder, "Theory and Design of a 30-hp Matrix converter, " *IEEE Trans. on Industrial Applications*, vol. 28, no. 3, pp. 546-551, 1992.

[98]  P. Wheeler and D. Grant, "Optimized input filter design and low loss switching techniques for a practical matrix converter" *in Proc. of industrial electronics*, vol. 144, no. 1, Jan. 1997, pp. 53–60.

[99]  D.G. Holmes and T.A. Lipo, "Implementation of a controlled rectifier using AC-AC matrix converter theory", *in Conf. Rec. PESC '89, Power Electronics Specialists Conf.*, June 1989, vol.1, pp. 353 – 359.

[100]  H.W. van der Broeck, H.-C. Skudelny, and G.V.Stanke, "Analysis and realization of a pulsewidth modulator based on voltage space vectors," *IEEE Tran. on Industry Applications*, vol. 24, pp: 142 – 150, Jan.-Feb. 1988.

[101]  J.Hltz, "Pulsewidth modulation- A survey," *IEEE Trans. on Industrial Electronics*, vol.39, No. 5, 1999, pp. 410-420.

[102]  L. Zhang, C. Wathanasarn, and W. Shepherd, "Switch sequencer circuit for safe commutation of a matrix converter," *Electronics Letters* , vol. 31, Issue: 18 , Aug. 1995, pp. 1530 -1532.

Bibliography

[103] S. Kim, S-K. Sul and T.A. Lipo, "AC/AC power conversion based on matrix converter topology with unidirectional switches, " *IEEE Tran. on Industry Applications*, vol .36, No. 1, 2000 , pp. 139-145.

[104] K. Iimori, K. Shinohara, O. Tarumi, Z. Fu, and M. Muroya, "New current-controlled PWM rectifier-voltage source inverter without DC link components" *in Proc. of the Power Conversion Conf.*, Nagaoka, Japan, vol. II, Aug. 1997, pp. 783-786.

[105] J.W. Kolar, M. Baumann, F. Schafmeister, and H. Ertl, "Novel three-phase AC-DC-AC sparse matrix converter," *in Proc. Applied Power Electronics Conf. and Exposition*, vol. 2, March 2002, pp. 777–791.

[106] S.M. Barakati, M. Kazerani, and X. Chen "A New Wind Turbine Generation System Based on Matrix Converter, " *in Proc. IEEE PES General Meeting, June 2005,* pp. 2083-2089.

[107] E.S. Adin and W. Xu, "Control Design and Dynamic Performance Analysis of a Wind Turbine-Induction Genrator Unit," *IEEE Trans. On Energy Conversion*, Vol. 15, NO. 1, MARCH 2000, pp 91-96.

[108] J.G. Slootweg, H. Polinder, and W.L. Kling, "Representing Wind Turbine Electrical Generating Systems in Fundamental Frequency Simulations," *IEEE Trans. on Energy Conversion*, Vol. 18, No.4, Dec. 2003, pp 516-524.

[109] J. G. Slootweg, S. W. H. de Haan, H. Polinder, and W. L. Kling, "General Model for Representing Variable Speed Wind Turbines in Power System Dynamics Simulations", *IEEE Trans. On Power Systems*, Vol. 18, NO. 1, FEB.2003, pp. 144-151.

[110] L.S.T. Ackermann, "Wind Energy Technology and current status. A Review", *Renewable and Sustainable Energy Review*, 4:315-375, 2000.

[111] E. Muljadi, C.P. Butterfield, "Power Quality Aspects in a Wind Power Plant," *IEEE Power Engineering Society General Meeting Montreal*, Quebec, Canada June, 2006, pp.

[112] Rolf Grünbaum, "Voltage and power quality control in wind power" *ABB Power Systems AB* available at http://library.abb.com/GLOBAL/SCOT/scot221.nsf/VerityDisplay/6B5A44E46B AD5D3DC1256FDA003B4D11/$File/PowerGenEurope2001.pdf,February 2008.

[113] Tomas Petru and T. Thiringer, " Modeling of Wind Turbines for Power System Studies," *IEEE Trans. On Power System*, Vol. 17, NO. 4, NOV. 2002,pp 1132-1139.

[114] A. D. Hansen, C. Jauch, P. Sørensen, F. Iov, F. Blaabjerg, "Dynamic wind turbine models in power system simulation tool DIgSILENT," *Risø National Laboratory, Roskilde,* available at http://www.digsilent.de/Software/Application_Examples/ris-r-1400.pdf, Dec. 2003.

Bibliography

[115] S. Seman, F. Iov, J. Niiranen, A. Arkkio, "Comparison of Simulators for Variable Speed Wind Turbine Transient Analysis," *International Journal of Energy Research*, 2006, Vol. 30, Issue 9, pp. 713-728.

[116] L. Mihet-Popa, F. Blaabjerg, and I. Boldea, "Wind turbine Generator modeling and Simulation where rotational speed is the controlled variable," *IEEE Trans. on Industry Application*, Vol. 40, Jan/Feb 2004, pp 3-10.

[117] B. K. Bose, *Power Electronics And Ac Drives*, Prentice-Hall, 1986.

[118] P. C. Krause, *Analysis of Electrical Machinery*, McGraw-Hill Book Co, 1987.

[119] T.F. Chan, and Loi Lei Lai, "Capacitance requirements of a three-phase induction generator self-excited with a single capacitance and supplying a single-phase load, " *IEEE Trans. on Energy Conversion,* vol. 17,  Issue 1,  pp. 90 – 94, March 2002.

[120] Electric Systems Consulting ABB Inc., "Integration of Wind Energy into the Alberta Electric System – Stages 2 & 3: Planning and Interconnection Criteria," *Prepared for Alberta Electric System Operator* Report Number: 2004-10803-2.R01.4.

[121] B. Ozpineci, L.M. Tolbert, "Simulink implementation of induction machine model- a modular approach", *in Proc. Electric Machines and Drives Conference, IEMDC'03*, Vol. 2, Jun. 2003, pp. 728-734.

[122] A. Munoz-Garcıa, T. A. Lipo,  and D. W. Novotny, "A New Induction Motor V/f Control Method Capable of High-Performance Regulation at Low Speeds," *IEEE Tran. on Industry Applications*, Vol. 34, NO. 4, July 1998 pp 813-821.

[123] Powersim Technologies inc, *Psim User Manual*, Version 4.1, Set.1999, available at http://www.powersimtech.com, February, 2008.

[124] P. M. Anderson and A. Bose, "Stability Simulation of Wind Turbine Systems," *IEEE Trans. Power Apparatus and system* , Vol. PAS-102, No. 12, pp. 3791-3795, Dec 1983.

[125] C. Nichita, D. Luca, B. Dakyo, E. Ceanga, " Large band simulation of the wind speed for real time wind turbine simulators", IEEE Trans. on Energy Conversion, Vol. 17, No. 4, Dec. 2002, pp 523 – 529.

[126] *Starting (and Stopping) a Turbine*, available at http://www.windpower.org/en/tour/wtrb /electric.htm, February, 2008.

[127] J. D. Aplevich, *The Essentials of Linear State-Space Systems*, New York: Wiley, 1999.

[128] Khalil, *H. Nonlinear Systems*, Prentice Hall Inc, second edition, 1996.

Bibliography

[129] Jong-Yeob Shin, "Quasi-Linear Parameter Varying Representation of General Aircraft Dynamic Over A Non-Trim Region", *National Institute of Aerospace Hampton, Virginia, NASA Report, 2007, NO.2005-08.*

[130] D. Davison, *Multivariable Control Systems*, Course Notes-Part B, Published by University of Waterloo, 2005.

[131] *Control System Toolbox for Use with Matlab*, Reference Version 6, available at www.mathworks.com, February, 2008.

[132] B.C. Moore, "Principal component analysis in linear systems controllability, observability, and model reduction", *IEEE Transactions on Automatic Control,* Vol. AC-26, (no. I), pages 17-32, February 1981.

[133] *Control tutorials for Matlab*, University of Michigan, available at http://www.engin.umich.edu /group/ctm/examples/pitch/SSpitch.html, February 2008.

[134] Joao P. Hespanha, *LQG/LQR Controller Design*, Lecture Note of ECE147C, University of Californi*a*, Santa Barbara, May 2006.

[135] D. Davison, "Feedback Control: Limitations on Tracking Performance," *Presented in graduated student talks seminar*, ECE department at university of Waterloo, January 2007.

[136] Wikipedia, *Typical Observer Model*, available at http://en.wikipedia.org/wiki/State_observer, February, 2008.

[137] *Matlab Robust Control Toolbox*, Reference Version 6, available at  www.mathworks.com, February, 2008.

[138] J. Medanic, H.S. Trap and W.R. Pekins, "Pole placement by performance criterion modification," *IEEE Transaction on Automatic Control, Vol. 33, No. 5, May 1988, pp. 596-472.*

[139] L. S. Shieh, H. M. Did and R. E. Yates, "Sequential Design of linear quadratic state regulator via the optimal root-locus techniques," *Control Theory and Applications, IEE proceedings, 1988, pp.289-294.*

[140] K. Sugimoto, "Partial pole placement by LQ regulators: An inverse problem approach," *IEEE Transaction on Automatic Control, Vol. 43, No. 5, May 1998, pp. 706-708.*

[141] D. Di Ruscio, "On the location of LQ-optimal closed-loop poles," *Proceedings of the 30th Conference on Decision and Control*, 1991, pp. 2317-2320.

[142] M. H. Hsueh and H. Sehitoglu, "A new eigenvalue placement method for linear dynamic systems," *Proceedings of the 36th Conference on Decision and Control, 1997, pp. 4286-4287.*

Bibliography

[143] D. A. Coly, "An introduction to genetic algorithms for scientists and engineers," *Word scientific, 1999.*

[144] D.E. Gol, *Genetic algorithms in search optimization and machine learning*, Addison Wesle, 1989.

[145] N. Mansouri, H. Khaloozadeh, "The GA approach to eigenvalue placement of an LQ optimal system," *Proceedings of the 2002 IEEE International Conference on Artificial Intelligence System,* 2002, pp.

[146] Blight, J.D., Dailey, R.L. and Gangsass, D. (1994), "Practical control law design for aircraft using multivariable techniques," *International Journal of Control,* Vol. 59, No. 1, 93-137.

[147] S. Skogestad, I. Postlethwaite, *Multivariable feedback control analysis and design*, Second edition, Wiley, 2005.

[148] J. Lunze, *Feedback control of large-scale systems*, Prentice Hall, 1992.

[149] G. Zames and D. Bensoussan," Multivariable feedback, sensitivity and decentralized control," *IEEE Transactions on automatic control, AC-28 (11), 1983, pp 1030-1035.*

[150] J.M. Maciejowski, "Multivariable feedback design," Addison-Wesley Publishing Company, 1989.

[151] G.F. Franklin, J.D. Powell, A. Emami-Naeini, *Feedback Control of Dynamic System*, Fourth Edition, Prentice-Hall, 2002.

[152] S. M. Barakati, J.D. Aplevich, M. Kazerani, "Controller Design for a Wind Turbine System Including a Matrix Converter, " *in Proc. IEEE Power Engineering Society General Meeting, 2007*, pp 1- 8.

[153] T. Thiringer and J. Linders, "Control by variable rotor speed of a fixed-pitch wind turbine operating in a wide speed range," *IEEE Trans. Energy Conv.,vol. EC-8,pp.520-526,Sept. 1993.*

[154] Q. Wang and L. Chang, "An intelligent maximum power extraction algorithm for inverter-based variable speed wind turbine systems, " *IEEE Trans. Power Electronics, vol. 19, Issue: 5, pp. 1242 – 1249, Sept. 2004.*

[155] E. Koutroulis, K. Kalaitzakis, "Design of a maximum power tracking system for wind-energy-conversion," *applications Industrial Electronics, IEEE Transactions on,* Vol. 53,  Issue 2, April 2006 pp. 486 – 494.

[156] C. Hua and C. Shen, "Comparative study of Peak Power Tracking Techniques for Solar Storage System," *Applied power Electronics Conference and Exposition*, vol.2,pp.679-685,Feb.1998.

Bibliography

[157] E. Koutroulis, K. Kalaitzakis, and N.C. Voulgaris, "Development of a microcontroller-based, photovoltaic maximum power point tracking control system," *IEEE Trans. on Power Electronics* vol. 16, Issue 1, pp. 46 – 54, Jan. 2001.

[158] T. Tanaka, T. Toumiya, "Output Control by Hill-Climbing Method For a Small Wind Power Generating System, " Renewable Energy, Vol. 12, No. 4, 1977, pp. 387-400.

[159] I.K. Buehring, L.L. Freris, "Control Policies for Wind Energy Conversion Systems," IEE Proc. , Vol. 128, pt. C, No. 5, Sept. 1981.

[160] M.Ermis, H.B. Ertan, E. Akpinar, F. Ulgut, Electric, "Autonomous wind energy conversion system with a simple controller for maximum-power transfer," *Power Applications, IEE Proceedings B,* Vol. 139, Issue 5, Sept. 1992, pp.421 – 428.

[161] R.J Wai, C.Y. Lin,Y.R. Chang, "Novel maximum-power-extraction algorithm for PMSG wind generation system, Electric Power Applications," *IET*, Vol.1, Issue 2, March 2007, pp:275–283.

[162] R. Chedid, F. Mard, and M. Basma, "Intelligent control of a class of wind energy conversion system," *IEEE Trans. Energy Conv.,* vol. EC-14,pp.1597-1604, Dec. 1999.

[163] G. Poddar, A. Joseph, and A.K. Unnikrishnan, " Sensorless variable-speed controller for existing fixed-speed wind power generator with unity-power-factor opration", *IEEE Trans. Industrial Electronics,* vol.50, N0.5, pp.1007-1015, Oct. 2003.

[164] T. Senjyu, Y. Ochi, E. Muhando, N. Urasaki, H. Sekine, "Speed and Position Sensor-less Maximum Power Point Tracking Control for Wind Generation System with Squirrel Cage Induction Generator, " *IEEE PES, PSCE '06.* Oct. 29 2006-Nov. 1 2006, pp. 2038 – 2043.

[165] S.M. Barakati, M. Kazerani, and J.D. Aplevich, "A Mechanical Speed-Sensorless Maximum Power Tracking Control for a Wind Turbine System Including a Matrix Converter, " *accepted in IEEE PES General Meeting,PES 2008.*